KOMUNIKÁCIE
COMMUNICATIONS

OPERATION AND ECONOMICS

MECHANICAL ENGINEERING

ELECTRICAL ENGINEERING

CIVIL ENGINEERING

SAFETY AND SECURITY ENGINEERING

Olga Blazekova - Maria Vojtekova*

USING OF PARALLEL COORDINATES IN FINDING MINIMUM DISTANCE IN TIME-SPACE

Airspace domain may be represented by a time-space consisting of a three-dimensional Cartesian coordinate system and time as the fourth dimension. A coordinate system provides a scheme for locating points given its coordinates and vice versa. The choice of coordinate system is important, as it transforms data to geometric representation. Visualization of the three and more dimensional data on the two-dimensional drawing - computer monitor is usually done by projection, which often can restrict the amount of information presented at a time. Using the parallel coordinate system is one of possibilities to present multidimensional data. The aim of this article is to describe basics of parallel coordinate system and to investigate lines and their characteristics in time-space.

Keywords: *parallel coordinates, time-space, air traffic control*

1. Introduction

During the peak air travel times in the United States, there are about 5,000 airplanes in the sky every hour. This translates to approximately 50,000 aircraft operating every day. How are these aircraft kept from colliding with each other? How does air traffic move into and out of an airport? A collision between aircrafts is one of the most sudden and catastrophic transportation accidents. Ensuring the highest level of passenger safety is a key goal for air traffic control (ATC) authorities. Air traffic controllers must coordinate all movements of thousands of aircrafts, keep them at safe distances from each other, direct them during the takeoff and landing aircrafts from and to airports, direct them around bad weather and ensure that traffic flows smoothly with minimal delays [1]. Many new conflict detection, resolution and visualization tools have been developed to support the needs of controllers. Data visualization tools portray the volume data in visual schemes that facilitate the human operator discovering the relationship that would not be apparent in tables and graphs. Visualization of the three and more dimensional data on the two-dimensional drawing - computer monitor is only possible by projection, which often can restrict the amount of information presented at a time. Using the parallel coordinates represents one of options to visualize the multidimensional data.

Airspace domain constitutes time-space consisting of three-dimensional Cartesian coordinate system and time as the fourth dimension. The x-axis represents altitude where the positive x direction is of the higher elevation and the negative x direction is of the lower elevation. The y-axis represents the east and west directions, the positive y direction points east and the negative y direction points west. The z-axis represents north and south with the positive z direction pointing north and the negative z direction pointing south. In the parallel 4 coordinate plot, each dimension (variable) corresponds to an axis, and the 4 axes are organized as uniformly spaced vertical lines. A data element in the 4-dimensional space manifests itself as a connected set of points, one on each axis. Points lying on a common line or plane create readily perceived structures in the image.

Parallel coordinates is a widely used visualization technique for multidimensional objects and multivariate relations. The system was invented by Philbert Maurice d'Ocagne in 1885 [2] and were independently re-discovered and popularized by Al Inselberg in 1959 and systematically has been developed as a coordinate system starting from 1977. The parallel coordinates methodology was used when the new air traffic control system in United States was formed around 1985 - US patent # 4,823,272, p. 100 [3]. Using of parallel coordinates for visualization of the high-dimensional data set is shown in [4-6]. The authors of [7] were concentrated on ordering and positioning of the coordinate axes. Authors of [8] compared scatterplots and parallel coordinate plots as visualization methods. A method for mobility analysis based on the parallel coordinates is presented by [9]. Application of the parallel coordinates in geographic visualization is shown in [10]. Moreover, the parallel coordinates coupled with statistical analysis can be used for more effective knowledge discovery and confirmation in complex, environmental data sets [11].

2. Parallel coordinates in space-time

Many applications are using the *space-time* which regards space as consisting of three dimensions, and time asconsituting the fourth dimension. The parallel coordinates are based on projective geometry and duality of points and hyperplanes in the n-dimensional space. Hyperplane in the projective space $\mathbb{P}^4$ is the three-dimensional space and a line is the intersection of three nonparallel hyperplanes [1]. Let a space-time have coordinates t,x_1,x_2,x_3; t is the time axis, x_1,x_2,x_3 axes assign three dimensional position of a point.

* **Olga Blazekova, Maria Vojtekova**
Faculty of Operation and Economics of Transport and Communications, University of Zilina, Slovakia
E-mail: olga.blazekova@fpedas.uniza.sk, maria.vojtekova@fpedas.uniza.sk

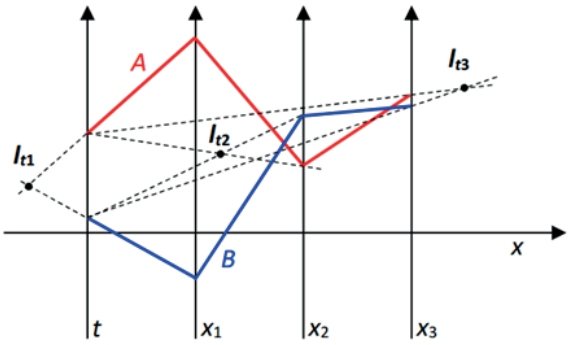

Figure 1 *Representation of the line l=AB in parallel coordinates t, x_1, x_2, x_3*

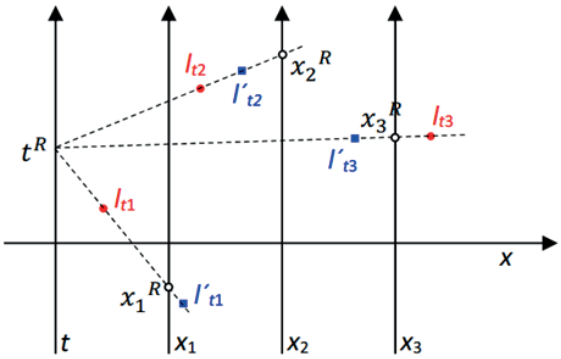

Figure 2 *Representation of intersecting lines $(l \cap l' = R)$ in parallel coordinates t, x_1, x_2, x_3*

2.1 Representation of a line in space-time

One can say that the line l is the set of points (specified by 4-tuples (t,x_1,x_2,x_3)) satisfying a set of the three linearly independent linear equations (at least one of coefficients a_t,a_1,a_2,a_3 must be nonzero and so on):

$$l:\begin{array}{l} a_t t + a_1 x_1 + a_2 x_2 + a_3 x_3 + a_0 = 0 \\ b_t t + b_1 x_1 + b_2 x_2 + b_3 x_3 + b_0 = 0 \\ c_t t + c_1 x_1 + c_2 x_2 + c_3 x_3 + c_0 = 0 \end{array} \quad (1)$$

and one wants to find a suitable representation of the line l.

After some arrangements and using equivalent matrix operations, one obtains (with the exception of some special cases but here is being dealt with the general situation):

$$\begin{pmatrix} a_1 & a_2 & a_3 & a_t & a_0 \\ b_1 & b_2 & b_3 & b_t & b_0 \\ c_1 & c_2 & c_3 & c_t & c_0 \end{pmatrix} \sim \begin{pmatrix} -1 & 0 & 0 & m_1 & q_1 \\ 0 & -1 & 0 & m_2 & q_2 \\ 0 & 0 & -1 & m_3 & q_3 \end{pmatrix}. \quad (2)$$

So, one can write the convenient form of the line representation:

$$l:\begin{array}{rcl} l_{t,1}{:}x_1 & = & m_1 t + q_1 \\ l_{t,2}{:}x_2 & = & m_1 t + q_2 \\ l_{t,3}{:}x_3 & = & m_3 t + q_3 \end{array}. \quad (3)$$

Each hyperplane $l_{t,1},l_{t,2},l_{t,3}$ is represented in the parallel coordinates by a point, so the line l is represented by three points, Figure 1.

Generally, each equation is containing a pair of adjacently indexed variables. In the x_{i-1},x_i plane, the relation labeled $l_{i-1,i}$ is a line, and by *point* $\leftrightarrow$ *line* duality it can be represented by the point $l_{i-1,i}$. Many applications are using the t variable as a basic one, so it is more comfortable to use tuples $(t,x_1),(t,x_2),(t,x_3)$.

Geometrically: a line l is defined by two points $A(t^A,x_1^A,x_2^A,x_3^A)$, $B(t^B,x_1^B,x_2^B,x_3^B)$ and one can obtain points $l_{t,i}$ as intersections of relevant line (line segments): $l_{t,i} = t^A x_i^B \cap t^B x_i^A$, $i = 1,2,3$ (Figure 1).

If the distance between each pair of adjacent parallel axes t,x_1,x_2,x_3 is taken as one unit and Cartesian plane coordinates x, y are defined (axis x is horizontal line and $y = t$ axis), then the homogeneous coordinates of points $l_{t,i}$ are:

$$l_{t,i}\left(\frac{i}{1-m_i},\frac{q_i}{1-m_i},1\right) \sim (i,q_i,1-m), m_i \neq 1, i = 1,2,3. \quad (4)$$

Let there be two lines l,l' with Equations (3):

$$\begin{array}{rcl} l_{t,1}{:}x_1 & = & m_1 t + q_1 \\ l_{t,2}{:}x_2 & = & m_1 t + q_2 \\ l_{t,3}{:}x_3 & = & m_3 t + q_3 \end{array} \quad \begin{array}{rcl} l'_{t,1}{:}x_1 & = & m'_1 t + q'_1 \\ l'_{t,2}{:}x_2 & = & m'_1 t + q'_2 \\ l'_{t,3}{:}x_3 & = & m'_3 t + q'_3 \end{array}. \quad (5)$$

For many interpretations, let t denote the elapsed time and (x_1,x_2,x_3) the space coordinates of a particle moving with constant velocity $\vec{v}$ and initial position P. The line l is the trajectory of the particle 1 with velocity $\vec{v} = (m_1,m_2,m_3)$ and initial position (q_1,q_2,q_3) and the line l' is the trajectory of the particle 2 with velocity $\vec{v} = (m'_1,m'_2,m'_3)$ and initial position (q'_1,q'_2,q'_3). Lines l,l' are represented in parallel coordinates by points $l_{t,1},l_{t,2},l_{t,3}$ and $l'_{t,1},l'_{t,2},l'_{t,3}$.

Lines l,l' have an intersection point R $(l \cap l' = R)$, if all lines $l_{t,i}l'_{t,i}$, i = 1, 2, 3, intersect t axis in the same point. This point corresponds to the t-coordinate of the intersection point R (Figure 2). Numerically, let the lines have Equations (5), so one can easily see that the intersection point exists, if

$$-\frac{q'_1-q_1}{m'_1-m_1} = -\frac{q'_2-q_2}{m'_2-m_2} = -\frac{q'_3-q_3}{m'_3-m_3} = t^R. \quad (6)$$

Lines l,l' are parallel, if vectors $\vec{m} = (m_1,m_2,m_3)$, $\vec{m'} = (m'_1,m'_2,m'_3)$ are linearly dependent. The representation of parallel lines l,l' are points $l_{t,i},l'_{t,i}$, i = 1, 2, 3 which have the same Cartesian coordinate x. Representation in parallel coordinates easily shows gaps on the x_1,x_2,x_3 axes at the same time t^c in Figure 3.

Let there be two lines l,l', which are represented in parallel coordinates by points $l_{t,1},l_{t,2},l_{t,3}$ and $l'_{t,1},l'_{t,2},l'_{t,3}$. Numerically, let the lines have Equations (5), then denote

$$t_1 = -\frac{q'_1-q_1}{m'_1-m_1}, t_2 = -\frac{q'_2-q_2}{m'_2-m_2}, t_3 = -\frac{q'_3-q_3}{m'_3-m_3}. \quad (7)$$

If any $t_i \neq t_j; i,j \in \{1,2,3\}$ then lines are nonintersecting (Figure 4). The absolute value $|\max t_i - \min t_i|$ converges to zero as the minimum distance D between the lines converges to zero (when the two lines intersect, D = 0).

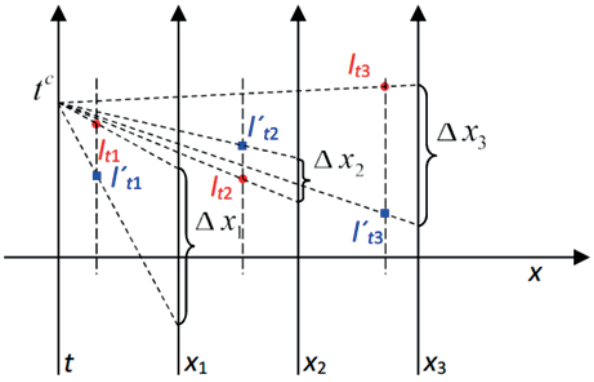

Figure 3 *Representation of the parallel lines l, l' in parallel coordinates t, x_1, x_2, x_3*

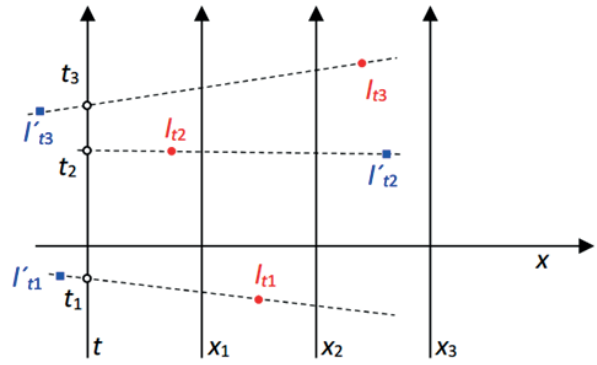

Figure 4 *Representation of nonintersecting lines in parallel coordinates t, x_1, x_2, x_3*

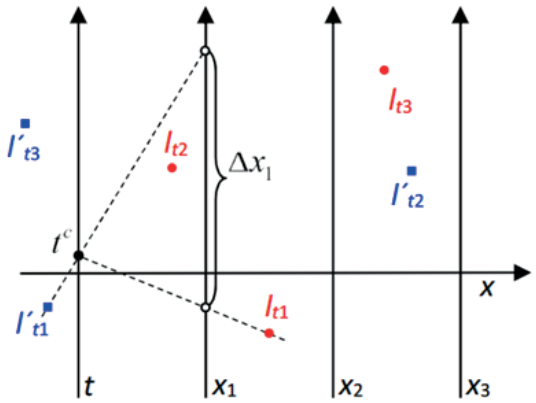

Figure 5 *Representation of nonintersecting lines in parallel coordinates t, x_1, x_2, x_3*

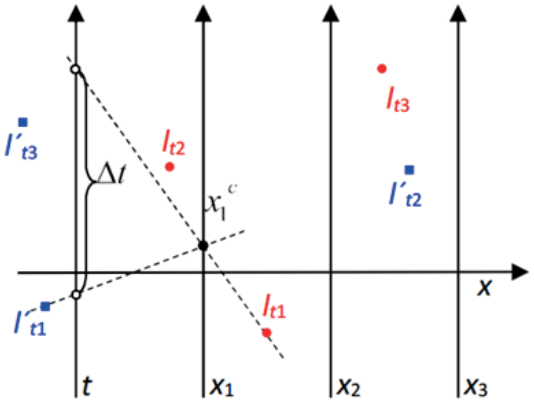

Figure 6 *Representation of nonintersecting lines in parallel coordinates t, x_1, x_2, x_3*

2.2 Minimum distance between the two lines in space-time

It is an interesting question to visualize the minimum distance between the two lines and points on each line where the minimum occurs. In many problems what is required is to minimize the distance when one or more of the variables are constrained to the same value for both lines. An example is air traffic control and motion planning in general, where knowing time and position, when two aircrafts are the closest, is needed. Let there be a point $P(t^P, x_1^P, x_2^P, x_3^P)$, $P \in l$ and the point $P'(t^{P'}, x_1^{P'}, x_2^{P'}, x_3^{P'})$, $P' \in l'$. Sometimes it is used *Manhattan distance* between points which is the sum of the lengths of the projections of the line segments between the points onto the coordinate axes [12]. The time is often constrained $(t^P = t^{P'})$ and one wants to find the minimum *Manhattan distance* between the points P, P' at that time:

$$L_1(P,P') = \sum_{i=1}^{3} \left| x_i^P - x_i^{P'} \right|. \tag{8}$$

If lines l, l' are parallel, one can see the visualization of gaps on axis at time t^c in Figure 3. If lines l, l' are nonparallel and nonintersecting one can see in Figure 5 the gap on the x_1 axis (altitude) at time t^c. One may easily recognize (Figure 6) the gap on the t axis when the coordinate x_1 is fixed to x_1^c (altitude).

If the time is not fixed, the *Manhattan distance* between points P, P' is:

$$L_1(P,P') = \left| t^P - t^{P'} \right| + \left| x_1^P - x_1^{P'} \right| + \left| x_2^P - x_2^{P'} \right| + \left| x_3^P - x_3^{P'} \right|. \tag{9}$$

Using expressions (7) for points on lines one can write:

$$\begin{aligned} L_1(t) &= \sum_{i=1}^{3} \left| x_i^P(t) - x_i^{P'}(t) \right| = \\ &= \sum_{i=1}^{3} \left| m_i - m_i' \right| \left| t + \frac{q_i - q_i'}{m_i - m_i'} \right|, \end{aligned} \tag{10}$$

denote $m_i - m_i' = \Delta m_i$ and t_i are intercepts defined in Equation (6)

$$L_1(t) = \sum_{i=1}^{3} \left| \Delta m_i \right| \left| t - t_i \right|. \tag{11}$$

The unique minimum value of $L_1(t)$ is attained at $t = t_i$ for at least one i = 1, 2, 3. The proof of this theorem one can find in [9] p. 93-96.

2.3 Illustrative example

Let there be two moving particles. The line l is the trajectory of the particle 1 with velocity $\vec{v} = \left(\frac{1}{2}, \frac{1}{2}, \frac{1}{2}\right)$ and initial position

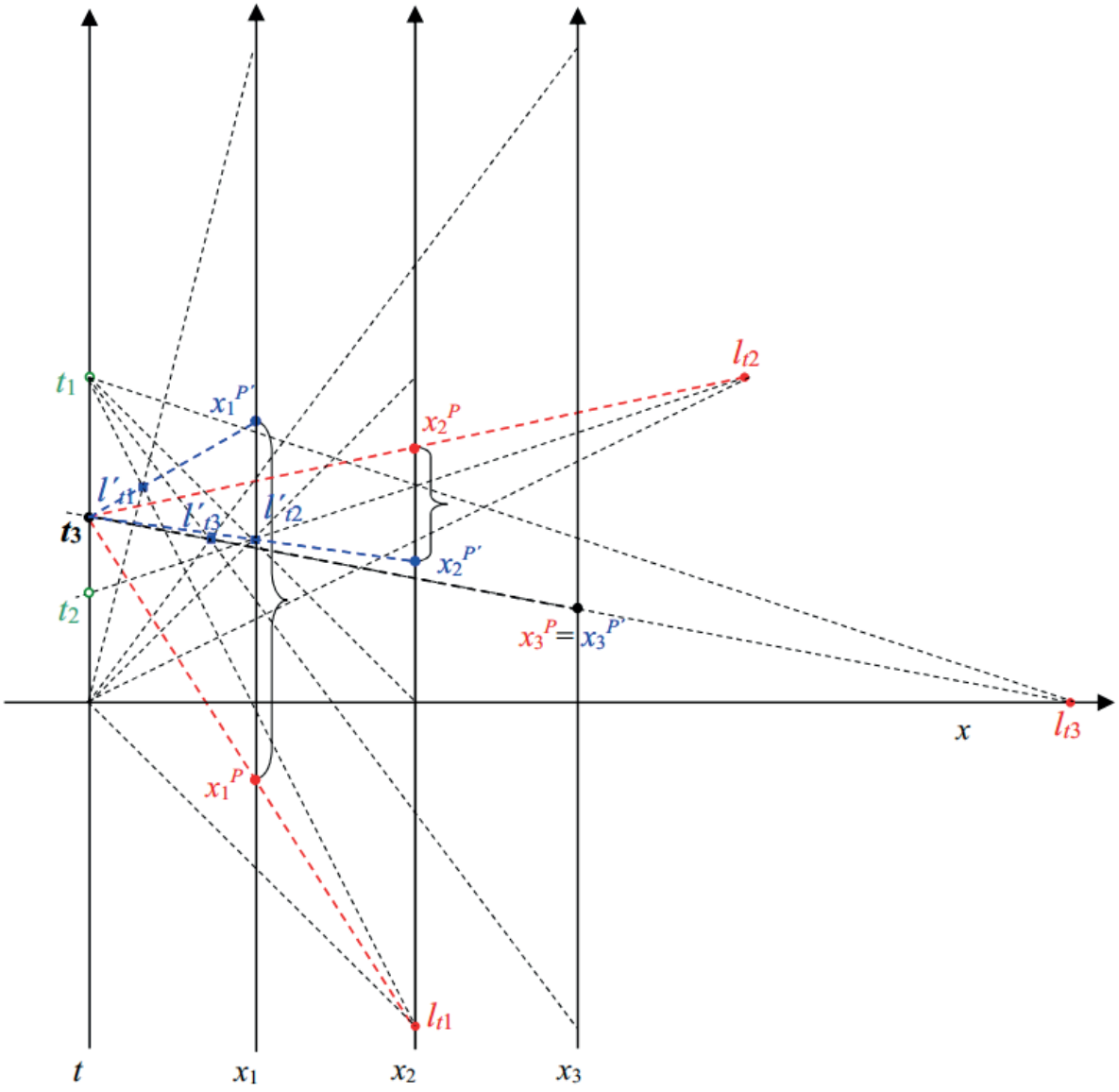

***Figure** 7 Minimal distance between lines*

$(-1,1,0)$ and the line l' is the trajectory of the particle 2 with velocity $\vec{v}=(-2,-1,-3)$ and initial position $(4,2,4)$, see Equation (3), Figure 7:

$$l: x_1 = -1 + t/2, x_2 = 1 + t/2, x_3 = t/2,$$
$$l': x_1 = 4 - 2t, x_2 = 2 - t, x_3 = 4 - 3t.$$

The lines are nonparallel and according to Equation (6) one obtains $t_1 = 2, t_2 = \frac{2}{3}, t_3 = \frac{8}{7}$.

The Manhattan distances for t_1 are:

$$L_1(t_1) = 0 + 2 + 3 = 5,$$
$$L_1(t_2) = 10/3 + 0 + 5/ += 5,$$
$$L_1(t_3) = 15/7 + 5/7 + 0 = 20/7.$$

The minimum Manhattan distance 20/7 occurs at time $t_3 = 8/7$.

The line l is given by points $(0,-1,1,0),(2,0,2,1)$. The line l' is given by points $(0,4,2,4),(2,0,0,-2)$. Lines are represented in the parallel coordinates by points $l_{t,1}, l_{t,2}, l_{t,3}$ and $l'_{t,1}, l'_{t,2}, l'_{t,3}$. Values of t_1, t_2, t_3: $t \cap l_{t,1}l'_{t,1} = t_1$, $t \cap l_{t,2}l'_{t,2} = t_2$, $t \cap l_{t,3}l'_{t,3} = t_3$. Coordinates of points P, P' (points of the minimal Manhattan distance) are obtained: $x_i^{P'} = x_i \cap t_i l'_{t,i}$, $i = 1,2,3$, and $x_i^{P'} = x_i \cap t_i l'_{t,i}, i = 1,2,3$. The minimum Manhattan distance is the sum of lengths of particular line segments on axis x_1, x_2, x_3.

3. Discussion and conclusion

The aim of this paper was to give the basic information on parallel coordinates and possibility of their using in air traffic control. Equations of lines are expressed in the time-space and stated conditions for their position illustrated by an example of finding the minimum distance between two nonintersecting lines.

Parallel coordinates may represent multidimensional data in wide range of applications: data mining (USA patent), computer vision (USA patent), as well as optimization, process control, clustering and classification problems and more recently in intrusion detection and elsewhere [3]. ParallAX is introduced as a new user-friendly tool for visualization and analysis of multivariate data using the parallel coordinates methodology [13]. Other possibilities of visualization via parallel coordinates are discussed in [14-16]. The increasing popularity of the parallel coordinates may be illustrated by the number of publications with the term "parallel coordinates" present in their title: It has been rising steadily from 14 in the year 1991 to approximately 543 in 2011, with a total of 5620 publications as reported by Google scholar on the 15th of December, 2012 [17]. While there is a large amount of papers about parallel coordinates, there are only a few notable software publicly available to convert databases into parallel coordinates graphics, e.g. XDAT, XLSDAT.

Acknowledgements

Publication of this paper was supported by the Centre of excellence for systems and services of intelligent transport II., ITMS 26220120050 supported by the Research & Development Operational Programme funded by the ERDF.

References

[1] FREUDENRICH, C. How air traffic control works. In: *How stuff works science* [online]. [accessed 2017-05-05]. Avalaible from: http://science.howstuffworks.com/transport/flight/modern/ air-traffic-control.htm

[2] D'OCAGNE, M. *Parallel and axial coordinates* [online]. Paris: Gauthier-Villars, 1885 [accessed 2017-05-05]. Avalaible from: http://archive.org/stream/coordonnespara l00ocaggoog #page/n9/mode/2up

[3] INSELBERG, A. *Parallel Coordinates: visual multidimensional geometry and its applications*. Dordrecht: Springer, 2009. ISBN 978-0-387-21507-5.

[4] WEGMAN, E. J. Parallel-coordinate plots and density plots. Encyclopedia of statistical sciences. New Jersey: John Wiley & Sons, 2004. ISBN 978-0-471-15044-2.

[5] GNAP, J., KALASOVA, A., GOGOLA, M., ONDRUS, J. The Centre of Excellence for transport service and control. *Communications - Scientific Letters of the University of Zilina* [online]. 2010, **12**(3A), p. 116-120. ISSN 1335-4205, eISSN 2585-7878. Available from: http://komunikacie.uniza.sk/index.php/communications/article/view/956

[6] GLENDENNING, K., WISCHGOLL, T., HARRIS, J., VICKERY, R., BLAHA, L. Parameter space visualization for large-scale datasets using parallel coordinate plots. *Electronic Imaging* [online]. 2016, **60**(1), p. 10406-1-10406-8(8). ISSN 2470-1173. Available from: https://doi.org/10.2352/J.ImagingSci.Technol.2016.60.1.010406

[7] PELTONEN, J., LIN, Z. Parallel coordinate plots for neighbor retrieval. In 12th International Joint Conference on Computer Vision, Imaging and Computer Graphics Theory and Applications : proceedings [online]. Vol. 3. IVAPP. 2017. ISBN 978-989-758-228-8, p. 40-51. Available from: https://doi.org/10.5220/0006097400400051

[8] LI, J., MARTENS, J. B., WIJK, J. J. Judging correlation from scatterplots and parallel coordinate plots. *Information Visualization* [online]. 2010, **9**(1), p. 13-30. ISSN 1473-8716, eISSN 1473-8724. Available from: https://doi.org/ 10.1057/ivs.2008.13

[9] COHAN, S. M. Mobility analysis of mechanisms through the parallel coordinate system. *Mechanism and Machine Theory* [online]. 1986, **21**(1), p. 63-71. ISSN 0094-114X, eISSN 1873-3999. Available from: https://doi.org/10.1016/0094-114X(86)90030-3

[10] OPACH, T., ROD, J. K. Do choropleth maps linked with parallel coordinates facilitate an understanding of multivariate spatial characteristics? *Cartography and Geographic Information Science* [online]. 2014, **41**(5), p. 413-429. ISSN 1523-0406, eISSN 1545-0465. Available from: https://doi.org/10.1080/15230406.2014.953585

[11] STEED, CH. A., FITZPATRICK, P. J., SWAN, J. E., JANKUN-KELLY, T. J. Tropical cyclone trend analysis using enhanced parallel coordinates and statistical analytics. In: *Cartography and Geographic Information Science* [online]. 2009 [accessed 2019-03-04]. Available from: https://pdfs.semanticscholar.org/259f/276799e697441424fd3d6be476e4a46e6381.pdf

[12] MUNOZ, D., LARA, F. B., VARGAS, C., ENRIQUEZ-CALDERA, R. *Position Location Techniques and Applications*. Academic Press, 2009. ISBN 978-0-123-74353-4.

[13] AVIDAN, T., AVIDAN, S. ParallAX - A data mining tool based on parallel coordinates In: *Computational Statistics* [online]. Physica-Verlag, 1999, **14**(1), p.79-89. ISSN 0943-4062. Available from: https://doi.org/10.1007/PL00022707

[14] VAIDYA, M. Survey of parallel data processing in context with MapReduce. *Computer Science and Information Technology* [online]. 2011, **1**, p. 69-80. ISSN 2231-5403 Available from: https://doi.org/10.5121/csit.2011.1307

[15] ONDRUS, J., DICOVA, J. Potential of prediction quantification and trends in transport requirements as tool of transport management and development. *Transport and Telecommunication* [online]. 2013, **14**(4), p. 316-324. ISSN 1407-6160. Available from: https://doi.org/10.2478/ttj-2013-0027

[16] OPACH, T., ROD, J. K. Augmenting the usability of parallel coordinate plot: The polyline glyphs. *Information Visualization* [online]. 2018, **17**(2), p. 108-127. ISSN 1473-8716, eISSN 1473-8724. Available from: https://doi.org/10.1177/1473871617693041

[17] HEINRICH, J., WEISKOPF, D. State of the art of parallel coordinates. In: *Eurographics* [online]. 2013 [accessed 2019-03-04]. Avalaible from: http://joules.de/files/heinrich_state_2013.pdf

Milos Poliak - Juraj Hammer - Kelvin Cheu - Marek Jaskiewicz*

IDENTIFICATION OF COSTS STRUCTURE CHANGE IN ROAD TRANSPORT COMPANIES

The costs of each company on the market are an essential component of financial decision making, not only on the price of the goods and services provided, but also about the business efficiency. In business, services have a significant impact on pricing, but also for deciding on the realization of performances. Costs structure is composed of fixed and variable costs. Changing the costs structure creates assumptions for other decisions, as well as the pricing of the entrepreneur. The goal of this article was to identify, whether there is a change in time of the costs structure.

Keywords: *costs, freight transport, transport companies, business*

1. Introduction

Pricing in the road freight transport, with regard to the provision of services, in a liberalized market in terms of price, is not regulated by the prescribed tariffs or pricing processes [1]. The price for transportation is decided only by agreement between the carrier and the shipper. Given this fact, the carrier must know the real costs that arise at him in providing of services, as a prerequisite for the agreement of the shipping costs. If the costs structure changes over time that would affect the price change of the realized performance. If one assumes that the carrier has created the two basic costs group - fixed and variable costs, their share would affect the development of the transport price. At a higher share of the fixed costs, the growth rate of total costs slows down, but there would be growth of realized costs [2]. However, the overall costs decrease more slowly when the performance declines, which reduces the competitiveness of the entrepreneur, because the price depends on the total costs [2]. The objective of this article was to identify whether there is a change in time of the costs structure, assuming that the price change option is influenced by the changing performance in time periods.

2. Analysis of current costs situation in transport companies

Considering that pricing in the road freight transport is liberalized, every carrier can come to the market with its own pricing policy. From this perspective, the following factors can be identified affecting the price of transport:

- Vehicle size and dimensions;
- Options of recovery transportation (demand impact);
- Unladen driving (empty ride);
- Referral availability and other services;
- Road and traffic conditions;
- Price input factor (work, vehicle, spare parts and fuel);
- Quality of management [3].

Based on output by Korzhenevych et al. [3], it is possible to define the share of individual costs, featured in Table 1.

Another factor, influencing pricing, is related to the maintenance of the rolling stock, analysed by Drozdiel a Piasecki [4]. Based on those author's outputs, it is possible to state, that the fleet is more economically efficient if prescribed maintenance is carried out.

2.1 Impact of costs structure on costs calculation by variable and fixed costs

There are currently several calculation methods, which however cannot be used economically to calculate the price in the road transport, since that is a service area. The aim of this part of the paper is to highlight the reality that the cost structure affects the price of realized services. Output of costs calculation, with their division into the variable and fixed parts, are the following price rates [5]:

- Per kilometer with cargo,
- For one hour of the vehicle's operation.

This calculation specifically approaches the individual costs groups. The variable costs, which can be labelled as costs dependent on distance (e.g. toll costs, fuel costs, tire costs), arise only when the vehicle is moving; this means that they shall be incurred by the carrier only if he realizes the transportation. If the carrier is unable to provide the shipment, the costs would not arise [6-7].

The second group of costs are the fixed costs, which are dependent on time and arise regardless of whether the carrier carries out the transport or the vehicle is in downtime (e.g.

* [1]Milos Poliak, [1]Juraj Hammer, [2]Kelvin Cheu, [3]Marek Jaskiewicz
[1]IDepartment of Road and Urban Transport, Faculty of Operation and Economics of Transport and Communications, University of Zilina, Slovakia
[2]Department of Civil Engineering, The University of Texas at El Paso, USA
[3]Department of Automotive Vehicles and Transportation, Faculty of Mechatronics and Machine Engineering, Kielce University of Technology, Poland
E-mail: milos.poliak@fpedas.uniza.sk

Table 1 *Typical share of transport costs for semi-trailers*

	Cost item	Share of operating costs (%)
Variable costs	Fuel	20-30
	Motor oil	1-5
	Tires	10-15
	Spare parts	15-20
Fixed costs	Drivers - wages	10-20
	Other work	5
	Depreciation and interest	15-20
	Burden costs	10-15

Table 2 *Average costs item values of the transport companies between 2004 and 2017*

	fuel (€/km)	toll (€/km)	tires (€/km)	oil (€/km)	driver's wages (€/km)	depreciation (€/km)	repair maintenance (€/km)	motor insurance (€/km)	accident insurance (€/km)	motor vehicle tax (€/km)	burden (€/km)	∑ (€/km)
2004	0.3142	0.063	0.02	0.00467	0.13	0.12	0.03	0.0155	0.016	0.015	0.012	0.74037
2005	0.3253	0.063	0.021	0.00467	0.135	0.13	0.035	0.0155	0.017	0.015	0.013	0.77447
2006	0.3498	0.063	0.022	0.0048	0.14	0.14	0.035	0.0155	0.017	0.015	0.014	0.8161
2007	0.3587	0.066	0.023	0.005	0.15	0.14	0.04	0.0155	0.018	0.016	0.014	0.8462
2008	0.3701	0.07	0.023	0.006	0.158	0.15	0.04	0.016	0.018	0.016	0.014	0.8811
2009	0.3594	0.078	0.024	0.0088	0.16	0.16	0.05	0.016	0.02	0.017	0.015	0.9082
2010	0.3627	0.1111	0.026	0.0125	0.165	0.165	0.054	0.016	0.02	0.017	0.0155	0.9648
2011	0.3788	0.1158	0.028	0.0178	0.17	0.17	0.055	0.165	0.022	0.017	0.016	1.1554
2012	0.3785	0.12	0.03	0.021	0.175	0.17	0.06	0.017	0.025	0.0175	0.016	1.03
2013	0.3822	0.12	0.033	0.022	0.18	0.175	0.06	0.017	0.025	0.0198	0.0165	1.0505
2014	0.3856	0.1242	0.038	0.024	0.185	0.18	0.065	0.0175	0.028	0.0198	0.017	1.0841
2015	0.3874	0.1287	0.048	0.025	0.19	0.185	0.065	0.018	0.028	0.0198	0.0185	1.1134
2016	0.3896	0.129	0.05	0.026	0.198	0.19	0.07	0.02	0.03	0.02	0.019	1.1416
2017	0.3914	0.13	0.052	0.0265	0.2	0.19	0.074	0.02	0.03	0.0208	0.019	1.1537

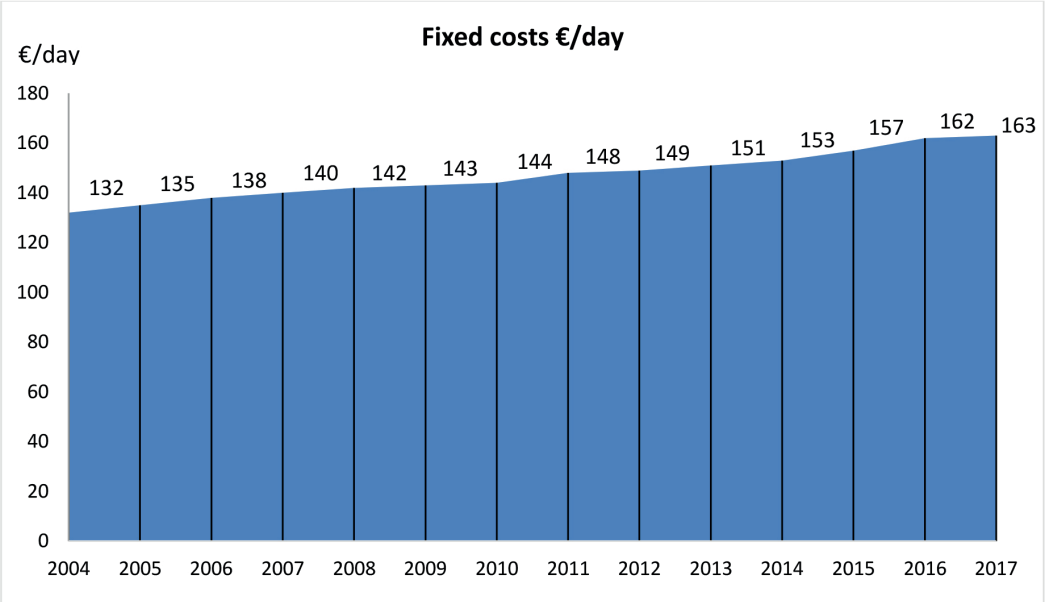

Figure 1 *The course of fixed costs for transport companies between 2004 and 2017 per vehicle - semi-trailer*

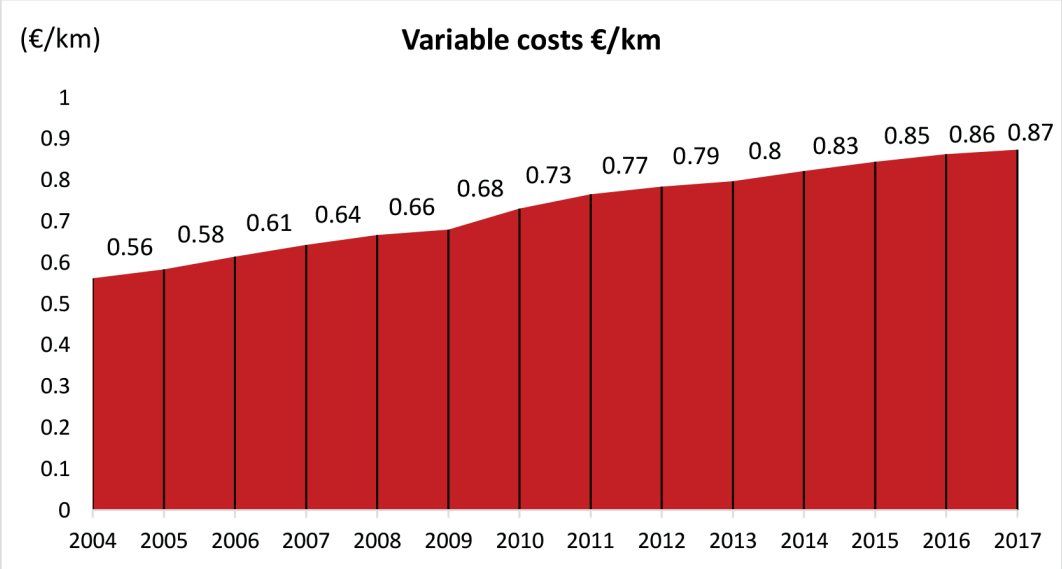

Figure 2 *The course of variable costs for transport companies between 2004 and 2017*

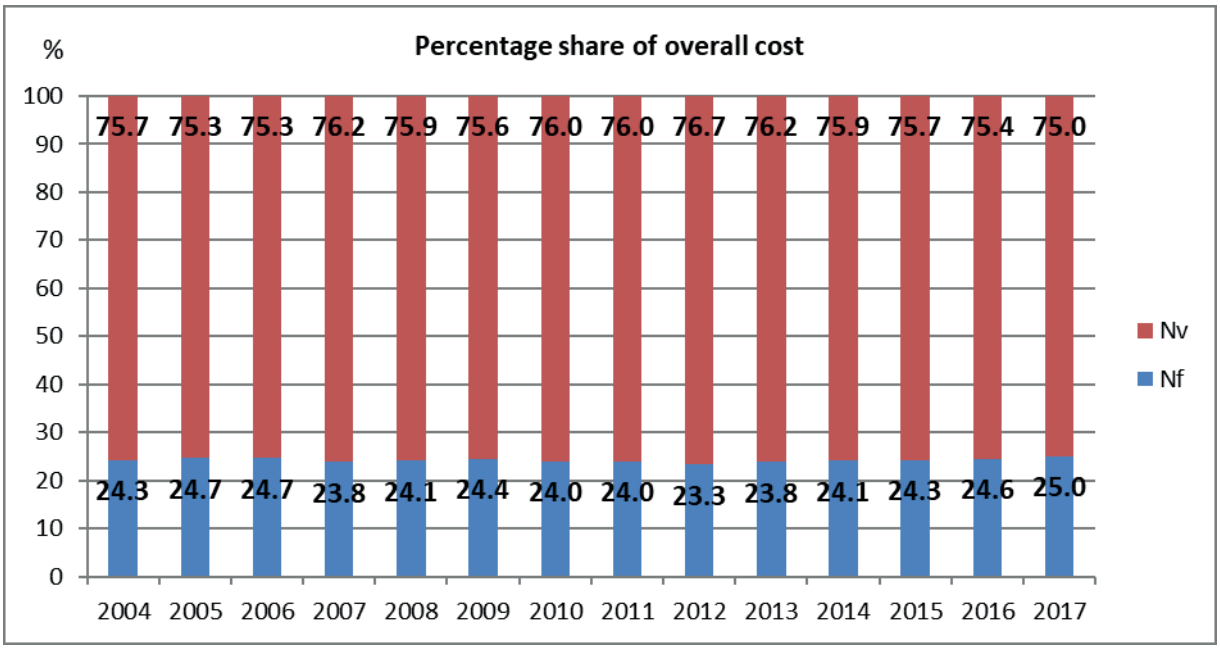

Figure 3 *Expressing the structure of costs and their shares from 2004 to 2017*

depreciation costs, vehicle insurance costs, the costs of motor vehicle tax) [8-9].

The principle of calculation is that per unit of realized power (e.g. km) variable costs are counted directly; the fixed costs expressed in time are converted into a calculation unit - the average speed, as follows [10-11]:

$$n_c = (n_v/\beta) + (N_f/v_t), \quad (1)$$

where:
n_c - total costs (€),
n_v - variable costs (€/km),
β - driving utilization coefficient (%),
N_f - fixed costs (€/km),
v_t - average speed (km/h).

The higher the proportion of the fixed costs in annual costs, then at higher performance are the higher level of overall costs, as well [12-13].

2.2 Impact of the costs structure on price at dynamic costing

Dynamic calculation is a costs calculation the output of which are the costs for performance [14-15]. In addition, the outputs of this costs calculation are dependent on the costs structure. The variable costs are set on a unit of realized performance, while the fixed costs are set for one day of vehicle operation. The total costs are set as the sum of the product of the unit of the variable costs and realized performance and the fixed costs per day of operation [16-18].

The fixed costs component of total costs for one day of operation is the same regardless of performance. The costs structure also has significant influence on pricing. With an increasing proportion of the fixed costs, the cost change becomes less flexible [19-20].

3. Research on the costs structure change in the road freight transport

In order to identify the change in the costs structure, costs need to be monitored for a longer period of time. At University of Zilina, a team of authors observed the cost of operating the vehicle, from 2004 to 2017, to identify change the costs structure. Costs were tracked across the multiple companies provided that they performed the fleet analysis. Costs were taken into account and statistical set only for the semi-trailers, weighing up to 40 tonnes with conversion to unit costs. Annual driving performance of one semi-trailer was about 100,000 kilometres with an average consumption of 30 litters per 100 kilometres [21]. Table 2 shows the average values for the transport companies in individual years. Table 2 is made over a span of 15 transport companies and their calculated cost items, who provided data for this research.

Authors divided the costs into two groups: the variable costs that are dependent on the distance travelled and the fixed costs that do not change based on distance travelled [22].

Fixed costs included depreciation, motor insurance, accidents' insurance, motor vehicle tax and burden. In Figure 1 the rising costs in transport companies can be observed in year-on-year comparisons [23]. In Figure 1, an increasing trend can be observed of the fixed costs, which has a uniformly rising character in year-on-year comparisons with a difference of about 5 % increase costs per year.

The second costs group of the transport company are the variable costs, among which authors have included fuel, vignette, respectively toll, engine oil, repair and maintenance and driver wage [24].

In Figure 2 a development of the variable cost items in transport companies can be seen. It can be stated that the biggest increase was recorded in 2010 when the toll item has risen, due to introduction of this charging method of the freight transport in Slovakia. Until 2010, the freight was charged with a highway stamp.

Based on Table 2, the combined fixed and variable costs are graphically represented in Figure 3, in the year-on-year range.

From 2004 to 2017, both costs groups increased. In 2004, the fixed and variable costs totalled 0.7404 €per kilometre. For 2017, this is already a sum of 1.1537 €per kilometre, what means in an increase of 64 % in 14 years period. Figure 3 shows that the costs structure lies year-on-year within range of ¾ for variable costs of the total costs and for the fixed costs of ¼ of the total costs in a transport company.

4. Conclusion

Based on a research conducted for a 14 year period in transport companies, the authors can state that there is very little change in the cost structure in road freight transport. For the identified period from 2004 to 2017, the fixed costs ratio was at the level of 25 % of the total costs while 75 % share belonged to the variable costs of operating vehicle. This research confirmed that, although the transport costs are increasing by the carriers in the 14 year period, the structure of their shares is changing only slightly and practically remains constant, which is good for planning calculation of economic efficiency of the transport company.

Acknowledgements

The contribution was realized with the support of the Ministry of Education of the Slovak Republic VEGA no. 1/0143/17 "Increasing the competitiveness of Slovak carriers providing road transport services in the common market of the European Union".

References

[1] POLIAK, M. The relationship with reasonable profit and risk in public passenger transport in the Slovakia. *Ekonomicky casopis / Journal of Economics*. 2013, **5**4(7), p. 668-684. ISSN 0013-3035.

[2] RIHA, Z., TICHY, J. The costs calculation and modelling in transport. 19th International Conference. Transport Means. 2015 : proceedings. 2015. ISSN 1822-296X, p. 388-391.

[3] KORZHENEVYCH, A., BROCKER, J. *Spillovers of European regional investment subsidies: analysing using a forward-looking spatial GCE model*. 2017.

[4] DROZDZIEL, P., PIASECKI, S. Study of the medthod of assessing the economic efficiency of exploitation cars in a transport company. *Folia Societatis Scientiarum Lublinensis*. 1995, p. 60-66. ISSN 1428-3646.

[5] BLENDON, R. BENSON, J. M., BRODIE, M., MORIN, R., ALTMAN, D. E., GITTERMAN, D., BROSSARD, M., JAMES, M. Bridging the gap between the public and economists views of the economy. *Journal of Economic Perspectives*. 1997, **11**(3), p. 105-118. ISSN 0895-3309, eISSN 1944-7965.

[6] GNAP, J., CAJCHAN, J., SULGAN, M. Measuring methodology form real bus-stop distances of mass passenger transport. *Communications - Scientific Letters of the University of Zilina* [online]. 2003, **5**(3), p. 8-9. ISSN 1335-4205, eISSN 2585-7878. Available from: http://komunikacie.uniza.sk/index.php/communications/article/view/1355

[7] LEWANDOWSKI, P. Attempts to protect the internal market for road transport in specific European Union countries. *Zeszyty Naukowe Akademii Morskiej w Szczecinie / Scientific Journals Of the Maritime University of Szczecin* [online]. 2016, **47**, p. 141-146. ISSN 1733-8670, eISSN 2392-0378. Available from: https://doi.org/10.17402/161

[8] CYPRICH, O., KONECNY, V., KILIANOVA, K. Short-term passenger demand forecasting using univariate time series theory. *Promet - Traffic&Transportation, Scientific Journal on Traffic and Transportation Research*. 2013, **25**(6), p. 533-541. ISSN 0353-5320, eISSN 1848-4069.

[9] POLIAK, M., POLIAKOVA, A. Relation of social legislation in road transport on driver's work quality. 15th International Conference on Transport Systems Telematics TST 2015 : proceedings [online]. 2015, ISBN 978-3-319-24576-8, eISBN 978-3-319-24577-5, p. 300-310. Available from: https://doi.org/10.1007/978-3-319-24577-5

[10] VUKOVIC, A. Units of account in international and domestic transport law (in Croatian). *Nase More*. 2013, **60**(1-2), p. 11-16. ISSN 0469-6255, e-ISSN 1848-6320.

[11] GRAND, L., DURET, B. Differences in competitiveness and relocation of European freight companies. *Transports*. 2000, **400**, p. 99.

[12] POLIAK, M., SEMANOVA, S., POLIAKOVA, A. Risk allocation in transport public service contracts. *Ekonomski Pregled*. 2015, **66**(4), p. 384-403. ISSN 0424-7558, eISSN 1848-9494.

[13] ROTONDO, E. The legal effect of EU Regulations. *Computer Law & Security Review* [online]. 2013, **29**(4), p. 437-445. ISSN 0267-3649. Available from: https://doi.org/10.1016/j.clsr.2013.05.003

[14] RADIONOV, N. Limitation of liability right in road freight carriage in Croatia: an extinct institute. *Uniform Law Review* [online]. 2016, **21**(4), p. 457-468. ISSN 1124-3694, eISSN 2050-9065. Available from: https://doi.org/10.1093/ulr/unw035

[15] LUBANSKI, N. Moving closer together - trade union europeanisation in the construction sector. Transfer: European Review of Labour and Research [online]. 2000, 6(1), p. 103-109. ISSN 1024-2589, eISSN 1996-7284. Available from: https://doi.org/10.1177/102425890000600110

[16] LORENC, A., KUZNAR, M. An intelligent system to predict risk and costs of cargo thefts in road transport. *International Journal of Engineering and Technology Innovation* [online]. 2018, **8**(4), p. 284-293. ISSN 2223-5329, eISSN 2226-809X. Available from: http://ojs.imeti.org/index.php/IJETI/article/view/1013

[17] MUKHERJEE, A., ZHAO, L. Profitable parallel trade in unionized. *Journal of Economics* [online]. 2012, **107**(3), p. 267-276. ISSN 0931-8658, eISSN 1617-7134. Available from: https://doi.org/10.1007/s00712-012-0267-7

[18] ZODROW, G. Tax competition and tax coordination in the European Union. *International Tax and Public Finance* [online]. 2003, **10**(6), p. 651-671. ISSN 0927-5940, eISSN 1573-6970. Available from: https://doi.org/10.1023/A:1026377819946

[19] OSTERLOH, S., DEBUS, M. Partisan politics in corporate taxation. *European Journal of Political Economy* [online]. 2012, **28**(2), p. 215-226. ISSN 0176-2680, eISSN 1873-5703. Available from: https://doi.org/10.1016/j.ejpoleco.2011.11.002

[20] EDWARDS, J., KEEN, M. Tax competition and Leviathan. *European Economic Review* [online]. 1996, **40**(1), p.113-134. ISSN 0014-2921. Available from: https://doi.org/10.1016/0014-2921(95)00057-7

[21] LAI, Y. B. The political economy of capital market integration and tax competition. *European Journal of Political Economy* [online]. 2010, **26**(4), p. 475-487. ISSN 0176-2680, eISSN 1873-5703. Available from: https://doi.org/10.1016/j.ejpoleco.2010.02.001

[22] BRENNAN, G., BUCHANAN, J. The power to tax: analytical foundations of a fiscal constitution. Cambridge UK: Cambridge University Press, 1980. ISBN 0521233291.

[23] JASKIEWICZ, M., WIECKOWSKI, D. The impact of the safety belt used for chairs used in buses and minibuses with small-speed collisions. *Zeszyty Naukowe Akademii Morskiej w Szczecinie / Scientific Journals Of the Maritime University of Szczecin*. 2014, **39**(111), p. 78-81. ISSN 1733-8670, eISSN 2392-0378.

[24] POLIAK, M., HAMMER, J., REUTER, R., POLIAKOVA, A. The impact of the transport route on the cost of the transfer. 11th International Scientific and Technical Conference on Automotive Safety Location : proceedings [online]. 2018. ISBN 978-1-5386-4579-6. Available from: https://doi.org/ 10.1109/AUTOSAFE.2018.8373319

Eva Brumercikova - Bibiana Bukova - Iwona Rybicka - Pawel Drozdziel*

MEASURES FOR INCREASING PERFORMANCE OF THE RAIL FREIGHT TRANSPORT IN THE NORTH-SOUTH DIRECTION

The article elaborates on measures aimed at increasing the performance of the rail freight transport carried out in the north-south direction. The measures are designed based on the implemented analyses focused on the analysis of the current situation of international trade and development of international transport as well as the analysis of the current situation of the European transport infrastructure. The north-south direction was selected due to the enormous increase of the transit road transportation.

Keywords: *rail freight transport, road infrastructure congestion, intermodal transport line, north-south direction*

1. Introduction

The global economy with growing liberalization brings along new logistic technologies as well as associated optimization of international transport. It is not driven only by the increasing competition within the transport market, but by many different external factors having impact on the international markets created by individual countries of the EU, as well. The external factors include unemployment, migration, air pollution etc. The growing global competition, volumes of transported goods as well as the capacity of the European transport infrastructure, bring about the conflicting situations for the production companies. Current approach is based on cooperation of individual transport modes. One of the possibilities is to use the transport capacity of the rail transport mode.

2. Road infrastructure congestion

In order to determine the level of congestion of the road infrastructure it is necessary to process an analysis, which is based on a national transport census carried out by the relevant road infrastructure administrator of a given country regularly every five years [1-2]. Consequently, the transport flows in international road transport are determined, based on the transport intensity within the given studied connections in the north-south direction and based on the available data on the structure of vehicles origin according to the vehicle registration numbers (hereinafter only VRN).

For the baseline comparison it is also necessary to determine the basic indicator of the labour division in international transport, according to individual modes of transport as well as specific countries. Specific values of the labour division in selected countries in the area of international transport are given in Figure 1. The source data for the figure are derived from available information of 2017 depending on the transport performance [3].

2.1 Analysis of the road infrastructure congestion in the Slovak Republic

In 2015 the Slovak Roads Administration carried out the most recent traffic census in the road network and in 2013 it published a document titled "Forecasting of Future Intensities within the Road network by 2040" [4]. For the sake of the objective of this article it is necessary to consider the outputs of the relevant sections, as well as regions for the current situation as well as expected development of the road infrastructure congestion. Information from the toll systems is not available due to refusal of relevant sources to provide it.

Figure 2 represents a model situation of the road infrastructure congestion elaborated in 2014 with the assistance of the Research Institute of Transport.

The graphical representation is based on the traffic census of 2010, as well as the document "Forecasting of Future Intensities in the Road Network by 2040", which includes coefficients of growth of transport intensity in individual Slovak regions given according to the forecasting methodology of the Slovak Roads Administration [6].

When comparing the average values of selected census stations of 2010 and 2015 as well as in comparing the forecasted development of intensity, it is possible to calculate a 5% increase of the number of trucks in case of D1 and a 9% decrease of the number of vehicles in case of R1. The estimated development according to the forecast is 13% in the case of D1 and 14% in the case of R1. The deviation in the forecast and census of vehicles in individual years can be caused by the census inaccuracy or the failure of the forecast.

2.2 Analysis of the road infrastructure congestion in Hungary

In 2015 the Hungarian Roads Administration (Kozlekedesi koordinacios kozpont - hereinafter only KKK) carried out a

* [1]Eva Brumercikova, [1]Bibiana Bukova, [2]Iwona Rybicka, [2]Pawel Drozdziel
[1]Department of Railway Transport, Faculty of Operation and Economics of Transport and Communications, University of Zilina, Slovakia
[2]Politechnika Lubelska, Lublin, Poland
E-mail: bibiana.bukova@fpedas.uniza.sk

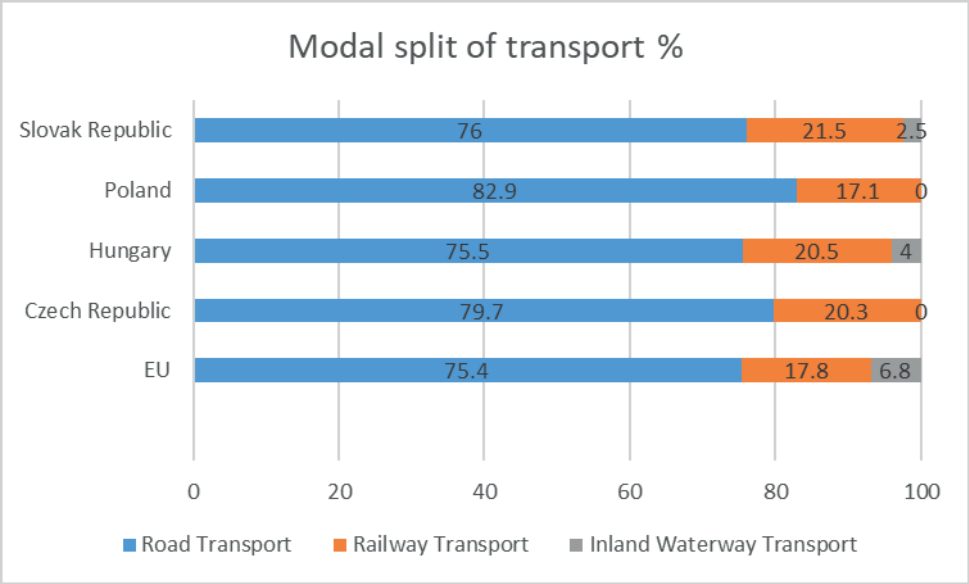

Figure 1 *Division of labour in international transport [3]*

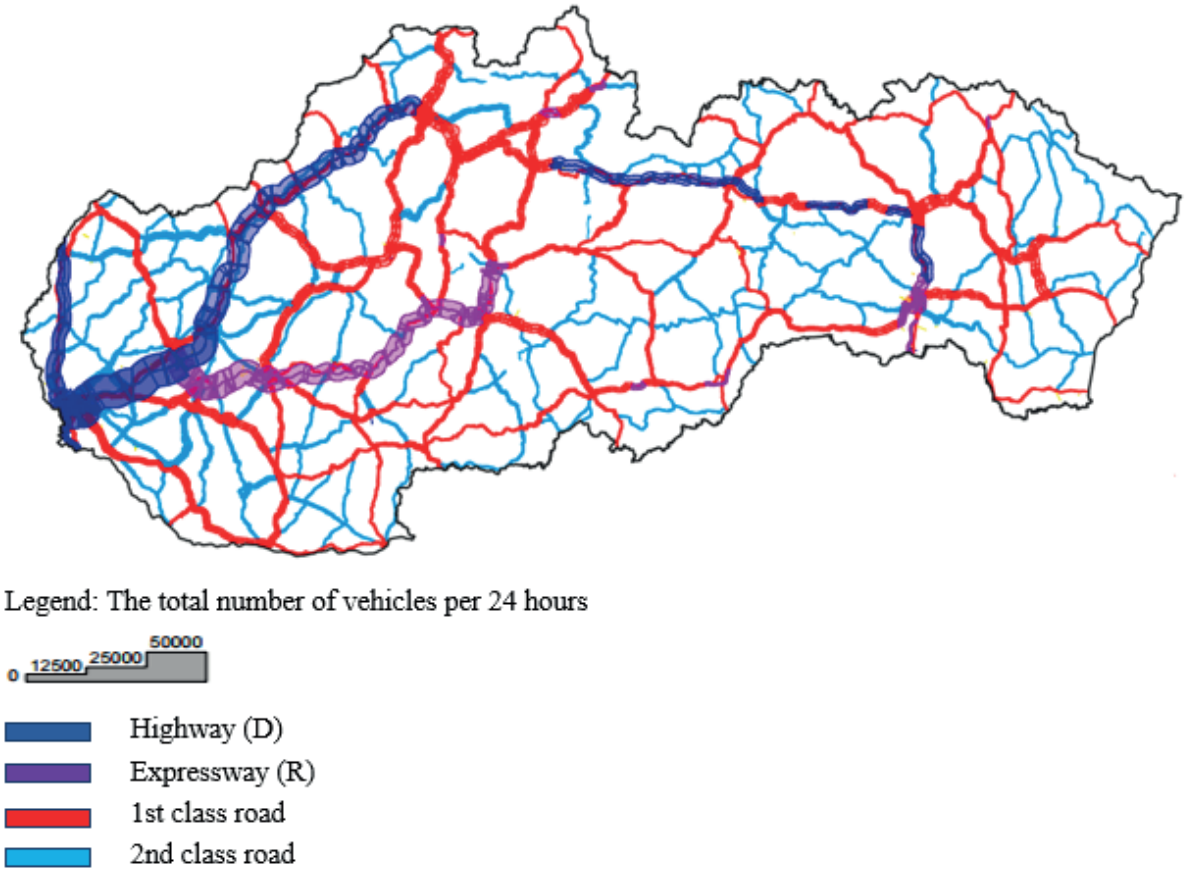

Figure 2 *The map of the road network congestion 2014 - Slovakia [5]*

national network-wide survey of the road infrastructure congestion as well as a survey of the state registration origin of vehicles over 12 tons having the obligation of the toll paying on the motorways and 1st class roads. The national pertinence of road vehicle combinations is graphically illustrated in Figure 3.

It is evident from the chart that 40% of trucks that entered the road network in Hungary in 2015 had the VRN originated in Rumania, 10% of vehicles originated in Poland, whereas the following 10% came from Bulgaria, 8% of vehicles have their origin in the Slovak Republic and 6% in Serbia [7].

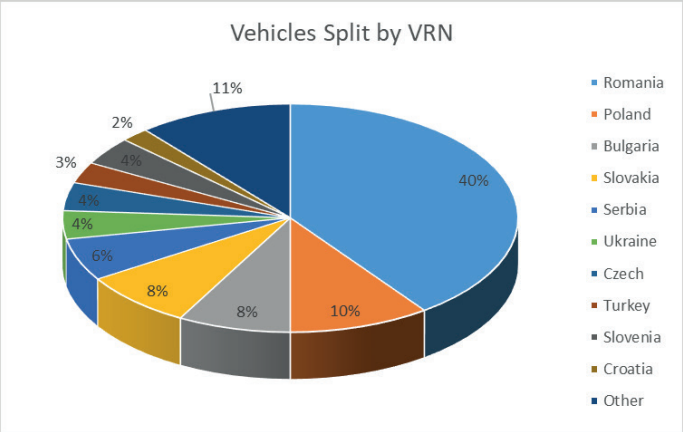

Figure 3 *Vehicles split by VRN [7]*

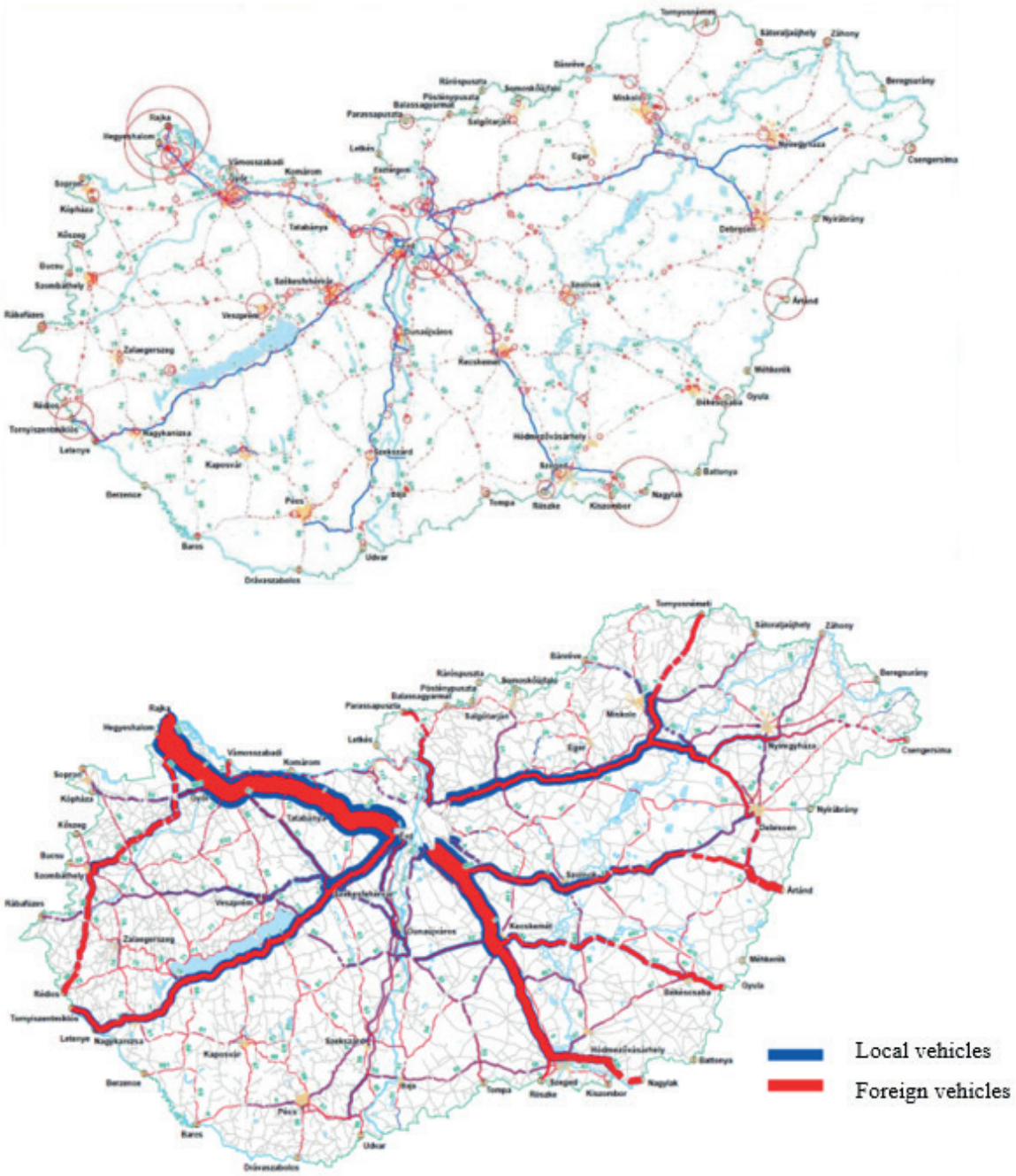

Figure 4 *The map of the road infrastructure congestion - Hungary [8]*

Figure 5 *The result of traffic census in 2015 [9]*

When considering the data of the directional survey of KKK it is evident that the highest intensity of the transit road semi-trailer combinations of over 12 tons on the road network of Hungary passes through the border crossings Rajka (Rusovce in Slovakia) and Hegyeshalom (Nickelsdorf in Austria) upon entry/exit from the border crossings Nagylak (Nadlac in Romania) and Artand (Bors in Romania).

Figure 4 shows a map from the KKK directional survey, whose first part depicts the intensity of over 12 ton trucks' destinations at the border crossing points by the size of the circle diameter. In the second part the map depicts the intensity of trucks divided by local and foreign VRN.

2.3 The analysis of the road infrastructure congestion in Poland

The Polish Roads Administration (Generalna dyrekcia drog krajowych i autostrad - hereinafter only GDDKA) carried out the traffic census last in 2015 (Figure 5). Details of the traffic census cannot be disclosed. The data have been processed into the graphic representation of the transport intensity in the V4 (Visegrad Group - Slovakia, Czechia, Poland, Hungary) countries in Figure 6.

2.4 The analysis of the road infrastructure congestion in the Czech Republic

The Directorate of Roads and Highways of the Czech Republic (hereinafter only ŘSD) carried out its most recent traffic census in 2010. For 2015 there is no data, the study has not been completed by the time of accomplishment of the project underlying the article. The information from the toll systems is not available [10]. The data have been processed into the graphical representation of the transport intensity in the V4 countries in Figure 5.

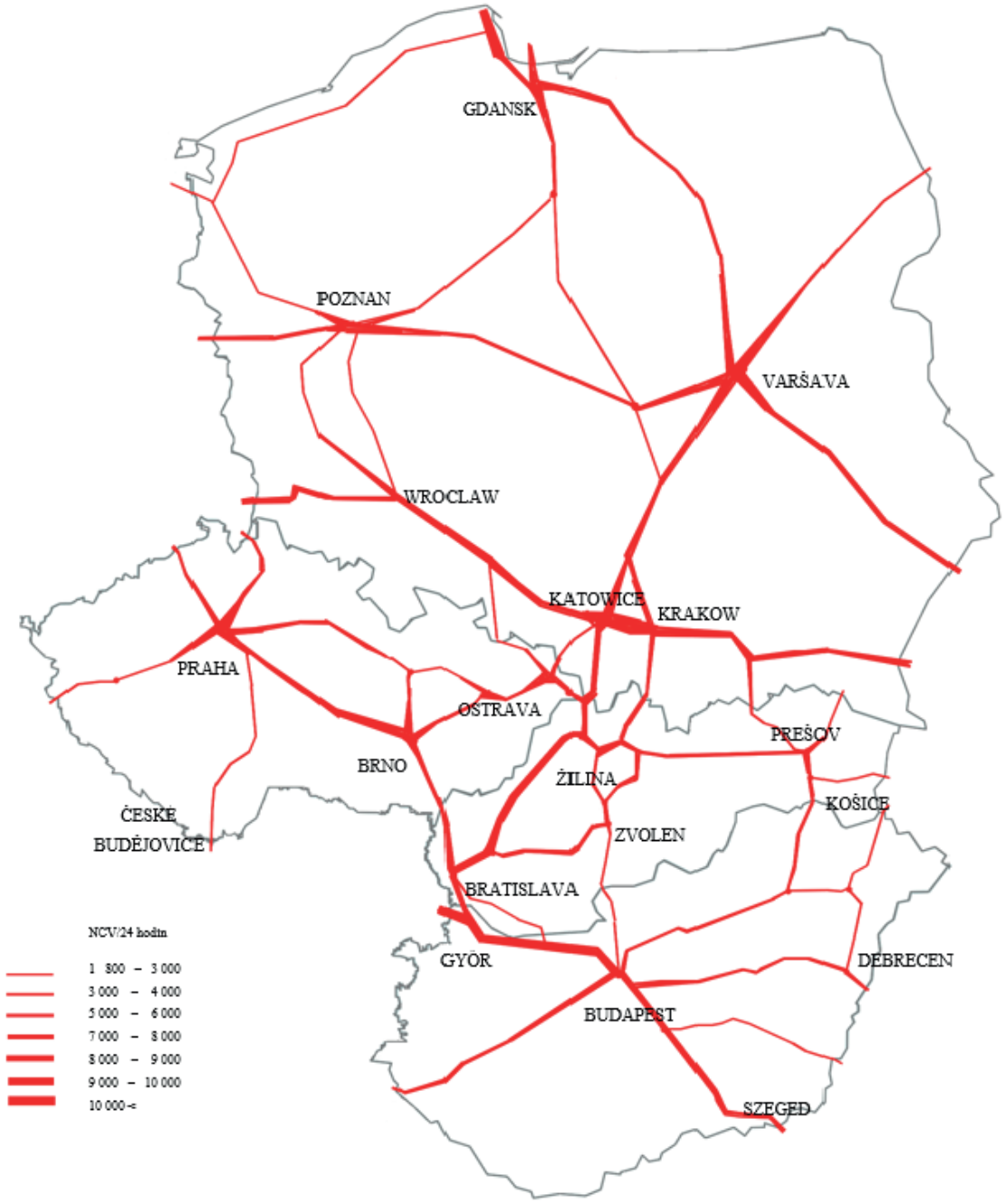

Figure 5 *The map of V4 countries with the transport intensity*

2.5 Result of analysis

Based on the provided data by e-mail communication, as well as annexes to the transport census studies, the graphical image in Figure 5 - the Map of V4 countries with the transport intensity has been set up. The methodology is based on determining the selected census stations in V4 countries and the consequent arrangement of intensities by the boldness of lines, which are given in the Figure 5 legend. The transport intensity in the Czech Republic was determined using the study of 2010, therefore the informative value of the graphical representation in the Czech Republic is not comparable with the rest of the V4 countries, nevertheless it has been included here for reasons of general overview.

Identified transit paths in the north-south direction, which pass through the territory of the Slovak Republic, correspond with the conclusions of the strategic document "The Strategic Plan of Transport Infrastructure Development of the Slovak Republic by 2020".

3. A proposal for an intermodal transport line

An increase in the train capacity utilisation (e.g. an increase in the net tonnes of products or number of containers) can

Figure 6 *The Modalohr wagon [14]*

be achieved only if sufficient rail infrastructure capacity exists (norms of length and weight).

A change in operating performance due to the increase in the train capacity utilisation is inversely proportional to the train weight. If the weight of the train increases by about Δ, the number of train kilometres is reduced. We can define this according to Equation (1):

$$\sum trkm^1 = \frac{\sum grtkm_z}{Q^1_{vl}} = \frac{\sum grtkm_z}{Q^1_{vl} * (1+\Delta)} = \sum trkm^0 * \frac{1}{1+\Delta} \quad (1)$$

where:
$\sum trkm^1$ - train kilometres after the increase,
$\sum trkm^0$ - train kilometres before the increase,
$\sum grtkm_z$ - gross tonnage kilometres (beside the locomotive),
Q^0vl - weight of the train before the increase,
Q^1vl - weight of the train after the increase.

Economic indicators change through the lower fees for the railway infrastructure (in the EU countries, train kilometres are the basic parameter by which the fees for the railway infrastructure are calculated), increased labour productivity and thus lower labour costs. Some costs can be higher, such as the energy cost (problems with accelerating resistance) [11].

Based on the conclusions of the analysis, the core proposal of this article is to launch an intermodal transport line between the agglomerations of Budapest and Gliwice [12].

Budapest area was selected due to an optimal accessibility of logistic centres in the vicinity of the intermodal transport terminal BILK Budapest, which concurrently provides for a possibility of trans-loading of semi-trailers with conventional body in the WIPPEN transport system. In comparison to the lines of the RO-La system operated in the past in the MAV network, with its terminal built in the Kiskundorozsma railway station, 17 km from the state borders with Rumania, the logistic centre BILK Budapest provides better accessibility for road semitrailer combinations driving from the port in Koper, Slovenia.

Gliwice agglomeration (PL) was determined based on the currently operated tri-modal terminal of intermodal transport - PCC Intermodal SA. The terminal is located 22 km from Katowice, a city, which, in the analysis of the road infrastructure intensity, demonstrated average values exceeding 10 000 truck at the measuring stations within the centre of the agglomeration.

A proposal for integration of the intermodal transport line Budapest - Gliwice in the planned lines of the company Lohr Group - the company Lohr Group was established in France and at present it provides comprehensive innovative solutions in the field of logistic services and intermodal transport. Figure 6 shows a wagon of the company Lohr Group located within a small terminal with moving ramps. The Modalohr wagon disposes with the ability of turning its middle part and thereby it enables simplified loading of vehicle combinations and semitrailers and trucks.

The company Lohr Group currently operates intermodal transport lines in the form of RO-MO and semitrailer transport system in its own flat wagons, which represent a technical compromise between the Saadkms and Sdgnss wagons. The lowered floor of the wagon to 225 mm from the top of the rail enables loading of the vehicle combinations horizontally, as well as loading of individual semi-trailers [13].

Figure 6 shows the Modalohr wagon and an example of the ramp positioning for the semi-trailer loading.

Figure 7 illustrates the planned, as well as currently operated, lines of the intermodal transport, which the company Lohr Group plans to operate using its own technical facilities and by construction of terminals from its own financial resources.

The company Lohr Group used the red colour to represent currently operated lines of the intermodal transport, the blue lines are the lines planned operated lines in the short-term and in yellow there are the lines, which have been planned in the long-term. The planned line of the intermodal transport passing through the territory of Hungary, Slovakia and the Czech Republic has been routed from the port in Istanbul through Bulgaria and Serbia to the logistic centre in the city of Poznan, in Poland.

For the territory of Slovakia a transit route has been planned, from the border passage station in Sturovo up to the border

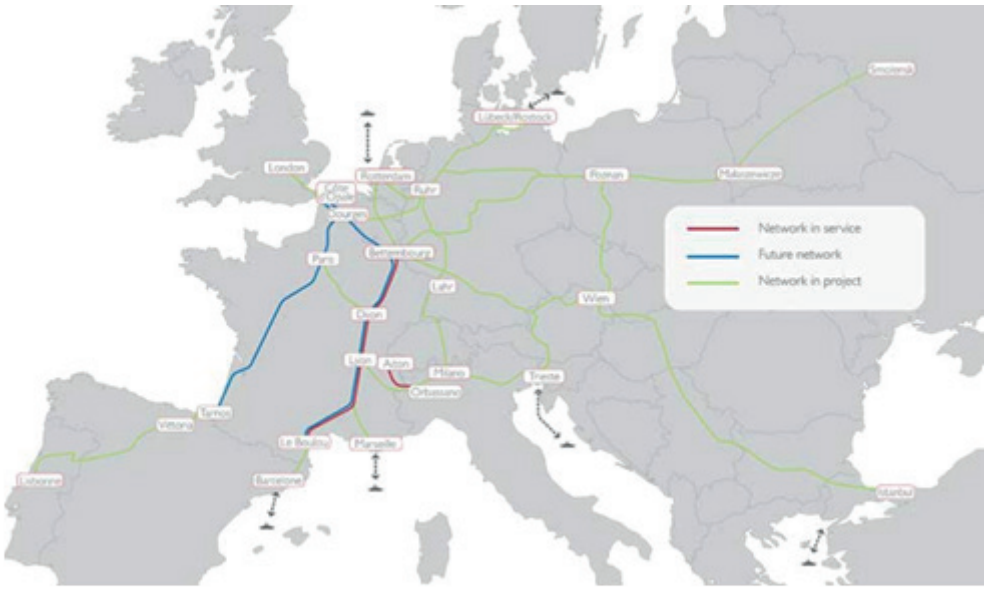

***Figure** 7 The map of the planned Modalohr routes [14]*

passage station in Devinska Nova Ves - i.e. 148 km. The routing has been planned alternatively through Budapest - Gyor - PPS (Border Crossing Station) Hegyeshalom - PPS Nickelsdorf (in Austria) due to the fact that inclusion of Vienna agglomeration is strategically more convenient for reasons of larger coverage of the territory in respect to dispatching and distribution of goods in road vehicle combinations [15-16].

4. Conclusion

Due to the growing economic globalization, the priority of production companies as well as shippers is to increase the quality of goods production as well as service delivery. The current situation of the European transport infrastructure does not fully enable to meet this priority. Based on the situational analysis, the article introduces a measure for increasing the performance of the rail freight transport in the north-south direction. The measure implies establishing a new intermodal transport line in the transportation of the so-called basket Wippen wagons. For the sake of the maximal accessibility and flexibility, a transiting route has been selected, passing through the Slovak Republic from Hungary to Poland. For launching of the intermodal transport line, all the operating conditions there have been considered, including the need of a contracted road transport operator, as well as concurrent coordination of activities with those of the logistics centres. In the case of establishment of such a line of intermodal transport, shortcomings in the area of rail infrastructure related to the insufficient capacity of border passage stations, were determined. Due to this deficiency it is proposed to introduce a fee for immobilization of the rolling stock.

Acknowledgment

This paper was developed under the support of project: Centre of excellence for systems and services of intelligent transport II., ITMS 26220120050 supported by the Research & Development Operational Programme funded by the ERDF.

References

[1] DOLINAYOVA, A., CAMAJ, J., DANIS, J. Evaluation of investment efficiency in the new database solution for rail freight transport in the context of globalization (in Slovak). 16th International Scientific Conference Globalization and its Socio-Economic Consequences : proceedings. 2016. ISBN 978-80-8154-191-9, p. 383-390.

[2] NESTEROVA, N. S., CONCHARUK, S. M., ANISIMOV, V. A., ANISIMOV, A. V. Strategy development management of multimodal transport network. 5th International Scientific Conference Integration, Partnership and Innovation in Construction Science and Education : proceedings [online]. Vol. 86. MATEC Web of Conferences, 2016. eISSN: 2261-236X. Available from: https://doi.org/10.1051/matecconf/20168605024

[3] Database - Eurostat [online]. [Viewed 2019-02-04]. Available from: https://ec.europa.eu/eurostat/data/database

[4] BRUMERCIK, F., LUKAC, M., KRZYSIAK, Z., KRZYWONOS, L. Model of integrated transportation system. *Communications - Scientific Letters of the University of Zilina* [online]. 2017, **19**(2), p. 23-26. ISSN 1335-4205, eISSN 2585-7878. Available from: http://komunikacie.uniza.sk/index.php/communications/article/view/177

[5] Transport model - Ministry of Transport and Construction of the Slovak Republic [online]. [Viewed 2019-02-04]. Available from: https://www.mindop.sk/ministerstvo-1/doprava-3/dopravne-modelovanie/dopravny-model-sr

[6] GASPARIK, J., LUPTAK, V., MESKO, P. New methodology for assessing transport connections depending on the integrated transport network. 3rd International Conference on Traffic and Transport Engineering : proceedings. 2016. ISBN 978-86-916153-3-8, p. 388-392.

[7] KRZYSIAK, Z., BARTNIK, G., SAMOCIUK, W., ZARAJCZYK, J., PLIZGA, K., RACHWAL, B., WIERZBICKI, S., KRZYWONOS, L., BRUMERCIK, F.: Analysis of explosion hazard at the liquid fuel station (in Polish). *Przemysl Chemiczny* [online]. 2017, **96**(2), p. 279-282. ISSN 0033-2496, e-ISSN 2449-9951. Available from: https://doi.org/10.15199/62.2017.2.5

[8] GUBOVA, K., RICHNAK, P. Development and use of intangible assets in the conditions of globalization. 16th International Scientific Conference Globalization and its Socio-Economic Consequences : proceedings. 2016. ISBN 978-80-8154-191-9, p. 572-579.

[9] General Director for National Roads and Motorways Website (Generalna Dyrekcja Drog Krajowych I Autostrad) [online]. Available from: www.gddkia.gov.pl

[10] CEMPIREK, V., NACHTINGALL, P., NOVAK, P., PLUHAR, M. The comparison of public rad and railway transport costs. 3rd International Conference on Traffic and Transport Engineering : proceedings. 2016. ISBN 978-86-916153-3-8, p. 855-860.

[11] DOLINAYOVA, A.: Optimisation of business processes and services in the rail transport market from two points of view: economic efficiency and management. Sustainable Rail Transport Conference : proceedings [online]. Springer, Cham, 2016. ISBN 978-3-319-58642-7, eISBN 978-3-319-58643-4, p. 31-44. Available from: https://doi.org/10.1007/978-3-319-58643-4_3

[12] LIUDVINAVICIUS, L., DAILYDKA, S., SLADKOWSKI, A. New possibilities of railway traffic control system. *Transport Problems.* 2016, **11**(2), p. 133-142. ISSN 1896-0596, eISSN 2300-861X.

[13] GONCHAROV, A. A., YUNDA, A. N., KOMSTA, H., ROGALSKI, P. Effect of structure on physicomechanical properties of transition metals diboride films. *Acta Physica Polonica A* [online]. 2017, **132**(2), p. 270-273. ISSN 0587-4246, eISSN 1898-794X. Available from: https://doi.org/10.12693/APhysPolA.132.270

[14] The Lohr System Terminals - Lohr Group [online]. Available from: https://lohr.fr/lohr-railway-system/the-lohr-system-terminals

[15] GNAP, J., KALASOVA, A., GOGOLA, M., ONDRUS, J. The Centre of excellence for transport service and control. *Communications : scientific letters of the University of Zilina* [online]. 2010, **12**(3A), p. 116-120. ISSN 1335-4205, eISSN 2585-7878. Available from: http://komunikacie.uniza.sk/index.php/communications/article/view/956

[16] ONDRUS, J., DICOVA, J. Potential of prediction quantification and trends in transport requirements as tool of transport management and development *Transport and Telecommunication* [online]. 2013, **14**(4), p. 316-324. ISSN 1407-6160. Available from: https://doi.org/10.2478/ttj-2013-0027

Emilia Szumska - Rafal Jurecki - Marek Pawelczyk*

ASSESSMENT OF TOTAL COSTS OF OWNERSHIP FOR MIDSIZE PASSENGER CARS WITH CONVENTIONAL AND ALTERNATIVE DRIVE TRAINS

The number of alternatively powered vehicles in Poland and EU is growing steadily. Different type of vehicle drive trains determine variations in their performances from economical and environmental technological aspects. The aim of this paper was to investigate the cost efficiency and environmental aspects of midsize passenger cars equipped with different drive train technologies: conventional, hybrid, electric and LPG fueled engine. To this purpose, the Total Cost of Ownership (TCO) method was used. Calculations were carried out by AFLEET Tool. The results show that the LPG fueled car has the lowest TCO, while the cars equipped with electric drivetrain indicate the highest TCO. However the electric car recorded the lowest cost of air pollutant emissions and externalities costs.

Keywords: *Total Cost of Ownership (TCO), alternatively powered vehicles, hybrid electric vehicles, air pollutant emission*

1. Introduction

Alternative fueled vehicles, as well as vehicles with alternative power train, offer the opportunity to reduce greenhouse gases emissions and limit the oil dependency. Air pollution is a big problem in Polish urban areas. For this reason, the Polish government has adopted a new law on electric mobility aimed to promote and disseminate the low-emission vehicles. In 2017 according to [1] a significant growth of registration new electric and hybrid electric passenger cars was observed in Poland. Number of electric cars (including plug-in hybrids) reported growth by 45% compared to previous year. The number of passenger cars equipped with hybrid electric drive train increased by 40% in comparison to 2016. It is worth noting that registrations of cars fitted with a diesel engine increased only by 2.8% related to the previous year. Figure 1 presents the share of propulsion type in registrations of new passenger cars in 2017.

In 2017, the largest share of the new registered passenger cars in Poland had the gasoline fueled vehicles, while in EU over a half of the new cars were equipped with diesel engine. In EU new registered cars fitted with electric and hybrid had higher share than in Poland. The reverse situation is in the case of natural gas fueled vehicles [1-2]. Various types of vehicle drive train demonstrate differences in their performances from economical, environmental and technological aspects [3-4]. Alternatively fueled or powered cars ensure lower emission compared to conventional vehicles. Hybrid and electric cars have higher manufacturing costs than the conventional vehicles, which results in higher acquisition price. However, the EVs and hybrids may provide low running costs. The Total Cost of Ownership (TCO) is a useful method to evaluate the costs related to the purchase and use of a car. The TCO may be applied for identification of the most economical type of a vehicle.

The aim of the paper is to evaluate the Total Cost of Ownership for six types of passenger cars: gasoline, diesel, hybrid electric, plug-in hybrid electric, electric and LPG fueled. In this study, the AFLEET Tool was used for the TCO calculation. The presented analysis includes the cost of externalities. Results presented in the paper could be useful in decision making on the purchase of an alternatively powered car.

2. Total Cost of Ownership (TCO)

The Total Cost of Ownership (TCO) includes the initial purchase price of vehicle as well as all direct and indirect expenses incurred at its operation, such as repairs, insurance and fuel. The TCO method provides all the costs arising during the acquisition, operation and decommissioning. According to authors of paper [5], the TCO analysis can be conducted in two categories: consumer oriented studies and the society oriented studies. In the first group, the costs distinguished by the consumers are incorporated and the different vehicle technologies are compared. In the case of the society oriented TCO studies, the consumer costs are extended to externalities, such as air pollutant, noise, accidents, congestions, climate change and environmental impacts.

Various studies have been conducted recently using the TCO method to analyze the costs effectiveness of the different vehicle technologies. For instance, the papers [6-8] present the TCO analysis for conventional, hybrid and electric cars. Studies [9-11] show the Total Cost of Ownership calculations for urban buses equipped with different types of propulsion drive. Research [12] delivers the TCO calculation conducted for plug-in hybrid electric vehicles for medium-duty truck.

Paper [5] provides the TCO analysis conducted for conventional, electric and hybrid electric passenger cars concerning three different car segments. Results show that the investigated electric vehicles from medium and small cars segment are less cost efficient then gasoline or diesel powered

* **Emilia Szumska, Rafal Jurecki, Marek Pawelczyk**
Kielce University of Technology, Poland
E-mail: eszumska@tu.kielce.pl

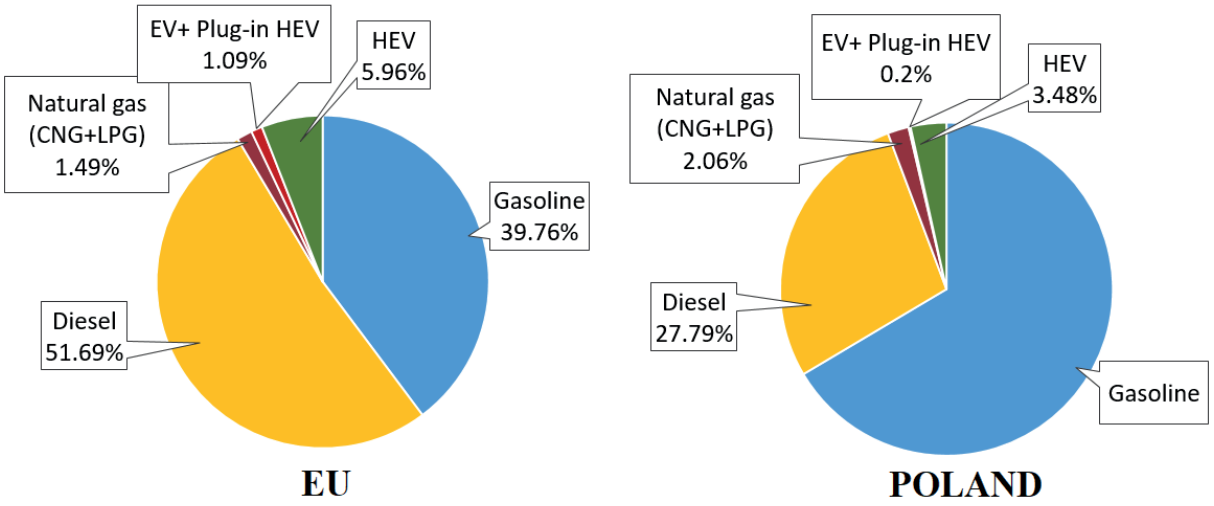

Figure 1 *Share of drive train type in registrations of new passenger cars in 2017 [1-2]*

cars. The difference in the TCO with conventional and electric vehicles is lower compared to the premium city car segment.

Numerous studies the Total Cost of Ownership calculation contain the environmental and/or social impacts of vehicles. Studies [13-14] present the Total Cost of Ownership including the emission cost, associated with air pollution, either greenhouse gases (CO_2, NO_2, CH_4) or local air pollutants (NO_x, SO_x, PM_x),. The TCO method was used to evaluate and compare the cost efficiency of vehicles with the different type of drive train. Research paper [15] presented the Total Cost of Ownership model for alternative vehicle technologies. The TCO was extended with external costs related to vehicle ownership and use. Authors interpreted the individual ownership to a societal perspective by describing the effect of the technologies on the costs for the society ("Total Cost for Society"). The results presented in the paper submit that battery electric vehicles, plug-in hybrid electric vehicles and hybrid electric vehicles have a lower societal cost than petrol, diesel and compressed natural gas vehicles.

The TCO method may be applied to evaluate the cost effectiveness of autonomous vehicles. The results of the research [16] show that the Total Cost of Ownership method can be used to compare fully automated vehicles with non-automated vehicles for personal cars, taxis and trucks. The presented TCO analysis included the costs of time spending for driving. The results show that highly automated vehicles would be attractive and beneficial to the high income groups as the time use related benefits can still be realized in the long-distance travel, but may not be attractive for taxi or mobility service operations, which primarily operate in an urban environment.

There are numerous studies on utilization of the TCO method to evaluate the perspectives of alternatively fueled and powered vehicles in automotive market of a specific region or country. For example, paper [17] provides analysis of the Total Cost of Ownership, social lifecycle cost and energy consumption obtained done for 66 cars with different types of powertrain available in Italy in 2013. The results show that the conventional cars (gasoline, diesel) have the lowest TCO. The electric vehicles indicate the lowest social lifecycle costs. Authors point out that alternative vehicles are still too expensive for consumers.

Study [18] presents the Total Cost of Ownership analysis of electric passenger vehicles in Germany. Results provided in this paper show that hybrid electric vehicles are already promising option from the economical point of view. Authors state that electric vehicles are currently not economically realizable in Germany without governmental subsidies. Similar conclusions were delivered in paper [19]. The contribution presents extensive Total Cost of Ownership analysis of conventional, hybrid and electric vehicles in three countries - the UK, Japan and USA (California and Texas) over a time period of 16 years. The authors indicate that the long term government support enables increasing the interest in hybrid and electric vehicles and growing the number of low-emission vehicles. Paper [20] and studies reffered above show how crucial the government subsidies are for development of electric mobility.

3. Assumptions for the TCO analysis

The TCO model includes costs of: acquisition, fuel, maintenance and repair, insurance and license and externalities. It should be noted that some of mentioned cost are relatively variable over the vehicle operational time. The Total Cost of Ownership analysis was conducted for midsize passenger cars equipped with different types of drive systems: conventional with gasoline powered engine (gasoline), conventional with diesel powered engine, hybrid electric with gasoline combustion engine (HEV), plug-in hybrid electric (PHEV), battery electric (EV), and with engine powered by liquid propane gas (LPG). Detailed parameters of investigated vehicles are presented in Table 1. Values of average fuel consumption have been taken from summary [21]. It has been assumed that all the cars operate in an urban driving conditions. The service life of the analyzed passenger cars is 15 years. The annual millage amounts to 20 000 km.

The fuel price on global fuel market is hard to predict. Estimate of the stable fuel price during the vehicle operation time is impossible to obtain. In this study, calculations were conducted with assumption that the costs of gasoline is 1.09 EUR/dm^3 (4.69 PLN/dm^3), costs of diesel: 1.15 EUR/dm^3 (4.97 PLN/dm^3), costs

Table 1 *Characteristics of analyzed passenger cars [21-25]*

	Average fuel consumption	Cost of acquisition [EUR]	Annual insurance costs [EUR]	Annual cost of repairs and maintenance [EUR]
Gasoline	6.7 [dm^3/100 km]	11600	320	580
Diesel	5.8 [dm^3/100 km]	13000	320	580
Gasoline Hybrid Electric Vehicle (HEV)	4.5 [dm^3/100 km]	32500	350	930
Gasoline Plug-in Hybrid Electric Vehicle (PHEV)	1.8 [dm^3/100 km]	35000	350	930
Electric Vehicle (EV)	10.8 [kWh/100 km]	35000	480	980
Liquid Propane Gas (LPG)	11.6 [dm^3/100 km]	12500	320	600

of LPG: 0.52 EUR/dm^3 (2.25 PLN/Nm^3) and the costs of electric energy is 0.44 EUR/kWh (1.90 PLN/kWh) [22-23].

The insurance costs depend on a number of different factors, such as age, sex, marital status, and location. Polish insurance companies make the insurance rates also dependent on the type of the drive propulsion. According to [24] the electric vehicles are more expensive to insure than conventional cars.

The repair and maintenance costs include costs of periodic inspections, costs of tires, operating fluids, parts and components replacing, and costs of necessary repairs. The cost of maintenance and repair differ between various drive types. The repair costs of electric and hybrid electric vehicles are higher than for the conventional cars. Some components of electric drive, like the lithium-ion batteries, are very expensive to repair if damaged. An additional reason is the availability of qualified staff to handle work on electric and hybrid cars. The level of repair and maintenance cost of analyzed cars have been provided from study [25]. In the presented TCO model the repair costs of electric and hybrid electric vehicles and the battery replacement costs are included.

The external costs have been calculated by use of the AFLEET Tool. In the TCO analysis described in the paper the externalities include costs of air pollutant emissions (Carbon Monoxide, Nitrogen Oxides, Sulfur Dioxide, Particular Matter: $PM_{2.5}$ and PM_{10}, Volatile Organic Compounds), costs of greenhouse gases emission, costs of noise, costs of accidents, costs of congestions, and costs of environmental degradation.

The TCO analysis was carried out using the AFLEET Tool, developed by the Argonne National Laboratory (ANL). The AFLEET Tool allows to estimate the lifetime fuel consumption and air pollutant emissions and costs of ownership for the light and heavy duty vehicles. The following drive system options have been taken into account:

- conventional: gasoline, diesel;
- hybrid: gasoline HEV, diesel HEV, diesel hydraulic hybrid, plug-in hybrid;
- electric: EV, EREV (Extended Range Electric Vehicle);
- alternative fuel: biodiesel, ethanol, hydrogen, LPG, CNG, LNG.

The vehicle types in the AFLEET Tool are based on the EPA's Motor Vehicle Emission Simulator (MOVES) as this allows the tool to estimate vehicle operation (e.g. tailpipe, brake and tire wear) emissions for various types of vehicle drives [26]. The user can modify the vehicle purchase price, fuel economy values, annual mileage, fuel and energy price, planned years of ownership, as well as the loan interest rate and term when purchase is financed by a loan.

The AFLEET tool includes the Simple Payback Calculator, Total Cost of Ownership Calculators, Fleet Footprint Calculator and Idle Reduction Calculator. The Simple Payback Calculator analyzes the acquisition and annual operating costs to evaluate a vehicle simple payback for purchasing, average annual petroleum use, greenhouse gases emissions and air pollutant emissions. The Total Cost of Ownership Calculator evaluates the net present value of operating and fixed costs over the operation time of a vehicle, lifetime fuel use, greenhouse gases emissions and air pollutant emissions. The Fleet Footprint Calculator estimates the annual petroleum use, greenhouse gases emissions and air pollutant emissions of investigated vehicle, taking into consideration that older vehicles typically have higher air pollutant emission rates than the newer ones. Finally, the Idle Reduction Calculator analyzes acquisition and annual operating costs to calculate a simple payback of a vehicle acquisition, average annual fuel use, greenhouse gases emissions and air pollutant emissions [26].

The AFLEET Tool displays simulation results in the outputs tables and graphs involving the Total Cost of Ownership and its components, fuel consumption, greenhouse gases emissions, and air pollutant emissions over the planned operation time.

4. Results

The Total Cost of Ownership values, estimated for the above mentioned vehicles are presented in Figure 2. The results of provided analysis show that the lowest TCO value has the car equipped with engine fueled by the LPG.

The LPG fueled car indicates 5% lower TCO compared to diesel vehicle. The Total Cost of Ownership values, reported for the conventional cars, are quite similar. The gasoline powered vehicle has 3% higher TCO than the diesel one. Car fitted with electric drive has the highest TCO level of the investigated passenger cars. The EV demonstrates 40% greater TCO in comparison to diesel fueled car. Hybrid cars show higher Total Costs of Ownership than conventional cars. Compared to diesel vehicle, the TCO values are bigger for plug-in hybrid - 40%, for HEV - 36%.

The running costs are referred to as the sum of the fuel costs, maintenance and repairs costs, and insurance costs. Significant differences of running costs of the analyzed vehicles were observed. In comparison to the diesel car, the LPG shows 5%

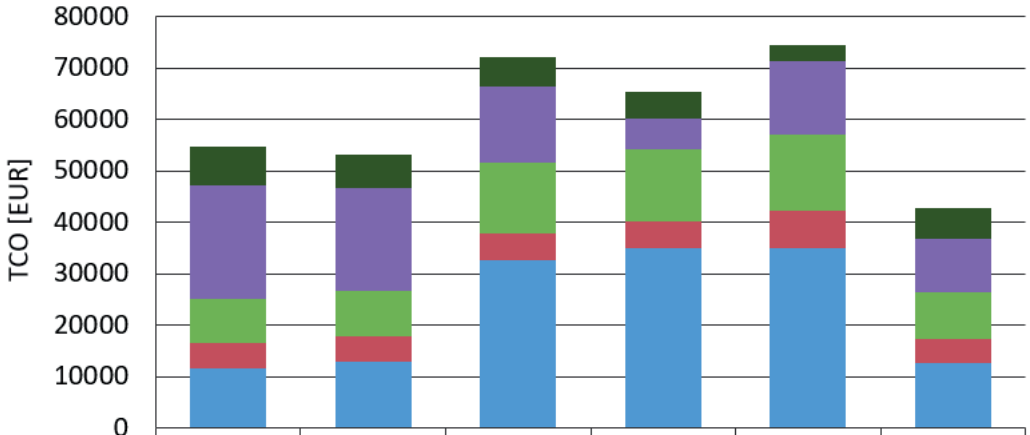

	Gasoline	Diesel	HEV	PHEV	EV	LPG
Cost of externalities	7544.32	6432.57	5652.95	5199.13	3128.42	5810.15
Cost of fuel consumption	21923.02	20111.16	14724.42	5889.77	14316.28	10360.47
Cost of repairs and maintenance	8720.93	8720.93	13953.49	13953.49	14651.16	9069.77
Cost of insurance	4883.72	4883.72	5232.56	5232.56	7325.58	4883.72
Cost of acquisition	11600.00	13000.00	32500.00	35000.00	35000.00	12500.00

Figure 2 *Total Cost of Ownership summary graph*

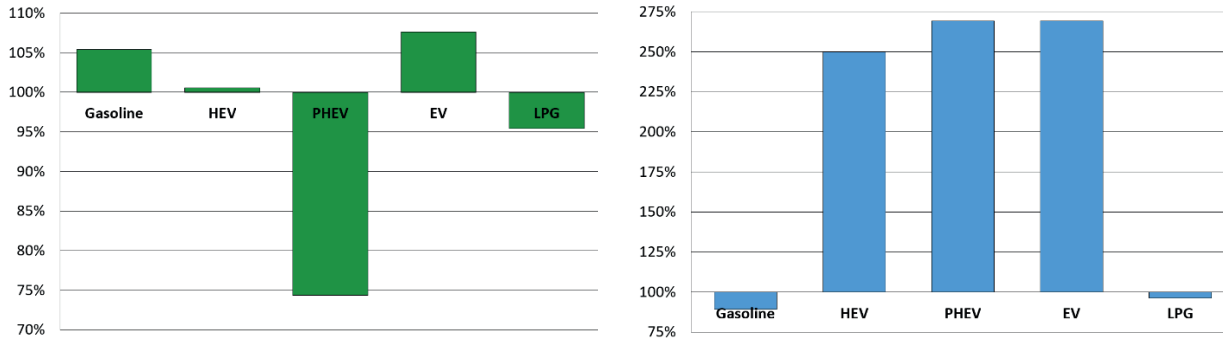

Figure 3 *Percentage difference of the running costs (left) and acquisition costs (right) compare to diesel fueled car (100%)*

lower running costs (Figure 3). The main and generally known reason is a lower price of liquefied petroleum gas compared to diesel and petrol.

The plug-in hybrid has the 26% lower running costs in comparison to diesel fueled car. The PHEV indicates the lowest costs of fuel consumption of the investigated passenger cars. Expenditures incurred on fuel represent approximately 9% of its TCO. The low values of fuel cost and the running costs could make the PHEV more competitive in the future. The plug-in hybrids are fitted with a large battery that can be recharged by plugging into an electrical outlet. It allows to obtain the fuel savings as using only electric drive until the battery pack is depleted. The conventional cars have the highest operating costs. This is due to high fuel consumption costs, which constitute the biggest share in their TCO. Compared to the diesel fueled car, the operational costs are respectively higher for gasoline - 5%, for HEV - 1%, for EV - 8%.

The largest part in the TCO of electric and hybrid vehicles represent the costs of acquisition. The purchase price is often the determining factor in purchasing a car. Another issue that can have a serious influence on acquisition decision is limited battery lifetime and the costs associated with its replacement. The purchase costs of EV and HEV constitute almost 47% of their TCO, while for the PHEV - 54%. Compared to the diesel fueled car, the costs of acquisition are higher for hybrid - 150%, for plug-in hybrid and electric - 169% (Figure 3).

The external costs provided in this analysis include the costs of air pollutant emission, cost of greenhouse gases emission, costs of noise, costs of accidents, costs of congestions, and costs of environmental degradation. The conventional cars indicate the highest externalities costs of the investigated passenger vehicles. The share of external costs in gasoline and diesel TCO value amounts to 14% and 12% respectively. The externalities in the PHEV and HEV constitute 8% of their Total Cost of Ownership. The electric vehicle shows a 51% lower costs externalities compared to diesel fueled car. Summary of air pollutant emissions during the operating time of investigated vehicles is shown in Figure 4.

The results show that the electric vehicle has the lowest emissions of harmful substances to air. The CO emission level for an EV is 52% lower compared to a diesel fueled vehicle. The LPG fueled car has the lowest particular matter emissions of

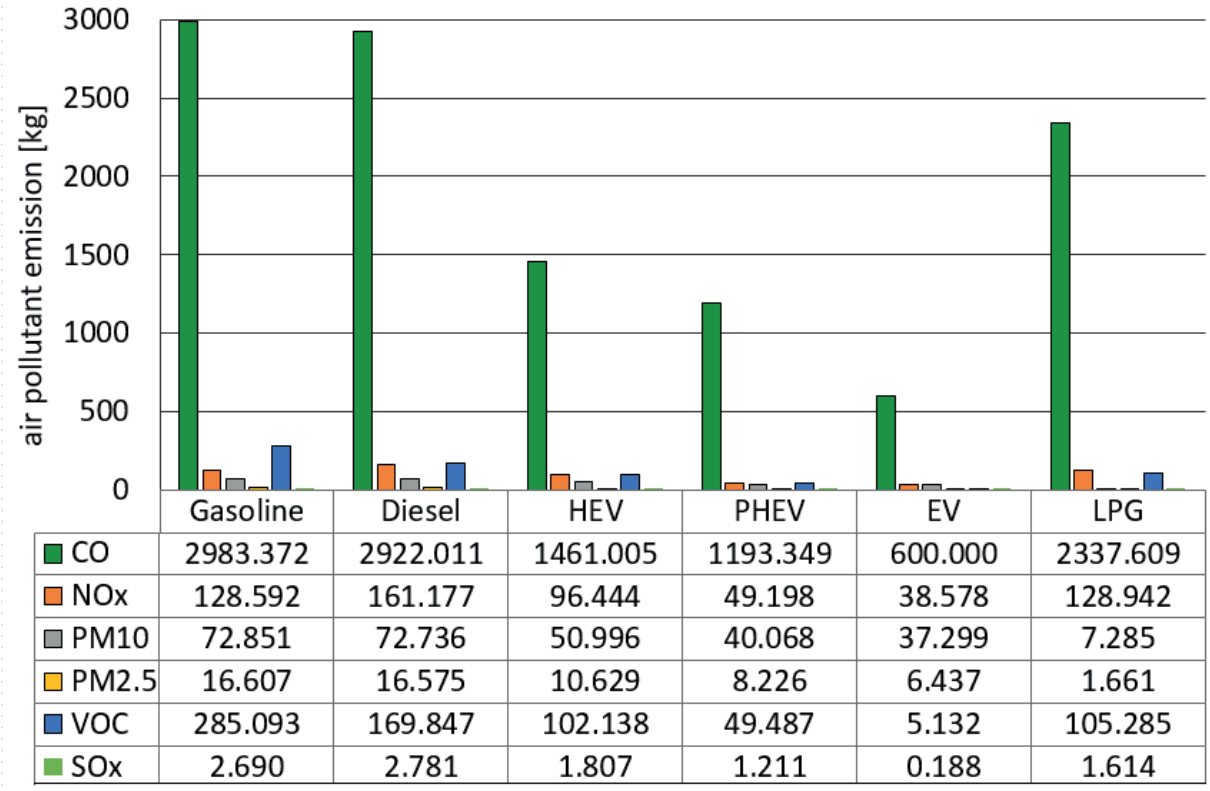

	Gasoline	Diesel	HEV	PHEV	EV	LPG
CO	2983.372	2922.011	1461.005	1193.349	600.000	2337.609
NOx	128.592	161.177	96.444	49.198	38.578	128.942
PM10	72.851	72.736	50.996	40.068	37.299	7.285
PM2.5	16.607	16.575	10.629	8.226	6.437	1.661
VOC	285.093	169.847	102.138	49.487	5.132	105.285
SOx	2.690	2.781	1.807	1.211	0.188	1.614

Figure 4 *Air pollutant emissions over the operating time of vehicle*

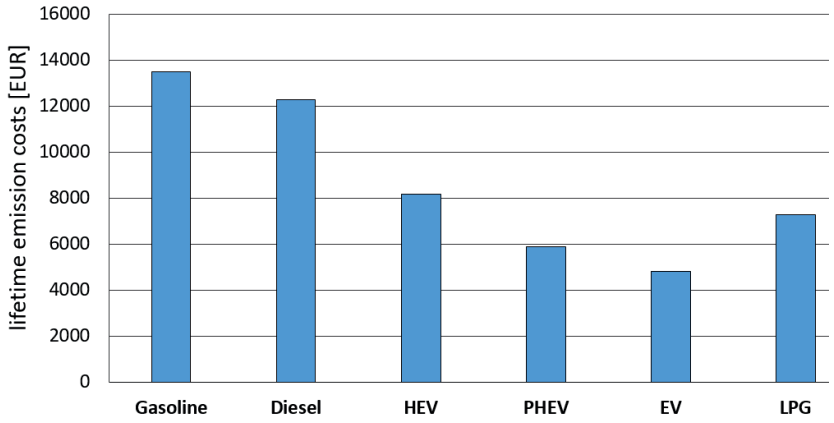

Figure 5 *Life air pollutant costs*

the investigated passenger vehicles. The cars fitted with hybrid electric drive can significantly reduce the NO_x emission. Nitrogen Oxides emission is respectively lower for the HEV - 40% and PHEV - 70% compared to diesel powered vehicle.

Figure 5 presents a comparison of costs associated with the lifetime air pollutant emission estimated by the investigated passenger cars.

Application of alternative powered or fueled drives can reduce the air pollutant costs significantly. The lowest lifetime air pollutant costs indicates the electric car. The EV has the 61% lower air pollutant costs than the diesel powered car. The gasoline fueled car shows the highest costs of air pollutant emissions of the investigated passenger vehicles. The gasoline car has 10% higher emission costs as compared to the diesel powered vehicle.

5. Conclusion

The presented analysis details the Total Cost of Ownership associated with the type of drivetrain. Provided comparison includes externalities costs. It was found that the LPG fueled car has the lowest TCO and indicates low air pollutant emission. Fuel consumption for the LPG is bigger than gasoline or diesel, but it is compensated by significantly lower price. The LPG fueled cars could be an alternative to replace the conventional cars. Hybrid electric drives train powering the vehicles have the potential to reduce the running costs and amount of environmental impact. Especially the plug-in hybrids can bring cost-savings for the long term use. However, their Total Cost of Ownership is significantly greater than for the conventional cars.

The results provided in this paper and in the studies presented earlier demonstrate that the hybrid and electric vehicles are still more expensive than the conventional cars. The disadvantages of the HEVs and EVs are high purchase costs and additional costs of battery replacement. The EVs and plug-in hybrids have limited range, thus causing the long-distance journeys much less convenient than gasoline, diesel or hybrid cars. It is promising that prices of the Lithium-Ion batteries are decreasing, while the gasoline and diesel prices are steadily increasing over time. The number of charging station and charging points vary significantly across the EU countries. The Norway has the highest number of installed charging points in Europe. Western EU countries, such as Germany, The Netherlands, France and the UK, already have more than 10,000 public charging points in place. In the Eastern Europe countries the electro mobility is significantly less developed. In Poland in 2018 were 150 charging station located mainly in large urban areas [27]. The European Commission focuses on reducing dependency on oil and oil-related products and foresees the use of common technical specifications for recharging and refueling stations. The EU regulatory requires Member States to develop national policy frameworks for the market development of alternative fuels and their infrastructure. For this purpose, EU elaborated funding programs to support and build a network of high power charging stations infrastructure along major routes across Europe.

References

[1] PZPM Automotive Industry Report 2018/2019 - Polish Automotive Industry Association [online]. Available from: http://www.pzpm.org.pl

[2] European Vehicle Market Statistic Pocketbook 2017/18, ICCT - International Council on Clean Transportation [online]. Available from: www.theicct.org

[3] CONRADIE, P. D. F., ASEKUN, O. O., SKRUCANY, T., KENDRA, M., STOPKA, O. The effect of fuel on the energy consumption and production of greenhouse gases in transport. *The Archives of Automotive Engineering - Archiwum Motoryzacji* [online]. 2018, **82**(4), p. 5-14. eISSN 1234-754X. Available from: https://doi.org/10.14669/AM.VOL82.ART1

[4] SARKAN, B., STOPKA, O., CHOVANCOVA, M., RYBICKA, I., KAPUSTINA, L. M. Research of individual factors affecting the engine power while a passenger car operation. *The Archives of Automotive Engineering - Archiwum Motoryzacji* [online]. 2018, **82**(4), p. 143-152. eISSN 1234-754X. Available from: https://doi.org/10.14669/AM.VOL82.ART11

[5] LEBEAU K., LEBEAU P., MACHARIS C., VAN MIERLO J. How expensive are electric vehicles? A total cost of ownership analysis. *World Electric Vehicle Journal* [online]. 2016, **6**, p. 996-1007. ISSN 2032-6653. Available from: https://doi.org/10.3390/wevj6040996

[6] HAGMAN J., RITZEN S., JANHAGER STIER J., SUSILO Y. Total cost of ownership and its potential implications for battery electric vehicle diffusion. *Research in Transportation Business and Management* [online]. 2016, **18**, p. 11-17. ISSN 2210-5395. Available from: https://doi.org/10.1016/j.rtbm.2016.01.003

[7] DUMORTIER J., SIDDIKI S., CARLEY S., CISNEY J., KRAUSE R. M., LANE B. W., RUPP J. A., GRAHAM J. D. Effects of providing total cost of ownership information on consumers' intent to purchase a hybrid or plug-in electric vehicle. *Transportation Research Part A: Policy and Practice* [online]. 2015, **72**(A), p. 71-86. ISSN 0965-8564, eISSN 1879-2375. Available from: https://doi.org/10.1016/j.tra.2014.12.005

[8] ZIROGIANNIS N., DUNCAN D., CARLEY S., SIDDIKI S., GRAHAM J. D. The effect of CAFE standards on vehicle sales projections: A total cost of ownership approach. *Transport Policy* [online]. 2019, **75**, p. 70-87. ISSN 0967-070X, eISSN 1879-310X. Available from: https://doi.org/10.1016/j.tranpol.2019.01.006

[9] SZUMSKA, E., PAWELCZYK, M. TCO comparison for city buses equipped with hybrid and conventional propulsion drive / Porownanie TCO autobusow miejskich z hybrydowym i konwencjonalnym ukladem napędowym (in Polish). *Prace Naukowe Politechniki Warszawskiej, seria Transport*. 2017, **118**, p. 277-285. ISSN 1230-9265. Available from: https://www.wt.pw.edu.pl/~ast/index.php/Badania-i-nauka/Prace-Naukowe-Politechniki-Warszawskiej-Transport/Zeszyty/Zeszyt-118

[10] NURHADI, L., BOREN, S., NY, H. A sensitivity of total ownership for electric public bus transport systems in Swedish medium sized cities. *Transportation Research Procedia* [online]. 2014, **2**, p. 818-827. ISSN 2352-1465. Available from: https://doi.org/10.1016/j.trpro.2014.10.058

[11] GOEHLICH, D., SPANGENBERG, F., KUNITH, A. Stochastic total cost of ownership forecasting for innovative urban transport systems. IEEE International Conference on Industrial Engineering and Engineering Management : proceedings. 2013. ISBN 978-1-4799-0986-5, p. 1-5.

[12] VORA A. P., JIN X., HOSHING V., SAHA T., SHAVER G., VARIGONDA S., WASYNCZUK O., TYNER W. E. Design-space exploration of series plug-in hybrid electric vehicles for medium-duty truck applications in a total cost-of-ownership framework. *Applied Energy* [online]. 2017, **202**, p. 662-672. ISSN 0306-2619. Available from: https://doi.org/10.1016/j.apenergy.2017.05.090

[13] MITROPOULOS, L. K., PREVEDOUROS, P. D., KOPELIAS, P. Total cost of ownership and externalities of conventional, hybrid and electric vehicle. *Transportation Research Procedia* [online]. 2017, **24**, p. 267-274. ISSN 2352-1465. Available from: https://doi.org/10.1016/j.trpro.2017.05.117

[14] BISHOP, J. D., MARTIN, N. P., BOIES, A. M. Cost-effectiveness of alternative powertrains for reduced energy use and CO2 emissions in passenger vehicles. *Applied Energy* [online]. 2014, **124**, p. 44-61. ISSN 0306-2619. Available from: https://doi.org/10.1016/j.apenergy.2014.02.019

[15] DE CLERCK Q., VAN LIER T., LEBEAU P., MESSAGIE M., VANHAVERBEKE L., MACHARIS C., VAN MIERLO J. How total is a total cost of ownership. *World Electric Vehicle Journal* [online]. 2016, **8**(4), p. 736-747. ISSN 2032-6653. Available from: https://doi.org/10.3390/wevj8040742

[16] WADUD, Z. Fully automated vehicles: A cost of ownership analysis to inform early adoption. *Transportation Research Part A: Policy and Practice* [online]. 2017, **101**, p. 163-176. ISSN 0965-8564, eISSN 1879-2375. Available from: https://doi.org/10.1016/j.tra.2017.05.005

[17] RUSICH, A., DANIELIS, R. Total cost of ownership, social lifecycle cost and energy consumption of various automotive technologies in Italy. *Research in Transportation Economics* [online]. 2015, **50**, p. 3-16. ISSN 0739-8859. Available from: https://doi.org/10.1016/j.retrec.2015.06.002

[18] BUBECK, S., TOMASCHEK, J., FAHL U. Perspectives of electric mobility: Total cost of ownership of electric vehicles in Germany. *Transport Policy* [online]. 2016, **50**, p. 63-77. ISSN 0967-070X, eISSN 1879-310X. Available from: https://doi.org/10.1016/j.tranpol.2016.05.012

[19] PALMERA K., TATEB J. E., WADUDC Z., NELLTHORP J. Total cost of ownership and market share for hybrid and electric vehicles in the UK, US and Japan. *Applied Energy* [online]. 2018, **209**, p. 108-119. ISSN 0306-2619. Available from: https://doi.org/10.1016/j.apenergy.2017.10.089

[20] POLIAK, M., SEMANOVA, S., MRNIKOVA, M., KOMACKOVA, L., SIMURKOVA, P., POLIAKOVA, A., HERNANDES, S. Financing public transport services from public funds. *Transport Problems* [online]. 2017, **12**(4), p. 61-72. ISSN 1896-0596. Available from: http://transportproblems.polsl.pl/pl/Archiwum/2017/zeszyt4/2017t12z4_06.pdf

[21] The fuel economy of vehicles - AutoCentrum.pl S.A. [online]. [Viewed 2019-02-06]. Available from: https://www.autocentrum.pl/spalanie

[22] Fuel price in Poland - Information Market S.A. [online]. [Viewed 2019-02-06]. Available from: www.e-petrol.pl

[23] The cost of electricity to charge an electric vehicle - Globenergia Sp. z o.o. [online]. [Viewed 2019-02-06]. Available from: globenergia.pl/miesieczne-koszty-ladowania-auta-elektrycznego

[24] Electric or hybrid car - How much does its insurance cost? - Ubea Sp. z o.o. [online]. [Viewed 2019-02-06]. Available from: https://ubea.pl/Elektryk-lub-hybryda-ile-kosztuje-ich-ubezpieczenie%2Cartykul%2C1349

[25] LEWICKI, W. The case study of the impact of the costs of operational repairs of cars on the development of electromobility in Poland. *The Archives of Automotive Engineering - Archiwum Motoryzacji* [online]. 2017, **78**(4), p. 107-116. eISSN 1234-754X. Available from: http://dx.doi.org/10.14669/AM.VOL78.ART8

[26] BURNHAM, A. *User guide for AFLEET Tool 2018*. Lemont, IL: Argonne National Laboratory, 2018.

[27] SPOTTLE, M., JORLING, K., SCHIMMEL, M., STAATS, M., GRIZZEL L., JERRAM, L., DRIER, W., GARTNER, J. *Research for TRAN Committee - Charging infrastructure for electric road vehicles* [online]. Brussels: Policy Department for Structural and Cohesion Policies, 2018. ISBN 978-92-846-2854-4, eISBN 978-92-846-2855-1. Available from: https://doi.org/10.2861/013597

Daniil A. Loktev - Alexey A. Loktev - Alexandra V. Salnikova - Anna A. Shaforostova*

DETERMINATION OF THE DYNAMIC VEHICLE MODEL PARAMETERS BY MEANS OF COMPUTER VISION

This study is devoted to determining the geometric, kinematic and dynamic characteristics of a vehicle. To this purpose, it is proposed to use a complex approach applying the models of deformable body mechanics for describing the oscillatory movements of a vehicle and the computer vision algorithms for processing a series of object images to determine the state parameters of a vehicle on the road. The model of the vehicle vertical oscillations is produced by means of the viscoelastic elements and the dry friction element that fully enough represent the behavior of the sprung masses. The introduced algorithms and models can be used as a part of a complex system for monitoring and controlling the road traffic. In addition, they can determine both the speed of the car and its dynamic parameters and the driving behavior of the individual drivers.

Keywords: *vehicle, mode of vertical oscillations, Kelvin-Voight and Maxwell viscoelastic elements, image processing, feature point method, Haar primitives, errors of the first and second kind, car motion parameters*

1. Introduction

At the present time, automobile transport systems, including infrastructure, roads and vehicles, as well as various automated control and monitoring systems, are under active development. The prospects of the transport networks that must be taken into consideration include a steadily increasing traffic speed (and this applies both to the maximum and the average values of movement speed in certain sections of the roads), greater axle loads and vehicle weight, as well as an overall growth in the number of automobiles. An important component of the safe traffic is the timely determination of parameters of the vehicle movement (speed, direction of movement, position at a particular moment of time relative to the roadway and to the other traffic participants) and their type. Timely detection of deviations from the generally accepted traffic trajectories, together with the critical distances between vehicles, as well as a possible overloading of an equipped vehicle or a road train will largely prevent the occurrence of emergencies or catastrophes. To this purpose, it is useful to monitor the position and the behavior of vehicles in some of the most dangerous places only or in the neighborhood of the certain transport objects, because the total control of the crew's movements is difficult enough and the processing of the information thus received is a rather complex computational task.

For such a monitoring, it is proposed to use passive methods for determining the state and traffic parameters of vehicles, by analyzing a series of images of the objects positioned on the roadway. While solving the problem of engineering passive methods for determining the object's geometrical and kinematic parameters, it is important that these methods would allow applying other methods that increase overall accuracy and reliability and reduce operating costs. The last task should be addressed by use of the mobile diagnostic tools, combining various functions of the mobile device, using the integrated controls with the binding of the monitoring results to the one coordinate of the roadway. Besides, it is intended to increase the speed of the diagnostics up to the level of the established speeds of the vehicles at the sections of the roads subject to control.

In the present study, a method is proposed for determining the vehicle parameters based on the procedures of the object's recognition by color and spatial characteristics by means of computer vision.

2. The simplest models of vertical oscillations

Modern vehicles can be classified by purpose, patency, wheel formula, the number of axles, climatic design, structural requirements, axle load, load-bearing capacity, as well as by type and distance of transportation. When organizing the line traffic on roads with its optimal loads, all vehicles should have the same traction-speed characteristics, the same acceleration and deceleration dynamics, regardless of the weight of the loaded car [1-2].

When determining the parameters of motion and condition of the vehicle, one must start with the elements whose parameters are known, for example, horizontal and vertical road markings. To study the dynamic behavior of the vehicle, especially pronounced in transient modes of motion, the most interesting are vertical oscillations, including a series of object images obtained at small time intervals that are easier to track with the help of passive methods of processing [3-4].

When constructing a model of the vehicle with which it is possible to determine parameters of the movement, it is proposed to follow from simple to complex, gradually increasing the number

* [1]Daniil A. Loktev, [2]Alexey A. Loktev, [3]Alexandra V. Salnikova, [4]Anna A. Shaforostova
[1]Department of Information Systems and Telecommunications, Bauman Moscow State Technical University, Moscow, Russia
[2]Department of Transport Construction, Russian University of Transport (MIIT), Moscow, Russia
[3]International Laboratory of Statistics of Stochastic Processes and Quantitative Finance of Tomsk State University, Russia and Department of Management Systems and Information Technologies in Building, Voronezh State Technical University, Russia
[4]Department of Radio Engineering, Voronezh State Technical University, Russia
E-mail: amicus.lat@yandex.ru

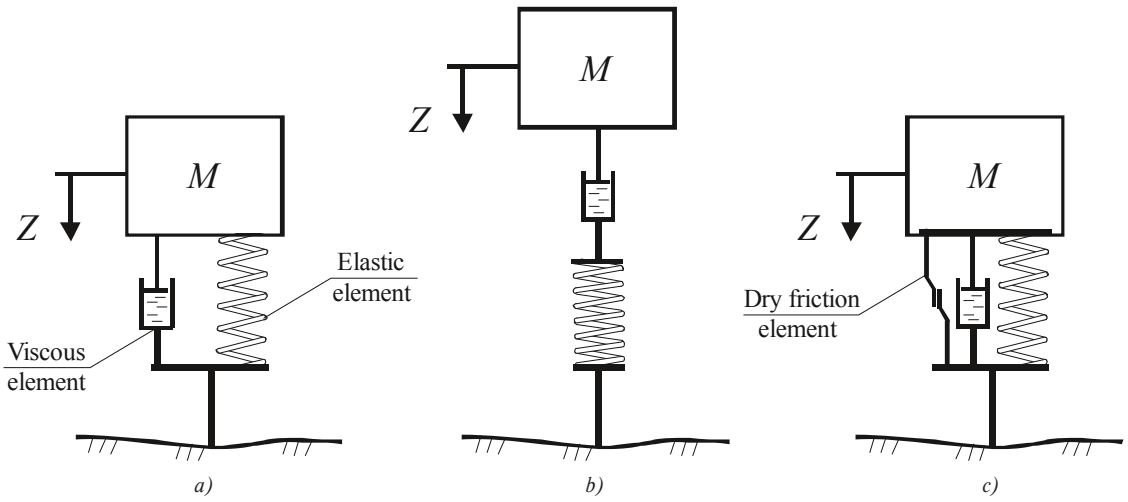

Figure 1 *Model of the vehicle with one degree of freedom, with viscoelastic elements that simulate the dynamic interaction of the vehicle and the road surface: a) Kelvin-Voigt element, b) Maxwell element, c) Kelvin-Voigt element with dry friction*

of defined characteristics and factors to be taken into account. In the beginning, to describe the vertical vibrations of the vehicle, one can choose a system with a single degree of freedom, the mass of which expresses the mass of a loaded car M (Figures 1a, 1b), as well as the system with two degrees of freedom (Figure 1c). Then, the lower mass determines the reduced mass of the wheel pair m, and the upper mass of the vehicle body and its load M_1. In the first case, the vertical displacement associated with the center of gravity of the system is denoted by Z; in the second case the displacement of the wheel pair is denoted by z_1, and the displacement of the vehicle body is Z_1. To simulate the interaction of various parts of the vehicle and the roadway, the elastic elements-springs are used, viscous dampers and dissipative dry friction elements. Various combinations of the listed connections make it possible to obtain adequate and accurate models of the dynamic behavior of both individual components, aggregates and elements and the entire vehicle. Figure 1a shows a viscoelastic Kelvin-Voigt element that simulates the interaction of the vehicle and the road surface. In Figure 1b, the Maxwell element is presented, which is a sequential connection of a viscous and elastic element. In Figure 1c, a dry friction element has been added to the Kelvin-Voigt element, which makes it possible to simulate springs of the vehicle more fully [1, 2, 5].

There is also a model of interaction of a vehicle with the road surface with the two degrees of freedom, a separate body with its mass; the wheel pair is represented by geometrical and mechanical parameters. This representation allows one to separately simulate the interaction between the body of a vehicle and a wheel pair, as well as the properties of springs, by introducing a dry-friction element into the system responsible for rheological properties of the suspension. The lower viscoelastic element of the Kelvin-Voight type allows simulating the interaction of the wheel pair and the roadway, and in the future it will allow taking into account various defects of the road surface.

The choice of a specific mathematical model for the vehicle depends on a number of factors. They include the type of the vehicle; the parameters determined and the assumptions made concerning, for example, the continuity of the movement, being either rectilinear or even. In this case, the theory of small oscillations applicable to the system of bodies and the presupposition that springs and the wheels of the vehicle have only vertical compliance are taken into account, while the horizontal forces of inertia of wheel pairs are not [1, 3, 6].

When describing vertical oscillations of models Figure 1a and Figure 1b, it is assumed that viscoelastic elements do not lose stability, i.e. points of the vehicle's body and the wheel in the area of contact with the road surface can move rectilinearly along the same straight line.

In this paper is proposed to consider the joint movement of the vehicle body and the wheel pair without taking into account those impacts that are actually present from the roadway and moving cargo. The movement of the two interacting bodies (the body of the vehicle and the wheel pair) after the start of the contact for the model of viscoelastic body of the Kelvin-Voigt type (Figure 1a), with respect to the fixed reference system, is described by a system of the second-order differential equations:

$$\begin{aligned} &M_1(\ddot{z}_1+\ddot{z}_3)+K(\dot{z}_1-\dot{z}_2)+C(z_1-z_2)=0,\\ &m_1(\ddot{z}_2+\ddot{z}_3)+K(\dot{z}_2-\dot{z}_1)+C(z_2-z_1)=0, \end{aligned} \tag{1}$$

if one takes the Maxwell's viscoelastic element as the basis of the buffer model simulating a wide range of vehicle suspension properties, then the system of determining equations will take the form:

$$\begin{aligned} &M_1(\ddot{z}_1+\ddot{z}_3)-K\int_0^t(\dot{z}_1-\dot{z}_2)\exp\left(-\frac{t-t'}{\tau_1}\right)dt'+\\ &+C(z_1-z_2)=0,\\ &m_1(\ddot{z}_2+\ddot{z}_3)-K\int_0^t(\dot{z}_2-\dot{z}_1)\exp\left(-\frac{t-t'}{\tau_1}\right)dt'+\\ &+C(z_2-z_1)=0, \end{aligned} \tag{2}$$

where M_1 and m_1 are the weights of the body and wheel pairs, respectively; z_1 and z_2 are the coordinates of the center of gravity

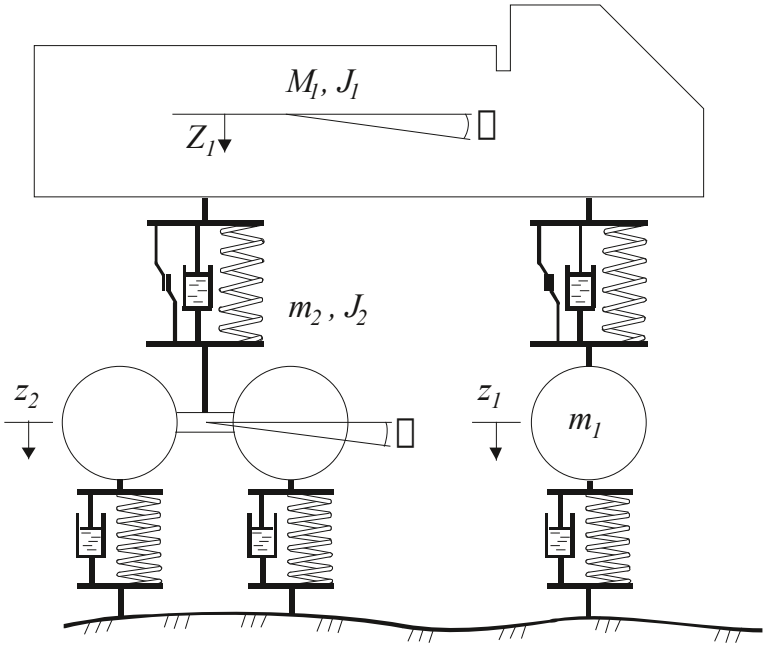

Figure 2 *Flat model of a three-axle car with five degrees of freedom*

of the body and the wheel pair relative to the upper point of the buffer, respectively; z_3 is the coordinate of the upper point of the buffer relative to the inertial reference frame; K is the coefficient of the viscous resistance of the buffer simulating the interaction of the vehicle and the road surface; C is the coefficient of rigidity of the elastic element in the buffer.

The system of defining equations (1) or (2) depending on the selected model must be supplemented with the initial conditions characterizing the state of the system of bodies at the initial time $t = 0$:

$$\begin{aligned} &z_1(t=0)=0, \quad z_2(t=0)=0,\\ &\dot{z}_1(t=0)=0, \quad \dot{z}_2(t=0)=0. \end{aligned} \tag{3}$$

To evaluate the interaction of the body of the vehicle, the wheel pair and the roadway, it is proposed to use three characteristics (power, geometrical and kinematic):

- the force of interaction between various sprung parts of the system $P(t)$, taking into account the influence of linear resistance, elastic forces and dry friction; in some cases, the greatest interest is the maximum value of this force - $\max\limits_{t\in[0,\infty)} P(t)$;
- the vertical movement of the vehicle's body $z(t)$, including its maximum value $\max\limits_{t\in[0,\infty)} z(t)$;
- the vertical acceleration of the vehicle points as one of the main criteria for the smooth running of the vehicle $\max\limits_{t\in[0,\infty)} \ddot{z}(t)$.

Depending on the type of the vehicle, more complex models can be used to describe the operation of the main components, assemblies, vehicle structures and their elements, as well as the behavior of cargos, driver and passengers. That will allow a more accurate study of the dynamic behavior and state of the vehicle under the different traffic conditions and depending on the quality of the road surface [1, 4].

3. Plane model of a vehicle with three wheel axles

In addition to the simplest models shown in Figure 1, in this paper is considered a flat model in the form of a system of solids (vehicle's body and wheel pairs), connected with each other and with the roadway by the viscoelastic elements with the elements of dry friction at the places of suspension of weights. In fact, those elements are elastic-dissipative bonds that are responsible for the model of interaction of various elements with each other and taking into account the rheological properties of specific materials and structural elements.

For accurate estimation of the computational models of a vehicle, it is necessary to carry out the frequency analysis of their own and forced oscillations, as well as to study the behavior of vehicle's structures in various design situations and under different driving conditions [2, 3, 5].

This study also considers the design of a three-axle vehicle with the five degrees of freedom (Figure 2). As the generalized coordinates the following ones are accepted: Z - vertical movement of the vehicle's body (center of gravity); φ - angular movement of the vehicle's body; z_1 - vertical movement of the first axis of the car; z_2 - reduced vertical movement of the second axle of the vehicle, in fact, this is a joint movement of the 2nd and 3rd bridges, connected to each other and representing a trolley; ψ - angular displacement of dual axles of the vehicle.

Functional equations describing the movement of the vehicle in differential form can be obtained in terms of the d'Alembert principle:

$$\begin{aligned} &M\ddot{Z}(t)+F_1(v_1,\dot{v}_1)+F_2(v_2,\dot{v}_2)-M_g=0,\\ &J_1\ddot{\varphi}(t)+F_1(v_1,\dot{v}_1)a_T-F_2(v_2,\dot{v}_2)b_T=0,\\ &m_1\ddot{z}_1(t)-F_1(v_1,\dot{v}_1)+R_1(u_1,\dot{u}_1)-m_1g=0,\\ &m_2\ddot{z}_2(t)-F_2(v_2,\dot{v}_2)+R_2(u_2,\dot{u}_2)+R_3(u_3,\dot{u}_3)-m_2g=0,\\ &J_2\ddot{\psi}(t)+R_2(u_2,\dot{u}_2)l_2/2-R_3(u_3,\dot{u}_3)l_2/2=0, \end{aligned} \tag{4}$$

where $F_i(v_i,\dot{v}_i)$ and $R_i(u_i,\dot{u}_i)$ are the viscous resistance forces in a buffer that simulates the interaction of the body and the *i*-th wheel pair; $v_i = v_i(t)$, $\dot{v}_i = \dot{v}_i(t)$ are the vertical displacement and the speed of the buffer deformation over the *i*-th wheel pair, respectively; $u_i = u_i(t)$, $\dot{u}_i = \dot{u}_i(t)$ are the vertical displacement and the wheel deformation speed related to the *i*-th axis, respectively.

The defining relations for the forces F_i and R_i can be represented taking into account the terms responsible for the dissipative properties of the buffer including the viscous resistance according to the Kelvin-Voigt model and dry sliding friction according to the Coulomb model:

$$\begin{aligned} F_i(v_i,\dot{v}_i) &= F_i(v_i) + k_{pi}\dot{v}_i + T_{pi}\operatorname{sign}(\dot{v}_i), \\ R_i(u_i,\dot{u}_i) &= R_i(u_i) + k_{si}\dot{u}_i, \end{aligned} \tag{5}$$

where k_{pi}, k_{si} are the damping coefficients of the viscoelastic buffer and the *i*-th axis of the wheel and T_{pi} is the coefficient of dry friction in the buffer over the *i*-th axis. The functions $F_i(v_i)$ and $R_i(u_i)$ usually take a piecewise linear exponential form [2, 5].

To reduce the number of unknown factors in the functional equations and the desired functions, one can represent the vertical displacements of axes of wheel pairs v_i and u_i through the generalized coordinates. Then, the parameters of the road profile are taken into account, allowing specifying the initial movements, for example, when the vehicle goes over the element of forced reduction of the vehicle speed («speed bump»).

4. Method for determining the motion parameters by analyzing images

To experimentally determine geometrical and kinematic characteristics of the vehicle's movement both in the horizontal and the vertical plane (direction of movement, speed and distance to the desired object), it is necessary to recognize the vehicle type, as well as to detect the number of wheel axes. Determining the movement parameters of the vehicle's body and its wheels can be carried out when considering rotational motion (wheels) and translational motion (body) [7-9].

At the stage of the primary image processing, the characteristic points of the image are distinguished, and the optical flow in their vicinity is calculated. In this case, the pixel of the object with the plane and time coordinates (*x, y, t*) and intensity *I*(*x, y, t*) receive increments (Δ*x,* Δ*y,* Δ*t*) during the change of one frame to another [10-12]. The changed pixel intensity can be represented in the form of a Taylor series, given the smallness of the possible displacements:

$$\begin{aligned} &I(x+\Delta x, y+\Delta y, t+\Delta t) = \\ &I(x,y,t) + \frac{\partial I}{\partial x}\Delta x + \frac{\partial I}{\partial y}\Delta y + \frac{\partial I}{\partial t}\Delta t. \end{aligned} \tag{6}$$

To calculate the optical flow of an image, it is proposed to use the Lucas-Canade method, which is based on the assumption that the optical flow is the same for all the pixels within a small rectangular image area, which includes a certain set of pixels $(q_i)_{i=1}^n$ [13]. The components of the optical flow velocity $v = [v_x, v_y]^T$ for the central pixel *p* of the set can be obtained by solving the defining system of equations, [14]:

$$I_x(q_i)v_x + I_y(q_i)v_y + I_t = 0 \tag{7}$$

where the fact is taken into account that the intensity depends [15] on the position of each pixel q_i.

An important task that one faces while solving the system of equations (6) is the choice of the size of a rectangular frame around the examined pixel [16-18]. It concerns with the comparison of the two mutually exclusive conditions: while reducing the frame allows one to separate the moving objects with a fixed background [19], the frame magnification allows one to detect and track large object movements [20]. To solve the dual problem of the Lucas-Canade method implementation, it is proposed to use the Bouguet iterative scheme [21-23].

Comparison of the two images of a video sequence can be represented as the following sequence of actions:

Step 1. Inputting images *I*, *J* and the coordinates of the examined pixel *u* into the image *I*.

Step 2. Creating interactive diagrams of the source images $\{I^L\}_{L=0\ldots Lm}$ and $\{J^L\}_{L=0\ldots Lm}$.

Step 3. Initializing the offset accumulated by the passed levels: $g^{Lm} = \begin{bmatrix} 0 \\ 0 \end{bmatrix}$.

Step 4. Cycling through *L* levels from L_m to 0 with the decrement –1.

Step 5. Calculating the coordinates (p_x, p_y) of the pixel *u* at the image I^L : $u^L = \frac{u}{2^L} = \begin{bmatrix} p_x \\ p_y \end{bmatrix}$.

Step 6. Calculating the derivatives of the image I^L at the spatial coordinates: $I_x(x,y) = \{I^L(x+1,y) - I^L(x-1,y)\}/2$.

Step 7. Calculating the gradient matrix in the image plane: $G = \sum_{x=p_x-w_x}^{p_x+w_x} \sum_{y=p_y-w_y}^{p_y+w_y} \begin{bmatrix} I_x^2(x,y) & I_x(x,y)I_y(x,y) \\ I_x(x,y)I_y(x,y) & I_x^2(x,y) \end{bmatrix}$.

Step 8. Initializing the offset accumulated by iterations: $v^0 = \begin{bmatrix} 0 \\ 0 \end{bmatrix}$.

Step 9. Subcycling of iterations *k* from 1 to 5.

Step 9.1. Image subtraction (evaluation of the time derivative of the image): $\delta I_k(x,y) = I^L(x,y) - J^L(x + g_x^L + v_x^{k-1}, y + g_y^L + v_y^{k-1})$.

Step 9.2. Calculating the vector differences: $b_k = \sum_{x=p_x-w_x}^{p_x+w_x} \sum_{y=p_y-w_y}^{p_y+w_y} \begin{bmatrix} \delta I_k(x,y)I_x(x,y) \\ \delta I_k(x,y)I_y(x,y) \end{bmatrix}$.

Step 9.3. Optical flow calculation: $\eta^k = G^{-1}b_k$, where $G = A^TA = \sum_{i=1}^n \begin{bmatrix} I_x^2(q_i) & I_x(q_i)I_y(q_i) \\ I_x(q_i)I_y(q_i) & I_y^2(q_i) \end{bmatrix}$ is the matrix of moments of the second order of the rectangular area of the image; $b = \sum_{i=1}^n \begin{bmatrix} -I_t(q_i)I_x(q_i) \\ -I_t(q_i)I_y(q_i) \end{bmatrix}$ is the vector of the mixed multiplication.

Step 9.4. Updating the offset accumulated by iterations: $v^k = v^{k-1} + \eta^k$.

Step 10. Calculating the offset for level L: $d^L = v^k$.

Step 11. Calculating the offset accumulated up to the next level $L-1$: $g^{L-1} = 2(g^L + d^L)$.

Step 12. Calculating the total offset: $d = g^0 + d^0$.

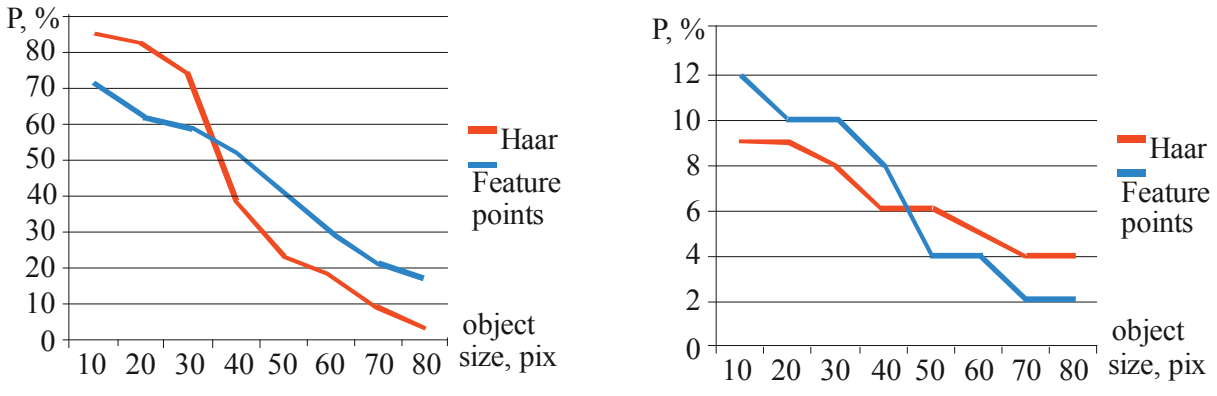

Figure 3 *The dependence of the error probability of the first (a) and second (b) kinds upon the object's size*

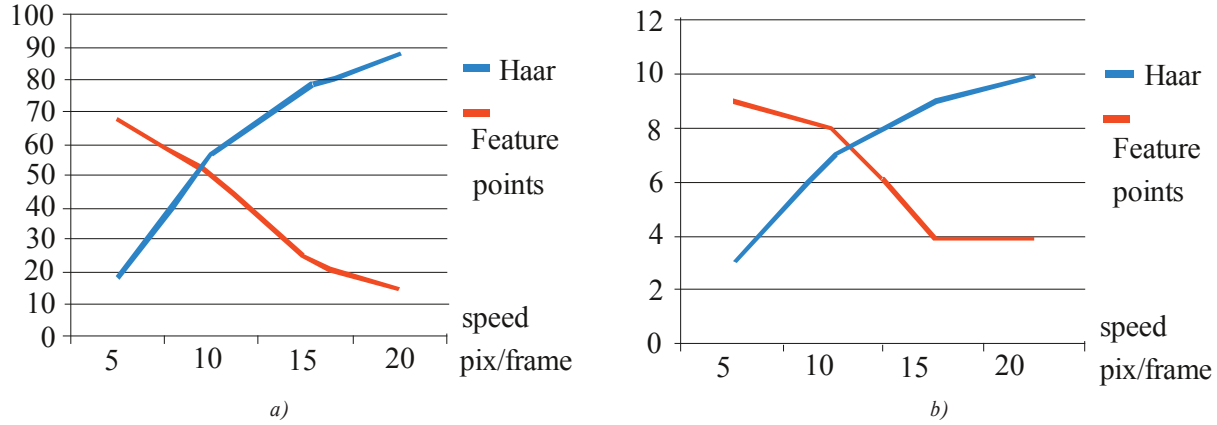

Figure 4 *Dependence of the error probability of the first (a) and second (b) kinds upon the object's speed*

Step 13. Calculating the coordinates of the examined pixel on the image J: $w = u + d$.

Step 14. Outputting the coordinates of the pixel w on to the image J.

The described algorithm can be used to determine, for the last N frames, the movements of the center of the selected frame relative to the background in the pixels ΔX_{ob}, ΔY_{ob} which is necessary to determine the velocities of object points [19, 24].

Having a priori camera information - the height H_{fr} and the width W_{fr} of the frame, the angles in the radians α_{fr} and β_{fr}, vertically and horizontally, - one can find the actual horizontal and vertical offsets of the object from the proportions of the right-angled triangles that define the positions of the image and the real object:

$$\frac{\Delta\alpha_{ob}}{\alpha_{fr}} = \frac{\Delta Y_{ob}}{H_{fr}} \Rightarrow \Delta\alpha_{ob} = \frac{\Delta Y_{ob}}{H_{fr}}\alpha_{fr},$$
$$\tan\Delta\alpha_{ob} = \frac{\Delta y}{l} \Rightarrow \Delta y = l\Delta\alpha_{ob} = \frac{\alpha_{fr}\Delta Y_{ob}}{H_{fr}}l. \quad (8)$$

Estimations of the velocity components v_x, v_y are obtained by dividing the offsets by the time interval $N\tau$ (τ - frame duration):

$$v_x = \frac{\Delta x}{N\tau} = \frac{\beta_{fr}\Delta X_{ob}}{W_{fr}}\frac{l}{N\tau},\ v_y = \frac{\Delta y}{N\tau} = \frac{\alpha_{fr}\Delta Y_{ob}}{H_{fr}}\frac{l}{N\tau} \quad (9)$$

When determining the distance to the vehicle, the height of the frame of the object H_{ob} in pixels [25-27] is referred to. Assuming that the vertical viewing angle of the camera in the radians is α_{fr}, the frame height in pixels is H_{fr}, the real height of the object in meters is h, it is possible to determine the actual distance to the object in meters that is l.

The angle at which the object is visible is determined by the proportion: $\alpha_{ob} = H_{ob}\alpha_{fr}/H_{fr}$.

Then the actual distance to the object, taking into account the small value of the viewing angle, is the following: $l = h/\alpha_{ob} = H_{fr}h/\alpha_{ob}H_{ob}$.

The estimation of the velocity projection v_z of the object is made by changing the height of the object during the time N_τ, then:

$$l(t) = \frac{H_{fr}}{\alpha_{fr}H_{ob}(t)}h, \quad (10)$$

$$l(t-N\tau) = \frac{H_{fr}}{\alpha_{fr}H_{ob}(t-N\tau)}h, \quad (11)$$

$$v_z = \frac{l(t)-l(t-N\tau)}{N\tau} = \left[\frac{H_{fr}}{H_{ob}(t)} - \frac{H_{fr}}{H_{ob}(t-N\tau)}\right]\frac{h}{\alpha_{fr}N\tau}. \quad (12)$$

The actual speed of the object is calculated by the geometrical sum of the projections: $v = \sqrt{v_x^2 + v_y^2 + v_z^2}$. Knowing the speed function, one can determine the acceleration of the vehicle and its projection on different coordinate axes.

5. Numerical investigation

In addition to the Lucas-Canade method, the Adaptive Boosting algorithm has been considered [28-30]. Probabilities of errors of the first and second kind have been determined [31-33], depending on the object's size at the image (Figure 3a, 3b) and on the object's speed (Figure 4a, 4b).

Figures 3 and 4 show that the for larger objects (more closely located) and for the slower objects the possibility of errors of the first and the second kind is less when the algorithm of the object recognition using the Haar primitives is applied, while for all the other objects, application of the algorithm, using the feature points, is the most suitable. Thus, to reduce the probability of errors during the recognition of the objects, it is proposed to use only two parameters for the initial recognition of the object: the distance from the camera and its speed. It is assumed that the speed of the objects can belong to one of the two groups - "fast" or "slow", and the distance to them - to the "far" or "close" groups. Establishing the boundaries of the definition of these groups is performed by means of the statistical analysis tools.

As a result, when determining the speeds of the vertical and horizontal movement of the vehicle, as well as the vertical linear and angular accelerations, the weight of the vehicle and the weights of the individual parts of the vehicle, reduced to the wheel axles can be determined. This will contribute to the control of the road congestion, the traffic density at the individual sections, as well as toe compliance with the regulatory requirements of the cargo transportation and traffic rules.

6. Conclusion

Algorithms, methods and models introduced in this study can be implemented as a part of an integrated hardware-software system for monitoring and controlling the motion that can allow one to determine the geometrical (movement, position), kinematic (speed, path) and dynamic (weight, acceleration) motion parameters of the car. As the primary information on the object is proposed to be obtained through its image in the optical range, this method is not associated with the additional electromagnetic radiation and thus it is not dangerous for living organisms. It is also rather more difficult to be detected and thus it is safer against possible counter detection systems. The conducted numerical studies, based on the developed algorithms and models, demonstrate the better occurrence values of errors of the first and the second kind during the system operation depending on the speed and size of the object being measured. The presented detection scheme can operate in the real time during its computer-based implementation.

Acknowledgement

This study was financially supported by the Russian Science Foundation (research project No. 17-11-01049).

References

[1] AZIMOV, S. Z., LEBEDEV, O. V., SHERMUKHAMEDOV, A. A. Optimization of calculation of the process of braking of wheel machines (in Russian). 8th Russian Congress of Theoretical and Applied Mechanics : proceedings. 2001, p. 211.

[2] SOUKUP, J., SKOCILAS, J., SKOCILASOVA, B. Vertical vibration of the vehicle model with higher degree of freedom. *Procedia Engineering* [online]. 2014, **96**, p. 435-443. ISSN 1877-7058. Available from: https://doi.org/10.1016/j.proeng.2014.12.113

[3] DEVYATERIKOV, E. A., MIKHAILOV, B. B. Vision system for measuring the path of a mobile robot (in Russian). *Mechanics, Control and Informatics*. 2012, **2**(8), p. 219-224. ISSN 2075-6836.

[4] ZAMOTAYLOV, O. V. Problems of image recognition of the device of subsurface radar on the basis of mobile road laboratory (in Russian). *T-Comm-Telecommunications and Transport*. 2010, **6**, p. 38-42. ISSN 2072-8735, eISSN 2072-8743.

[5] LOKTEV D. A. Determination of object parameters by a series of its images in the integrated monitoring system (in Russian). *Path and Track Facilities*. 2015, 2, p. 31-33. ISSN 0131-5765

[6] SUN, Z., BEBIS, G., MILLER, R. On-road vehicle detection using optical sensors: A review. 7th International IEEE Conference on Intelligent Transportation Systems : proceedings [online]. 2004. ISBN 0-7803-8500-4. Available from: https://doi.org/10.1109/ITSC.2004.1398966

[7] BEDER, C., BARTCZAK, B., KOCH, R. A comparison of PMD-cameras and stereo-vision for the task of surface reconstruction using patchlets. 2007 IEEE Conference on Computer Vision and Pattern Recognition : proceedings [online]. Vol. 4. IEEE Service Center : Piscataway, NJ, 2007. ISBN 1-4244-1179-3, eISBN 1-4244-1180-7, p. 17-22. Available from: https://doi.org/10.1109/CVPR.2007.383348

[8] WIEDEMANN, M., SAUER, M., DRIEWER, F., SCHILLING, K. Analysis and characterization of the PMD camera for application in mobile robotics. 17th World Congress - International Federation of Automatic Control : proceedings [online]. 2008. ISBN 978-1-1234-7890-2. Available from: https://doi.org/10.3182/20080706-5-KR-1001.3304

[9] LITOMISKY, K. *Consumer RGB-D cameras and their applications* [online]. Ph.D. Thesis. University of California: Riverside, 2012. Available from: http://alumni.cs.ucr.edu/~klitomis/files/RGBD-intro.pdf

[10] HAHNE, U. *Real-time depth imaging* [online]. Ph.D. Thesis. Technische Universitat Berlin: Berlin, 2012. Available from: https://d-nb.info/1023762218/34

[11] GIL, P., POMARES, J., TORRES, F. Analysis and adaptation of integration time in PMD camera for visual serving. 20th International Conference on Pattern Recognition : proceedings [online]. 2010. ISSN 1051-4651. Available from: https://doi.org/10.1109/ICPR.2010.85

[12] SINGH S., WEST J. *Cyclone: A laser scanner for mobile robot navigation*. Technical Report CMU-RI-TR-91-18. The Robotics Institute, Carnegie Mellon University: Pittsburgh, 1991.

[13] DANKO, M., TARABA, M., ADAMEC, J., DRGONA, P. Visualization of Scoda instrument cluster. *Communications - Scientific Letters of the University of Zilina* [online]. 2018, **20**(1), p. 27-31. ISSN 1335-4205, eISSN 2585-7878. Available from: http://komunikacie.uniza.sk/index.php/communications/article/view/39

[14] VELAS, A., LOVECEK, T., VALOUCH, J., DWORZECKI, J., VNENCAKOVA, E. Testing radio signal range of selected components. *Communications - Scientific Letters of the University of Zilina* [online]. 2018, **20**(2), p. 68-77. ISSN 1335-4205, eISSN 2585-7878. Available from: http://komunikacie.uniza.sk/index.php/communications/article/view/90

[15] BOROS, M., SISER, A., KEKOVIC, Z., MAZAL, J. Mechanical characteristics of cylinder pin tumbler locks as they relate to resistance testing. *Communications - Scientific Letters of the University of Zilina* [online]. 2018, **20**(2), p. 96-101. ISSN 1335-4205, eISSN 2585-7878. Available from: http://komunikacie.uniza.sk/index.php/communications/article/view/94

[16] BENDER, C., DENKER, K., FRIEDRICH, M., HIRT, K., UMLAUF, G. A hand-held laser scanner based on multi-camera stereo-matching. IRTG 1131 - Visualization of Large and Unstructured Data Sets Workshop 2011 : proceedings [online]. 2011. Available from: https://doi.org/10.4230/OASIcs.VLUDS.2011.123

[17] DESCHENES, F., ZIOU, D. Depth from defocus estimation in spatial domain. *Computer Vision and Image Understanding* [online]. 2001, **81**(2), p. 143-165. ISSN 1077-3142. Available from: https://doi.org/10.1006/cviu.2000.0899

[18] RAJABZADEH, T., VAHEDIAN, A., POURREZA, H. R. Static object depth estimation using defocus blur levels features. 6th International Conference on Wireless Communications Networking and Mobile Computing : proceedings. 2010. ISBN 978-1-4244-3709-2.

[19] BORACHI, G., CAGLIOTI, V. Motion blur estimation at corners. 3rd International Conference on Computer Vision Theory and Applications : proceedings. 2008. ISBN 978-989-8111-21-0.

[20] ZHUO, S., SIM, T. Defocus map estimation from a single image. *Pattern Recognition* [online]. 2011, **44**(9), p. 1852-1858. ISSN 0031-3203. Available from: https://doi.org/10.1016/j.patcog.2011.03.009

[21] ELDER, J. H., ZUCKER, S. W. Local scale control for edge detection and blur estimation. *IEEE Transaction on Pattern Analysis and Machine Intelligence* [online]. 1998, **20**(7), p. 120-127. ISSN 0162-8828, eISSN 1939-3539. Available from: https://doi.org/10.1109/34.689301

[22] LOSCH, S. *Depth from blur combining image deblurring and depth estimation*. Bachelor's Thesis. Saarland University: Homburg, 2009.

[23] LIN, H.-Y., CHANG, C.-H. Depth from motion and defocus blur. *Optical Engineering* [online]. 2006, **45**(12), p. 127201-1- 127201-12. ISSN 0091-3286, eISSN 1560-2303. Available from: https://doi.org/10.1117/1.2403851

[24] ALEXIEV K., NIKOLOVA I., ZAPRYANOV G. 3D scenes recovery through an active camera based on blur assessment of the resulting image. *Information Technologies and Control*. 2008, **3-4**, p. 10-20. ISSN 1392-124X, eISSN 2335-884X.

[25] LOKTEV, D. A., ALFIMTSEV, A. N., LOKTEV, A. A. Modeling of an integrated system of video monitoring inside the building. Part 2. The Algorithm of Recognition of Objects (in Russian). *Vestnik MGSU*. 2012, **5**, p. 124-131. ISSN 1997-0935, eISSN 2304-6600.

[26] LUCAS, B. D., KANADE, T. An iterative image registration technique with an application to stereo vision. 7th International Joint Conference on Artificial Intelligence : proceedings. 1981.

[27] BOUGUET J.-Y. *Pyramidal implementation of the lucas-kanade feature tracker*. Intel Corporation Microprocessor Research Labs: Santa Clara, CA, USA, 2000.

[28] HARRIS, C., STEPHENS, M. A combined corner and edge detector. 4th Alvey Vision Conference : proceedings [online]. 1988. Available from: https://doi.org/10.5244/C.2.23

[29] LOKTEV, A. A., SYCHEV, V. P., LOKTEV, D. A., DMITRIEV, V. G. Automated system for identifying defects in wheels of the rolling stock on the basis of assessment of shock nonaxisymmetric impact of wheels on rail when modeling the track structure with orthotropic plate (in Russian). *Engineering and Automation Problems*. 2017, **4**, p. 59-70. ISSN 0234-6206.

[30] VIOLA P., JONES M. J. Robust real-time object detection. Second Workshop on Statistical and Computational Theories of Vision: procedings. 2001.

[31] CHERNOYAROV, O. V., VACULIK, M., SHIRIKYAN, A., SALNIKOVA, A. V. Statistical analysis of fast fluctuating random signals with arbitrary-function envelope and unknown parameters. *Communications - Scientific Letters of the University of Zilina* [online]. 2015, **17**(1A), p. 35-43. ISSN 1335-4205, eISSN 2585-7878. Available from: http://komunikacie.uniza.sk/index.php/communications/article/view/410

[32] LELEGARD, L., VALLET, B., BREDIF, M. Multiscale haar transform for blur estimation from a set of images. ISPRS Conference PIA 2011. International Archives of Photogrammetry, Remote Sensing and Spatial Information Science : proceedings [online]. 2011. Available from: https://doi.org/10.5194/isprsarchives-XXXVIII-3-W22-65-2011

[33] LOKTEV, D. A., LOKTEV A. A. Determination of object location by analyzing the image blur. *Contemporary Engineering Sciences* [online]. 2015, **8**(9), p. 467-475. ISSN 1313-6569, eISSN 1314-7641. Available from: http://dx.doi.org/10.12988/ces.2015.52198

Eva Schmidova - Premysl Hojka - Bohumil Culek - Filip Klejch - Michal Schmid*

DYNAMIC STRENGTH AND ANISOTROPY OF DMLS MANUFACTURED MARAGING STEEL

This paper deals with maraging steel, as a prospective material for the 3D printed lightened structural parts of transport means. Direct Metal Laser Sintering technology was tested for creation of a thin-wall structure with defined internal geometry. The referential samples prepared by the DMLS technology were examined under quasi-static and high strain rate loading using a servo-hydraulic testing machine at strain rates up to 1400 s-1. Microstructural analyses served for evaluation of structural homogeneity and metallurgy quality, including the influence of crystallization gradient. The stabile ductile fracture mode was proven by fractography analyses, even at a maximal strain rate. The post-impact tests were conducted to evaluate the local residual plasticity by indentation tests.

Keywords: *DMLS technology, 3D printing, maraging steel, impact tensile tests*

1. Introduction

Additive manufacturing (AM), as the industrial version of the 3D-printing, is already used mainly for plastic prototypes. It works directly with graphic models, so designers can devise new shapes without regards for existing manufacturing limitations. However, its application to critical metal alloy parts is still a significant milestone for the technology. It is necessary to explore how to use additive manufacturing with a wider range of metal alloys, how to combine different alloys for functional graded materials, and so on [1].

Another promising research focus is fabrication and study of the lightweight designs based on complex internal designs - from the micro- up to the macro-scale. The direct laser writing system provides a basis for fabrication of the controlled 3D micro-trusses. While the micro-production process enables the high-resolution structuring of arbitrary 3D patterns mainly determined by the laser spot size [2], the macro-scale is typified by regular internal geometry. Majority of studies regarding the high strain rate loading of cellular foam cores are predominantly limited to metallic foam cores, such as aluminum [3-4].

The additive manufacturing approach is used both for rapid prototyping, as it decreases development time for new products and production manufacturing, to simplify assemblies and complex geometries. The range of currently available metal materials for the 3D printing ranges from titanium alloys and nickel alloys to the high-grade stainless steels, and this range is expanding rapidly together with increases in quality requirements.

The Direct Metal Laser Sintering (DMLS) and electron beam melting are the main representative processes of the powder-based fusion technologies. The DMLS uses uncoated pre-alloyed metal powders as the sintering material [5]. It is a laser-based rapid prototyping and tooling process by means of which the net-shaped parts are fabricated in a single process. Complex parts can be produced directly from the 3D CAD models by layer-wise solidification of metal powder layers in portions of the layer corresponding to the cross section of the 3D part in the respective layer [6]. It needs to be pointed out that only very limited information about serial production and usage of complex parts exists.

The presented experimental study of maraging steel is focused on dynamic fracture behaviour using samples 3D printed by the DMLS technology. The obtained results will serve for internal geometry design of lightweight high-performance products. The main macro- and microstructural parameters, together with mechanical responses at defined geometrical and loading conditions, are necessary for precise numerical simulation of products with complex internal geometries.

2. Material and methods

The experimental analyses were focused on:

- evaluation of dynamic hardening capacity under different strain rates and
- study of internal phase and structural conditions including metallurgical quality.

The defined samples geometry prepared by the DMLS technology is documented in Figure 1, printing direction is indicated by arrow. Direct measurement by strain gauges was considered necessary for the precise measurement of dynamic responses; the crucial requirement is to suppress the dynamic response of the loading and clamping system in the case of increased strain rate and complex sample shapes.

The static stress-strain response was evaluated by the standard tensile test using a *ZWICK*/ROEL Z-030 machine and the dynamic behaviour was tested using an AH 40-100 M062 electro-hydraulic system with Inova TestControl control system at two loading rates - 5 m/s and 10 m/s.

The maraging steels are generally characterized by a high nickel content, very low carbon content and use of the substitutional elements or precipitates to produce the

* **Eva Schmidova, Premysl Hojka, Bohumil Culek, Filip Klejch, Michal Schmid**
Faculty of Transport Engineering, University of Pardubice, Czech Republic
E-mail: eva.schmidova@upce.cz

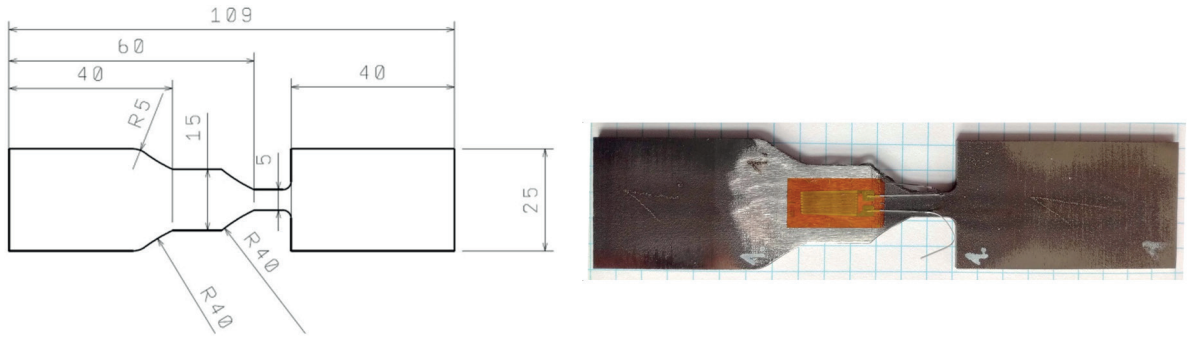

Figure 1 *Samples geometry*

Table 1 *Chemical composition of the tested steel [wt. %]*

	C	Si	Mn	P	S	Cr	Mo	Ni	Co	Ti	Al
MS1	≤ 0.03	≤ 0.1	≤ 0.1	≤ 0.01	≤ 0.01	≤ 0.5	4.5	17.0	8.5	0.6	0.05
							5.2	19.0	9.5	0.8	0.15
1.2709	≤ 0.03	≤ 0.1	≤ 0.15	≤ 0.01	≤ 0.01	≤ 0.25	4.5	17.0	8.5	0.8	-
							5.2	19.0	10	1.2	

age hardening. The material used - Maraging Steel MS1 - is a steel powder, which has been optimised especially for the 3D processing; it is a martensite-hardenable steel corresponding to 1.2709 (X3NiCoMoTi 18-9-5). The chemical composition, in comparison to conventional maraging steel is given in Table 1. This kind of steel is characterised by excellent strength combined with high toughness; in the 3D printed form it is intended for high-load tools. The parts are easily machinable after the building process and can be easily post-hardened to more than 50 HRC by age-hardening at 490 °C (914 °F) for 6 hours. They also have excellent weldability and polishability. The tested samples were in the primary stage - without the post-hardening, to find out influence of the used technology including the natural surface relief.

The fractography analyses served for the fracture mode identification. Impurities were identified using the energy dispersive X-ray spectroscopy.

The local mechanical heterogeneity, due to direction of the layer cladding, together with the plastic flow at maximal strain rate, were evaluated by specific indentation test, using the cylindrical indenter and Hencky theory of plasticity.

3. Results and discussion

3.1 Microstructural characterisation

The resulting DMLS 3D printed parts have different material structures and therefore different mechanical properties than parts obtained through the conventional techniques, depending upon the materials. Due to the layer-wise building method, the parts have a certain anisotropy. Figure 2 illustrates the perpendicular versus longitudinal features in a macroscopic view. Visible are the effects of a layer-by-layer build process, which can be reduced or removed by appropriate heat treatment.

Especially for metal powder, there are some specific problems of the DMLS technology related to powder quality: particle size distribution, morphology, internal porosity, chemical composition, roughness. Due to this, the internal continuity and prospective presence of imperfections along the layers interphase were checked. No effects of process instabilities were observed as defective filling of layers, porosity in final parts, or lack of fusion defects.

The powder is generally discussed as one of the major costs (and problems) contributing to the additive manufacturing process. It is useful for technology optimization to distinguish each source of obtained product quality. The observed micro-impurities were identified by the energy chemical microanalysis mainly as TiN (TiCN), without substantial influence on the fracture response.

The basic principle of the DMLS technology is to melt down very thin layers (20-60 μm) of metal powder with an electronically driven laser beam. A layer of metal powder with the grain size fractions below 6 μm is spread on a steel base plate. It is possible to build complex geometries, even those that are impossible to obtain with any other kind of technology, with accuracy up to ± 0.05 mm [7]. The SEM image in Figure 3 shows the typical microstructure in the longitudinal direction. A very fine cellular microstructure without typical martensitic morphology was documented in the natural stage of the printed steel. Epitaxial crystallisation at the grains bound together with chemical heterogeneity is the typical result of a very high cooling rate.

The present microstructure is mainly influenced by the energy deposition, which depends on the beam diameter and the raster speed. In addition, the re-melt strategy will selectively and often systematically alter the microstructure and therefore the residual product properties. The product volume (or size) will also influence the thermal issues, primarily cooling or rate of cooling, which can also have a significant effect on the microstructure.

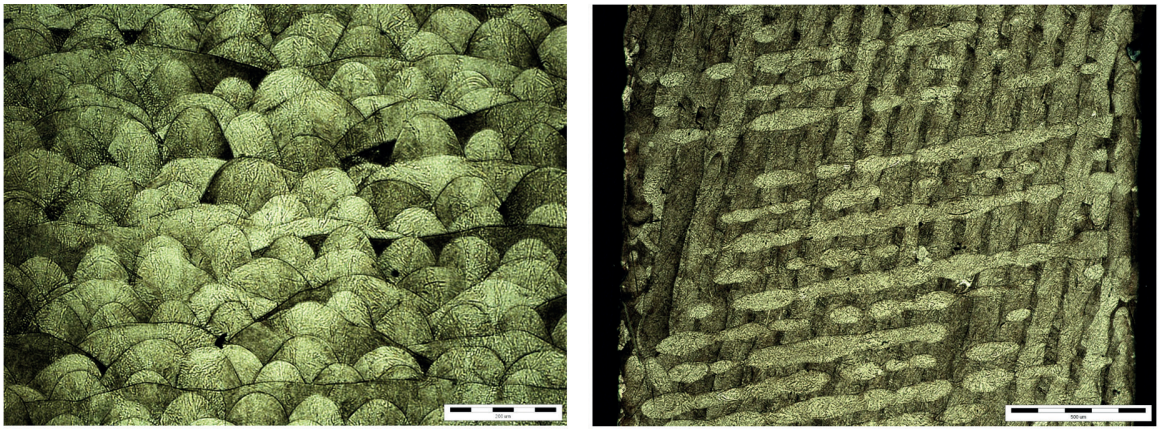

a) Horizontal (XY) direction *b) Vertical direction (Z)*

Figure 2 *Macro-structure of printed layers*

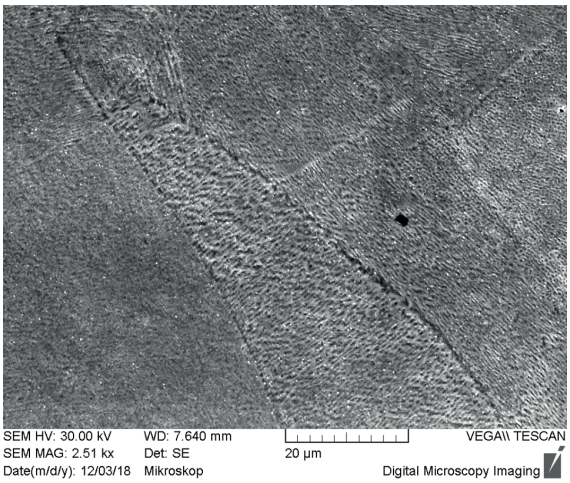

Figure 3 *Typical microstructure in the longitudinal direction*

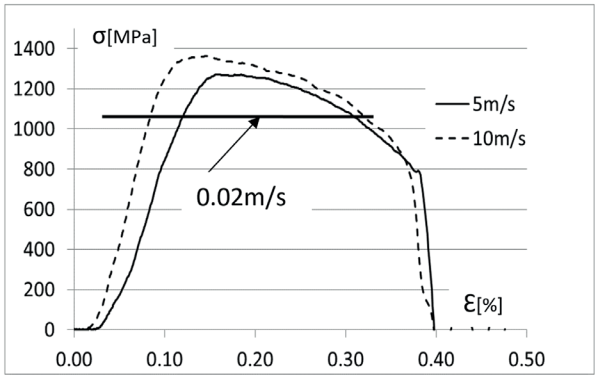

Figure 4 *Dynamic records after the uniaxial loading*

Different thermal boundaries are acting during the build-up process (by heating up or cooling down) of the single layers.

3.2 Static and dynamic fracture behaviour

The maraging steels are typical by capacity to an ultimate tensile strength of 1 500 MPa or greater, in the form of sheet, with a wall or plate thickness equal to or less than 5 mm. The tensile strength of the maraging Steel MS1 in vertical direction, without the age hardening, typically reaches 1100 MPa, yield strength 1000 MPa [8-10]. Performed static test in the vertical direction confirmed this capacity; the same orientation of the uniaxial loading was used for dynamic fracture tests.

The tested 3D process resulted in dynamic behaviour, reflected in the stress/strain records in Figure 4. Applied average strain rates (3 s^{-1}, 700 s^{-1}, 1400 s^{-1}) revealed a significant dynamic hardening capacity. An almost 25% increase of UTS at strain rate 700 s^{-1} and 38% at strain rate 1400 s^{-1} was measured compared to standard static strength, using 3 samples for each loading regime.

The aforementioned strengthening effect has proven the presence of a dislocation hardening process. The performed fractography analysis confirmed the ductile fracture mode (Figure 5), even at the maximal loading rate. The local presence of impurities did not lead to a change in the fracture mode. This fracture behaviour is very promising from the point of resistance to internal defects at impact loading.

The main generally considered shortcoming of the 3D printed maraging steel is a mechanical anisotropy. Heterogeneous residual stress distribution due to intensive temperature gradient, contributes to an oriented microstructure influence. The comparative indentation test was used for evaluation of elasto-plastic capacity in vertical vs. horizontal direction (Table 2).

Measured relaxation coefficient, as the ratio of elastic and the total energy consumption using the Wickers indenter ($\eta = (W_{elast} / W_{total}).100[\%]$)) reflects the residual plastic capacity. Comparative yield stress (CYS) [N/mm^2], was determined by a cylindrical indenter 0.5 mm in diameter. According to hypothesis about behavior of material during the extrusion of a cylindrical indenter [11], the shear yield stress was determined by defined ratio to the Equivalent Yield Force at the elastic limit of material response (Figure 6). An important parameter of dynamic material response is residual strengthening. Therefore, in order to fully understand the impact response of the tested high strength steel, an extension of deformation and strengthening has been considered. Effect of dynamic deformation at strain rate 1400 s^{-1} is reflected by the same indentation parameters in Table 2.

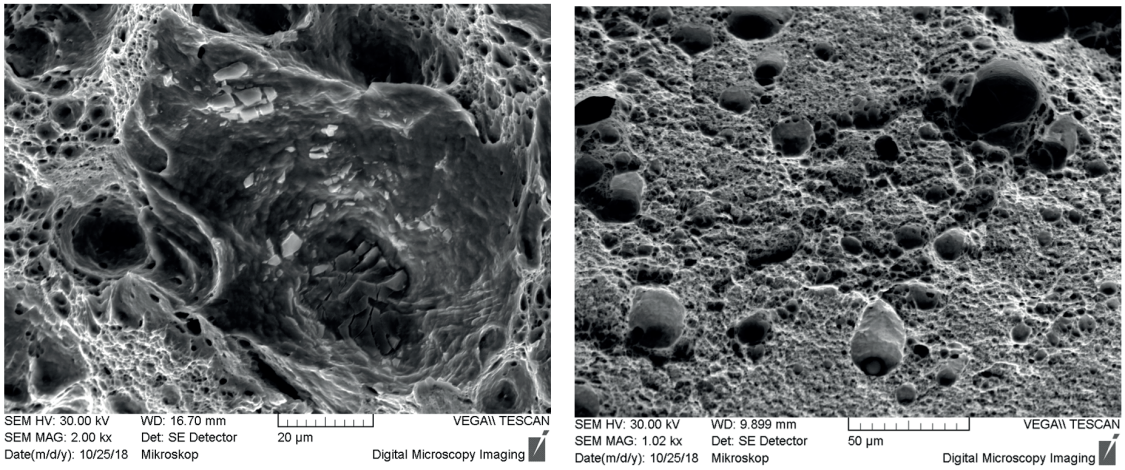

(a) 0.02m/s *(b) 5m/s*

Figure 5 *Fracture morphology of the printed maraging steel*

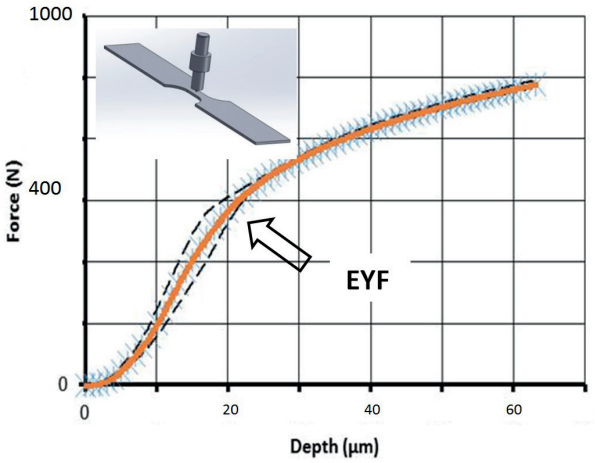

Figure 6 *Indentation curve evaluation*

Table 2 *Mechanical anisotropy measured by indentation test*

	relaxation coefficient η [%]	Equivalent Yield Force EYF [N]	Equivalent Yield Displacement [µm]	Comparative yield stress CYS [MPa]	σ_y [MPa]
vertical	36±1.4	462±2.3	18.48±1.9	2354±12	941±9
horizontal	29±2.0	412±19	19.37±2.9	2099±98	839±11
horizontal hardened	43	454	23.07	2314	925

* after dynamic hardening, i.e. close to dynamic fracture at 10 m/s

4. Conclusions

The AM is still a young technology and it exhibits a number of process problems that need to be understood when developing a part to be produced by the AM, especially by the DMLS. The main process problems are connected with the primary quality of powder and very complex technology requirements. When using the additive manufacturing, several boundary conditions are changed compared to traditional designs and processes. Different technological parameters need to be considered for the lightweight structure topology optimisation, many factors can alter the mechanical properties of the printed steel.

Material structures differ from casting/forging; thanks to the very fine microstructure of the tested maraging steel, high static and also dynamic strength values were obtained even in their natural stage. Significant strengthening effect was proven at different strain rates, without a tendency to change the primary ductile fracture mode.

The used technology parameters led to a high-quality inner structure with negligible influences of metallurgical defects.

A restrictive factor could be the surface roughness driven by the deposition layer thickness, mainly in connection with the fatigue strength. When considering the aim of forming lightweight structures with complex inner designs, the roughness is internal and external, which could influence the flow behaviour of internal

channels. The design of internal geometry has to avoid large thermal stresses.

Considerable plastic anisotropy has been confirmed in the as-built condition by indentation tests. Anisotropy can be reduced by aging heat-treatment of maraging steel. However, as was verified in some experimental studies [8], a degree of transverse strain anisotropy is likely to remain due to the AM alloy's fabrication history for the MS1 material. With use of the comprehensive material analyses, considering the constructed contour of printed geometry, the final mechanical response can be tailored to meet the desired design requirements for the part production purposes.

Acknowledgement

This article was made thanks to the support from project FV30149.

References

[1] BUCHANAN, C., GARDNER, L. Metal 3D printing in construction: A review of methods, research, applications, opportunities and challenges. *Engineering Structures* [online]. 2019, **180**, p. 332-348. ISSN 0141-0296, eISSN 1873-7323. Available from: https://doi.org/10.1016/j.engstruct.2018.11.045

[2] MURR, L. E., JOHNSON, W. L. 3D metal droplet printing development and advanced materials additive manufacturing. *Journal of Materials Research and Technology* [online]. 2017, **6**(1), p. 77-89. ISSN 2238-7854. Available from: https://doi.org/10.1016/j.jmrt.2016.11.002

[3] THOMAS, T., MAHFUZ, H., CARLSSON, L.A., KANNY, K., JEELANI, S. Dynamic compression of cellular cores: temperature and strain rate effects. *Composite Structures* [online]. 2002, **58**(4), p. 505-512. ISSN 0263-8223, eISSN 1879-1085. Available from: https://doi.org/10.1016/S0263-8223(02)00159-9

[4] DANNEMANN, K. A., LANKFORD, J. High strain rate compression of closed-cell aluminum foam. *Materials Science and Engineering: A* [online]. 2000, **293**(1-2), p. 157-64. ISSN 0921-5093. Available from: https://doi.org/10.1016/S0921-5093(00)01219-3

[5] DUDA, T., RAGHAVAN, L. V. 3D metal printing technology. *IFAC-PapersOnLine* [online]. 2016, **49**(29), 2016, p. 103-110. ISSN 2405-8963. Available from: https://doi.org/10.1016/j.ifacol.2016.11.111

[6] BHAVAR, V., KATTIRE, P., PATIL, V., KHOT, S., GUJAR, K. SINGH, R. A Review on powder bed fusion technology of metal additive manufacturing. 4th International Conference and Exhibition on Additive Manufacturing Technologies AM 2014: proceedings. Additive Manufacturing Society of India (AMSI), 2014.

[7] SUREL, A. Direct metal laser-sintering (DMLS). Avec l'EOSINT M 270. Eighteenth International Conference & Exhibition Moulding 2008 : proceedings. 2008.

[8] MOONEY, B., KOUROUSIS, K. I., RAGHAVENDRA, R. Plastic anisotropy of additively manufactured maraging steel: influence of the build orientation and heat treatments. *Additive Manufacturing* [online]. 2019, **25**, p. 19-31. ISSN 2214-8604, eISSN 2214-7810. Available from: https://doi.org/10.1016/j.addma.2018.10.032

[9] SUN, Y., LI, Q. M. Dynamic compressive behavior of cellular materials: A review of phenomenon, mechanism and modelling. *International Journal of Impact Engineering* [online]. 2018, **12**, p. 74-115. ISSN 0734-743X. Available from: https://doi.org/10.1016/j.ijimpeng.2017.10.006

[10] SHA, W., GUO, Z. *Maraging steels, modelling of microstructure, properties and applications*, Cambridge UK: Woodhead Publishing, 2009. ISBN 978-1-84569-686-3.

[11] BOWMAN, K. J. Mechanical behavior of materials. Hoboken, NJ: John Wiley, 2004. ISBN 978-0-471-24198-0.

Agata Wronska - Jacek Andres - Tomasz Altamer - Agata Dudek - Robert Ulewicz*

EFFECT OF TOOL PIN LENGTH ON MICROSTRUCTURE AND MECHANICAL STRENGTH OF THE FSW JOINTS OF AL 7075 METAL SHEETS

The Friction stir welding (FSW) is a complex process, depending on many factors: machine, clamping device, material and tools. Parameters that have a direct impact on the quality of the joint include the rotational speed, welding speed, clamping force, geometry and tool plunging depth. The paper presents the results of experimental studies concerning the effect of tool pin length on the microstructure and mechanical strength of joints of thin sheets made of Al 7075 alloy. A tool with an adjustable pin with concave shoulder was used to weld the joints. Different pin lengths were used, which were selected with respect to the thickness of the welded joint. The specimens were subjected to visual evaluation, metallographic tests and mechanical strength testing. The results indicate that the pin length has a decisive effect on the microstructural changes in the joint and thus influencing the strength of the FSW joints.

Keywords: *FSW lap joints, aluminium alloys, transportation industry*

1. Introduction

The Friction stir welding (FSW) is a relatively new technology for materials joining. Constantly developing, technology is becoming more and more widely used in many sectors of industry, e.g. in the automotive industry, railway, shipbuilding, aviation and space industry [1-2]. At present, Polskie Zaklady Lotnicze / A Sikorsky Company in Mielec, as part of the INNOLOT sector programme, perform the R&D work to develop and adapt the FSW technology to joining the structures of currently built aircrafts.

Compared to conventional joining technologies, the FSW has a number of unquestionable advantages, such as no need for transforming the material into the liquid state because the welded parts are joined together in a solid state [3-4]. This prevents from shrinkage, hot cracking, pores, inclusions and other defects typical of welding or resistance welding. Therefore, the method allows for joining, among others, components made of metal alloys, considered to be weldable or hardly weldable, i.e. Al alloys of 2xxx and 7xxx series. Furthermore, this method does not require the use of connectors, does not emit noise, does not generate welding dusts and gases and is considered to be energy efficient [5-10]. Friction welded joints are characterized by very good metallurgical quality, mechanical strength and repeatability, but only if the process is automated and fully controlled. It should be emphasized that despite a relatively small number of parameters of the FSW process (rotational speed, welding line speed, forces in the x and z axes, angle of inclination of the tool, shoulder plunging depth, depth of pin plunging into the lower sheet metal in overlapping joints), the choice of the best combination is representing a challenge. For comparison, in the case of the MIG, TIG and plasma welding, good joint quality depends on cca. 13, 15 and 24 parameters, respectively [11-13].

The above mentioned parameters and the FSW tool, or rather the geometry of its basic elements (pin and shoulder), have a direct effect on the flow of deformed metal within the weld [1, 14-17].

In the FSW overlapping joints, the material of the joined components is mixed as a result of the rotary motion of the tool. The main difficulty in obtaining joints with high mechanical strength is mainly the formation of hooking on the advancing side and cold lap on the retreating side. These are defects associated with contact line deformation, which very often constitute the initial points for breaking the joint. They also cause thinning of the sheet metal, which also adversely affects the joint strength. These defects result from the upward flow of the material, caused by too high a temperature and excessive plasticization of the material [18-20]. The authors of the studies [19-20] agree that the rising movement of the material in the weld can be limited by using a lower rotational speed of the tool or higher feed rate. Depending on the set process parameters, contact line deformation on the advancing side can be directed upwards or downwards, whereas on the retreating side, the contact line deviates upwards. Furthermore, a characteristic feature of hooking is a rapid change in shape, while the contact line on the retreating side usually has a milder course [19-20]. The defects are determined by the work of the tool, which, with each rotation, "cuts off" new portions of material on the advancing side and pushes them to the retreating side. A parameter that has an equally important effect on material mixing in the weld and the level of its characteristic features (e.g. hooking and cold lap) is the length of the tool pin, which directly impacts the depth of the material mixing in the joint. Few publications have described the effect of this factor on the properties and microstructure of welds, e.g. [17, 20-22]. As

* [1]Agata Wronska, [1]Jacek Andres, [1]Tomasz Altamer, [2]Agata Dudek, [2]Robert Ulewicz
[1]Polskie Zaklady Lotnicze Sp. z o.o., Mielec, Poland
[2]Czestochowa University of Technology, Poland
E-mail: robert.ulewicz@wz.pcz.pl

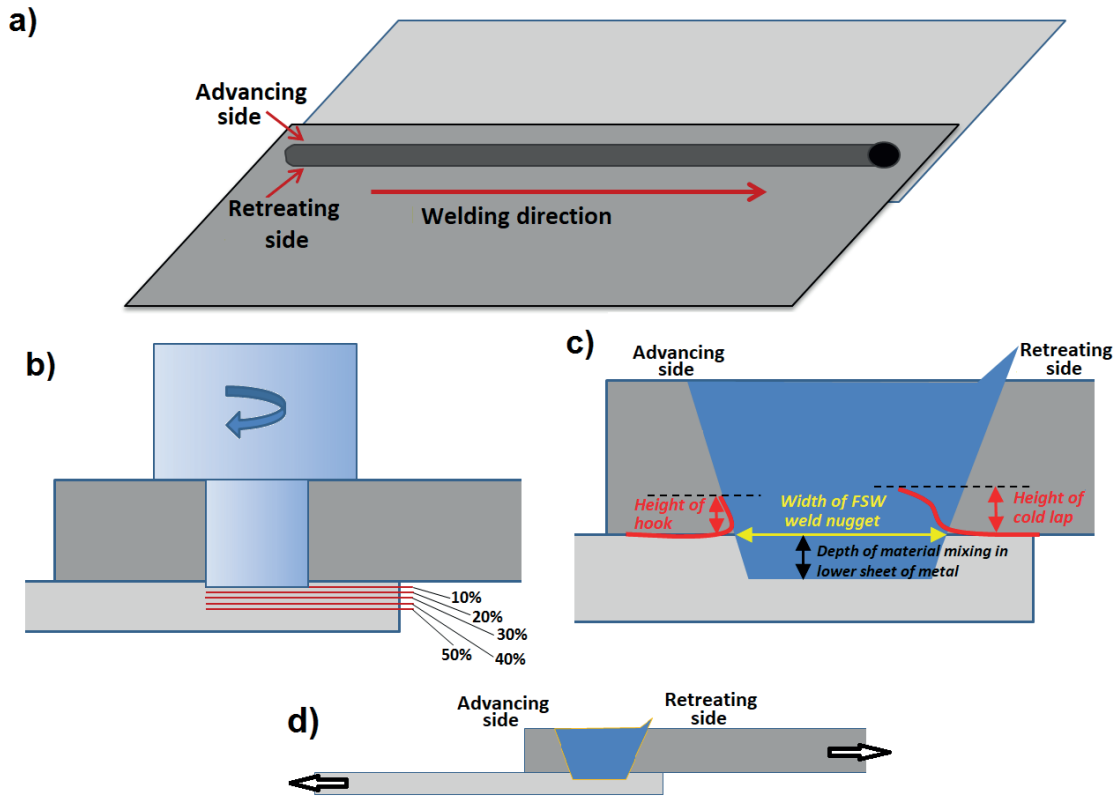

Figure 1 *FSW lap joint: a) general view, b) applied tool plunging in lower sheet, c) methodology of measurement of characteristic features of the FSW lap joint, d) lap orientation in the FSW joint and tensile force direction during strength tests*

emphasized by the authors, the pin length should be chosen while taking into account the specific rotational speed and feed rate of the tool. The pin length, which, for one set of rotational speed and feed rate, is sufficient to connect the welded component, may prove to be too small for another set. Furthermore, this parameter has a direct effect on the contact line deformation: when the mixing depth is small, i.e. when the pin length corresponds approximately to the thickness of the upper sheet metal of the overlapping joint, the upward flow of material is small. Therefore, the contact line deformation is also limited, but it is likely that the mixing of material at the contact point of the connected elements will be negligible. By increasing the pin length, the height of the hook and cold lap is also increased, leading to increased thinning of the upper sheet metal and weakening of the entire joint [17, 20]. Furthermore, the studies [21-22] proved that the strength of the joint is higher for the longer pin lengths, even exceeding 40% of the thickness of the lower sheet metal.

In conclusion, the problem of the effect of the pin length on the microstructure and strength of overlapping joints made of Al alloys remains insufficiently described in the literature. It should be stressed that this topic is complex and the discrepancies in the effect of the pin length on the strength of welds result from the fact that the tests have been performed using different tool geometries, different thickness and grades of materials. Therefore, the authors of this paper conducted an experiment, whose aim was to clarify how a change in a pin length affects the formation of the FSW weld when joining the thin-walled components (up to 1.6 mm) used in aircraft structures.

2. Material and research methodology

Sheets of Al 7075 T6 alloy (chemical composition according to AMS-QQ-A-250_13), coated on both sides with a plating layer with thickness corresponding to 4% of the workpiece thickness were used in the study.

Sheets of 356 mm x 10 mm, with thickness of 1.6 mm (upper sheet) and 0.8 mm (lower sheet), were welded. The sheets were joined in the overlapping rolling direction, with the overlap of 30 mm. The welded sheet metal was fixed with a special device to prevent it from moving during the welding process. The FSW lap joint is shown in Figure 1a. The FSW process was performed by means of a CNC machine using a concave shoulder and a threaded cylindrical pin. This pin geometry provides a more efficient mixing of the plasticized weld material. Welding was performed for two different sets of rotational speed and feed rate: a) ω = 700 rpm / v = 100 mm min^{-1} and b) ω = 1300 rpm / v = 300 mm min^{-1}. Further part of the study used the following denotation of the specimen sets: 700/100 and 1300/300. Five different pin lengths were used for each set of rotational speed and feed rates, corresponding to the sum of the upper sheet metal thickness and the percentage of the lower sheet metal thickness fraction: 10, 20, 30, 40, 50% (corresponding to 1.68; 1.76; 1.84; 1.92; 2.0 mm) (Figure 1b). This approach allowed not only for verification of the effect of the pin length on weld properties (and therefore material mixing depth), but also made it possible to determine whether the effects were similar at different linear and rotational speeds.

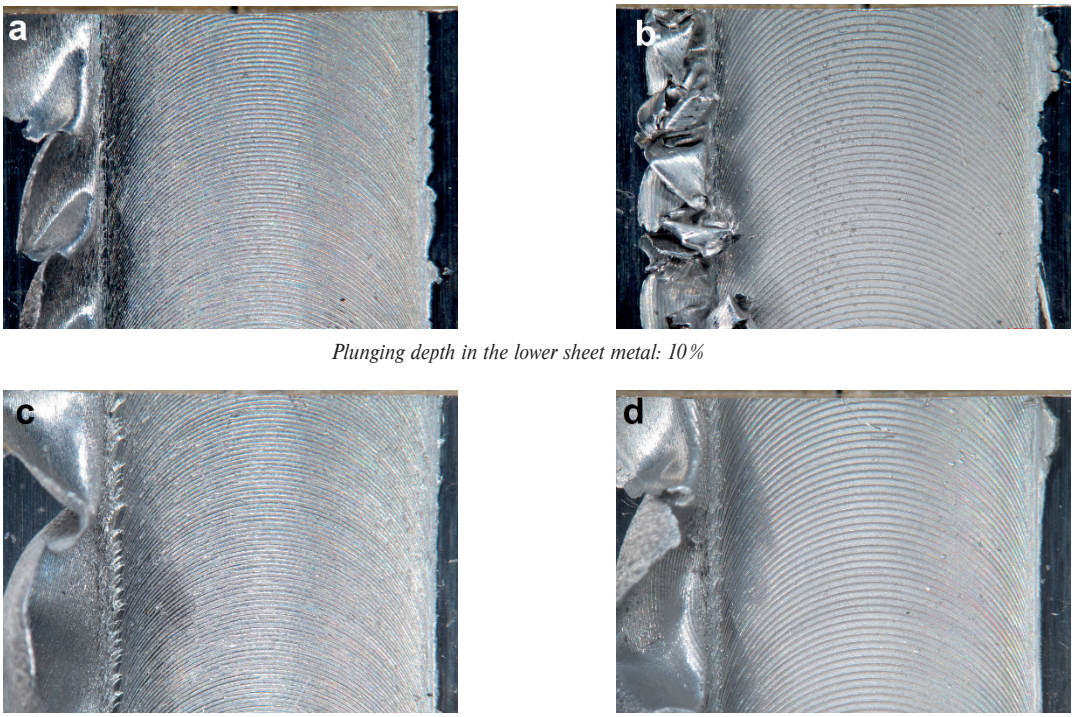

Figure 2 *Weld face view of the FSW joints prepared using tool pin plunge depth of 10% and 50% and process parameters: a, b) ω = 700 rpm; v = 100 mm min^{-1}, c, d) ω = 1300 rpm; v = 300 mm min^{-1}*

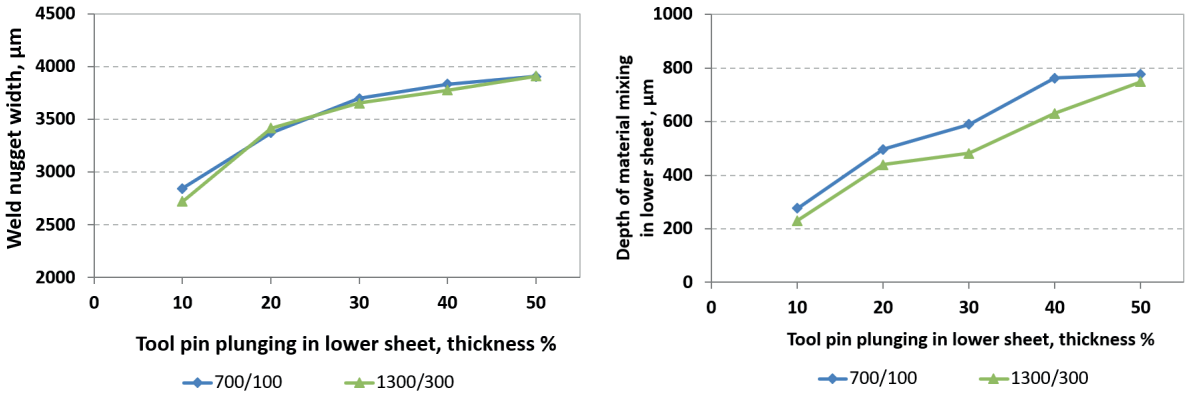

Figure 3 *Effect of the FSW process parameters on: a) weld nugget width, b) material mixing depth in the lower sheet*

The joints were assessed visually: the face of the welds was evaluated for defects, mainly discontinuities. Four specimens for the static strength testing and three specimens for microscopic tests were cut out from each joint.

Specimens for metallographic testing were ground, polished and etched at ambient temperature in Keller's reagent (5 ml HF, 15 ml HCl, 25 ml HNO_3, 955 ml H_2O). The prepared microsections were subjected to microstructural observations by means of the Zeiss digital optical microscope. On the recorded images, the width of the weld nugget and mixing depth were measured and the heights of the so-called hook and cold lap were determined. The measurement diagram is shown in Figure 1c.

The tensile strength tests were performed by means of a Landmark MTS machine equipped by the force and displacement sensors. Arrows in Figure 1d show the direction of specimen extending in relation to the position of the advancing and retracting sides. A breaking strength [kN] was recorded for each specimen. The broken specimens were visually assessed in order to determine the joint breaking point.

3. Results and discussion

The joints were visually inspected. All the welds were characterized by an acceptable face and no discontinuities were found. Figures 2a÷d illustrate the examples of welding faces made at different parameters. Different density of characteristic rings on the faces of welds can be observed depending on the applied rotational speed and feed rate. In the case of welded specimens with the depth of pin plunging into lower sheet of 50%, the upset metal was greater than in the case of specimens with a 10% pin plunge depth, even though the same shoulder plunging depth was ensured. This is due to the fact that with a larger pin plunge, a larger volume of the plasticised weld material is mixed and

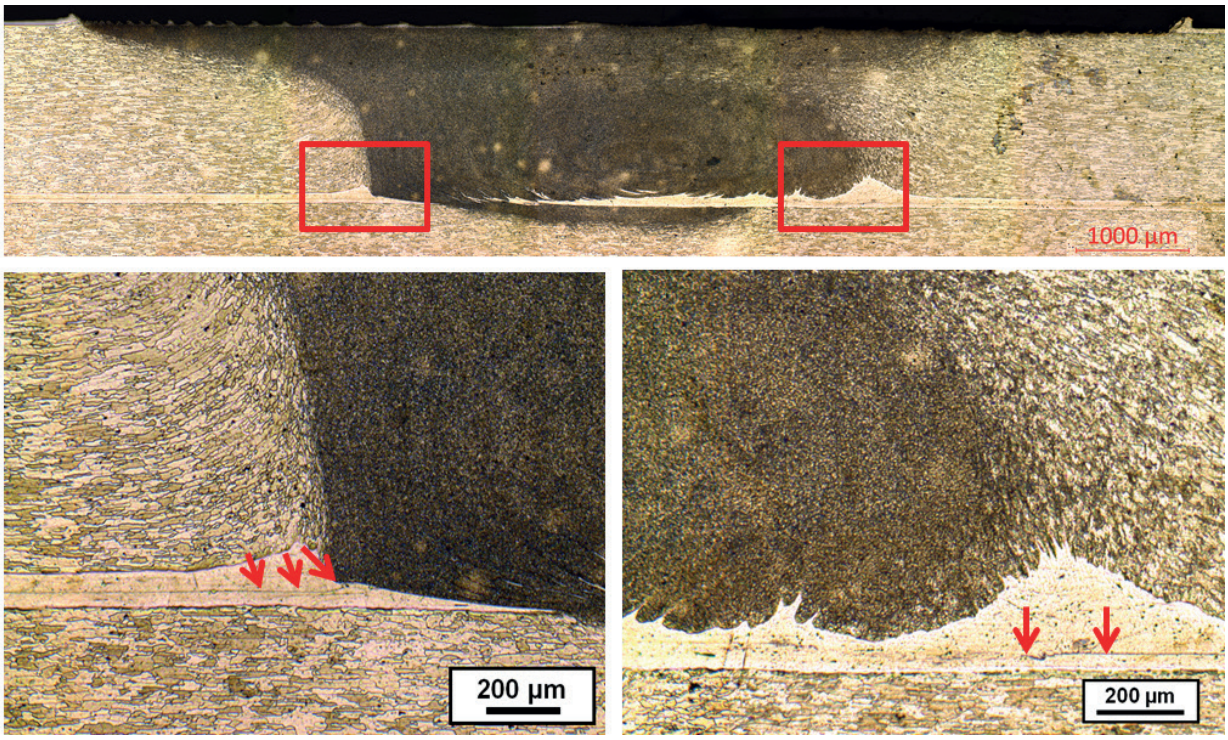

Figure 4 *Microstructure of the joint welded according to the parameters: ω = 1300 rpm; v = 300 mm min^{-1}; tool plunging in the lower sheet of 10 %: a) total view of the weld cross section, b) contact line at advancing side, c) contact line on retreating side*

transported to the surface of the upper sheet metal. The material is then pressed through the shoulder into the weld area. However, a certain volume remains on the weld surface on the retreating side.

Figure 3 shows the results of measurements of the weld nugget width and mixing depth of the lower sheet metal depending on the welding parameters. For the linear and rotational speed range used, the measured values for the individual tool plunging depths are comparable. However, the larger the pin plunging depth, the larger the mixing zone. Therefore, it can be expected that the amount of heat supplied to the joint is also higher, thus increasing the risk of joint deformation.

With the literature data, e.g. [15, 20], increasing the pin plunging depth intensifies the vertical movement of the weld material and the formation of the hook and cold lap. Those observations are also confirmed by the analysed joints. Figures 4÷6 show the microstructure of selected joints welded at a rotational speed of ω = 1300 rpm and a linear velocity of v = 300 mm min^{-1} and a pin length of 10 %, 30 % and 50 %. Figure 7 shows the relationship between the height of the hook and cold lap and the tool pin plunging depth. With a pin plunging depth of 10 % of the lower sheet thickness, the hook and cold lap are not observed. The contact line retains a straight line character throughout the joint until it is interrupted at the boundary of the weld nugget and the heat-affected zone on both sides of the weld (Figure 4). When using a pin plunging depth equal to 20 % of the lower sheet thickness, the hook still does not occur, while on the retreating side, the contact line is deformed upwards, reaching a height of cca. 50 µm (Figure 7). With the plunging depth of 30 %, an increase in contact line deformation is already noticeable on both sides of the weld (Figure 5). The hook height reaches ~ 70÷180 µm, while the cold lap height exceeds 350 µm (Figure 7). With plunging depths of 40 % and 50 % (Figure 6), the cold lap height is similar to the case of plunging depth of 30 % (~ 250÷350 µm), but the hook is much higher (in most specimens its height exceeds 200 µm) (Figure 7). Microstructural observations also revealed that the increase in pin plunging depth also leads to changes in the character of the weld material mixing. This is particularly noticeable in the specimens analysed in the study because a threaded pin was used. Thus, increasing its depth of plunging into the joined set of metal sheets results in increase of the effect of thread coils on material mixing. Comparison of the microstructure of the tested joints (Figures 4÷6) reveals that for larger depths, the plating layer is broken down and is distributed in the weld nugget. Furthermore, the shape of the weld also changes: for the small pin plunging depths, the weld nugget retains its oval shape (Figure 4a), while for min. 30 %, the areas corresponding to the effect of individual thread edges can be clearly distinguished. Figure 6a illustrates the shape of these areas indicated by a dashed line. Special attention should be paid to the fact that both the hook and cold lap, "trapped" in the plating layer, actually occur in the area of the effect of the last coil (Figures 5, 6). The next coil, mixing the material in the area of the upper sheet metal, limited contact line deformation, thus preventing the upper sheet thinning. Perhaps the use of a smooth pin without thread for the same plunging depth values would lead to the formation of a much higher hook and cold lap.

Figure 8 shows the results of the static strength tests of the joint, while the images of selected broken specimens are presented in Figure 9a÷d. The high strength values (~ 7 kN) were recorded for all the analysed sets of rotational speed and feed rate at the depth of plunging into the lower sheet of 10 % of its thickness.

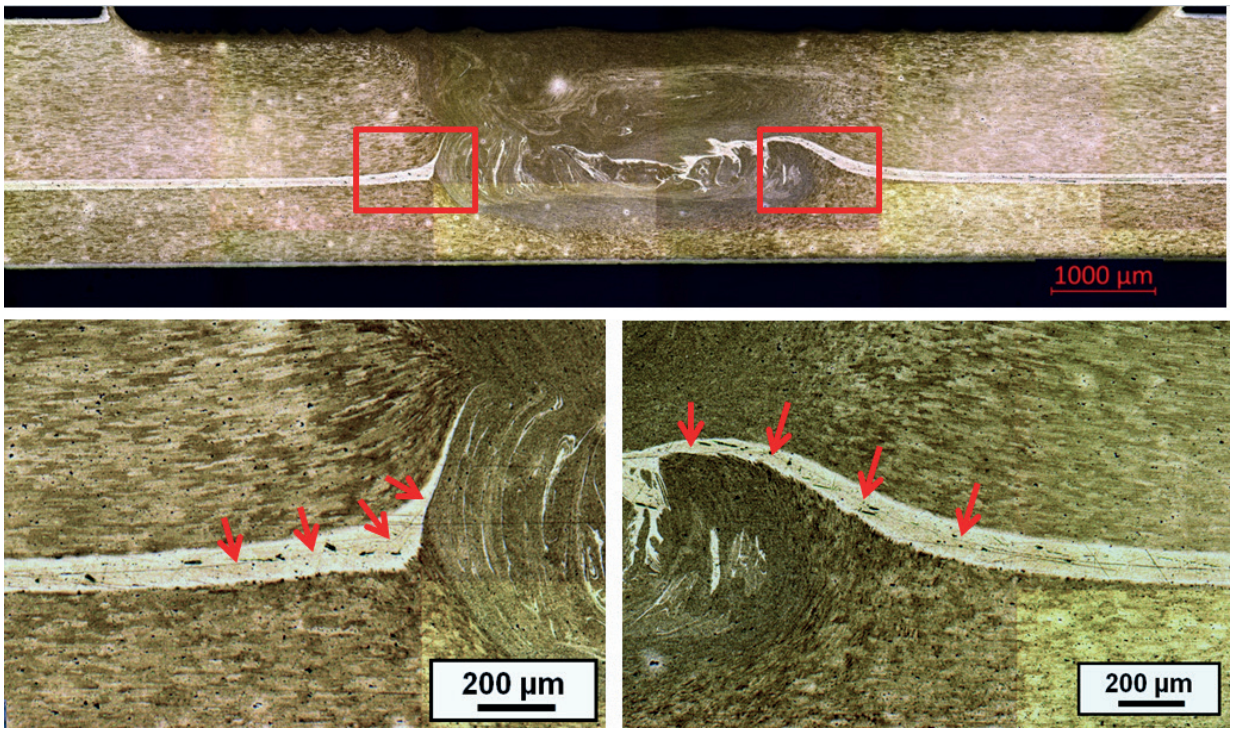

Figure 5 *Microstructure of the joint welded according to the parameters: ω = 1300 rpm; v = 300 mm min^{-1}; tool plunging in the lower sheet of 30 %: a) total view of the weld cross section, b) contact line at advancing side, c) contact line at retreating side*

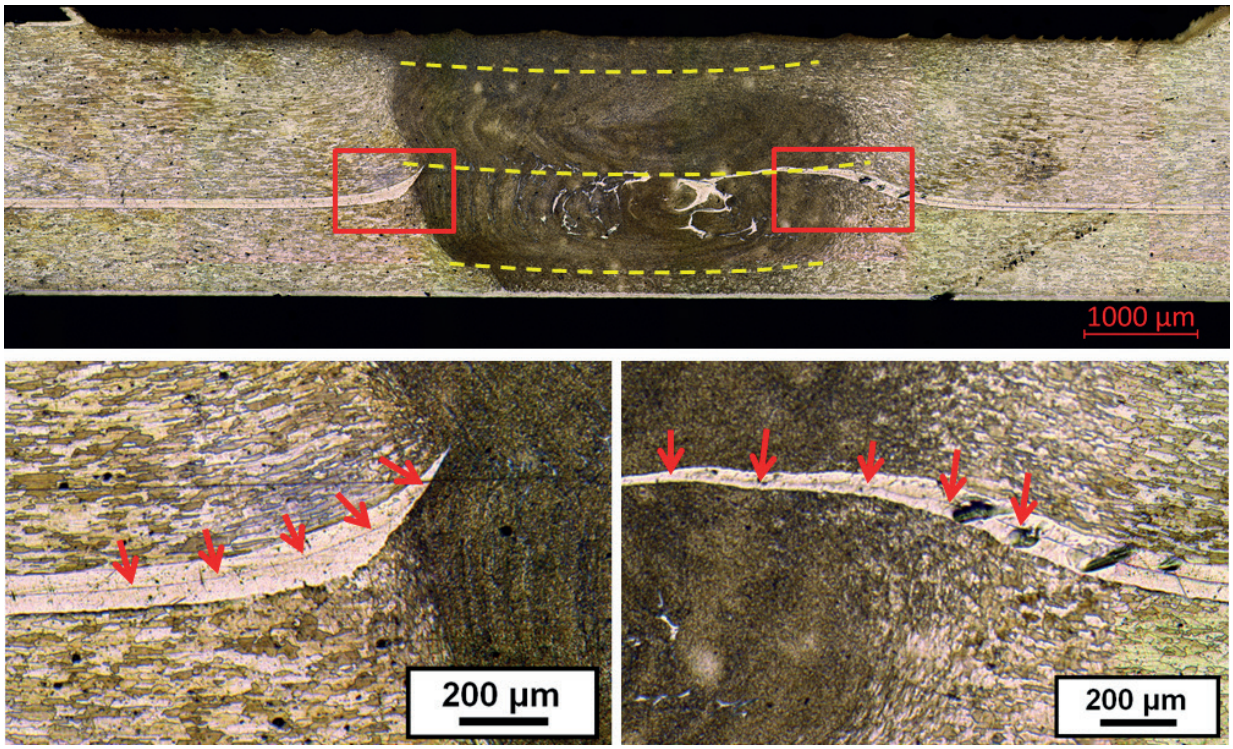

Figure 6 *Microstructure of the joint welded according to the parameters: ω = 1300 rpm; v = 300 mm min^{-1}; tool plunging in the lower sheet of 50 %: a) total view of the weld cross section, b) contact line at advancing side, c) contact line at retreating side*

No contact line deformations were found in these joints, and the specimens were broken outside the weld in the lower sheet in the heat affected zone or by shear (sheet delamination) (Figure 7).

Welded specimens for the tool plunging depth of 20 % were destroyed in the upper (thicker) sheet metal in the weld area on the retreating side, where the cold lap occurs. Although the cold lap height did not exceed 60 µm, this defect contributed significantly to the weakening of the joints, as it was characterized by a sharp tip pointing towards the surface of the upper sheet, similar to the case of the hook. During the tensile test, the cold lap apex was

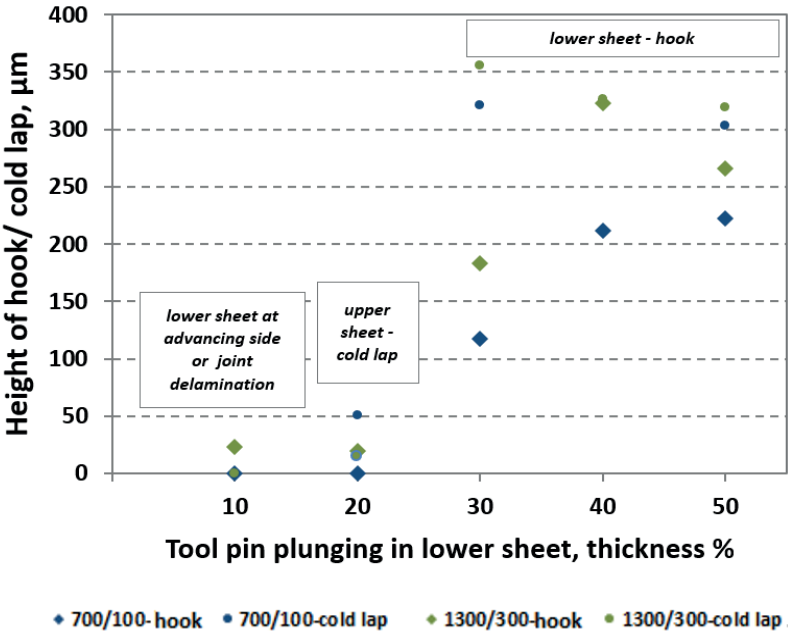

Figure 7 Effect of the tool pin plunging depth on defects size

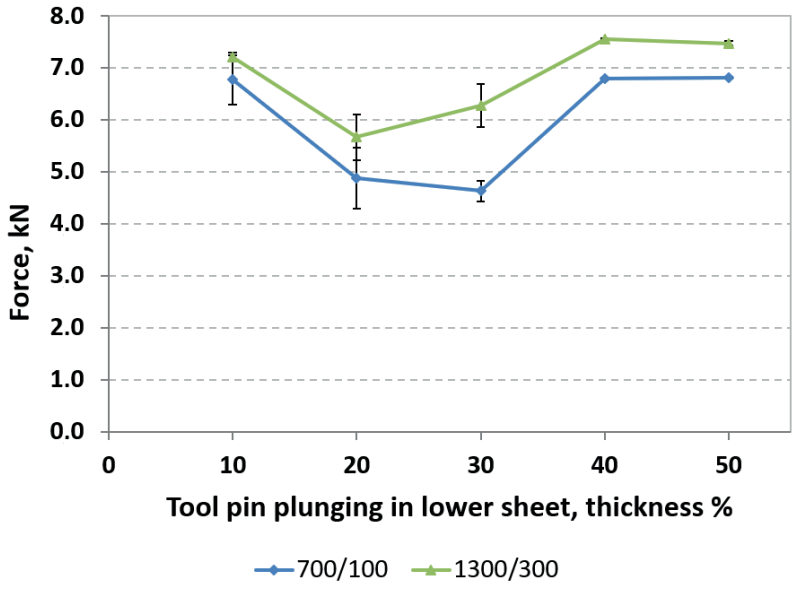

Figure 8 Effect of the FSW process parameters on mechanical strength of the joints

a particularly stress-sensitive site and initiated cracking of the upper sheet metal (Figure 9c).

Joints welded with a pin plunging depth of 30÷50 % were in the majority of cases broken in the thinner sheet metal in the location of the hook (Figure 9d). Breaking of the joint occurred along the line of contact between the sheet metal and the hook and then through the lower sheet metal, along the boundary between the weld nugget (recrystallization zone) and the thermomechanical deformation zone. In other words, the lower sheet metal was pulled from the weld.

Welded specimens with plunging depths of 40 % and 50 % and parameters ω = 700 rpm, v = 100 mm min^{-1} and ω = 1300 rpm, v = 300 mm min-1 were broken at ˜ 7 kN (Figure 8). Despite the significant height of the cold lap defect (Figure 7), these specimens were destroyed due to the presence of the hook on the advancing side. Comparison of the shapes of both defects reveals that the cold lap was characterized by a much smoother shape (Figure 6b), while the hook represented a sharp geometric notch (Figure 6a), sensitive to mechanical stresses and thus initiating breaking of the joint.

4. Conclusion

The results of examinations presented in this study lead to the following conclusions:

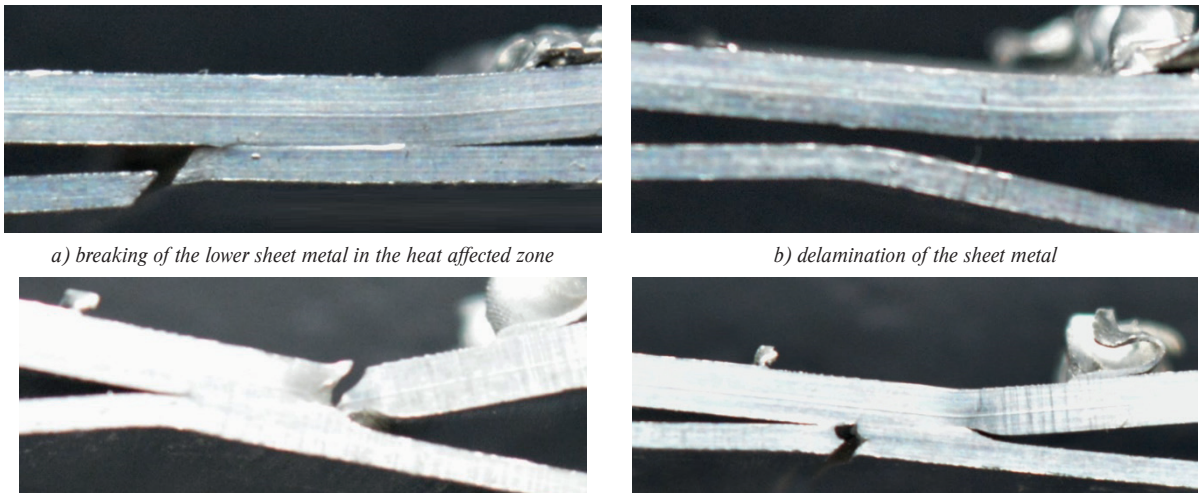

a) breaking of the lower sheet metal in the heat affected zone

b) delamination of the sheet metal

c) breaking of the joint on the retreating side of the upper sheet metal, initiated along the cold lap

d) breaking of the joint on the advancing side of the lower sheet metal, initiated along the hook

Figure 9 *The FSW lap joints breaking sites*

- Length of the pin, which is involved in mixing of the material of the overlap joint is a parameter determining the quality of the joint: the occurrence of geometric defects or their lack and the joint strength,
- Increased pin exposure intensifies the vertical movement of the weld material. This leads to increase in the contact line deformation (increasing the hook and cold lap, which is accompanied by increasingly high thinning),
- The results of the strength testing showed that for the tested set of sheets there are two ranges of pin plunging depths, ensuring high strength of the joint: 10%, and 40% and 50%. The recommended plunging depth of the tool is 10%, because regardless of the rotational speed and feed rate used, the strength of the joints reaches ˜ 7 kN and the hook and cold lap do not occur. The specimens are broken in the lower sheet metal outside the weld or by shear. In the case of the plunging depths of 40% and 50%, breaking of the specimens occurred in most cases in the lower sheet metal as a result of the presence of a hook,
- In the case of a cold lap defect, it is recommended that it has a smooth shape (as in the case of joints welded with plunging depth of 40÷50 %). This defect does not represent a sharp geometric notch and the joints can carry high loads (˜ 7 kN). If the contact line on the retreating side is clearly pointing upwards despite its low height, it causes the joint to break at low load values (as in the case of joints welded with pin plunging depth of 20 %).

Acknowledgements

The research was conducted as part of Project No. INNOLOT/I/4/NCBR/2013 “Advanced techniques for manufacturing airframe structure components with the use of innovative FSW technology” in the Operational Programme: Innovative Economy (OP IE). The project is co-financed by the National Centre for Research and Development, the European Union and PZL Mielec / A Sikorsky Company, under the European Regional Development Fund.

References

[1] MISHRA, R. S., MAHONEY, M. W. *Friction stir welding and processing*. ASM International, 2007. ISBN 978-0-87170-840-3.

[2] COLLIGAN, K. J. *Friction stir welding for ship constructions* [online]. Harrisburg, PA: Concurrent Technologies Corporation, 2009, p. 1-6 [accessed 2019-03-10]. Available from: https://cyberships.files.wordpress.com/2009/11/fswshipconstruction.pdf

[3] BUSSU, G., IRVING P. The role of residual stress and heat affected zone properties on fatigue crack propagation in friction stir welded 2024-T351 aluminium joints. *International Journal of Fatigue* [online]. 2003, **25**(1), p. 77-88. ISSN 0142-1123. Available from: https://doi.org/10.1016/S0142-1123(02)00038-5

[4] LIU, H., FUJII, H., MAEDA, M., NOGI, K. Tensile properties and fracture locations of friction-stir-welded joints of 2017-T351 aluminum alloy. *Journal of Materials Processing Technology* [online]. 2003, **142** (3), p. 692-696. ISSN 0924-0136, eISSN 1873-4774. Available from: https://doi.org/10.1016/S0924-0136(03)00806-9

[5] SURESH BABU, A., DEVANTHAN, C. An overview of friction stir welding. *International Journal of Research in Mechanical Engineering and Technology*. 2013, **3**(2), p.259-265. ISSN 2249-5770, eISSN 2249-5762.

[6] KUDLA, K., WOJSYK, K., KUCHARCZYK, Z. Wlasnosci zakladkowych zlaczy spajanych metoda zgrzewania tarciowego z przemieszaniem / FSW- Friction Stir Welding (in Polish). *Obrobka Plastyczna Metali*. 2013, **XXIV**(3), p. 179-191. ISSN 0867-2628.

[7] ZHANG, Y. N., CAO, X., LAROSE, S., WANJARA, P. Review of tools for friction stir welding and processing. *Canadian Metallurgical Quarterly* [online]. 2012, **51**(3) p. 250-160. ISSN 0008-4433, eISSN 1879-1395. Available from: https://doi.org/10.1179/1879139512Y. 0000000015

[8] KIMAPONG, K., WATANABE, T. Effect of welding process parameters on mechanical property of FSW lap joint between aluminum alloy and steel. *Materials Transactions* [online]. 2005, **46**(10), p. 2211-2217. ISSN 1345-9678, eISSN 1347-5320. Available from: https://doi.org/10.2320/matertrans.46.2211

[9] ABDOLLAH-ZADEH, A., SAEID, T., SAZGARI, B. Microstructural and mechanical properties of friction stir welded aluminum/copper lap joints. *Journal of Alloys and Compounds* [online]. 2008, **460**(1-2), p. 535-538. ISSN 0925-8388, eISSN 1873-4669. Available from: https://doi.org/10.1016/j.jallcom.2007.06.009

[10] SHINODA, T., SUZUKI, J. Observation of metal flow phenomenon of lap joints during friction stir welding. Materials Science Forum [online]. 2004, **449-452**, p. 421-424. ISSN 1662-9752. Available from: https://doi.org/10.4028/www.scientific.net/MSF.449-452.421

[11] DE BACKER, J., VERHEYDEN, B. *Robotic friction stir welding for automotive and aviation applications* [online]. University West, Trollhattan. 2009, p. 23-24 [accessed 2019-03-10]. Available from: https://pdfs.semanticscholar.org/6c3c/82374be11b1861a732e8de7af3a342aa2a1a.pdf

[12] LAGO, J., BOKUVKA, O., NOVY, F. The weld toe improvement of advanced HSLA steel by laser remelting. *Materials Today: Proceedings* [online]. 2016, **3**(4), p. 1037-1040. ISSN 2214-7853. Available from: https://doi.org/10.1016/j.matpr.2016.03.043

[13] JAMBOR, M., NOVY, F., MICIAN, M., TRSKO, L., BOKUVKA, O., PASTOREK, F., HARMANIAK, D. Gas metal arc welding of thermo-mechanically controlled processed s960mc steel thin sheets with different welding parameters. *Communications - Scientific Letters of the University of Zilina* [online]. 2018, **20**(4), p. 29-35. ISSN 1335-4205, eISSN 2585-7878. Available from: http://komunikacie.uniza.sk/index.php/communications/article/view/636

[14] ARBEGAST, W. J. A flow-partitioned deformation zone model for defect formation during friction stir welding. *Scripta Materialia* [online]. 2008, **58**(5), p. 372-376. ISSN 1359-6462. Available from: https://doi.org/10.1016/j.scriptamat.2007.10.031

[15] CHEN, Z. W., YAZDANIAN, S. Friction stir lap welding: material flow, joint structure and strength. *Journal of Achievements in Materials and Manufacturing Engineering* [online]. 2012. **55**(2), p. 629-637. ISSN 1734-8412. Available from: http://jamme.acmsse.h2.pl/papers_vol55_2/ 58263.pdf

[16] KUMAR, K., KAILAS, S. V. The role of friction stir welding tool on material flow and weld formation. *Materials Science Engineering A* [online]. 2008, **485**(1-2), p. 367-374. ISSN 0921-5093. Available from: https://doi.org/10.1016/j.msea.2007.08.013

[17] WANG, M., ZHANG, H., ZHANG, J., ZHANG, X., YANG, L. Effect of pin length on hook size and joint properties in friction stir lap welding of 7B04 aluminum alloy. *Journal of Materials Engineering and Performance* [online]. 2014, **23**(5), p. 1881-1886. ISSN 1059-9495, eISSN 1544-1024. Available from: https://doi.org/10.1007/s11665-014-0936-5

[18] YAZDANIAN, S., CHEN, Z. W. Effect of friction stir lap welding conditions on joint strength of aluminium alloy 6060. *IOP Conference Series: Materials Science and Engineering* [online]. 2009, **4**(1), p. 1-5. ISSN 1757-8981, eISSN 1757-899X. Available from: https://doi.org/10.1088/ 1757-899X/4/1/012021

[19] ZHANG, H., WANG, M., ZHANG, X., ZHU, Z., YU, T., YANG, G. Effect of welding speed on defect features and mechanical performance of friction stir lap welded 7B04 aluminum alloy. *Metals* [online]. 2016, **6**(87), p. 1-11. eISSN 2075-4701. Available from: https://doi.org/10.3390/ met6040087

[20] CEDERQVIST, L., REYNOLDS, P. Factors affecting the properties of friction stir welded aluminum lap joints. *Welding Journal*. 2001, **80**, p. 281-287. ISSN 0043-2296.

[21] CAO, X., JAHAZI, M. Effect of tool rotational speed and probe length on lap joint quality of a friction stir welded magnesium alloy. *Materials and Design* [online]. 2011, **32**(1), p. 1-11. ISSN 0261-3069. Available from: https://doi.org/10.1016/j.matdes.2010.06.048

[22] YAZDANIAN, S., CHEN, Z. W., LITTLEFAIR, G. Effects of friction stir lap welding parameters on weld features on advancing side and fracture strength of AA6060-T5 welds. *Journal of Material Science* [online]. 2012, **47**, p. 1251-1261. ISSN 0022-2461, eISSN 1573-4803. Available from: https://doi.org/10.1007/s10853-011-5747-6

Patrik Beno - Miroslav Gutten - Milan Simko - Jozef Sedo*

STABILIZATION AND CONTROL OF SINGLE-WHEELED VEHICLE WITH BLDC MOTOR

To stabilize a single-wheel vehicle is necessary to know the angle of gradient of the platform with respect to the horizontal axis and also the movement of the vehicle. This can be detected in several ways. Accelerometers and gyroscopes are small, accurate and energy-saving today. They provide analogue or digital output. In the introduction we will describe the basic parameters of accelerometer and gyroscope. We will describe the principle of digital signal processing from both sensors. In the next section we look at the effect of dynamic acceleration on the sensors and the elimination of this phenomenon with a complementary filter. We explain, what it is a complementary filter, benefits and internal structure. We will include a short code in the C language for data processing from the output.

Keywords: *stabilize, accelerometer, gyroscope, complementary filter, DSP*

1. Introduction

We can find stabilization systems in many electrical devices where they are used to control the vehicle's direction or to stabilize the platform. For example, the force that acts on a platform deflects this platform from balance. However, this is undesirable. Therefore, we try to keep the platform in the surface using a proposed stabilisation system. One way is to use tilt sensors and design a suitable hardware. It is necessary to know the physical model of the platform and to determine the correct system parameter.

2. Theoretical knowledge of stabilization systems

To stabilize a single or two-wheeled vehicle, it is necessary to know the angle of inclination of the platform against the horizontal axis and also what motion of the vehicle is carried out. It can be detected by several ways, such as with the mercury tube, which was used in the tilt sensor technologies in motor vehicles. Today, accelerometers and gyroscopes are small, accurate and energy-saving. They provide analogue or digital output.

2.1 Accelerometer

Accelerometer is an electromechanical device that measures the acceleration force. This force may be static, such as the force of gravity or dynamic by motion or vibration of the accelerometer. There are many types of accelerometers. The most sensors are based on piezoelectric devices using crystals, but they are large. Therefore, MEMS (micro electro-mechanical system) are used most often. They are able measure power in three axes.

A typical MEMS accelerometer consists of a movable mass with attached membranes through a mechanical suspension to the frame as shown in Figure 1 [1].

Movable plates and solid external boards represent capacitors. The deflection of the movable plate towards the center is measured by the difference in capacity. The capacity of the free space (air) between the movable plate and the two stationary outer plates x_1 and x_2 is a function corresponding to the displacement x_1 and x_2:

$$C_1 = \in_A \frac{1}{x_1} = \in_A \frac{1}{d+x} = C_0 - \Delta C \tag{1}$$

$$C_2 = \in_A \frac{1}{x_2} = \in_A \frac{1}{d-x} = C_0 + \Delta C \tag{2}$$

where ϵ_A is the permittivity of the separating material and d is the distance between electrodes.

If acceleration is zero, the capacity C_1 and C_2 are the same, because $x_1 = x_2$. If $x \neq 0$, the capacity will be:

$$C_2 - C_1 = 2\Delta C = 2 \in \frac{x}{d^2 - x^2} \tag{3}$$

By adjusting we get a nonlinear algebraic equation:

$$\Delta C x^2 + \in_A x - \Delta C d^2 = 0 \tag{4}$$

We can simplify the equation. But for small shifts ΔCx^2 is obscure, so ΔCx^2 we can ignore. Then:

$$x := \frac{d^2}{\in_A} \Delta C = d \frac{\Delta C}{C_0} \tag{5}$$

Capacitors C_1 and C_2 represent a simple voltage prescaler.

$$(V_x + V_0) C_1 + (V_x + V_0) C_2 = 0 \tag{6}$$

* [1]Patrik Beno, [1]Miroslav Gutten, [1]Milan Simko, [2]Jozef Sedo
[1]Department of Measurements and Applied Electrical Engineering, Faculty of Electrical Engineering and Information Technology, University of Zilina, Slovakia
[2]Department of Mechatronics and Electronics, Faculty of Electrical Engineering and Information Technology, University of Zilina, Slovakia
E-mail: gutten@fel.uniza.sk

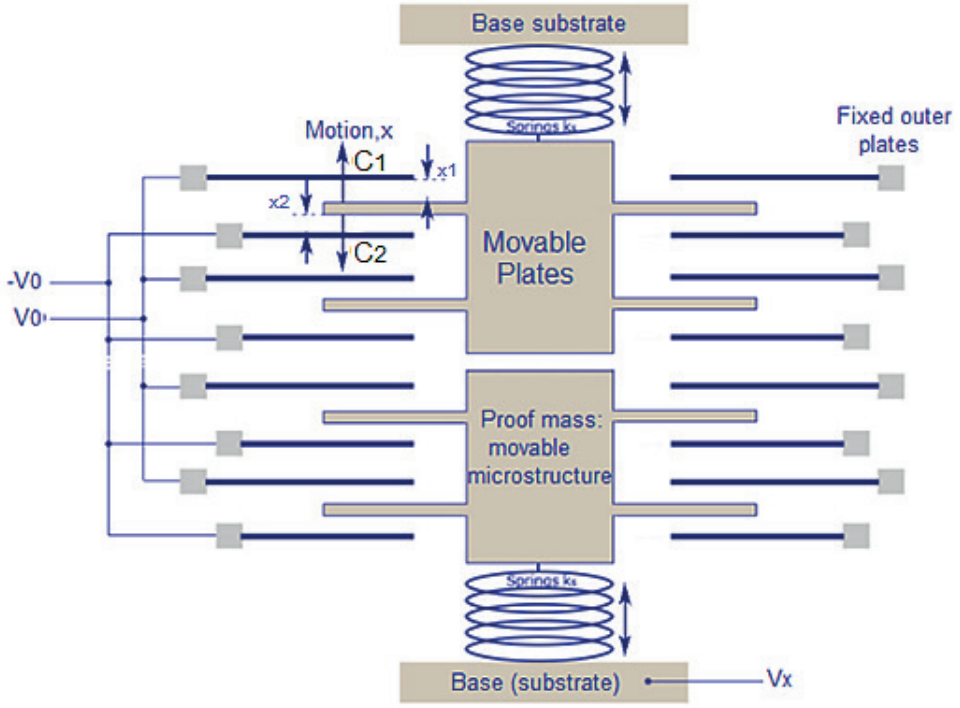

Figure 1 *Structure of accelerometer*

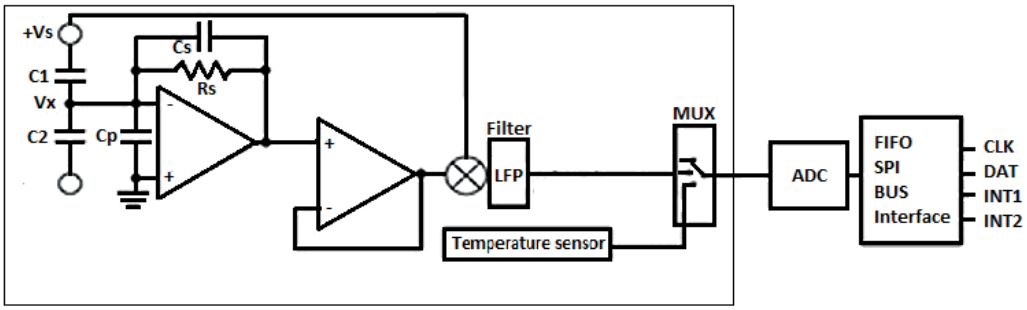

Figure 2 *Accelerometer measurement circuit*

Then we get the output voltage V_x:

$$V_x = V_0 \frac{C_2 - C_1}{C_2 + C_1} = \frac{x}{d} V_0 \tag{7}$$

The output signal V_x cannot be used without filtering because the signal is noisy. Therefore, it is necessary to use a circuit consisting of an integrated amplifier, a separator, a low pass filter and a multiplexer. It is also necessary to convert the signal into digital form to get the data from the accelerometer and gyroscope via the I2C bus. This connection is shown in Figure 2.

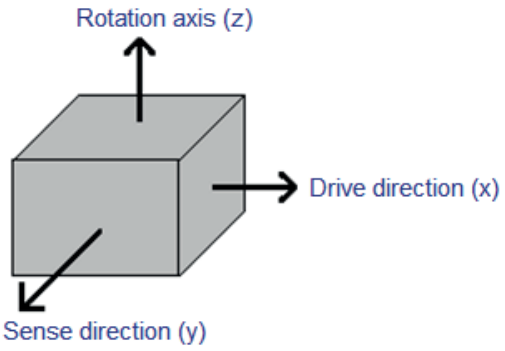

Figure 3 *Gyroscope measurement axis*

2.2 Gyroscope and integration

The classic gyroscope is defined as a symmetrical rotating object around one axis. These are very large for use in electronics. Now, we are using new types of piezoelectric gyroscopes or laser ray gyroscopes, which works on the principle of laser ray deflection. Vibrating gyroscopes MEMS work on the principle of mass resonance inside the structure. The direction which we will consider the motion of a body is marked x, see Figure 3 [2].

The output signal of the gyroscope is digital and is dependent on the system rotation speed in degree per second ($^o/s$). MEMS gyroscopes are radically less sensitive to the applied acceleration than accelerometers [3]. To obtain a tilt value at time t_1, the output signal must be integrated in time according to (Figure 4):

$$\varphi = \int_0^{t1} \omega(t)dt + \varphi(0) \tag{8}$$

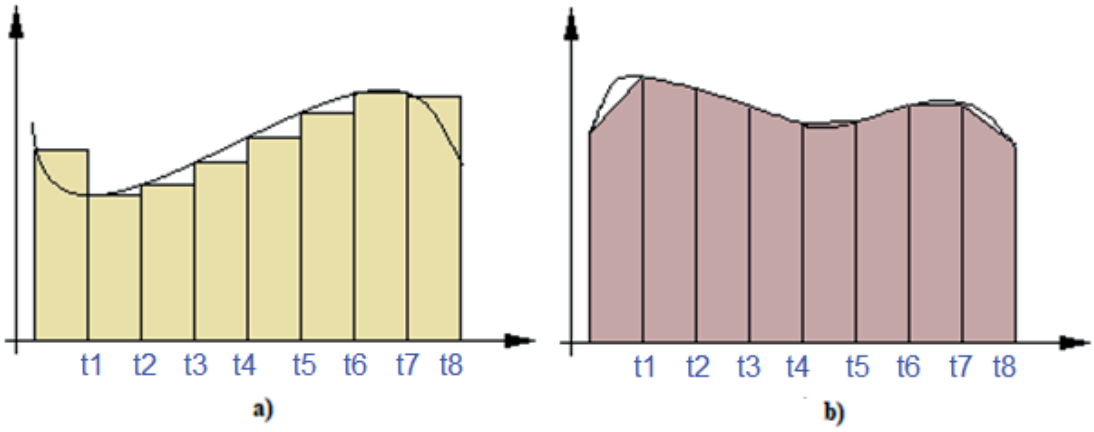

Figure 4 *(a) Rectangular integration, (b) Trapezoidal integration*

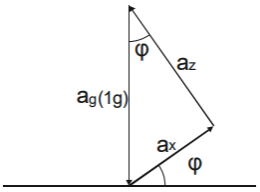

Figure 5 *Trigonometry of angle measurement by accelerometer*

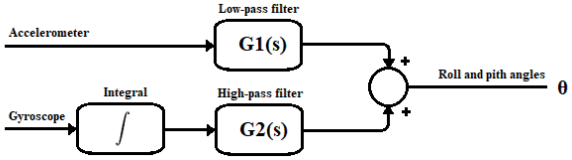

Figure 6 *Complementary filters with constant gain*

2.3 Accelerometer and angle measurement system

MEMS accelerometers can measure static and dynamic acceleration. If we have a system which we incline around the Y axis, we can observe the change of the measured value of the acceleration α_x a α_z depending on gravity acceleration α_g [4].

This results in relations for angles (Figure 5):

$$\alpha_x = \alpha_g \sin \varphi \tag{9}$$

$$\alpha_z = \alpha_g \cos \varphi \tag{10}$$

Then we can calculate the resulting angle φ by gravity acceleration α_x and α_z with expression [5]:

$$\varphi = atan\left(\frac{\alpha_x}{\alpha_z}\right) \tag{11}$$

By using the 3-axis accelerometer, we obtain tilt angles in the NED (North-East-Down) coordinate system. It is also necessary to define the angle of elevation, which i is marked θ and angle of pitch is marked as Φ [6]:

$$\theta = atan\left(\frac{\alpha_x}{\alpha_z}\right) \tag{12}$$

$$\Phi = atan\left(\frac{\alpha_x}{\sqrt{\alpha_y^2 + \alpha_x^2}}\right) \tag{13}$$

3. Design of complementary filter with constant gain

The MPU6050 sensor with an integrated accelerometer and gyroscope was used for the tilt sensing. A complementary filter has been designed to evaluate the data, which includes all signal processing requirements for control. [7]. The complementary filter is one of the filtering techniques in the frequency domain. Two or more variables are entering to the complementary filter. Only part of the spectrum is used from each sensor, and all sensors cover the frequency spectrum [8]. The proposed block diagram of the filter is shown in Figure 6, where the input parameters are the real accelerometer values and the gyroscope values must be first integrated. [9].

This applies:

$$G1\ (s\ ) + G2\ (s) = 1 \tag{14}$$

where $G1(s)$ is a high pass filter and $G2(s)$ is the low pass filter.

The proposed calculation in C code is shown below. The „alpha“ is variable, in this case 0.9.

Then apply:

$$angle = (1\text{-}alpha)*(gyro) + (alpha)*(acc) \tag{15}$$

where:

- angle = output angle from filter
- gyro = measured angle from the gyroscope
- acc = measured angle from the accelerometer

This filter has been implemented into the control unit for the BLDC motor of a one-wheeled vehicle with the NXP MC56F8006 processor. MPU6050 sensor is connected via connector SV7, see Figure 7.

The processor every 10ms takes a value from the accelerometer and gyroscope and computes the result value of the angle, which then enters to the PI controller. Then it discards the difference between the actual and the desired value. [10]. The constants of the PI controller are determined by the Ziegler Nicholson

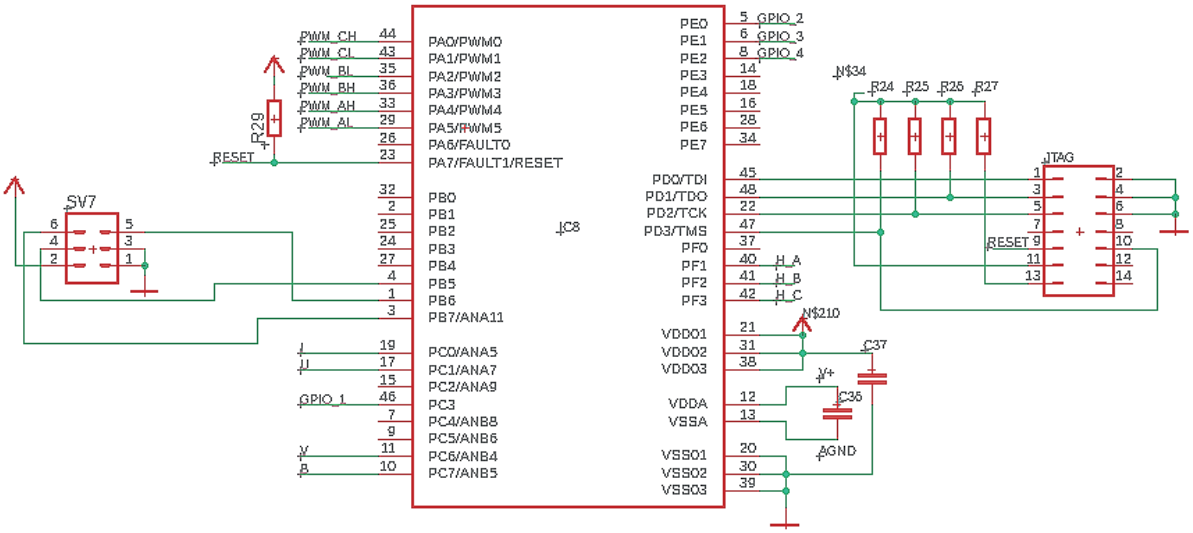

Figure 7 *Controlling processor*

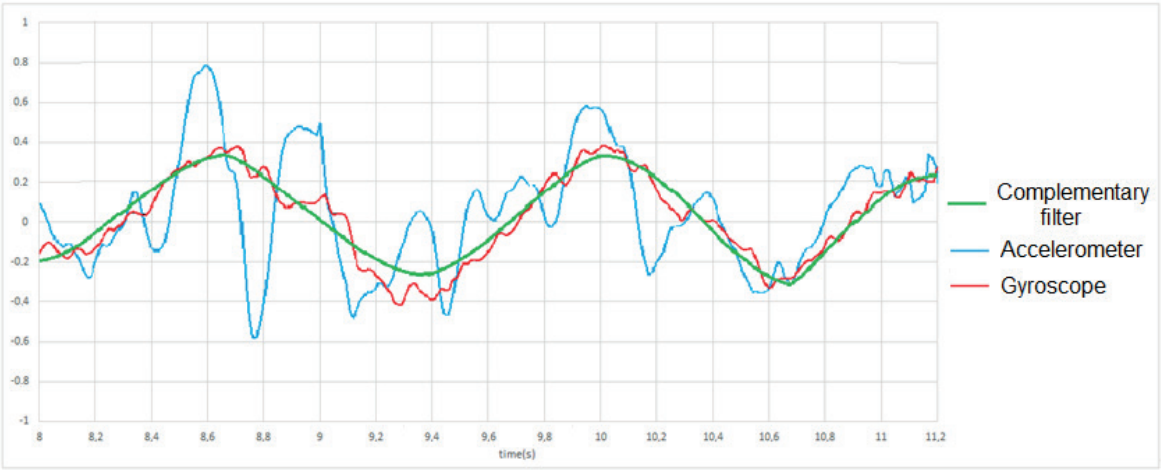

Figure 8 *Output of accelerometer, gyroscope and complementary filter*

method. This value is entered into other calculations and PD controller for electric motor drive.

We can see output values of the accelerometer, a gyroscope and a complementary filter in Figure 8.

4. Conclusion

We see a lot of differences between the accelerometer and gyroscope, but by their use we get sufficient inclination measuring system in one axis. The system will then be modified by adding a tilt measurement of the two remaining axes for parameter improvement.

The designed complementary filter is suitable for controlling the one-wheeled or two-wheeled platform. We can see the graph, where the filter softens the accelerometer and the gyroscope values and the resulting course is usable for controlling the converter.

Acknowledgements

This article is the result of a project implementation: Modern methods of teaching of control and diagnostic systems of engine vehicles, ITMS code 26110230107, supported by the Operational Programme Educational.

References

[1] WAGNER F., SCHMUKI R., WAGNER T., WOLSTONHOLME P. *Modeling software with finite state machines: a practical approach*. Boca Raton, FL: Taylor & Francis Group, 2006. ISBN 978-0-8493-8086-0.

[2] BURG A., MERUANI A., SANDHEINRICH B., WICKMANN M. *Mems gyroscopes and their applications. A study of the advancements in the form, function, and use of mems gyroscopes*. Final Report. Northwestern University, Mechanical Engineering Department, ME 381 - Introduction to MENS, prof. H. D. Espinosa, 2002.

[3] ELLIOTT, K. S., GUPTA, P., REED K. B., RODRIGUEZ R. C. *Micromachined vibrating gyroscopes: design and fabrication*. Final Report. Northwestern University, Mechanical Engineering Department, ME 381 - Introduction to MENS, prof. H. D. Espinosa, 2002.

[4] RODINA, J. *Application of inertial sensors for the control of mobile robotic platforms.* Autoreport of dissertation work. 2014.

[5] MCGILVRAY S., *Self-erecting inverted pendulum: swing up and stabilization control*. Central Canada Council for the IEEE Student Paper Contest, 2002.

[6] ANDREJASIC M. *Mems accelerometers*. Seminar. University of Ljubljana, Faculty for mathematics and physics, Department of physics, 2008.

[7] ELLIOTT-LABORATORIES. *The anschutz gyro-compass and gyroscope engineering*. Kiel, Germany: Wexford College Press, 2003, p. 7-24. ISBN 978-1-929148-12-7.

[8] MUCHERU G. *Operation of gyro sensor and 3-axis accelerometer*. Thesis. Helsinki Metropolia University of Applied Sciences, 2014.

[9] SEDO, J., KASCAK, S. Design of output LCL filter and control of single-phase inverter for grid-connected system. *Electrical Engineering* [online]. 2017, **99**(4), p. 1217-1232. ISSN 0948-7921, eISSN 1432-0487. Available from: https://doi.org/10.1007/s00202-017-0617-0

[10] DOBRUCKY B. *Discrete control of power electronic systems.* Zilina: EDIS - Publishing House of the University of Zilina, 2003.

Martin Kralik - Michaela Hola - Stanislav Jurecka*

OPTICAL PROPERTIES OF POROUS SILICON SOLAR CELLS FOR USE IN TRANSPORT

Porous silicon (pSi) samples were prepared by electrochemical etching of p-type silicon (p-type Si) substrate. Three pSi samples with different parameters of electrochemical etching (electrical potential, etching time, etching current) were prepared and analyzed. We studied the influence of electrochemical etching parameters on spectral reflectance of pSi structure. A modification of interference pattern was observed due to changes of microstructure. We determined the thickness of pSi layers from spectral reflectance. Solar cells with a porous structure achieve high efficiency and long life. These solar cells are predestined for use in transport.

Keywords: *electrochemical etching, black silicon, porous silicon, spectral reflectance, thin film interference*

1. Introduction

Porous silicon (pSi) has become a distinguished material in solar applications. Monocrystalline Si (mono-Si) produced by the Czochralski method is the most commonly substrate for pSi production. The pSi is used to produce solar cell with high conversion efficiency (over 21 %) [1]. Solar cells with a porous structure may be used in transport as part of electric vehicles, electric bicycles and other means of transport using electric drive. These highly efficient solar cells can be used to charge the electric conveying means. Spectral reflectance *R* of Si has a significant impact on efficiency of solar cells. *R* values of untreated mono-Si are over 40 % in range of spectrum relevant for solar cell applications [2]. This high spectral reflectance can be reduced by using anti-reflection layers or by additional surface treatment. The most common methods of surface treatment are for example wet etching (anisotropic, isotropic), electrochemical etching, plasma etching, or metal-assisted chemical etching. The result of application of plasma, electrochemical and metal-assisted chemical etching is pSi known as black Si (b-Si) [1, 3-4]. The most commonly used method of pSi production is electrochemical etching of p-type or n-type Si substrate in a solution of hydrofluoric acid (HF) and acetonitrile (CH_3CN). Porous silicon can also be prepared by electrochemical etching of Si substrate in solution of HF and dimethylformamide (C_3H_7NO) [4-5]. The basic scheme of the principle of electrochemical etching is shown in Figure 1. The principle of electrochemical etching is that an electrical voltage is applied between the anode and the cathode. The cathode is usually made of platinum (Pt) due to its high chemical resistivity. The Pt cathode is separated from the Si electrode by a few mm to several cm of electrolyte solution. There are two regimes of etching of silicon depending on current density: pore formation and electropolishing. Regimes of silicon electrochemical etching in HF solution are shown in Figure 2 [6-7].

The reactions that take place in HF electrolyte are given by equation (pore formation, low current density) [7]:

$$Si + 6\ HF \rightarrow H_2SiF_6 + H_2 + 2\ H^+ + 2\ e^-. \quad (1)$$

The reactions for electropolishing at high current density are given by equation [7]:

$$Si + 6\ HF \rightarrow H_2SiF_6 + 4\ H^+ + 4\ e^-. \quad (2)$$

In this paper we experimentally study the influence of electrochemical etching conditions to spectral reflectance. Following parameters were changed at electrochemical etching: voltage, etching time and current. The spectral reflectance was significantly modified depending on etching conditions.

2. Theory of spectral reflectance

Light impact on the material can be absorbed, reflected, scattered or passed through the medium. The reflection of light can occur from any interface at which the refractive index changes [8]. When light hits a material that has multiple layers with different refractive indices, each layer can reflect light as it is shown in Figure 3. In particular, in the case of the thin layer shown in Figure 3 there is a reflection of the incident wave on its upper and lower surface. The wave reflected from the upper surface of the thin layer is numbered 1 and the wave reflected from the lower surface is numbered 2. The total reflected light is given by the superposition of the reflected waves 1 and 2. This effect is called interference of light. Interference can be constructive or destructive depending on the phase difference [9].

If the light hits from an interface with a lower refractive index on an interface with a higher refractive index, then the phase shift between reflected and incident light is 180°. Otherwise there will be no phase shift between reflected and incident light [8]. Both cases are shown in Figure 4.

Constructive interference is defined by equation [9]:

$$2n_2 t\cos\beta = m\lambda,\ \ m = 0, 1, 2, \ldots. \quad (3)$$

* **Martin Kralik, Michaela Hola, Stanislav Jurecka**
Institute of Aurel Stodola, Faculty of Electrical Engineering and Information Technology, University of Zilina, Liptovsky Mikulas, Slovak Republic
E-mail:kralik@lm.uniza.sk

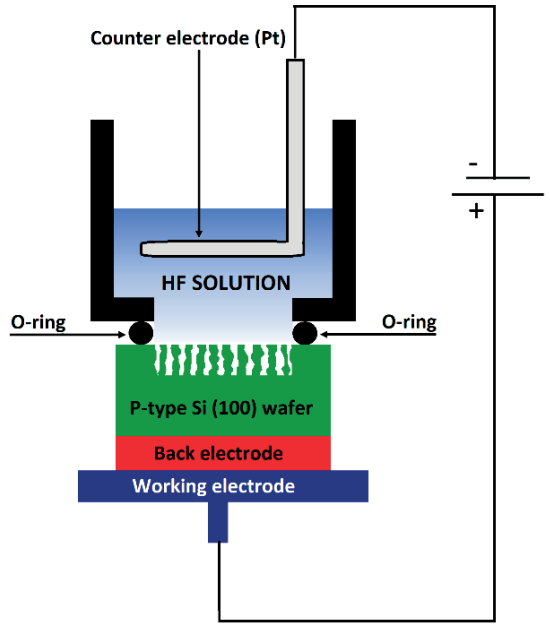

Figure 1 *The basic scheme of the principle of electrochemical etching*

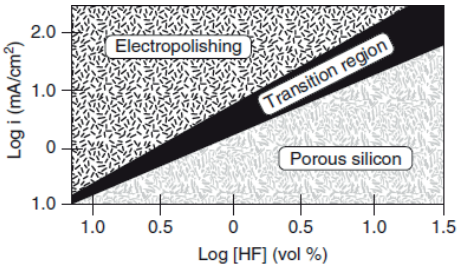

Figure 2 *Regimes of silicon electrochemical etching in HF solution: porous silicon formation and electropolishing [7]*

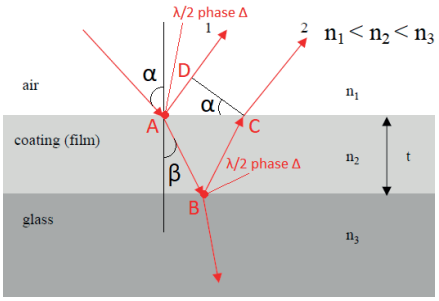

Figure 3 *Thin film interference [8]*

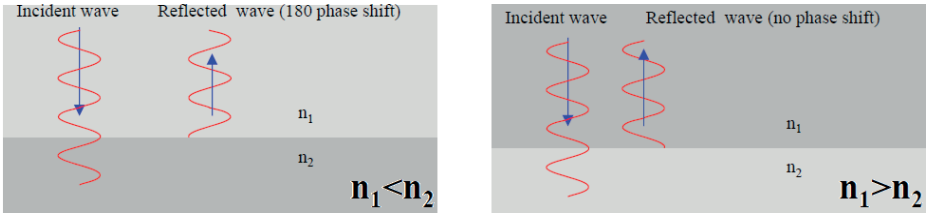

Figure 4 *Phase shift between reflected and incident wave is λ/2 (left), no phase shift between reflected and incident wave (right) [8]*

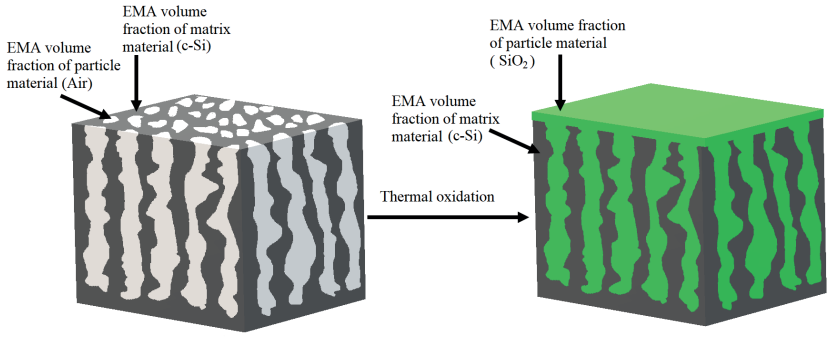

Figure 5 *Schematic representation of porous silicon and used volume fractions in Looyenga EMA formula*

where n_2 is refractive index of surface that reflected the wave, t is thickness of layer and λ is the wavelength of the incident wave. Destructive interference is defined by equation [9]:

$$2n_2 t\cos\beta = \left(m-\frac{1}{2}\right)\lambda,\ m = 0,1,2,\ldots. \tag{4}$$

The thickness of layer can be determined from the results of measurement of spectral reflectance by using equation [10]:

$$t = \frac{m}{2\sqrt{n^2-\sin^2\theta}}\frac{1}{\frac{1}{\lambda_1}-\frac{1}{\lambda_2}}, \tag{5}$$

where m is number of fringes in wavenumber region used, n is refractive index, θ is angle of incidence, λ_1 a λ_2 are the wavelengths of the used region.

When determining the thickness of the thin layer according to the Equation 5, it is necessary to know the refractive index of the studied material. The refractive index is the function of wavelength. The effective medium approximations (EMA) are the most commonly used for determining the refractive index of pSi. The schematic representation of pSi structure before and after thermal oxidation process and influence of this process on volume fractions used in Looyenga EMA formula is shown in Figure 5.

3. Experimental

The pSi samples published in this paper were prepared within the project APVV-15-0152. The production of pSi samples was performed by the method of electrochemical etching of p-type

Table 1 *Parameters of electrochemical etching*

Sample	Voltage [V]	Current density [mA/cm^2]	Etching time [min]	Annealing temperature [°C]	Annealing time [min]
A	24.8	40	1		
B	4.2	50	2.5	850	10
C	4.2	50	5		

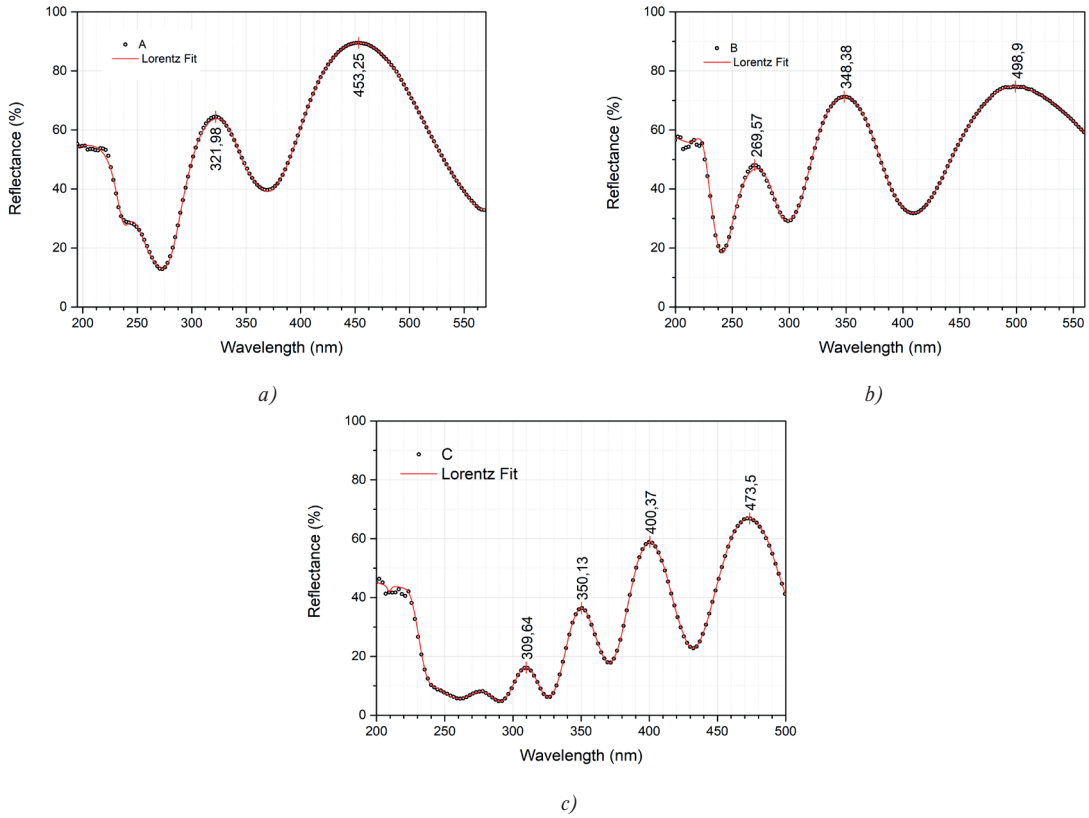

Figure 6 *Spectral reflectance of pSi sample a) A, b) B, c) C (dots) and theoretical model - by using a superposition of Lorentzian functions (curve)*

Si substrate. After etching samples were annealed in oxygen atmosphere for 10 minutes at 850 °C. The electrochemical etching parameters used for pSi samples forming are shown in Table 1.

Optical properties of samples were analyzed by using UV/VIS spectrometer AvaSpec-2048 for experimental spectral reflectance determination. The combination of deuterium and halogen lamps was used as a light source in the wavelength range 200-1100 nm. Al mirror was used as a reference sample.

4. Results and discussion

The aim of the experiment was to study the influence of electrochemical etching conditions on spectral reflectance of pSi. Parameters of electrochemical etching are shown in Table 1. The result of electrochemical etching of Si substrate is porous structure. The role of porous structure is to reduce the reflectivity of formed Si structure. Experimental spectral reflectance of pSi samples A, B and C are shown on Figure 6 (dots). A modification of interference pattern was observed due to changes of microstructure. Increasing number of local spectral reflectance extremes is observed for increasing time and increasing etching current. The thickness of pSi layer is related to the number of local extremes during the spectral reflectance [10-11]. The thickness of one or more layers in a layer stack can be determined from spectral reflectance by several methods: fast Fourier transformation (FFT) analysis, regression analysis with χ^2 test, by using interference pattern and other [10-13].

In this paper we determined the thickness of pSi layers by using theory of thin-film interference by using Equation 5 and Looyenga EMA formula. The results of both methods were compared. The angle of incidence during the reflection measurement was 0 degrees.

The first method for determining layer thickness (theory of thin-film interference) by using Equation 5: Accurate peak positions and number of interference fringes were used for the determination of thicknesses of pSi layers. Peak positions of the interference fringes were determined by using mathematical model of experimental spectral reflectance. This theoretical model was constructed by using a superposition of Lorentzian functions [14-15]:

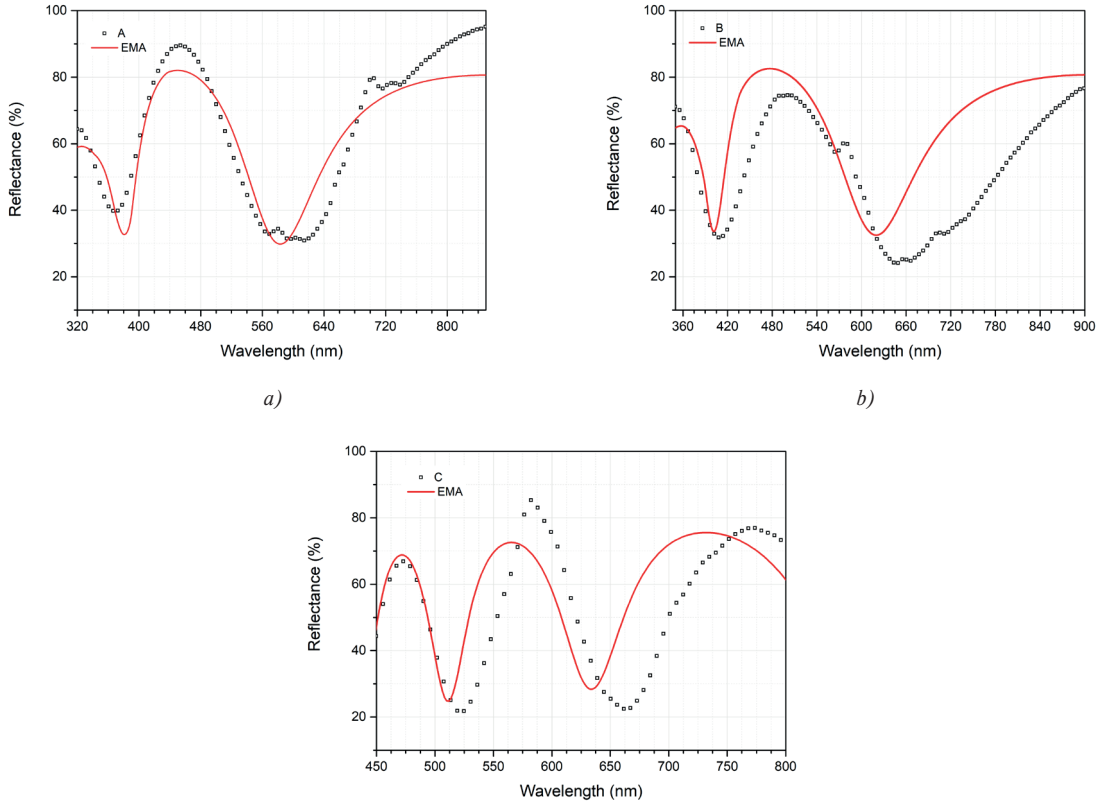

Figure 7 *Spectral reflectance of pSi sample a) A, b) B, c) C (dots) and theoretical model - by using Looyenga EMA formula (curve)*

Table 2 *Thickness of pSi layers*

Sample	Layer thickness (theory of thin-film interference) (nm)	Layer thickness (Looyenga EMA) (nm)
A	206	238
B	217	262
C	497	537

$$y = y_0 + \frac{2A}{\pi}\frac{w}{4(x-x_c)^2 + w^2}, \tag{6}$$

where y_0 is offset, x_c is center, A is amplitude, w is width of the Lorentzian peak. Theoretical models of spectral reflectance with marked positions of interference fringes are shown in Figure 6 a), b) and c) (curve). The value of refractive index used in the Equation 5 was 2.7 (50% volume fraction of SiO_2 (n ~ 1.4585) and 50% volume fraction of c-Si (n ~ 3.9766)). Calculated thicknesses of pSi layers are shown in Table 2.

The determination of film thickness based on Equation 5 is suitable only for thin film with negligible changes of optical constants in examined wavelength region. Refractive index used in construction of theoretical model of thin film spectral reflectance is obviously determined by suitable dispersion relation or by using selected effective media approximation. Optical properties of porous semiconductor structures are often modeled by using Looyenga EMA approximation due to its low sensitivity to geometrical properties of porous morphology. The Looyenga EMA approximation is defined by equation [16]:

$$\varepsilon_{eff}^{1/3} = (1-p)\varepsilon_m^{1/3} + p\varepsilon_p^{1/3}, \tag{7}$$

where p is the porosity, ε_m and ε_p are the complex dielectric constants of matrix and particle material. We implemented EMA model described by Equation 7 in computation of the spectral reflectance. In our approach crystalline Si is used as matrix material and SiO_2 oxide as particle fraction. Constructed theoretical model was optimized in the SCOUT software. Light scattering from the bottom interface of silicon substrate was not included in the spectral reflectance model due to the thickness of Si substrate (1 mm). In applied spectral region the light penetration depth in the crystalline Si substrate is very small [17]. Resulting theoretical models of spectral reflectance are shown in Figure 7 a), b) and c) (curve). Calculated thicknesses of pSi layers are shown in Table 2.

5. Conclusion

A modification of interference pattern was observed due to the changes of sample microstructure. We observed increasing thickness of pSi layers influenced by increasing etching time and current density. The increase in thickness due to etching is caused by the formation of porous microstructure on the surface of silicon substrate. The thicknesses of pSi layers in the first case were calculated by using theory of thin film interference. The thicknesses of pSi layers in the second case were calculated in SCOUT software by using Looyenga EMA in construction of theoretical model of spectral reflectance.

As the samples were thermally oxidized, it is likely that the pores were closed on the upper layer, which prevents the diffusion of oxygen to the remaining silicon [18]. For this reason, two volume fractions (SiO_2 and c-Si) were used in the Looyenga EMA model.

The results of both methods were compared. Creating an optical model using EMA has been challenging and the results are not ideal, but in this case the results are more reliable than results obtained by using the theory of thin film interference. In the future we will use spectral ellipsometry and Fourier analysis for the determination pSi layer thickness and other important structural properties. We will also work on refinement of optical models.

Acknowledgement

The work was supported by project H2020-MSCA-RISE-2016-6260922, grant of Science and Technology Assistance Agency APVV-15-0152, Scientific Grant Agency of the Ministry of Education of Slovak Republic and the Slovak Academy of Sciences project VEGA 1/0676/17, Centre of Excellence of Power Electronics Systems and Materials ITMS 26220120003, No. OPVaV-2008/2.1/01-SORO, ITMS 26220120046, and by project ITMS 26210120021, co-funded from EU sources and European Regional Development Fund.

References

[1] SAVIN, H., REPO, P., VON GUILLAUME, G., ORTEGA, P., CALLE, E., GARIN M., ALCUBILLA, R. Black silicon solar cells with interdigitated back-contacts achieve 22.1 % efficiency. *Nature Nanotechnology* [online]. 2015, **10**, p. 624-628. ISSN 1748-3387, eISSN 1748-3395. Available from: https://doi.org/10.1038/nnano.2015.89

[2] RAGHUNATHAN, D. Black silicon for higher efficiency in solar cells. Applied Mechanics and Materials [online]. 2015, **787**, p. 92-96. ISSN 1662-7482. Available from: https://doi.org/10.4028/www.scientific.net/AMM.787.92

[3] PLAKHOTNYUK, M., DAVIDSEN, R., S., SCHIMDT, M., S., MALUREANU, R., STAMATE, E., HANSEN, O. Lifetime of nano-structured black silicon for photovoltaic applications. 32nd European Photovoltaic Solar Energy Conference and Exhibition : proceedings. 2016. ISBN 978-1-5108-3651-8, p. 764-767.

[4] LOSIC, D., SANTOS, A. *Electrochemically engineered nanoporous materials - methods, properties and applications*. Springer, 2015. ISBN 978-3-319-20346-1.

[5] LEHMANN, V. *Electrochemistry of silicon* [online]. Wiley-VCH Verlag GmbH, 2002. ISBN 9783527293216, eISBN 9783527600274. Available from: https://doi.org/10.1002/3527600272

[6] SAILOR, M. J. *Porous silicon in practice, preparation, characterization and applications*. Wiley-VCH Verlag GmbH, 2012. ISBN 978-3-527-31378-5.

[7] FRANSSILA, S. *Introduction to microfabrication* [online]. 2 ed. John Wiley & Sons, Ltd, 2010. ISBN 9780470749838, eISBN 9781119990413. Available from: https://doi.org/10.1002/9781119990413

[8] ROORDA, A. *Thin Film Interference*. VS203B Lecture Notes, 2011.

[9] SERWAY, R., A., JEWETT, J., W. *Physics for scientists and engineers*. 6 ed. Belmont, CA, Thomson Brooks/Cole, 2004. ISBN 978-0534408466.

[10] HIND, A., R., CHOMETTE, L. *The determination of thin film thickness using reflectance spectroscopy*. *Application note*. Agilent Technologies Inc., SI-A-1205, 2011.

[11] FILMETRICS, Inc. *Advanced thin-film measurement systems*. Rev. 02.06, 2006.

[12] JURECKA, S., MULLEROVA, J., PINCIK, E. Optical methods for analysis of thin dielectric films. 19th International Conference on Applied Physics of Condensed Matter - APCOM 2013. 2013. ISBN 978-80-227-3956-6, p. 233-236.

[13] GOLDSTEIN, F. Film thickness of 'thick thin films' by spectroscopy. Society of Vacuum Coaters 1998 Meeting. Boston, MA, 1998.

[14] DIRDAL, CH. A., SKAAR, J.: Superpositions of Lorentzians as the class of causal functions. *Physical Review A* [online]. 2013, **88**(3), 033834. ISSN 2469-9926, eISSN 2469-9934. Available from: https://doi.org/10.1103/PhysRevA.88.033834

[15] Origin software: X-Function Register [online]. Avaliable from: https://www.originlab.com/doc/Origin-Help/Lorentz-FitFunc

[16] RAMIREZ-GUTIERREZ, C. F, CASTANO-YEPES, J. D., RODRIGUEZ-GARCIA, M. E. Porosity and roughness determination of porous silicon thin films by genetic algorithms. *Optik - International Journal for Light and Electron Optics* [online]. 2018, **173**, p. 271-278. ISSN 0030-4026. Available from: https://doi.org/10.1016/j.ijleo.2018.08.019

[17] SZE, S. M., KWOK, K. N. *Physics of semiconductor devices*. Hoboken, John Wiley & Sons, 2007. ISBN 978-0-471-14323-9.

[18] FODOR, B., AGOCS, E., BARDET, B., DEFFORGE, T., CAYREL, F., ALQUIER, D., FRIED, M., GAUTIER, G., PETRIK, P. Porosity and thickness characterization of porous Si and oxidized porous Si layers - an ultraviolet-visible-mid infrared ellipsometry study. *Microporous and Mesoporous Materials* [online]. 2016, **227**, p. 112-120. ISSN 1387-1811. Available from: https://doi.org/10.1016/j.micromeso.2016.02.039

Zuzana Judakova - Ladislav Janousek*

SOURCES OF ELECTROMAGNETIC FIELD IN TRANSPORTATION SYSTEM AND THEIR POSSIBLE HEALTH IMPACTS

Exposure to electromagnetic field caused by transportation systems is a cause of concern for many people. In public and personal transport there are many sources of electromagnetic field. Plenty of dosimetric analyses of electromagnetic field carried out by various research groups found out very high exposure values in the transport. Although the measured fields in transport remain well below the general limit for public exposure as defined by ICNIRP (1998) standards, they are relatively high compared to other micro-environments in daily life, especially for children seated in the rear seat, as field strengths are comparatively high there and children are a sensitive part of the population. How long-term effects of these fields affect the human organism and what is the mechanism of action, are questions without known answers. Several studies point to the potential association of various diseases with exposure to electromagnetic field. The key to understanding the effect of the electromagnetic field on the human organism is to reveal the mechanism of action of the field.

Keywords: *Intelligent Transportation System, wireless communications, electromagnetic field, exposure, health impact*

1. Introduction

The general public is exposed to an ever-increasing number of electromagnetic field (EMF) sources due to new infrastructure deployments, smart environments, novel wireless devices, various electric equipment and technologies (i.e., transmission lines, transformers, typical household appliances and their power supplies, public/personal transport and their technologies). Public/personal transport is a considerable source of EMF exposure.

Transport is a source of both low-frequency and high-frequency EMF. Sources of low-frequency EMF are various vehicle components requiring electric energy. Those components produce low-frequency EMF in the cables and components that conduct the electricity. The frequency range of such fields is wide, ranging from a few Hz to several kHz. Electric and hybrid vehicles produce stronger EMF than traditional vehicles fitted with only petrol or diesel engines. The sources of high-frequency fields are various security systems to enhance passenger comfort, traffic efficiency, the safety of passengers and so on, by forwarding upcoming traffic information in a timely manner through wireless communication.

Exposure to electromagnetic field caused by the transportation system is a cause of concern for many people. Throughout the history of Earth's development (nearly 4 billion years), living organisms have been exposed to very low intensities of this type of radiation and therefore have not developed sufficient protection against electromagnetic radiation. The long-term effects of electromagnetic field can cause various health problems not only to people with electromagnetic hypersensitivity (EHS). To determine impact of electromagnetic fields on human health, it is needed to know values of EMF quantities. The quantities can be verified by dosimetric analyses and simulations.

The article summarizes EMF values in various microenvironment and links them to potential health risks.

2. Sources of radiation in vehicles

Today's cars typically have more than 50 electronic control units and many sensors that produce EMF (Figure 1) [1]. Almost all new cars on the market today contain at least some wireless inputs to these computers. It works with large volumes of vehicle driving history, including information technologies – navigation systems, telematics, emergency assistance systems, and remote-control locks to ensure greater driver safety.

Electronic dashboard is the basic source of high-frequency radiation in cars. Radio frequencies are used in a number of applications. The most commonly implemented technologies are: electronic security system, ad-hoc vehicle network (VANET), dedicated short-range communication (DSRC), GPRS / GSM / GPS localization systems, Bluetooth, Wi-Fi and other vehicle control systems.

Another problem may pose electric vehicles. In electric vehicles passengers sit very close to an electric system of significant power, usually for a considerable amount of time. The relatively high currents used in these systems and the short distances between the power devices and the passengers mean that the latter could be exposed to relevant magnetic field. It is considered necessary to perform a detailed analysis of the radiated EMF from electromotor and cables, in order to avoid exposure to not permissible limits. Due to the importance of the overall vehicle weight on the autonomy and performance characteristics, excessive shielding in cables of electric vehicles is not tolerated. This involve that it becomes requirement to evaluate

* **Zuzana Judakova, Ladislav Janousek**
Department of Electromagnetic and Biomedical Engineering, Faculty of Electrical Engineering and Information Technology, University of Zilina, Slovakia
E-mail: zuzana.judakova@fel.uniza.sk

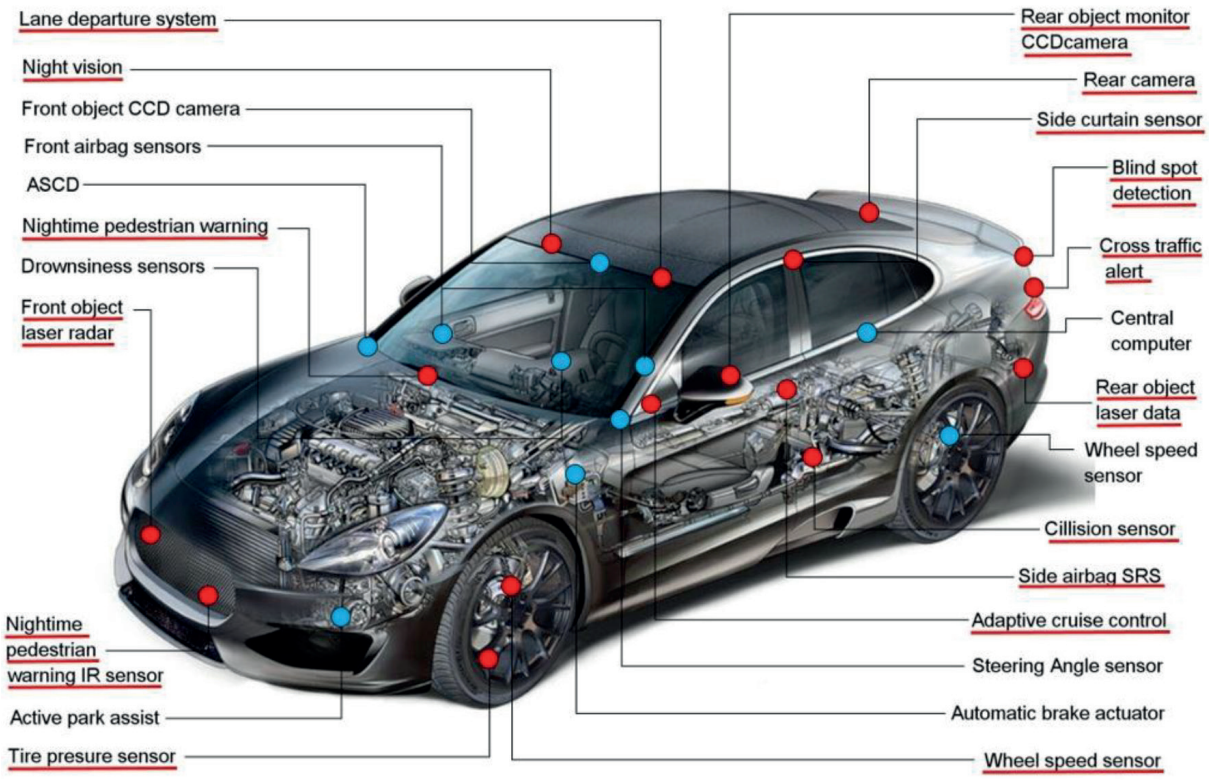

Figure 1 *Radar and wireless sensors in car*

the electromagnetic environment in the interior of these vehicles before placing them in the market [2].

Other major source of radiation that does not come directly from the vehicle but is very often used in vehicles is the cell phone. It transmits pulsed radio signals using the GSM mobile network (900–1800 MHz). Using mobile phone in partially closed environments of transportation vehicles, there are special situations for several reasons: the metallic structures produce large reflections, the structure itself is large compared to the wavelength, but the near field effects must be considered and the reflective surfaces are mostly curved. For whole body deposition, when the phone is far from the user, usage a cell phone inside a vehicle produces an increase of Specific Absorption Rate (SAR) values over the whole body. The vehicle structure is responsible for large relative changes in SAR [3].

3. EMF values in various microenvironments

Electricity is used substantially and sources of electromagnetic field are, unavoidably, everywhere. The transportation system is a source of the field, to which a large proportion of the population is exposed. In this part of the contribution the dosimetric analysis of EMF carried out by various research groups are summarized.

Eeftens et al. [4] collected simultaneous real-time personal measurements of radiofrequency electromagnetic fields (RF-EMF) over 24 to 72 h in 294 parent-child pairs from Denmark, the Netherlands, Slovenia, Switzerland, and Spain. The devices measured the power flux density (mW/m^2) in 16 different frequency bands every 4 seconds. Exposure during activities where most of the time is spent (home, school and work) was relatively low whereas exposure during travel and outside activities was higher. Figure 2 describe means of personal mean exposure to broadcast, DECT, downlink, uplink, and Wi-Fi per activity for children and parents. The total number of participants whose measurements contributed to each summary is shown, as well as the total number of measurement hours. The highest exposure values can be seen in the transport.

Measurements outside European countries were carried out by Choi et al. [5]. They monitored 50 child-adult pairs, living in Seoul, Cheonan, and Ulsan, South Korea. RF-EMF measurements were performed between September and December 2016, using a portable exposure meter tailored to capture 14 Korean radiofrequency bands ranging from 87.5 to 5875 MHz. The participants wear the device for 48 h and kept a time activity diary using a smartphone application in flight mode. To enhance accuracy of the exposure assessment, the body shadowing effect was compensated during the statistical analysis with the measured RF-EMF exposure. The compensation was transferred using the hybrid model that represents the decrease of the exposure level due to the body shadowing effect. The arithmetic (geometric) means of the total power density were 174.9 (36.6) $\mu W/m^2$ for all participants, 226.9 (44.6) for fathers, 245.4 (44.8) for mothers, and 116.2 (30.1) for children. By compensating for the body shadowing effect, the total RF-EMF exposure increased marginally, approximately 1.4 times. Among the three regions, total RF-EMF exposure was highest in Seoul, and among the activities, it was highest in the metro, followed by foot/bicycle, bus/car, and outside (Figure 3). Total RF-EMF exposure levels in Korea were higher than those reported in European countries.

The aim of the study [6] was to quantify RF-EMF exposure applying a tested protocol of RF-EMF exposure measurements using portable devices with a high sampling rate in 94 microenvironments and 18 public transport vehicles

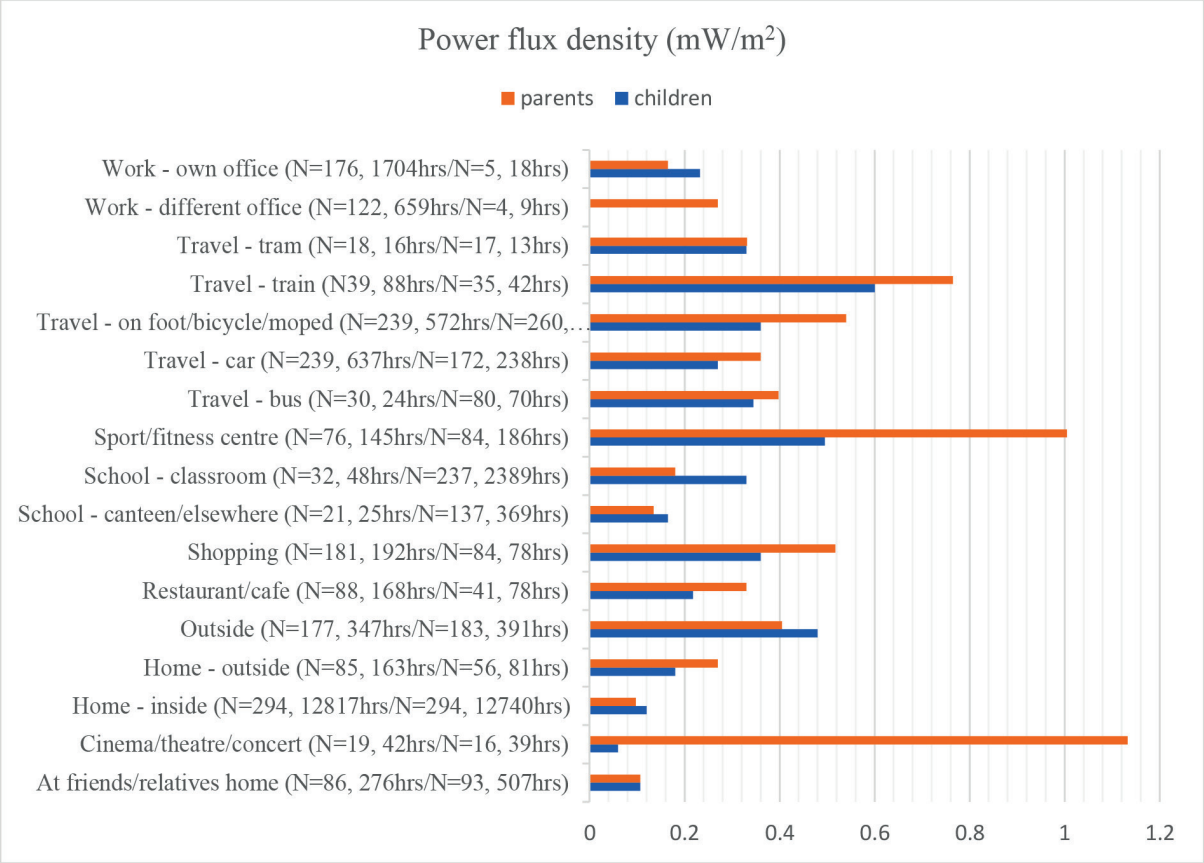

Figure 2 *Means of personal mean exposure [4]*

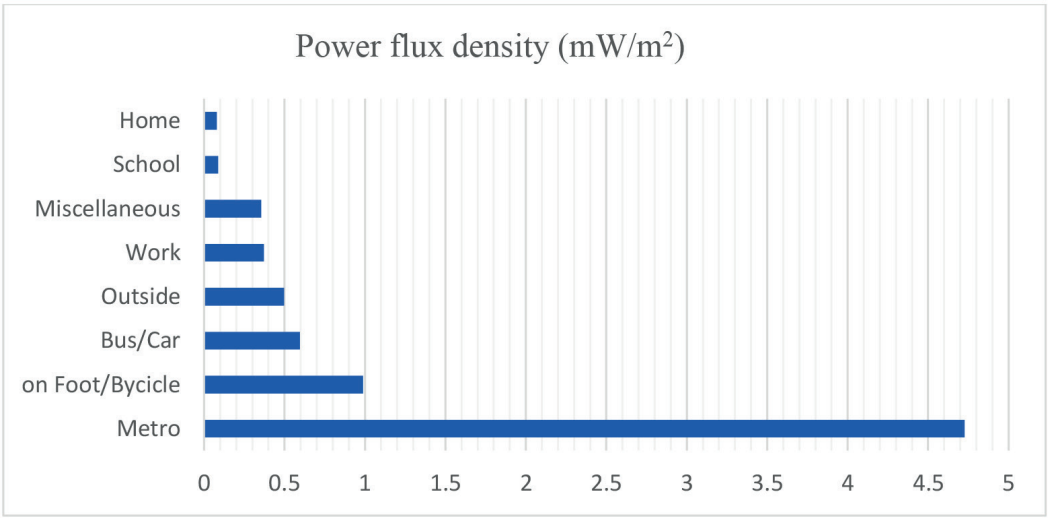

Figure 3 *RF-EMF exposure levels by activities in Korean children and parents [5]*

of Switzerland (15), Ethiopia (18), Nepal (12), South Africa (17), Australia (24) and the United States of America (8). The measurements were taken either by walking with a backpack with the devices at the height of the head and 20–30 cm from the body or driving a car with the devices mounted on its roof, which was 170–180 cm above the ground. The measurements were taken for about 30 min while walking and about 15–20 min while driving in each microenvironment, with a sampling rate of once every 4 seconds (ExpoM-RF) and 5 seconds (EME Spy 201). The highest RF-EMF exposure levels across public transportation were measured in auto rickshaw (Lalitpur, Nepal), taxi (Lalitpur, Nepal) and in train (Zurich, Switzerland) (Figure 4).

The main goal of study [7] is to determine the exposure level and spatial and temporal variances during 39 everyday activities in 12 frequency bands used in mobile telecommunication and broadcasting. Therefore, 24 h measurements were gathered from 98 volunteers living in or near Amsterdam and Purmerend, The Netherlands. They carried an activity diary to be kept to the minute, a GPS logger sampling at an interval of 1 s, and an EME Spy exposimeter with a detection limit of 0.0066 mW/m^2

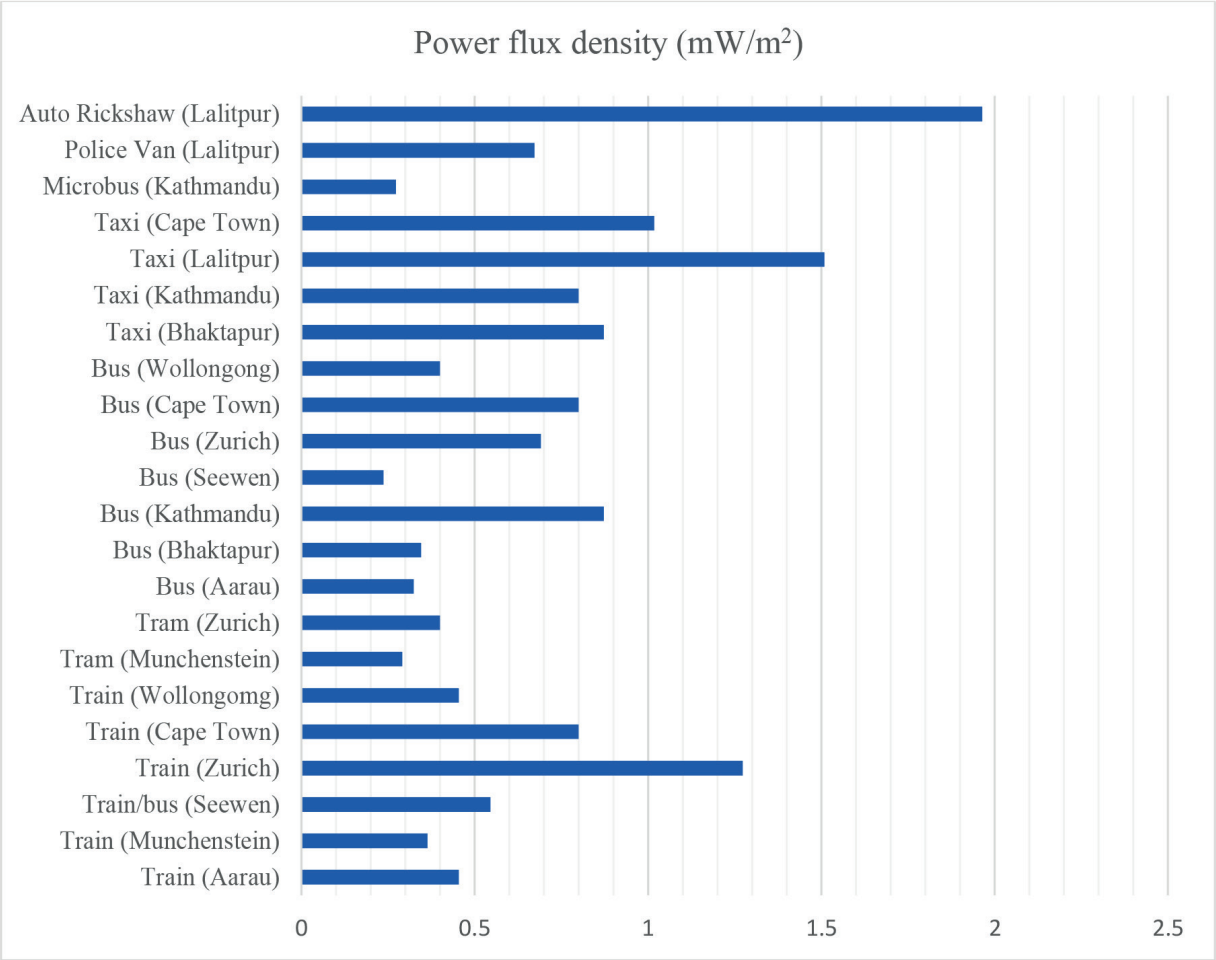

Figure 4 *Mean RF-EMF exposure per type of microenvironment [6]*

sampling at an interval of 10 s in 12 frequency bands. The mean exposure over 24 h, excluding own mobile phone use, was 0.180 mW/m^2. The highest mean exposure relates to the activities with high people density, such as travelling by public transport, visiting social events, pubs or shopping malls. The highest exposure during public transport was from the GSM and DCS uplink bands (0.162 mW/m^2, 56.1 %; 0.048 mW/m^2, 16.6 %), but driving a car led to a higher exposure in case a passenger was calling (0.314 mW/m^2, 40.5 %; 0.381 mW/m^2, 49.2 %). At railway stations and bus/tram stops the highest contributors were the downlink bands. Travelling by tram led to higher exposure in the downlink bands than for other means of transport.

In work [8], RF-EMF exposure of 166 volunteers from Basel, Switzerland, was measured with personal exposure meters (exposimeters). Participants carried an exposimeter for 1 week (two separate weeks in 32 participants) and completed an activity diary. Mean values were calculated using the robust regression on order statistics (ROS) method. Mean weekly exposure to all RF-EMF sources was 0.13 mW/m^2 (0.22 V/m) (range of individual means 0.014–0.881 mW/m^2). Exposure was mainly due to mobile phone base stations (32.0 %), mobile phone handsets (29.1 %) and digital enhanced cordless telecommunications (DECT) phones (22.7 %). Persons owning a DECT phone (total mean 0.15 mW/m^2) or mobile phone (0.14 mW/m^2) were exposed more than those not owning a DECT or mobile phone (0.10 mW/m^2). Mean values were highest in trains (1.16 mW/m^2), airports (0.74 mW/m^2) and tramways or buses (0.36 mW/m^2), and higher during daytime (0.16 mW/m^2) than nighttime (0.08 mW/m^2). Mean RF-EMF exposure (power flux density) at different locations is showed in Figure 5. The hours indicate the total time of all study participants spent at each location.

In this study [9] measurements of electric and magnetic fields emitted from Australian trams, trains and hybrid cars in urban and suburban areas were investigated. Exposure values at the floor level and seat level were investigated. The magnetic field strength was measured at different points inside and near the moving train, trams and the hybrid car. Further conclusions that can be drawn from this work are: (1) magnetic field strength are higher in the front side (closer to driver's cabin) than the rear side of trams and trains; (2) when several trams or trains passed by, higher peaks in the fields occur; (3) the frequency and magnetic field strengths vary with speed and these are higher during acceleration; (4) magnetic field strength are higher at the rear side than at the front side of the hybrid car; (5) magnetic field strength are higher at the left side than at the right side of the hybrid car and (6) the maximum levels of recorded magnetic field strength are emitted at 50 Hz in the tram, 15.25–16.50 Hz in the train and 12 Hz in the hybrid car. Maximum of magnetic field was measured on rear left floor of hybrid car – 3.5 μT, on front floor of train – 8.7 μT and on the middle floor of tram – 7.6 μT.

Stankowski et al. [10] measured alternating magnetic fields in a variety of different cars. Magnetic fields in cars in the μT

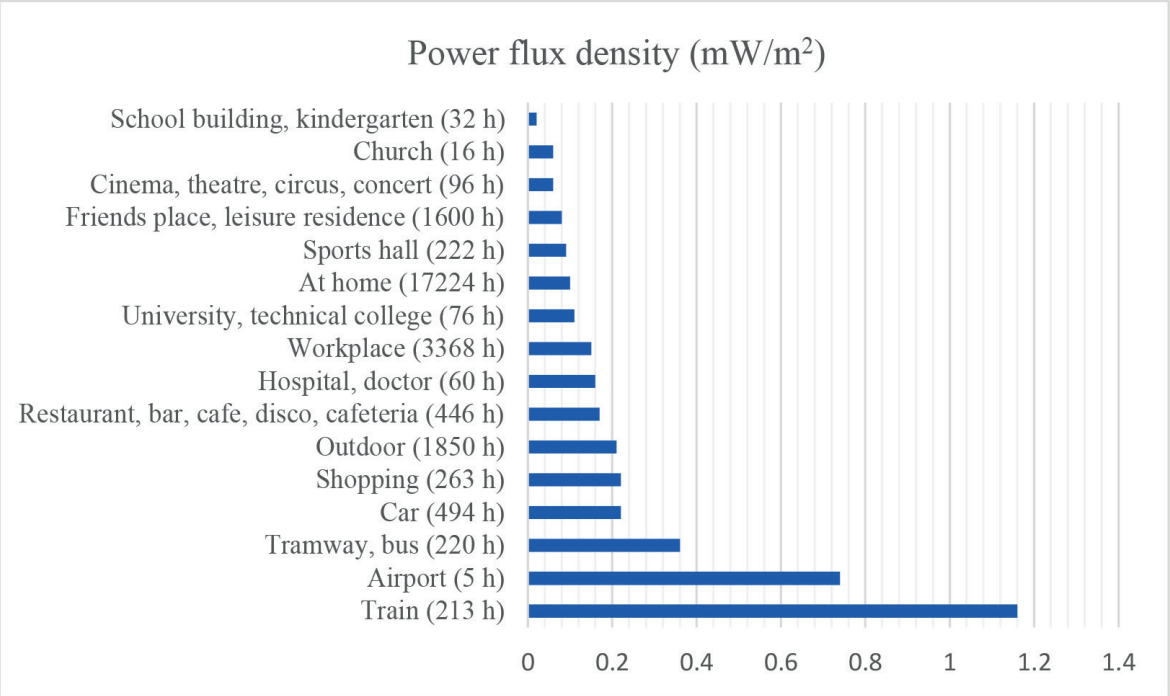

Figure 5 *Mean RF-EMF exposure (power flux density) at different locations [8]*

domain have been found to be produced by magnetized tires. In cars travelling at 80 km/h originate low-frequency field. The magnetic fields were measured at frequencies from 5 Hz to 2 kHz in 12 different cars. Higher values were measured in the foot area of the passenger seat and on the back seat. In 33% of the cars, values above 2 μT were measured; in 25% of the cars values were above 6 μT. The fundamental frequency of the magnetic fields is 10–12 Hz at a speed of 80 km/h. Considering the higher frequency harmonics, summed-up peaks reach values of up to 20 μT. Although the measured fields in cars remain well below the general limit for public exposure as defined by ICNIRP (1998) standards [11], they are relatively high compared to other exposures in daily life, especially for children seated in the rear seat, as field strengths are comparatively high there and children are a sensitive part of the population.

Presented research shows that humans are in modern world unavoidably exposed to considerable values of EMF. The highest values of the EMF power flux were measured in transport means. It should be noted that all the measured values are below limits given by the ICNIRP (1998). However, those limits are adjusted only based on the known thermal effects of EMF exposure. Those associated with the non-thermal phenomena are uncovered. Therefore, one should be aware that long-term exposure even to low level EMFs can lead to various health problems.

4. Possible health impact

Electromagnetic fields are packets of energy that have no mass. They fluctuate in frequency and wavelength. EMFs used for communications (RF-EMFs, 30 kHz – 300 GHz) and those generated by electricity (extremely low-frequency or ELF-EMFs, 3 Hz – 3 kHz) do not have sufficient energy to directly cause ionization and are therefore known as non-ionizing radiation. RF-EMFs at sufficient intensity cause tissue heating.

Exposing frequency EMF greater than ~ 100 kHz can cause considerable energy absorption and increased temperature. In general, EMF exposure creates unequal energy storage in the body. Physical magnitude used to describe the absorption of electromagnetic field by living tissue is SAR. SAR should be minimized so that blood flow and other body heat distribution mechanisms can dissipate this heat. Thermal effects are associated with energy absorption, which causes an increase in the body temperature, with a significant increase in temperature being detected at the earliest after six minutes of exposure. In published data, the effects of heat are most often reported as damage to the inner ear, clouding of the eye lens and damage to the cornea as a result of eye warming.

The current subject of the investigation are secondary human health effects due to exposures to non-ionizing EMFs at low intensities that do not cause measurable heating. Thermal hazards are associated with acute exposures and are thought to be characterized by thresholds, below which they are not present. However, many studies have suggested that RF exposure at lower than thermal levels may have biological effects, but they have either not been consistently replicated or else their significance for human health cannot be adequately assessed using information currently available. Exposure to low frequency and radiofrequency electromagnetic fields at low intensities poses a significant health hazard. There is a strong proof that excessive exposure to mobile phone-frequencies over long periods of time enhance the risk of brain cancer both in humans and animals. Other possible consequences of exposure to EMFs are negative effects on male and female reproduction, risk for glioma, meningioma and acoustic neuroma, risk of leukemia among children (living near to very high intensity radio transmission towers), breast cancer, ipsilateral parotid tumors. There are other diseases or physiologic alterations

which have been reported to be associated with exposure to non-thermal EMFs in humans and in animals: Alzheimer disease, increase neuropsychiatric and behavioral disorders, trigger cardiac rhythm alteration and peripheral arterial pressure instability, induce changes in immune system function and alter salivary and thyroid function, cognitive and neurobehavioral problems in children, idiopathic environmental intolerance. There is increasing evidence the exposures can result in neurobehavioral decrements and that some individuals develop a syndrome of EHS or microwave illness. While the symptoms are non-specific, new biochemical indicators and imaging techniques allow diagnosis that excludes the symptoms as being only psychosomatic. [12]

5. Conclusion

New technological developments during recent years are leading to the introduction of new sources of electromagnetic field. For example, inductive battery charging for electric cars (not only hybrids), are bearing exposure potential for occupants staying nearby, commonly implemented technologies than VANET or Bluetooth, and others present some future challenges for the exposure of the general population. Plenty of dosimetric analyses of electromagnetic field carried out by various research groups found out the highest exposure values in the transport. Drivers and passengers spend considerable amounts of time in these vehicles, and health risks might increase with the duration of exposure. We do not advocate going back to the age before electricity, wireless communication or transport without vehicles, but we want to show the possible adverse effects of EMFs on human health. It becomes requirement to evaluate the electromagnetic environment in the interior of vehicles before placing them in the market and before their daily application.

All measurement results presented in the paper show that the values are below the ICNIRP limits. However, it should be noted that those limits are adjusted, based only on the known thermal effects. Those associated with the non-thermal phenomena especially in case of long-term exposure are still uncovered. Critical amount of relevant data and exact mechanism/s of action are still missing concerning the non-thermal effects. It is thus recommended to use those technologies cautiously, especially by children. Children are a risk group because they are under development and therefore their organism is more susceptible to possible EM field effects.

Acknowledgement

This work was supported by project ITMS: 26210120021, co-funded from EU sources and European Regional Development Fund.

References

[1] GAJSEK, P., RAVAZZANI, P., GRELLIER, J., SAMARAS, T., BAKOS, J., THUROCZY, G. Review of studies concerning electromagnetic field (EMF) exposure assessment in Europe: low frequency fields (50 Hz – 100 kHz). *International Journal of Environmental Research and Public Health* [online]. 2016, **13**(9), p. 875. ISSN 1661-7827, eISSN 1660-4601. Available from: https://doi.org/10.3390/ijerph13090875

[2] MORENO-TORRES, P., LAFOZ, M., BLANCO, M., ARRIBAS, J. R. Passenger exposure to magnetic fields in electric vehicles. In: *Modeling and simulation for electric vehicle applications* [online]. 2016, IntechOpen, p. 47–71. ISBN 978-953-51-2637-9, eISBN 978-953-51-2636-2. Available from: https://doi.org/10.5772/64434

[3] ANZALDI, G., SILVA, F., FERNANDEZ, M., QUILEZ, M., RIU, P. J. Initial analysis of SAR from a cell phone inside a vehicle by numerical computation. *IEEE Transactions on Biomedical Engineering* [online]. 2007, **54**(5), p. 921–930. ISSN 0018–9294, eISSN 1558-2531. Available from: https://doi.org/10.1109/TBME.2006.889776

[4] EEFTENS, M., STRUCHEN, B., BIRKS, L. E., CARDIS, E., ESTARLICH, M., FERNANDEZ, M. F., GAJSEK, P., GALLASTEGI, M., HUSS, A., KHEIFETS, L., MEDER, I. K., OLSEN, J., TORRENT, M., TRCEK, T., VALIC, B., VERMEULEN, R., VRIJHEID, M., VAN WEL, L., GUXENS, M., ROOSLI, M. Personal exposure to radio-frequency electromagnetic fields in Europe: Is there a generation gap? *Environment International* [online]. 2018, **121**(1), p. 216–226. ISSN 0160-4120, eISSN 1873-6750. Available from: https://doi.org/10.1016/j.envint.2018.09.002

[5] CHOI, J., HWANG, J.-H., LIM, H., JOO, H., YANG, H.-S., LEE, Y.-H., EEFTENS, M., STRUCHEN, B., ROOSLI, M., LEE, A.-K., CHOI, H.-D., KWON, J.h., HA, M. Assessment of radiofrequency electromagnetic field exposure from personal measurements considering the body shadowing effect in Korean children and parents. *Science of The Total Environment* [online]. 2018, **627**, p. 1544–1551. ISSN 0048-9697, eISSN 1879-1026. Available from: https://doi.org/10.1016/j.scitotenv.2018.01.318

[6] SAGAR, S., ADEM, S. M., STRUCHEN, B., LOUGHRAN, S. P., BRUNJES, M. E., ARANGUA, L., DALVIE, M. A., CROFT, R. J., JERRETT, M., MOSKOWITZ, J.M., KUO, T., ROOSLI, M. Comparison of radiofrequency electromagnetic field exposure levels in different everyday microenvironments in an international context. *Environment International* [online]. 2018, **114**, p. 297–306. ISSN 0160-4120, eISSN 1873-6750. Available from: https://doi.org/10.1016/j.envint.2018.02.036

[7] BOLTE, J. F., EIKELBOOM, T. Personal radiofrequency electromagnetic field measurements in the Netherlands: Exposure level and variability for everyday activities, times of day and types of area. *Environment International* [online]. 2012, **48**, p. 133–142. ISSN 0160-4120, eISSN 1873-6750. Available from: https://doi.org/10.1016/j.envint.2012.07.006

[8] FREI, P., MOHLER, E., NEUBAUER, G., THEIS, G., BURGI, A., FROHLICH, J., BRAUN-FAHRLANDER, C., BOLTE, J., EGGER, M., ROOSLI, M. Temporal and spatial variability of personal exposure to radio frequency electromagnetic fields. *Environmental Research* [online]. 2009, **109**(6), p. 779–785. ISSN 0013-9351, eISSN 1096-0953. Available from: https://doi.org/10.1016/j.envres.2009.04.015

[9] HALGAMUGE, M. N., ABEYRATHNE, C. D. MENDIS, P. Measurement and analysis of electromagnetic fields from trams, trains and hybrid cars. *Radiation Protection Dosimetry* [online]. 2010, **141**(3), p. 255–268. ISSN 0144-8420, eISSN 1742-3406. Available from: https://doi.org/10.1093/rpd/ncq168

[10] STANKOWSKI, S., KESSI, A., BECHEIRAZ, O., MEIER-ENGEL, K., MEIER, M. Low frequency magnetic fields induced by car tire magnetization. *Health Physics*. 2006, **90**(2), p. 148–153. ISSN 0017-9078, eISSN 1538-5159.

[11] INTERNATIONAL COMMISSION ON NON-IONIZING RADIATION PROTECTION, VECCHIA, P., HIETANEN, M., MATTHES, R., AHLBOM, A., BREITBART, E., DE GRUIJL, F. R., FEYCHTING, M., GREEN, A., JOKELA, K., LIN, J., SAUNDERS, R., SCHULMEISTER, K., SODERBERG, P., STUCK, B., SWERDLOW, A., TAKI, M., VEYRET, B., ZIEGELBERGER, G., REPACHOLI, M. H., ICNIRP ELF TASK GROUP, MATTHE, R., AHLBOM, A., JOKELA, P., ROY, C., SAUNDERS, R. Guidelines for limiting exposure to time-varying electric and magnetic fields (1 Hz to 100 kHz). *Health Physics* [online]. 2010, **99**(6), p. 818–836. ISSN 0017-9078, eISSN 1538-5159. Available from: https://doi.org/10.1097/HP.0b013e3181f06c86

[12] BELPOMME, D., HARDELL, L., BELYAEV, I., BURGIO, E., CARPENTER, D. O. Thermal and non-thermal health effects of low intensity non-ionizing radiation: an international perspective. *Environmental Pollution* [online]. 2018, **242**(A), p. 643–658. ISSN 0269-7491, eISSN 1873-6424. Available from: https://doi.org/10.1016/j.envpol.2018.07.019

Jan Kanuch - Peter Girovsky*

ANALYSIS OF THE PM MOTOR WITH EXTERNAL ROTOR FOR DIRECT DRIVE OF ELECTRIC WHEELCHAIR

The paper deals with analysis of properties of synchronous motor with external permanent magnets rotor. The mathematical analysis and equivalent circuit of permanent magnet synchronous motor (SMPM) is presented. In the parts of the paper the electromagnetic design, construction design and FEM Simulation of a SMPM is described and its properties are analysed. In the paper the results of simulation in Matlab/Simulink of torque, speed and current on the base mathematical model are shown.

Keywords: *direct drive, electric vehicle, external rotor, permanent magnet machine, synchronous motor, wheelchair*

1. Introduction

Due to some of its advantageous features, such as high efficiency, high torque-to-current ratio, low noise, and robustness has permanent magnets synchronous motor (PMSM) received widespread acceptance in industrial applications [1]. Electric machines present main parts of the electric vehicle power train, whilst demands for electric machines differ. In general, characteristics as large torque, high rotation speed, high power density, quick response and good reliability are in high demand. Synchronous machines supplied by electronic converter are first of all widely used as the permanent magnet synchronous machine in variable speed drives and applied to small electric vehicles [2].

The manufacturers produce small electric vehicles with various types of drives. Drives of small electric vehicles are nowadays the subject of research of many manufacturers and institutes [3]. Design solutions bring several alternatives that differ in technical parameters [4]. Most of the parameters of drive depend directly on design solutions of the electric motor, on its power, battery voltage, dimensions of frequency converter and others. The development of high-quality permanent magnet materials in commercial production has encouraged several manufacturers to introduce various PMSM to the market.

The most practical for the electric wheelchair is a direct drive that is a motor with an external rotor using permanent magnets in-wheel operation. The drive can be designed with an inverse DC motor with permanent magnets or an AC synchronous motor with permanent magnets an external rotor, respectively. Optimal design of synchronous motor parameters is influenced by utilization of inverters [5-6]. The study [7] examines the effects of motor parameters on the torque and speed capability.

The characteristics of a permanent magnet machine are highly dependent on the rotor structure. The rotor can be implemented in various ways. When employing modern permanent magnet materials, the rotor can be constructed even completely without iron.

Designed and produced for direct drive of the wheelchair has been the prototype of an inverse AC synchronous motor with permanent magnets [8] and this motor is assessed and simulated in the following parts of the paper.

2. Mathematical analysis and equivalent circuit of permanent magnet synchronous motor

As to the modelling, it is common practice to transform all variables from the three-phase system (abc) to an orthogonal (dq) reference frame with a direct (d) and quadrature (q) axis (see Figure 1), where X represents the voltage, current or magnetic flux and θ_r is the rotor angle.

Clarke Transformation abc→αβ, see Equation (1), and Park Transformation αβ→dq, see Equation (2), can be applied regarding reference frame theory.

$$\begin{bmatrix}\alpha\\ \beta\end{bmatrix}=\frac{2}{3}\cdot\begin{bmatrix}1 & \cos(2\pi/3) & \cos(4\pi/3)\\ 0 & \sin(2\pi/3) & \sin(4\pi/3)\end{bmatrix}\cdot\begin{bmatrix}a\\ b\\ c\end{bmatrix}, \tag{1}$$

$$\begin{bmatrix}d\\ q\end{bmatrix}=\begin{bmatrix}\cos(\theta_r) & \sin(\theta_r)\\ -\sin(\theta_r) & \cos(\theta_r)\end{bmatrix}\cdot\begin{bmatrix}\alpha\\ \beta\end{bmatrix}. \tag{2}$$

The transformation of a three-phase quantity in abc-coordinate system to dq-system is called Clarke-Park's Transformation. Written in matrix form, see Equation (3), the Clarke-Park's Transformation is defined as

$$\begin{bmatrix}d\\ q\end{bmatrix}=\frac{2}{3}\cdot\begin{bmatrix}\cos(\theta_r) & \cos(\theta_r-2\pi/3) & \cos(\theta_r+2\pi/3)\\ \sin(\theta_r) & \sin(\theta_r-2\pi/3) & \sin(\theta_r+2\pi/3)\end{bmatrix}\cdot\begin{bmatrix}a\\ b\\ c\end{bmatrix}, \tag{3}$$

Permanent magnet synchronous motors (PMSM) are usually modelled in the rotor reference frame, i.e. in the Clarke-Park's d-q model. In this synchronous reference frame, the PMSM with PM rotor is generally described by the following set of equations [8-9]:

$$u_d = R\cdot i_d + L_d\cdot\frac{di_d}{dt} - \omega L_q i_q\,, \tag{4}$$

$$u_q = R\cdot i_q + L_q\cdot\frac{di_q}{dt} - \omega L_d i_d + \omega\psi_{Md}\,. \tag{5}$$

* **Jan Kanuch, Peter Girovsky**
Department of Electrical Engineering and Mechatronics, Faculty of Electrical Engineering and Informatics, Technical University in Kosice, Slovakia
E-mail: jan.kanuch@tuke.sk

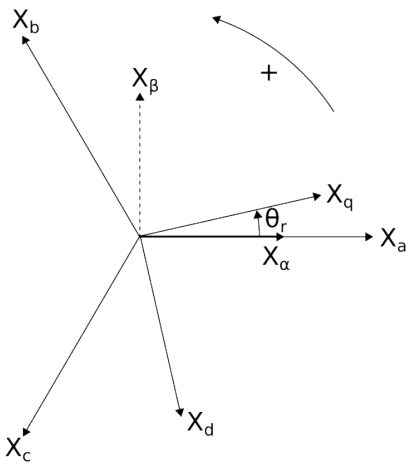

Figure 1 *Rotating reference frames*

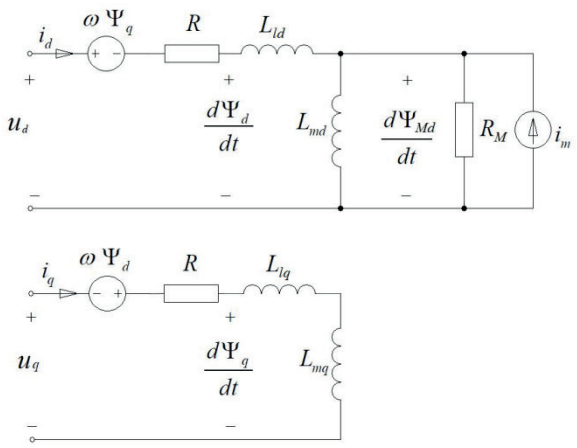

Figure 2 *Equivalent circuit of the PMSM in d-axis and q-axis*

where: u_d and u_q are the d and q axes voltages,
i_d and i_q are the d and q axes currents,
R is the stator resistance,
ω is the electrical angular speed,
Ψ_{Md} is the permanent magnet flux,
L_d and L_q are inductances of the stator d and q axes.

The PMSM can be described in Equation (4) and (5) with the following assumptions:

- saturation is negligible,
- the induced back EMF is sinusoidal,
- eddy currents and hysteresis losses are negligible,
- no field current dynamics,
- no cage on the rotor.

The electromagnetic torque can be expressed as follows:

$$T_{em} = \frac{3}{2} \cdot \frac{P}{2} \cdot [\psi_{Md} \cdot i_d - (L_q - L_d) \cdot i_d \cdot i_q]. \quad (6)$$

where P is the number of poles, i_d and i_q are the d-axis and q-axis components of the stator current vector. Thus, the magnitude of I_S is given by equation:

$$I_S = \sqrt{i_d^2 + i_q^2}. \quad (7)$$

The equivalent circuit of the PM machine shown in Figure 2 is similar to the one for the synchronous machine.

The permanent magnet is modelled by a current source i_m parallel to the resistance R_M. In the magnetizing inductance, this current source produces the permanent magnet's share of the air gap flux linkage:

$$\psi_{Md} = i_m \cdot L_{md}. \quad (8)$$

However, due to the saturation the magnetizing inductance L_{md} and i_m are not constant. The flux linkage components in Figure 2 are determined by the equations:

$$\psi_d = i_d \cdot L_d + \psi_{Md} = i_d \cdot (L_{1d} + L_{md}) + \psi_{Md}, \quad (9)$$

$$\psi_q = i_q \cdot L_q = i_q \cdot (L_{1q} + L_{mq}). \quad (10)$$

Phasor diagram of the PMSM for motor operation is shown in Figure 3. The phasor diagram represents a stationary mode of operation, hence effective values for currents and voltages are used (indicated by capitals).

In Figure 3 the E_f is the phase back electromotive force (EMF), or excitation voltage, induced in the stator winding by PMs at synchronous speed (E_f depends directly on rotor speed and PM flux), I_S is the phase current, R is the stator resistance, X_{md} and X_{mq} are the d-axis and q-axis components of the synchronous reactance.

3. Electromagnetic and construction design of synchronous motor with permanent magnets on external rotor

Main results of the electromagnetic and construction design of synchronous motor with permanent magnets on external rotor is described in paper [8]. For the design and electromagnetic calculations of PMSM, the basic equations and information were used referring to [9-15]. The calculation of parameters and dimensions of SMPM was done by using a debugged m-file in MATLAB 2013a. Table 1 presents data of the designed motor. A schematic cross-section of the electromagnetic circuit with winding is presented in Figure 4.

4. FEM Simulation of SMPM with external rotor

The analytical design is validated by means of comparison to FEM simulations [8]. It was used in 2D FEM simulation that compared with 3D simulation needed a much shorter time to be calculated [16-19]. In the paper [8] presented are results from open-circuit and load simulation. The FEM simulation results correspond fairly well to the results obtained from the analytical design. The airgap flux density waveform of the machine at open-circuit simulation is presented in Figure 5. The back-EMF waveforms of the machine at open-circuit simulation are presented in Figure 6.

Table 1 *Data of the PM synchronous motor [8]*

Quantity	Value	Quantity	Value
rated power [W]	250	efficiency [%]	92
rated voltage [Vrms]	12	pole pieces of stator	9
rated speed [rpm]	150	pole pieces of rotor	12
outer machine diameter [mm]	160	number of coils per phase	3
total machine width [mm]	70	number of turns per coil	86
maximum torque [Nm]	20	number of winding layers	2

Table 2 *Results from load simulation [8]*

Quantity	Value
Peak phase current [A]	7.071
Maximum rotor iron flux density [T]	1.207
Maximum stator iron flux density [T]	1.949
Fundamental airgap flux density [T]	0.4558
Peak flux linkage, q-axis [Wb]	0.0452
Peak flux linkage, d-axis [Wb]	0.1122

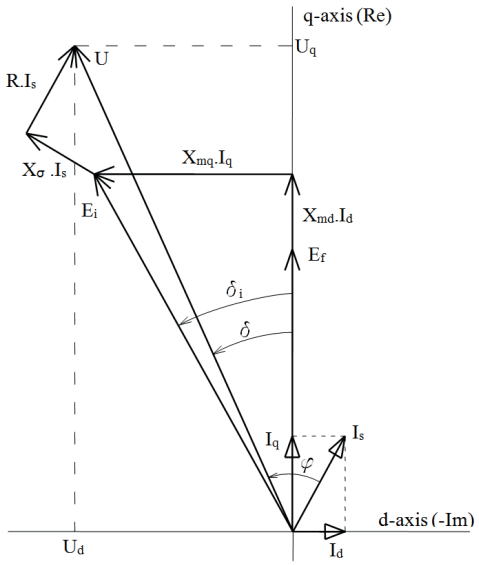

Figure 3 *Phasor diagram of the PMSM in dq-axes*

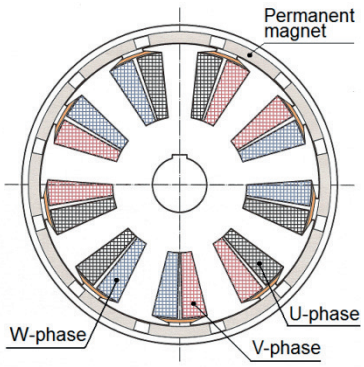

Figure 4 *Electromagnetic circuit of SMPM [8]*

Table 3 *Data of simulated torque of the motor [8]*

Quantity	Value
Mean airgap torque (by flux linkage and current) [Nm]	9.047
Mean airgap torque (by Maxwell stress tensor) [Nm]	9.0
Torque reduction due to iron losses [Nm]	0.1868
Torque ripple [%]	11.62

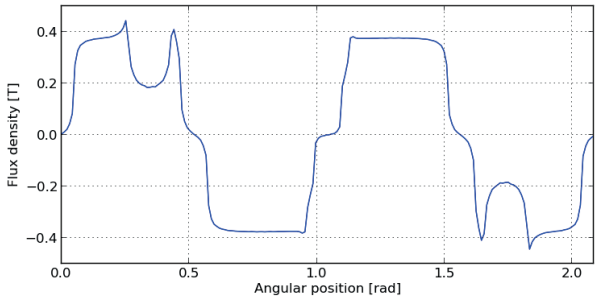

Figure 5 *The airgap flux density waveform at open-circuit simulation [8]*

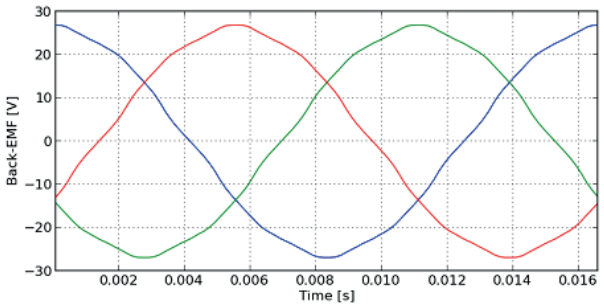

Figure 6 *The back-EMF waveforms at open-circuit simulation [8]*

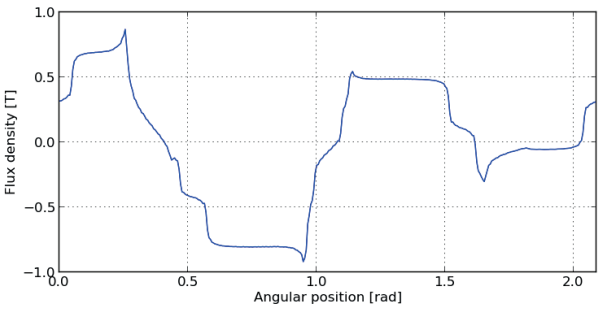

Figure 7 *The airgap flux density waveform at load simulation [8]*

Results from load simulation are presented in Table 2 and data for the torque motor at load simulation are presented in Table 3. The airgap flux density waveform of the machine at load simulation is presented in Figure 7. In Figure 8 presented is torque waveform of the machine at load simulation.

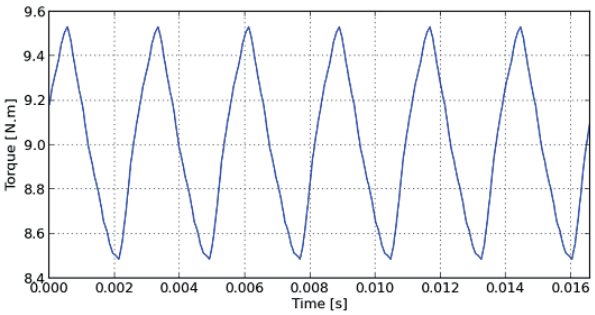

Figure 8 *The torque waveform of SMPM at load simulation [8]*

Figure 9 *Photograph of prototype SMPM without bearing plate [8]*

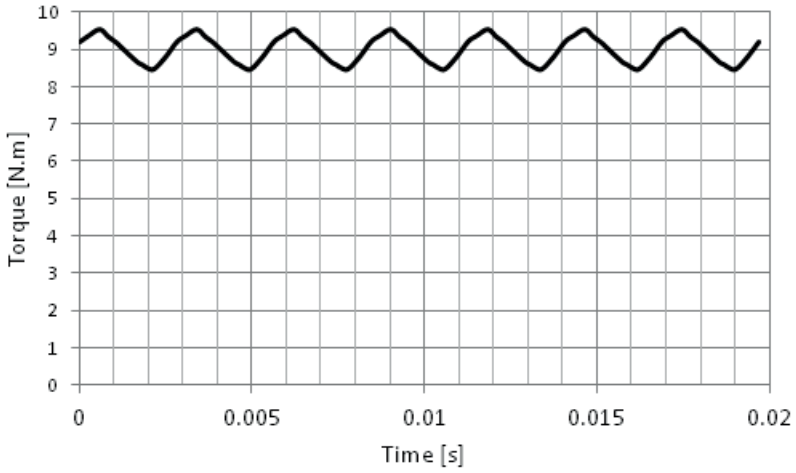

Figure 10 *Torque as a function of time at the loading in motoric mode [8]*

5. Prototype of SMPM with external rotor and measured results of the machine

The construction of prototype with outer rotor permanent magnet synchronous machine is described in [8] in detail. Photograph of the motor without bearing plate is shown in Figure 9.

Experimental measurements of the machine prototype were performed in laboratories. The motor was supplied from a frequency converter. Measurements of the stator quantity (voltage, current and frequency) were performed both on the frequency converter and measurement of the power on a digital wattmeter. The measurements were done in generator mode of operation for the speed of 200 rpm and for two values of speed - 120 and 200 rpm in the motor mode of operation, respectively. Measured torque ripple presented in Figure 10 is comparable with FEM simulation of torque (see Figure 8).

6. Matlab/Simulink simulation of synchronous motor with permanent magnets on external rotor

In this section presented are results of the mathematical model simulation created by Equations (4)-(10).

A) Simulation model of the permanent magnet synchronous motor

Matlab/Simulink® enables "to view" dynamic characteristics and to analyse transient performance of the motor. The mathematical model of the permanent magnet synchronous motor, is suitable for implementation of the Matlab/Simulink method based on d,q transformations known from the reference frame theory of electrical machinery [20]. The mathematical model must correspond with the analysed motor and represents the physical phenomena as close as possible. The simulation model of the PMSM is presented in Figure 11.

The electromagnetic torque T_{em} in Fig. 11 is determined by Equation (6) and the loading torque T_L can be expressed as follows:

$$T_L = T_{em} - J \cdot \frac{d\omega_m}{dt}. \tag{11}$$

where J is the rotor inertia and ω_m is angular speed of the rotor. The angular speed of the rotor is expressed by the time derivation of its displacement θ_m:

$$\omega_m = \frac{d\theta_m}{dt}. \tag{12}$$

The d-q components of the armature current I_S of the PMSM (see Figure 3), in terms of the permanent magnet flux linkage Ψ_{md} and load angle δ, are introduced.

B) Simulation results

On the basis of the simulation model of PMSM (see Figure 11), the simulation of torque, speed and current characteristics has been carried out. The stator windings parameters, flux linkage

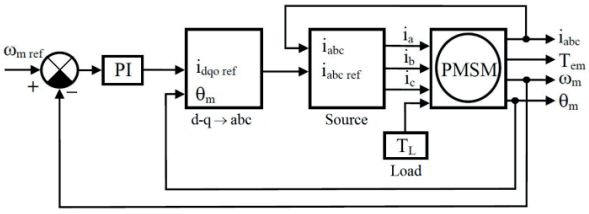

Figure 11 *The simulation model of PMSM*

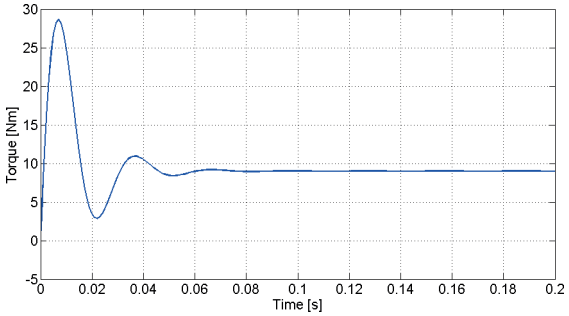

Figure 12 *The dynamic torque characteristic of PMSM at rated load start-up*

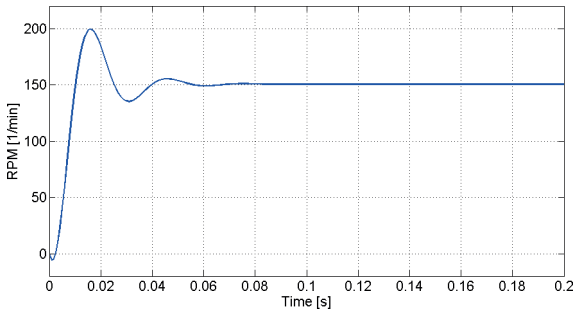

Figure 13 *The mechanical speed of PMSM at rated load start-up*

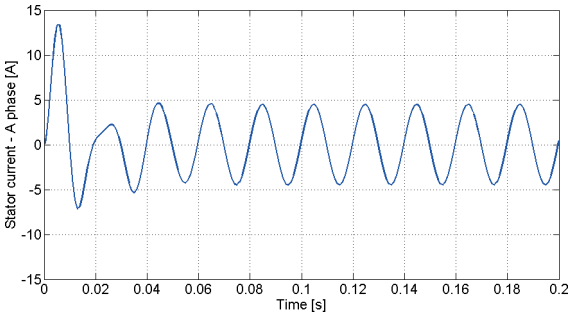

Figure 14 *Motor stator current - A phase*

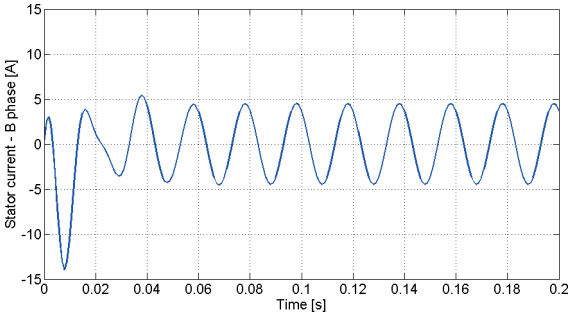

Figure 15 *Motor stator current - B phase*

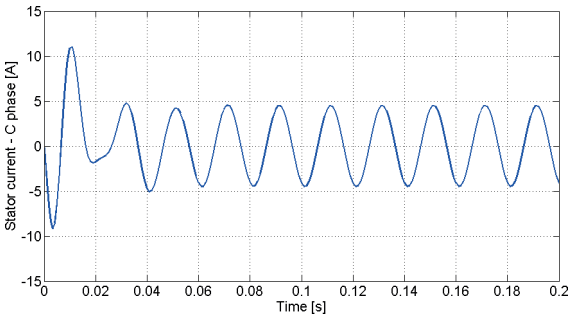

Figure 16 *Motor stator current - C phase*

and synchronous d and q reactance of the motor are obtained from the FEM computations. The load torque is given as input data. The simulation procedure is performed for rated supply conditions and motor starting at the rated load T_L=T_N. The result of simulation torque characteristic for analyzed case is presented in Figure 12.

After the transients are suppressed, the obtained value of the simulated torque corresponds to the torque at the steady-state operating mode (see Table 3).

Figure 13 shows the mechanical speed of the PMSM. The stator currents are shown in Figures 14-16 respectively.

As it is shown in Figures 12-16, the PMSM has a good dynamic response.

7. Conclusion

The present paper describes the simulations and shows initial results of measurements of a synchronous machine prototype with an external rotor and permanent magnets. The design, FEM simulations and results of measurements are presented in paper [8].

The present paper shows the result of simulation of torque, mechanical speed and stator currents. The torque of the considered PMSM in present paper is verified in three ways: simulated results in Matlab/Simulink (Figure 12) and FEM Simulation (Figure 8 and Table 3) are compared with measured value (Figure 10). Showing a very good agreement, they prove that the applied methodologies as accurate.

Mechanical properties of the prototype of the inverse synchronous motor were verified too. The SMPM was supplied from the three-phase frequency converter at the speed corresponding to operation conditions. Results of measurements obtained at the constant speed in load mode, when the inverse synchronous motor was loaded up to 130 % of the nominal current, confirm suitability of inverse synchronous motor for the direct drive in-wheel operation of the electric wheelchair. On the SMPM verified have been the dynamic properties. From the results one sees that the presented inverse SMPM has good dynamic and static properties.

Acknowledgments

The financial support of the Slovak Research and Development Agency under the contract no. APVV-16-0270 is acknowledged.

References

[1] RUI-HUA, L., JIAN-FEI, Z., BO, H., GUO-QING, X. Adaptive inverse control of permanent magnet synchronous motor drive in a micro-electric vehicle. 8th International Conference on Machine Learning and Cybernetics : proceedings [online]. Vol. 4. Piscataway, NJ : IEEE, 2009. ISBN 978-1-4244-3703-0, p. 1909-1914. Available from: https://doi.org/10.1109/ICMLC.2009.5212190

[2] QIANFAN, Z., XIAOFEI, L. Permanent magnetic synchronous motor and drives applied on a mid-size hybrid electric car. Vehicle Power and Propulsion Conference VPPC '08 : proceedings. IEEE, 2008. ISBN 978-1-4244-1849-7, p. 1 - 5.

[3] SKALA, B. The heat and cooling of electronically switching synchronous machine as a main drive of a car. International Conference on Applied Electronics. IEEE, 2011, ISSN 1803-7232, p. 349-352.

[4] SATO, E. Permanent magnet synchronous motor drives for hybrid electric vehicles. *IEEJ Transactions on electrical and electronic engineering* [online]. 2007, **2**(2), p. 162-168. eISSN 1931-4981. Available from: https://doi.org/10.1002/tee.20122

[5] SOONG, W. L., MILLER, T. J. E. Field-weakening performance of brushless synchronous AC motor drives. *IEE Proceedings - Electric Power Application* [online]. 1994, **141**(6), p. 331-340. ISSN 1350-2352. Available from: https://doi.org/10.1049/ip-epa:19941470

[6] SCHIFERL, R. F., LIPO, T. A. Power capability of salient pole permanent magnet synchronous motor in variable speed drive applications. *IEEE Transactions on Industry Applications* [online]. 1990, **26**(1), p. 115-123. ISSN 0093-9994, eISSN 1939-9367. Available from: https://doi.org/10.1109/28.52682

[7] SEBASTIAN, T., SLEMON, G. R. Operating limits of inverter-driven permanent magnet motor drives. *IEEE Transactions on Industry Applications* [online]. 1987, **23**(2), p. 327-333. ISSN 0093-9994, eISSN 1939-9367. Available from: https://doi.org/10.1109/TIA.1987.4504909

[8] KANUCH, J., GIROVSKY, P. Motor for direct drive of electric wheelchair. *International Journal of Engineering Research in Africa* [online]. **31**, 2017, p. 94-103. ISSN 1663-4144. Available from: https://doi.org/10.4028/www.scientific.net/JERA.31.94

[9] OSIN, I. L., KOLESNIKOV, V. P., YUFEROV, F. M. *Permanent magnet synchronous micromotors* (in Rusian). Moscow, Energia 1976.

[10] GIERAS, J. F., WING, M. *Permanent magnet motor technology, design and aplications.* New York, Marcel Dekker, Inc., 2002. ISBN 0-8247-0739-7.

[11] CAMPBELL, P. *Permanent magnet materials and their application*. Cambridge, University Press, 1994. ISBN 0521249961.

[12] GIERAS, J. F. Analytical approach to cogging torque calculation in PM brushless motors. IEEE International Electric Machines and Drives Conference IEMDC'03 : proceedings. Vol. 2. 2003. eISBN 0-7803-7817-2, p. 815-819.

[13] SCHMIDT, E., SUSIC, M., EILENBERGER, A. Finite element analysis of an external rotor permanent magnet synchronous machine with star- and delta-connected tooth coil windings. XIX International Conference on Electrical Machines ICEM : proceedings [online]. IEEE, 2010. ISBN 978-1-4244-4175-4. Available from: https://doi.org/10.1109/ICELMACH.2010.5608233

[14] MARKO, R. *Design of salient pole PM synchronous machines for a vehicle traction application - analysis and implementation*. Ph.D. Thesis. University of Technology Lappeenranta, 2012. ISBN 978-952-265-337-6.

[15] BRANDT, M., GUTTEN, M., KOLTUNOWICZ, T., ZUKOWSKI, P. Analysis of winding fault in electric machines by frequency method. 12th International Conference ELEKTRO 2018 : proceedings [online]. 2018, p. 1-4. ISBN 978-1-5386-4758-5A. vailable from: https://doi.org/ 10.1109/ELEKTRO.2018.8398298

[16] SCHMIDT, E., EILENBERGER, A. Calculation of position dependent inductances of a permanent magnet synchronous machine with an external rotor by using voltage driven finite element analyses. *IEEE Transactions on Magnetics* [online]. 2009, **45**(3), p. 1788-1791. ISSN 0018-9464, eISSN 1941-0069. Available from: https://doi.org/10.1109/TMAG.2009.2012822

[17] JIN, J. *The finite element method in electromagnetics.* 3. ed. New York: John Wiley & Sons, 2014. ISBN 978-1-118-57136-1.

[18] BASTOS, J. P. A., SADOWSKI, N. *Electromagnetic modeling by finite element methods.* New York: Marcel Dekker Ltd., 2003. ISBN 0-8247-4269-9.

[19] PETKOVSKA, L., CVETKOVSKI, G. FEM based simulation of a permanent magnet synchronous motor performance characteristics. CES/IEEE 5th International Power Electronics and Motion Control Conference : proceedings [online]. Vol. 3. 2006. eISBN 1-4244-0448-7. Available from: https://doi.org/10.1109/IPEMC.2006.4777986

[20] ONG, CH-M. *Dynamic simulation of electric machinery: using MATLAB/ SIMIULINK.* New Jersey: Prentice Hall, 1998. ISBN 0137237855.

Sergey B. Kosytsyn - Vladimir Y. Akulich*

STRESS-STRAIN STATE OF A CYLINDRICAL SHELL OF A TUNNEL USING CONSTRUCTION STAGE ANALYSIS

The work is aimed at research of the stress-strain state of a cylindrical shell of a tunnel using the non-linear static analysis and construction stage analysis. Research is carried out on the example of determining the stress-strain state of the tubing (shells) of the main line tunnel, constructed using a tunnel powered complex (slurry shield). Based on obtained results, a comparative analysis of the computational models with the corresponding conclusions is presented.

Keywords: *construction stages, soil massif, shell, slurry shield, finite elements*

1. Introduction

The technology of construction of artificial constructions, as a rule, assumes construction of objects in several stages: installation of the bridge span, installation of tubing of the main line tunnels, etc. However, now at the stage of design of such artificial constructions, computational models usually do not consider stage-by-stage construction of an object, standard and methodical documentation also does not tell anything about it. At the same time, it is worth noting that the introduction of computational models capable of changing in time is a necessary step for development of design and building of artificial constructions both on the domestic and the world scales. This is due to the fact that the stress-strain state of the computational model can significantly change when taking into account its changes in time. In this regard the comparative analysis of computational models, with and without taking into account their changes in time, is of a particular interest.

The authors of the article are aimed at the task of carrying out the comparative analysis of the final stress-strain state of the cylindrical shell of the main line tunnel, constructed using a tunnel powered complex (slurry shield). Besides the two computational models, which take or do not take into account changes in time, the third case participated in comparative analysis. It takes into account a construction gap between the tunnel shell and the soil environment, whose emergence is caused by use of the slurry shield. In addition, it was necessary to give an assessment for need of creation of a computational model taking into account change in time, when determining the stress-strain state of the complex objects constructed in several stages.

2. General provisions of calculation models

The calculation of the stress-strain state of a tunnel shell was performed by a finite element method in the ANSYS Mechanical software package. This is a complex multi-purpose software package for numerical simulation of physical processes and phenomena in the field strength, fluid dynamics, thermal physics, electromagnetism and acoustics.

The spatial calculation model (Figure 1) consisted of the isotropic uniform massif modeling the soil environment, represented by the three-dimensional quadratic isoparametric elements Hex20, each consisting of twenty nodes, and the cylindrical shell consisting of fifteen separate rings simulating the main line tunnel (Figure 2) placed in the center of the massif. The cylindrical shell is approximated by the two-dimensional flat four-node Quad4 elements. The local coordinate systems of the shell elements were co-directed, for a correct display of results.

Geometrical characteristics of the tunnel shell:

- external diameter 5800 [mm];
- internal diameter 5300 [mm];
- average length of a face ring along the tunnel 1400 [mm];
- block thickness 250 [mm].

The shell is presented by a model of linear-elastic material with the following characteristics of reinforced concrete: density - 2300 kg/m^3, elastic modulus E - 30000 MPa, Poisson's ratio μ - 0.18 (the tunnel is designed in monolithic reinforced concrete from B45 concrete and bars of A240, A400).

It is worth noting that the shell was modeled taking into account eccentricity between the geometrical shape of the cross section necessary for creation of constructive positioning of elements and the average line of a shell, along which the loading is placed and results are calculated [1].

The soil massif was set by dimensions of 65 m × 65 m × 21 m on Mohr-Coulomb model with the following characteristics of clay: density - 2000 kg/m^3, deformation modulus E_{def} - 30.0 MPa, Poisson's ratio μ - 0.30, friction angle ϕ - 20.0°, cohesion C_u - 50.0 kPa.

The problem was solved in geometrically, physically (nonlinearity of material behavior) and constructively (change of the status of contact) nonlinear statement.

The geometry of some types of designs, such as shells, having small thickness in comparison to other dimensions, can significantly change during the loading process. The stiffness of such designs changes in the course of deformation, as well [2].

* **Sergey B. Kosytsyn, Vladimir Y. Akulich**
Department of Theoretical Mechanics, Russian University of Transport (MIIT), Moscow, Russia
E-mail: 79859670635@yandex.ru

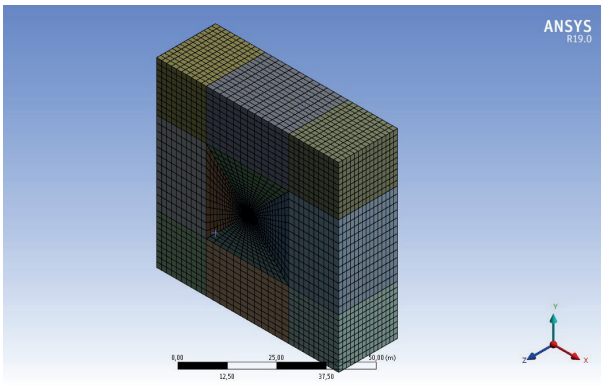

Figure 1 Spatial calculation model in ANSYS Mechanical

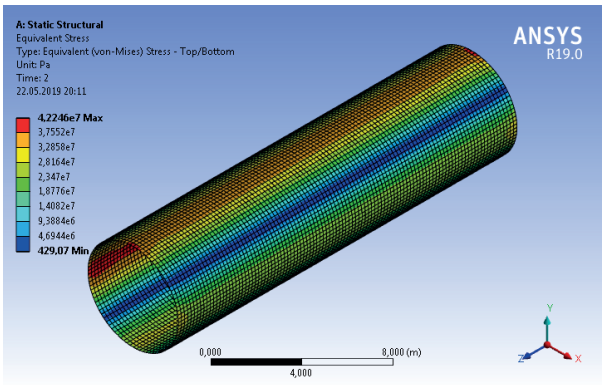

Figure 3 Computational model No. 1 - fields intensities of von Mises stresses σ_v of the shell

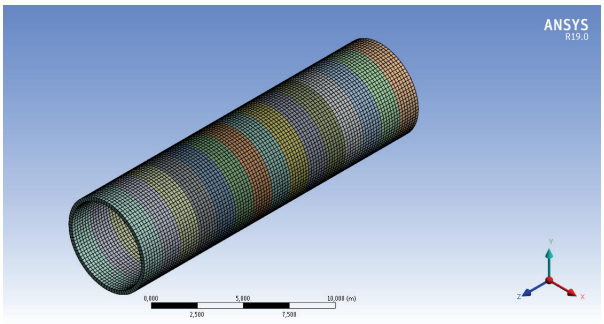

Figure 2 The mesh of the cylindrical shell tunnel

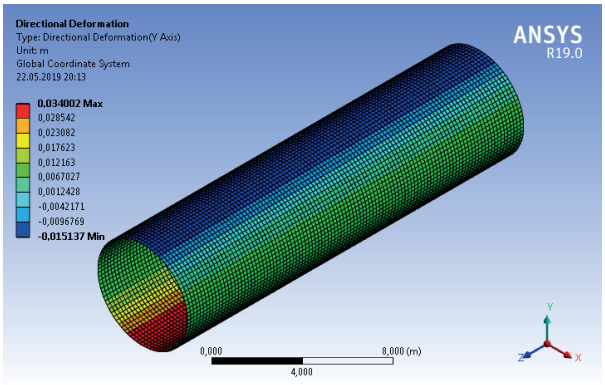

Figure 4 Computational model No. 1 - fields of vertical displacements of the shell

When modeling similar designs, it is necessary to work out the equilibrium equations, taking into account change of a shape and sizes of research objects. The ANSYS software package allows to take into account the following nonlinearity: large deformations, large deflections, changes in the effective bending stiffness and effective rotational stiffness.

Physical nonlinearity is shown by nonlinear connections between components of the generalized tensions and deformations and characterizes the work of design material in nonlinearly elastic and plastic stages of deformation.

Constructive nonlinearity needs to be considered as the shell enters the work step by step and during this process can be with or without contact with the soil environment. The contact was defined as contact pairs between the shell and the soil environment with the ability to split and slip between objects [3].

3. Computational model No. 1 does not take into account changes in time

For the first calculation model (without taking into account change of the calculation model in time) calculation was carried out in two stages: determination of the stress-strain state of the isotropic uniform massif in a household state (under the influence of a body weight) and after construction of the whole cylindrical shell in the body of the massif [4].

In Figure 3 are shown the maximum equivalent stresses according to the IV strength theory (von Mises), [5]. The maximum stress was 42.2 MPa, minimum was 429.1 Pa.

In Figure 4 are shown the vertical displacements of a shell, whose maximum values were 0.034 m (shell displacements were cleared after the first stage of calculation).

4. Computational model No. 2 taking into account changes in time

For the second computational model (taking into account the change of the calculation model in time), calculation was carried out in sixteen stages: determination of the stress-strain state of the isotropic uniform massif in a household state (under the influence of a body weight) and after construction of each separate ring of the cylindrical shell in the body of the massif.

In Figure 5 are shown the maximum equivalent stresses according to the IV strength theory (von Mises). The maximum stress was 65.1 MPa, minimum was 744.9 Pa.

In Figure 6 are shown the vertical displacements of a shell, whose maximum values were 0.055 m (shell displacements were cleared after the first stage of calculation).

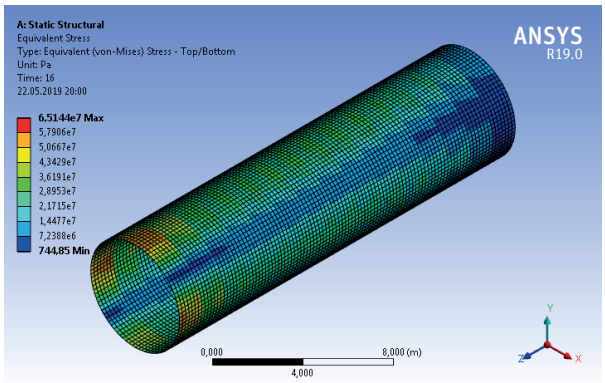

Figure 5 Computational model No. 2 - fields intensities of von Mises stresses σ_v of the shell

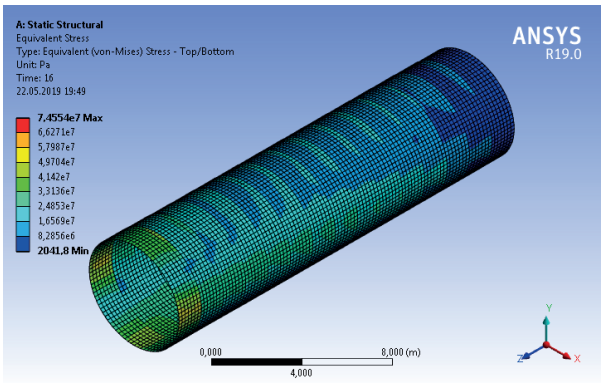

Figure 7 Computational model No. 3 - fields intensities of von Mises stresses σ_v of the shell

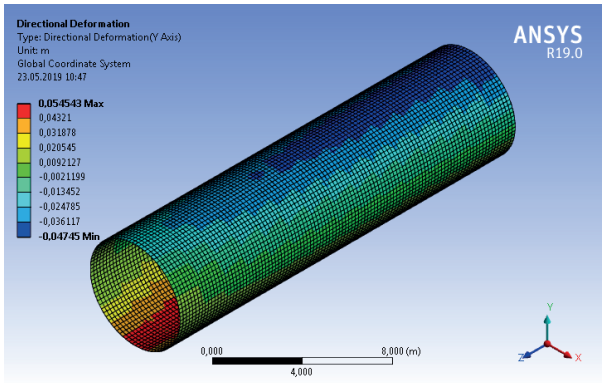

Figure 6 Computational model No. 2 - fields of vertical displacements of the shell

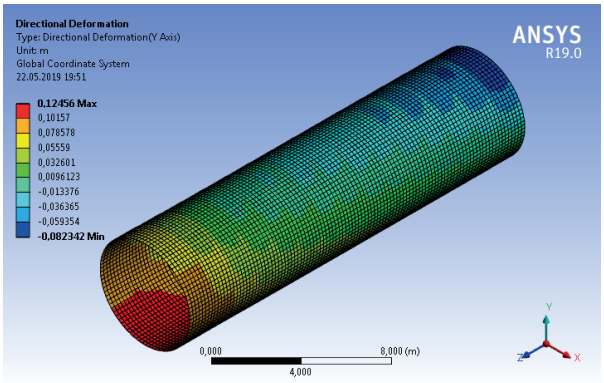

Figure 8 Computational model No. 3 - fields of vertical displacements of the shell

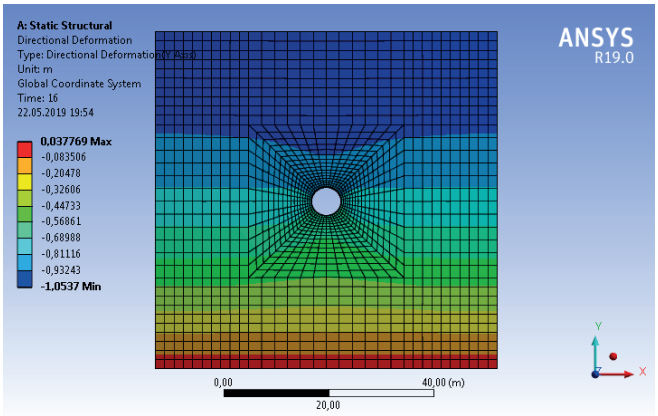

Figure 9 Computational model No. 3. Fields of vertical displacements of the soil massif

5. Computational model No. 3 taking into account changes in time and construction gap

In the third computational model the construction gap between the tunnel shell and the soil massif was additionally considered. During the work of a tunnel powered complex (slurry shield), in a face of a tunnel the excess soil is displaced, owing to what the amount of the withdrawn soil always exceeds the theoretically counted quantity, proceeding from a longitudinal profile of a tunnel. This additionally withdrawn soil carries the name “the lost volume”. In order to count “the lost volume” in computational model, the gap between a tunnel shell and the soil massif which volume was equal to the volume of additionally withdrawn soil, was created. Such a model most plausibly reflects the stress-strain state of the soil environment.

In Figure 7 are shown the maximum equivalent stresses according to the IV strength theory (von Mises). The maximum stress was 74.6 MPa, minimum was 2041.8 Pa.

In Figure 8 are shown the vertical displacements of a shell, whose maximum values were 0.125 m (shell displacements were cleared after the first stage of calculation).

The special attention should be paid to characteristic change of the deformed view of the soil massif - it is possible to observe formation of subsidence trough on the top surface of the massif, what is confirmed by the experimental data when passing tunnels by means of a tunnel powered complex (slurry shield).

Table 1 *Summary table of calculation results*

Characteristic	Computational model No. 1	Computational model No. 2	Computational model No. 3
von Mises stress σ_v (Max/Min)	42.2 MPa/ 429.1 Pa	65.1 MPa/ 744.9 Pa	74.6 MPa/ 2041.8 Pa
Vertical displacements of the shell	0.034 m	0.055 m	0.125 m

6. Comparative analysis of the stress-strain state of computational models

Calculation results are presented in Table 1. Equivalent stresses σ_v according to the IV strength theory (von Mises) are more preferable in the current analysis because the shell is experiencing a combined stress-strain state. They are determined by the following formula [6]:

$$\sigma_v = \sqrt{\frac{1}{2}[(\sigma_1 - \sigma_2)^2 + (\sigma_2 - \sigma_3)^2 + (\sigma_3 - \sigma_1)^2]} \quad (1)$$

where σ_1, σ_2, σ_3 - principal stress.

In Figure 9 fields of vertical displacements of the soil massif are shown.

Now, the attention is devoted to a significant increase in displacements of a surface of the soil massif over a tunnel shell in the third computational model, which considers a construction gap between the tunnel shell and the soil massif.

Such a behavior of the soil massif describes the generalized semi-empirical method of determination of subsidence trough of the land surface, for the case of construction of a single tunnel in uniform soils, which was offered by Attewell and Woodman [7-9]. Subsidence trough of the land surface, which is formed as a result of the tunnel construction, can be described by dependence:

$$S = \frac{V_s}{\sqrt{2\pi} i_x} e^{-\frac{x^2}{2i_x^2}} \left[G\left(\frac{y - y_i}{i_x}\right) - G\left(\frac{y - xy_f}{i_x}\right) \right] \quad (2)$$

where S is the size of displacements of the land surface at a point (x, y); x is the distance from the considered point to the tunnel longitudinal; y is the point coordinate on the tunnel longitudinal; V_S is the net volume of subsidence trough of the land surface; y_i is an initial position of a tunnel; y_f is location of a tunnel face; i_x is width of subsidence trough, $i_x = kZ$; k is the dimensionless constant that characterizes soil parameters; Z is the distance from the Earth's surface to the tunnel longitudinal axis, [10].

Thus, the third computational model is closer to reality and it reflects behavior not only of a tunnel shell, but of the soil environment a tunnel shell, as well.

It should also be noted that emergence of a construction gap between a shell and the soil massif in the third computational model was carried out step by step - the construction gap appeared together with emergence of the corresponding ring of a tunnel shell.

7. Conclusions

Having carried out calculation of the stress-strain state for three computational models – with or without taking into account changes in time and also taking into account a construction gap between the tunnel shell and the soil massif the following conclusions can be drawn:

- Computational model taking into account changes in time gave significant changes in value of the internal forces in the shell. Obtained equivalent stresses, according to the IV strength theory (von Mises), by the second computational model, in which change of computational model in time was considered, were about 54% higher than values obtained by the first computational model, which was carried out without taking into account the changes of computational model in time. Obtained equivalent stresses, according to the IV strength theory (von Mises), by results of the third computational model, in which change of computational model in time and construction gap between the tunnel shell and the soil massif was considered, were about 76% higher than values obtained by the first computational model. Obtained values of the vertical displacements of the tunnel shell, by results of the second computational model, were for about 2.1 cm bigger that values obtained from the first computational model. Obtained values of the vertical displacements of the tunnel shell, by results of the third computational model were for about 9.1 cm bigger than values obtained from the first computational model.
- Taking into account changes in computational model over time has led not only to a significant change in values of internal forces in a shell, it also led to redistribution of those forces on a shell, what essentially changes principle of work of a shell. In addition, the computational model taking into account its change in time makes it possible to estimate the stress-strain state of a shell in each separate ring.
- Accounting of a construction gap allows to reflect behavior not only of a tunnel shell, but also the soil environment a tunnel shell. It is caused by emergence of subsidence trough on the surface of the soil massif.

According to the above said, when determining the stress-strain state of artificial constructions, whose construction is carried out in several stages (installation of bridge spans, installation of tubing of main line tunnels, etc.), it is desirable to consider all the stages of installation of designs when developing computational model, as this approach allows to obtain more correct values of internal forces in the considered object and distribution of those forces is closer to the real one. Calculations of the stress-strain state taking into account change of computational model in time need to be introduced intensively in design of the building constructions.

References

[1] KLEIN, G. K. *Calculation of underground pipelines.* Moscow: Stroiizdat, 1969.

[2] KOSITSYN, S. B., DOLOTKAZIN, D. B. *Calculation of beam systems interacting with an elastic foundation by finite element method using the software complex MSC/Nastran for Windows*. Textbook. Moscow: MIIT, 2004.

[3] KOSITSYN, S. B., LINH, T. X. Numerical analysis of stress - strain state of orthogonal intersecting cylindrical shells with and without taking into account their unilateral interaction with the soil environment. *International Journal for Computational Civil and Structural Engineering*. 2014, **10**(1), p. 72-78. ISSN 2587-9618, eISSN 2588-0195.

[4] LEONTIEV, N. N. A practical method of calculation of thin-walled cylindrical pipe on an elastic foundation. *Proceedings of Moscow Construction Engineering University*. 1957, **27**, p. 47 - 69.

[5] ALEXANDROV, A. V., POTAPOV, V. D. *Foundations of the theory of elasticity and plasticity: Book for universities of construction*. Moscow: High school, 1990. ISBN 5-06-000053-2.

[6] ZIENKIEWICZ, O. C., TAYLOR, R. L. *The finite element method.* Volume 2: *Solid mechanics*. 5. ed. Oxford: Butterworth-Heinemann, 2000. ISBN 0-7506-5055-9.

[7] ATTEWELL, P. B. Ground movements caused by tunnelling in soil. Large ground movements and structures conference: proceedings. London: Pentech Press. 1978, p. 812-948.

[8] ATTEWELL, P. B., SELBY, A. R. Tunnelling in compressible soils: Large ground movements and structural implications. *Tunnelling and Underground Space Technology*. 1989, **4**(4), p. 41-54. ISSN 0886-7798.

[9] BROMS, B. B., BENNERMARK, H. Stability of clay in vertical openings. *Journal of the Soil Mechanics and Foundations Division*. 1967, **93**(1), p. 71-94. ISSN 0044-7994.

[10] PECK, R. B. Deep excavations and tunnelling in soft ground. 7-th ICSMFE : proceedings. 1969, p. 225-290.

Mykola Sysyn - Olga Nabochenko - Franziska Kluge - Vitalii Kovalchuk - Andriy Pentsak*

COMMON CROSSING STRUCTURAL HEALTH ANALYSIS WITH TRACK-SIDE MONITORING

Track-side inertial measurements on common crossings are the object of the present study. The paper deals with the problem of measurement's interpretation for the estimation of the crossing structural health. The problem is manifested by the weak relation of measured acceleration components and impact lateral distribution to the lifecycle of common crossing rolling surface. The popular signal processing and machine learning methods are explored to solve the problem.

The Hilbert-Huang Transform (HHT) method is used to extract the time-frequency features of acceleration components. The method is based on Ensemble Empirical Mode Decomposition (EEMD) that is advantageous to the conventional spectral analysis methods with higher frequency resolution and managing nonstationary nonlinear signals. Linear regression and Gaussian Process Regression are used to fuse the extracted features in one structural health (SH) indicator and study its relation to the crossing lifetime. The results have shown the significant relation of the derived with GPR indicator to the lifetime.

Keywords: *common crossing, structural health monitoring, track-side inertial measurements, rolling contact fatigue, Ensemble Empirical Mode Decomposition, Hilbert-Huang transform, Gaussian Process Regression*

1. Introduction

The expectation of growth of the passenger and freight transportation in Europe demands the high efficiency, reliability and availability of operation of the European railway systems [1]. The railway infrastructure is characterized by the high costs of scheduled maintenance and, at the same time the significant impact of failures on the overall functioning of the railway system operation. The high maintenance costs are due to high share of maintenance to permanent way and switch and crossings (S&C) that according to [2], can reach up to 50 % of overall maintenance costs. The renewal and maintenance of S&C is one of the main cost divers and is estimated in [3] as almost 33 % of the total maintenance costs of railways. The high S&C costs are the result of frequent and cost-expensive, mainly low atomized manual inspections works.

On the other side, the S&C are a significant factor of the railway system availability and safety. According to study [4], the 6 % of unplanned turnout maintenance works cause up to 55 % of train delays. Therefore, railway turnouts have an indirect influence on operational costs due to delays and follow-up delays, rail replacement service, cancellation of train services, alternative routing. The impact on the safety is assessed to 31 % of the track related derailments caused by the S&C faults on the networks of Great Britain [5].

Therefore, the enhancement of the S&C inspection system, by applying the concept of prognostics and health management (PHM), is the key element to the improvement of reliability and availability. The projects and investments that are based on the S&C monitoring have significantly increased in the past years in the railway networks [6-9]. German railways (DB AG) are developing and testing the system ESAH-M (Electronic Analysis System of Crossing - Portable), that is used for common crossing monitoring [9] (Figure 1, left). The system ESAH-M is based on measurement of the spatial accelerations in the frog nose, impact position and train velocities.

The measurement information that is collected over the lifetime of crossings is used to predict the failures of crossing elements: rails, fastenings sleepers and ballast. The most crucial element of common crossing, that usually first limits its lifecycle, is the rolling surface (Figure 1, right). The rolling contact fatigue (RCF) of crossings is a failure that occurs more suddenly that other failures and therefore is often a reason of unplanned maintenance works.

The fault detection and prediction that is based on monitoring of infrastructure objects is the subject of many recent studies. The generalisation of modern data mining approaches with application to the railway track infrastructure is presented in book [10]. A machine learning approach with image processing methods is proposed in [11] for early detection and prediction of the RCF failures in rails of common crossing. An overview of modern diagnostic methods for the common crossings and based on measurements study of the crossing improvement is presented in [12-13]. Monitoring and prediction of the track substructure quality development of ballasted and ballastless track in transition areas is studied in [14-15]. Theoretical and experimental studies of dynamic loading on the crossing frogs, with relation to the crossing geometry are considered in [16]. A comparative study of statistical and mechanical approaches for recovering the relation in inertial measurements to the crossing lifetime is shown in [17].

* [1]Mykola Sysyn, [2]Olga Nabochenko, [1]Franziska Kluge, [2]Vitalii Kovalchuk, [3]Andriy Pentsak
[1]Institute of Railway Systems and Public Transport, Technical University of Dresden, Germany
[2]Department of the Rolling stock and Track, Lviv Branch of Dniprovsk National University of Railway Transport, Lviv, Ukraine
[3]Department of Construction Industry, Lviv Polytechnic National University; Lviv, Ukraine
E-mail: mykola.sysyn@tu-dresden.de

Figure 1 *The track-side inertial measurement systems (left - ESAH-M, right - RCF initiation on the frog nose)*

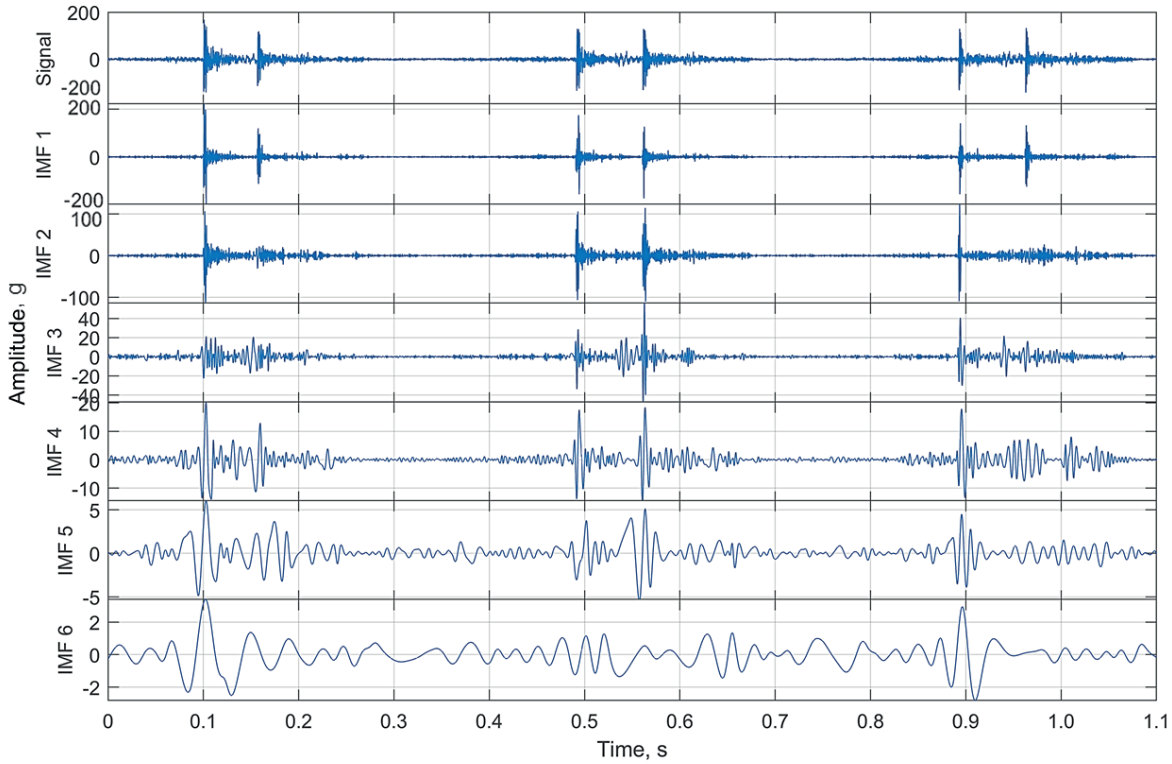

Figure 2 *Vertical acceleration signal and its IMF components at the beginning of the crossing lifecycle*

Scale modelling of an on-board inertial measurement system for detection of the track geometry failures is performed in [18]. The problem of early fault detection on common crossings with on-board inertial measurements with application of the machine learning methods is considered in study [19]. The application of the machine learning methods for evaluation of the railway ballast compaction is shown in [20]. Use of reinforcement learning for adjustment of the disturbance parameters in the railway operational simulation is offered in [21]. The model-based prediction of the crossing geometry deterioration is presented in [22]. An analysis of the critical failures on the railway turnouts and failure prediction using expert approach is proposed in [23]. Numerical predictions of the long-term accumulation of plastic deformation and wear are shown in [24]. Development of indicators for structural health monitoring of common crossing, with track-side inertial measurements, is presented in [25]. The time and spectral features were extracted from inertial measurements, principal component analysis was used to develop the indicator. Studies of the strain-stress distribution in the flange rail assemblies of railway switch is presented in [26]. The optimized flange rail is proposed using mathematical modeling methods for the flange rail assemblies of various designs.

The goal of this paper is an exploration of the modern signal processing machine learning methods according to their application for inertial measurement interpretation and recovering the relation to the crossing lifetime. The study is divided in two subsequent steps: degradation feature extraction and feature fusion with regression techniques. Two alternative approaches of crossing lifecycle prediction are studied.

2. The HHT based features extraction of crossing degradation

The measurements of accelerations were carried out on the switch EW 60-500-1:12 with stiff common crossing. The switch was constructed on a main line with mixed traffic and train velocities range 90-160 km/h. The common crossing of the switch is of the assembly type from steel R350HT. The switch was monitored over its overall lifecycle 29 Mt. The monitoring wad performed with portable measurement system at 11 time

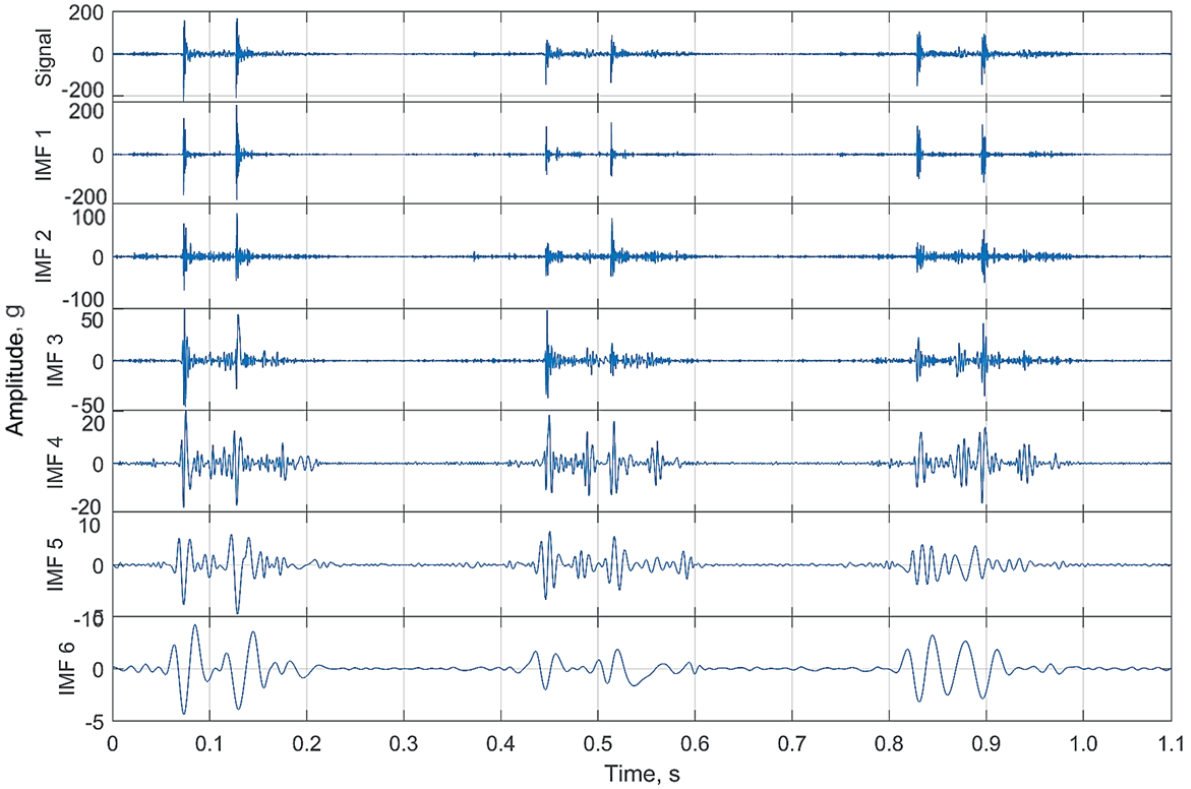

Figure 3 *Vertical acceleration signal and its IMF components at the end of the crossing lifecycle*

Table 1 *Feature set for one observation*

Abbr.	Description
Vi	wheel longitudinal velocity
AufsPos	impact longitudinal position on the frog nose
xEn1 ... xEn7	energy features for the lateral acceleration IMFs
yEn1 ... yEn7	energy features for the vertical acceleration IMFs
zEn1 ... zEn7	energy features for the longitudinal acceleration IMFs

moments during the lifecycle. The measurement results consist of information for each wheel axle: 3 components of acceleration, wheel impact position, longitudinal wheel speed. The overall data set contains the information for 2701 wheel axles.

The feature extraction from acceleration signals is performed with HHT transform. The HHT consists of two steps: empirical mode decomposition (EMD) and Hilbert spectral analysis. The EMD decomposes signal to the intrinsic mode functions (IMFs) during the so-called "sifting process" where the mean signal envelopes are sequentially extracted [10]. The EMD provides many advantages compared to the short-time Fourier transform (STFT) and wavelet transform (WT): analysis of nonlinear and nonstationary signals, better time and frequency resolution. Numerous recent papers approve the successful application of the EMD in mechanical and civil engineering [27-28] for fault detection and prediction. In the present paper the Ensemble Empirical Mode Decomposition (EEMD) is used, that has no drawback of the mode mixing of EMD.

The results of the EMD decomposition in seven IMF for the two measured vertical accelerations, at the beginning and the end of the crossing lifecycle for the same and rolling stock and similar train velocity, are shown on the Figures 2 and 3.

Results of the decomposition show the significant differences in range of the intrinsic mode functions, especially for IMF4-6. In addition, there are evident differences in form and spectrum of the functions. The second step of the HHT is the Hilbert spectral analysis that is applied to each IMF and yields instantaneous frequency and amplitude. The Hilbert transform $H(\omega,t)$, for the data $X(t)$ is defined as follows:

$$H(\omega,t)=\frac{1}{\pi}P\int_{-\infty}^{\infty}\frac{X(t)}{t-\tau}d\tau\,, \tag{1}$$

where: P - is the Cauchy principal value.

The instantaneous frequency is defined as:

$$\omega(t)=\frac{d\theta(t)}{dt}\,, \tag{2}$$

where: $\theta(t)$ - the instantaneous phase that is defined as $\theta(t)=\tan^{-1}\frac{H(\omega,t)}{X(t)}$.

The Hilbert energy spectrum is described as:

$$E(\omega)=\int_0^T H^2(w,t)dt\,. \tag{3}$$

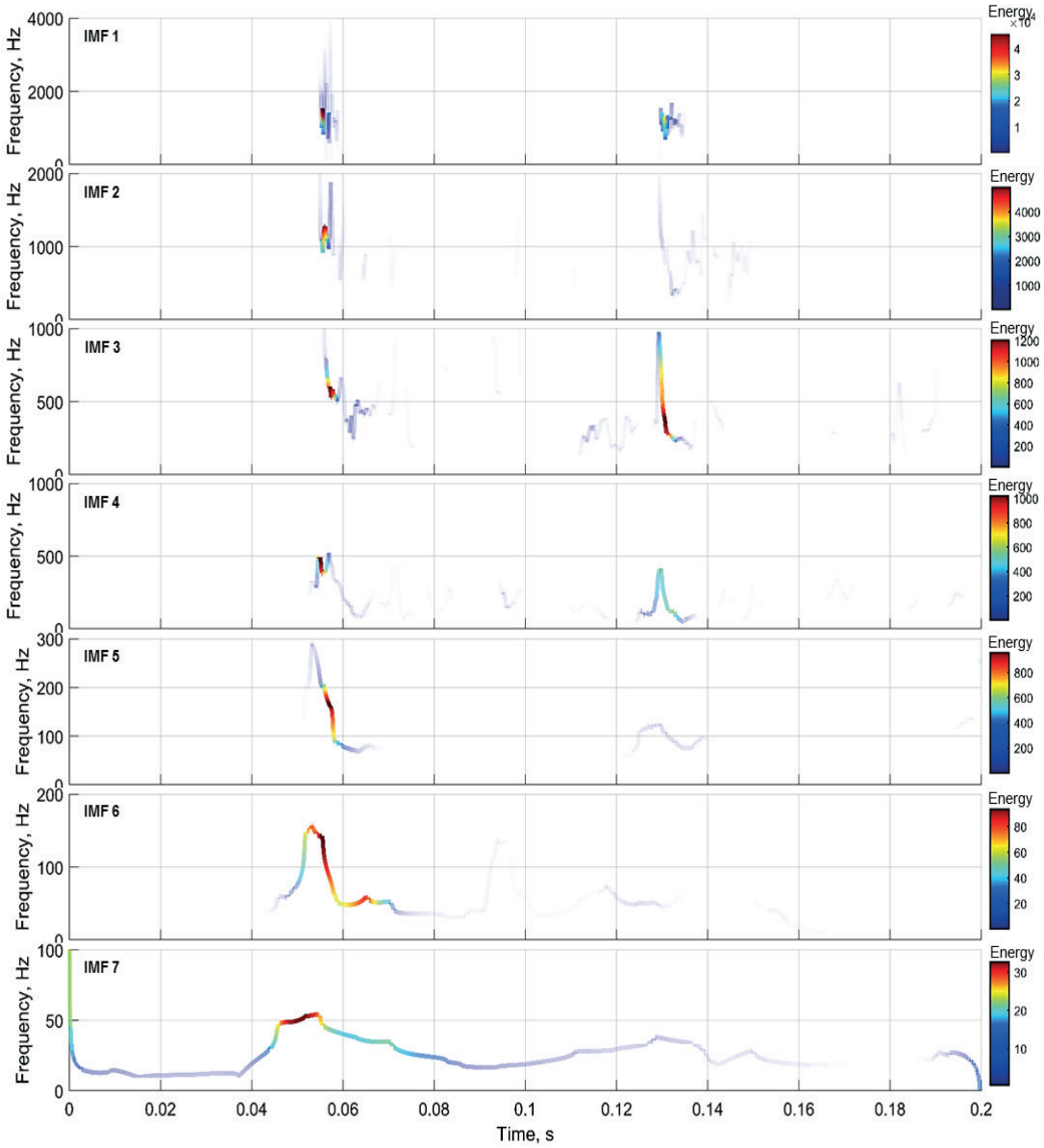

Figure 4 *The HHT spectra for IMF components and their energies for 2 axles*

The energy spectrum features are extracted from each IMF by the Hilbert transform. There are seven energy features for each of the three acceleration components. Additionally, two operation conditions are included to the data set: the wheel longitudinal velocity and the impact longitudinal position on the frog nose. Therefore, 23 features correspond to one measurement or one wheel passing. The acronyms and description of the features are shown in Table 1.

Results of the Hilbert transform in form of instantaneous frequency for each IMF and the energy spectrum highlighting are shown in Figure 4. The diagrams correspond to the first two axle passages to provide the simpler visualization. The energy spectrum distribution among the IMFs and along the time axis is inhomogeneous. The highest energy spectrum is present in IMF1 and IMF2 for the frequency range 1000-1500 Hz that contain more that 90 % of the total energy spectrum. The IMF has the highest energy spectrum in range of about 50 Hz.

3. Assessment of the SH indicator relation to the crossing lifetime

All the extracted 23 features have some relation to the lifetime, but they are subjected to the high noise due to random or systematic factors, as well. Therefore, none of the single features is good enough to be used as the SH indicator. The best features should be selected and fused in one SH indicator. There are many approaches to fusing of the extracted features in one SH indicator. Often used are the linear methods Principal Components or Partial Least Square Regression [29]. Another group of methods is based on regularization techniques, like Ridge or Lasso regression that can provide the optimal features set selection and generalized linear regression. Advantage of the linear regression is a simple interpretation of the machine learning models due to analytical relation between the predictors and regressor. The nonlinear methods, like Support Vector Regression (SVR), Regression Trees, GPR provide much better prediction, however at the same time they are difficult for interpretation.

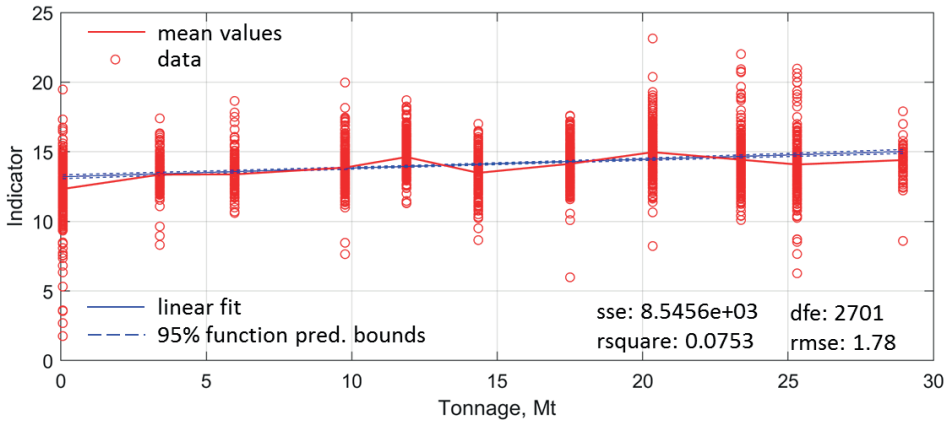

Figure 5 *Linear regression of the structural health indicator*

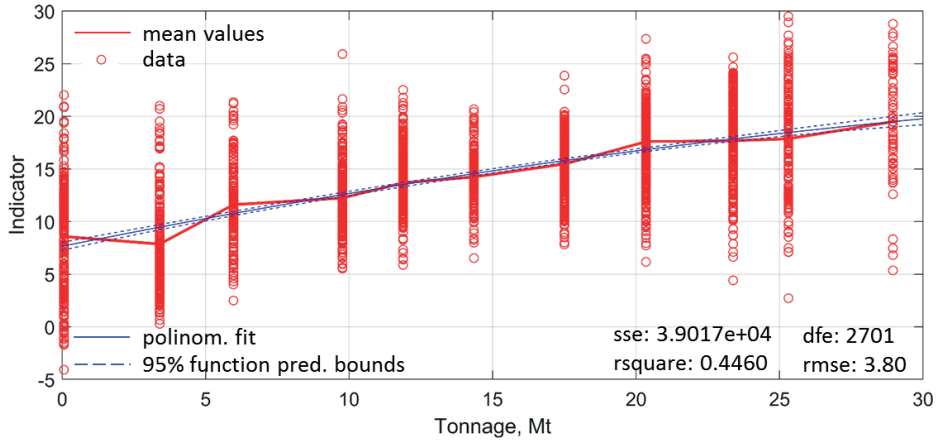

Figure 6 *Gaussian process regression of the structural health indicator*

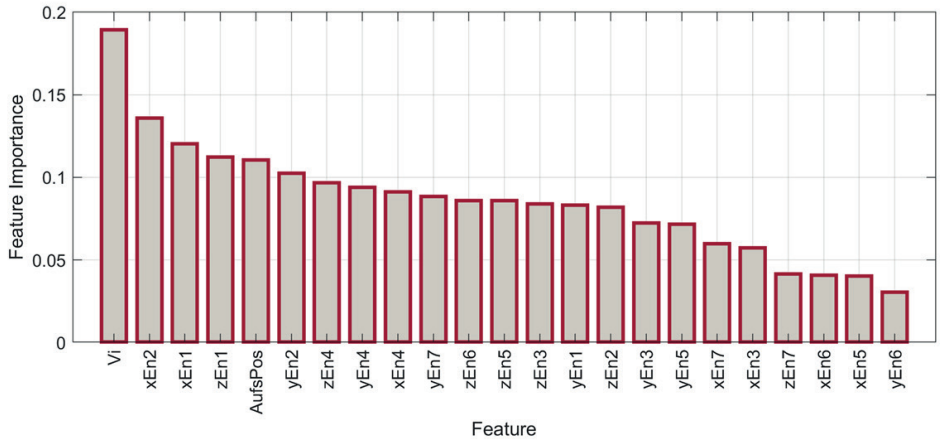

Figure 7 *Feature importance ranking*

3.1 Linear regression

The linear regression with the Lasso regularisation is used for the lifetime prediction of the common crossing. A multiple linear regression model is defined as follows:

$$\hat{y}_i = b_1 x_{i1} + b_2 x_{i2} + \cdots + b_p x_{ip}\,, \tag{4}$$

where:

$\hat{y}_i$ - estimated response,

b_p - the fitted coefficients for *p*-predictor or feature,

x_i - the features of *i*-observation.

The Lasso regularization technique is used to identify important prediction among the redundant ones and therefore to obtain the lower prediction errors. The optimal b_p coefficients are found by solving the following problem:

$$\min_{b0,b}\left(\frac{1}{2N}\sum_{i=1}^{N}(y_i - b_0 - x_i b)^2 + \lambda\sum_{j=1}^{p}|b_j|\right) \tag{5}$$

where:

λ - a positive regularization parameter,

N - the number of observations.

Figure 5 demonstrates the results of the linear regression together with the SH indicator points for each measurement day

during the overall lifecycle of the common crossing. Results show some relation of the indicator to the lifetime but it is relatively weak one with the low coefficient of determination. One possible explanation of that fact could be the nonlinear behavior extracted from the EEMD features that could be explained by the nonlinear regression methods.

3.2 Gaussian Process Regression

In contrast to the linear regression, the Gaussian process regression is a non-parametric approach that finds a distribution over the possible functions that are consistent with the observed data. The Gaussian process is specified by its Kernel covariance function $K(x,x')$ and mean function $m(x)$. It can be defined as follows [30]:

$$f(x) \sim GP(m(x),K(x,x')), \tag{6}$$

where: $m(x) = E[f(x)]$,
$K(x,x') = E[\{f(x)-m(x)\}\{f(x')-m(x')\}]$.

The Gaussian process based fault assessment and prediction are used in many studies [31-32]. The squared exponential Kernel covariance function is used in the present study for the model learning. The resulting SH indicator prediction, with the learned GPR model in 5 fold cross validation, is shown in Figure 6.

Figure 6 shows the clear ascending trend of the SH indicator data points with monotonous growth of the mean values. The results of the GP regression, different to those of the linear regression, demonstrate much better relation of the SH indicator to the crossing lifetime. The polynomial fit shows narrow function bounds that are relatively low, compared to the explained function variation. Figure 7 shows the feature importance ranking for the GP regression. The highest influence has the operation condition feature - the train velocity. The high influence of the energy spectrum features, corresponding to the interaction in the lateral and longitudinal direction, is remarkable. The lowest influence have the features extracted from IMF6-7.

4. Discussion and conclusion

The study results have explored the possibilities of the HHT and EEMD application for monitoring and fault diagnostics of the common crossings. The methods allow to recover the deep relations to the crossing deterioration in the inertial measurement information. The undoubtable advantage of the applied feature extraction methods is the meaningful representation of the nonlinear and non-stationary processes. However, the extracted features show the nonlinear relations to the lifetime. That causes difficulties during the following feature fusion to the SH indicator by the linear regression methods. The linear regression with regularization provide the low prediction quality. The quality of prediction could be substantially enhanced by the nonlinear regression methods. The applied GP regression provides higher determination coefficient than the linear regression and therefore much better relation of SH indicator to the crossing lifetime. However, the better result of prediction brings also more difficult interpretation by the non-parametrical nonlinear GP regression with multiple predictor set.

Despite the relatively good results of the HHT and GPR techniques application for the common crossing deterioration estimation, the possible challenges of their application should be noted, as well as the future solution ways. The prediction is performed for one common crossing and the model trained could not be applicable for another one. One model for many crossings should be developed and tested. The wide scatter range of the developed SH indicator can cause the low prediction quality for low number of observations. The scatter range could be explained by the acceleration measurements from different train types. That factor can be potentially taken into account what in turn could improve the prediction.

References

[1] MAHBOOB, Q., ZIO, E. *Handbook of RAMS in railway systems: theory and practice* [online]. Boca Raton: CRC Press, 2018. eISBN 978-1-315-26935-1. Available from: https://doi.org/10.1201/b21983

[2] FENDRICH, L., FENGLER, W. *Handbuch Eisenbahninfrastruktur / Field manual railway infrastructure* (in German) [online]. Berlin Heidelberg: Springer-Verlag, 2013. ISBN 978-3-642-30020-2, eISBN 978-3-642-30021-9. Available from: https://doi.org/10.1007/978-3-642-30021-9

[3] LETOT, C., DERSIN, P., PUGNALONI, M., DEHOMBREUX, P., FLEURQUIN, G., DOUZIECH, C., LA-CASCIA, P. A data driven degradation-based model for the maintenance of turnouts: A case study. *IFACPapersOnLine* [online]. 2015, **48**(21), p. 958-963. ISSN 2405-8963. Available from: https://doi.org/10.1016/j.ifacol.2015.09.650

[4] XIN, L. *Long-term behaviour of railway crossings: wheel-rail interaction and rail fatigue life prediction* [online]. PhD Thesis. TU Delft, 2017. ISBN 978-9-462-95631-5. Available from: https://doi.org/10.4233/uuid:7ee5405a-85f1-4bd2-b776-2013715c8783

[5] BARKHORDARI, P., GALEAZZI, R. Statistical model of railway's turnout based on train induced vibrations. *IFAC-Papers on Line* [online]. 2018, **51**(24), p. 1278-1284. ISSN 2405-8963. Available from: https://doi.org/10.1016/j.ifacol.2018.09.570.

[6] BOHM, T., WEISS, N. Turnout analytics - smart sensors and artificial intelligence for the all-round healthy turnout (in German). *Eisenbahntechnische Rundschau*. 2017, 5, p. 42-45. ISSN 0013-2845.

[7] SCHOLZ, S., LOMMOCK, R. models for onboard train diagnostics data to improve condition-based maintenance. *16th International Conference on Automated People Movers and Automated Transit Systems 2018: Moving to the Future, Building on the Past: proceedings* [online]. Tampa, Florida: American Society of Civil Engineers, 2018. ISBN 978-0-784-48131-8, p. 85-93. Available from: https://doi.org/10.1061/9780784481318.010

[8] CHUDZIKIEWICZ, A., BOGACZ, R., KOSTRZEWSKI, M., KONOWROCKI, R. Condition monitoring of railway track systems by using acceleration signals on wheelset axle-boxes. *Transport* [online]. 2017, **33**(2), p. 555-566. ISSN 1648-4142, eISSN: 1648-3480. Available from: https://doi.org/10.3846/16484142.2017.1342101

[9] ZOLL, A., GERBER, U., FENGLER, W. Das Messsystem ESAH-M / The measuring system ESAH-M (in German). *EI-Eisenbahningenieur Kalender*. 2016, p. 49-62, ISSN 0934-5930.

[10] ATTOH-OKINE, N. *Big data and differential privacy: analysis strategies for railway track engineering* [online]. John Wiley & Sons, Inc., 2017. ISBN 978-1-119-22904-9, eISBN 978-1-119-22907-0. Available from: https://doi.org/10.1002/9781119229070

[11] SYSYN, M., GERBER, U., NABOCHENKO, O., GRUEN, D., Kluge, F. Prediction of rail contact fatigue on crossings using image processing and machine learning methods. *Urban Rail Transit* [online]. 2019, **5**(2), p. ISSN 2199-6687, eISSN 2199-6679. Available from: https://doi.org/10.1007/s40864-019-0105-0

[12] KOVALCHUK, V., SYSYN, M., SOBOLEVSKA, J., NABOCHENKO, O., PARNETA, B., PENTSAK, A. Theoretical study into efficiency of the improved longitudinal profile of frogs at railroad switches. *Eastern-European Journal of Enterprise Technologies* [online]. 2018, **94**(4), p. 27-36. ISSN 1729-3774, eISSN 1729-4061. Available from: https://doi.org/10.15587/1729-4061.2018.139502

[13] KOVALCHUK, V., SYSYN, M., HNATIV, Y., BAL, O., PARNETA, B., PENTSAK, A. Development of a promising system for diagnosing the frogs of railroad switches using the transverse profile measurement method [online]. *Eastern European Journal of Enterprise Technologies* [online]. 2018, **92**(2), p. 33-42. ISSN 1729-3774, eISSN 1729-4061. Available from: https://doi.org/10.15587/1729-4061.2018.125699

[14] IZVOLT, L., SESTAKOVA, J., SMALO, M. Analysis of results of monitoring and prediction of quality development of ballasted and ballastless track superstructure and its transition areas. *Communications - Scientific Letters of the University of Zilina* [online]. 2016, **18**(4), p. 19-29. ISSN 1335-4205, eISSN 2585-7878. Available from: http://komunikacie.uniza.sk/index.php/communications/article/view/284

[15] IZVOLT, L., SESTAKOVA, J., SMALO, M. The railway superstructure monitoring in Bratislava tunnel no. 1 - Section of ballastless track and its transition areas. *MATEC Web of Conferences* [online]. 2017, **117**, 00063. eISSN 2261-236X. Available from: https://doi.org/10.1051/matecconf/201711700063

[16] BOIKO, V., MOLCHANOV, V., TVERDOMED, V., OLIINYK, O. Analysis of vertical irregularities and dynamic forces on the switch frogs of the underground railway. *MATEC Web of Conferences* [online]. 2018, **230**, 01001. eISSN 2261-236X. Available from: https://doi.org/10.1051/matecconf/201823001001

[17] SYSYN, M., GERBER, U., NABOCHENKO, O., KOVALCHUK, V. Common crossing fault prediction with track based inertial measurements: statistical vs mechanical approach. *Pollack Periodica*. 2019, at press. ISSN 1788-1994, eISSN 1788-3911.

[18] RAPP, S., MARTIN, U., STRAHLE, M., SCHEFFBUCH, M. Track-vehicle scale model for evaluating local track defects detection methods. *Transportation Geotechnics* [online]. 2019, **19**, p. 9-18. ISSN 2214-3912. Available from: https://doi.org/10.1016/j.trgeo.2019.01.001

[19] SYSYN, M., GRUEN, D., GERBER, U., NABOCHENKO, O., KOVALCHUK, V. Turnout monitoring with vehicle based inertial measurements of operational trains: a machine learning approach. *Communications - Scientific Letters of the University of Zilina*, 2019, **21**(1), p. 42-48. ISSN 1335-4205, eISSN 2585-7878. Available from: http://komunikacie.uniza.sk/index.php/communications/article/view/1166

[20] SYSYN, M., NABOCHENKO, O., KOVALCHUK, V., GERBER, U. Evaluation of railway ballast layer consolidation after maintenance works. *Acta Polytechnica* [online]. 2019, **59**(1), p. 77-87. ISSN 1210-2709, eISSN 1805-2363. Available from: https://doi.org/10.14311/AP.2019.59.0077

[21] CUI, Y., MARTIN, U., ZHAO, W. Calibration of disturbance parameters in railway operational simulation based on reinforcement learning. *Journal of Rail Transport Planning and Management* [online]. 2016, **6**(1), p. 1-12. ISSN 2210-9706. Available from: https://doi.org/10.1016/j.jrtpm.2016.03.001

[22] SYSYN, M., GERBER, U., GRUEN, D., NABOCHENKO, O., KOVALCHUK, V. Modelling and vehicle based measurements of ballast settlements under the common crossing. *European Transport / Transporti Europei - International Journal of Transport Economics, Engineering and Law*. 2019, **71**, p. 1-25. ISSN 1825-3997.

[23] PANCHENKO, S., SIROKLYN, I., LAPKO, A., KAMENIEV, A., BUSS, D. Critical failures of turnouts: expert approach. *Procedia Computer Science* [online]. 2019, **149**, p. 422-429. ISSN 1877-0509. Available from: https://doi.org/10.1016/j.procs.2019.01.157

[24] SKRYPNYK, R., EKH, M., NIELSEN, J. C. O., PALSSON, B. A. Prediction of plastic deformation and wear in railway crossings - comparing the performance of two rail steel grades. *Wear* [online]. 2019, **428-429**, p. 302-314. ISSN 0043-1648, eISSN 1873-2577. Available from: https://doi.org/10.1016/j.wear.2019.03.019

[25] SYSYN, M., GERBER, U., NABOCHENKO, O., LI, Y., KOVALCHUK, V. Indicators for common crossing structural health monitoring with track-side inertial measurements. *Acta Polytechnica* [online]. 2019, **59**(2), p. 170-181. ISSN 1210-2709, eISSN 1805-2363. Available from: https://doi.org/10.14311/AP.2019.59.0170

[26] GLUSBERG, B., SAVIN, A., LOKTEV, A., KOROLEV, V., CHERNOVA, L., LOKTEV, D. Counter-rail special profile for new generation railroad switch. *Advances in Intelligent Systems and Computing* [online]. 2020, **982**, p. 571-587. ISSN 21945357. Available from: https://doi.org/ 10.1007/978-3-030-19756-8_54

[27] NASIR, N. N. M., SINGH, S., ABDULLAH, S., HARIS, S. M. Accelerating the fatigue analysis based on strain signal using Hilbert-Huang transform. *International Journal of Structural Integrity* [online]. 2019, **10**(1), p. 118-132. ISSN 1757-9864. Available from: https://doi.org/10.1108/IJSI-06-2018-0032

[28] LI, Y., LIU, J., WANG, Y. Railway wheel flat detection based on improved empirical mode decomposition. *Shock and Vibration* [online]. 2016, 4879283, p. 1-14. ISSN 1070-9622, eISSN 1875-9203. Available from: http://dx.doi.org/10.1155/2016/4879283

[29] HASTIE T., TIBSHIRANI R., FREIDMAN J. *the elements of statistical learning: data mining, inference, and prediction* [online]. 2. ed. New York: Springer-Verlag, 2009. ISBN 978-0-387-84857-0, eISBN 978-0-387-84858-7. Available from: https://doi.org/10.1007/978-0-387-84858-7

[30] RASMUSSEN, C. E. *Gaussian Processes for Machine Learning.* MIT Press. Cambridge, Massachusetts, 2006.

[31] HONG, S., ZHOU, Z. Remaining useful life prognosis of bearing based on Gauss process regression. 5th International Conference on Biomedical Engineering and Informatics BMEI 2012: proceedings [online]. 2012. 6513123, p. 1575-1579. Available from: https://doi.org/10.1109/BMEI.2012.6513123

[32] JONES, S., HUNT, H. E. M. Predicting surface vibration from underground railways through inhomogeneous soil. *Journal of Sound and Vibration* [online]. 2012, **331**(9), p. 2055-2069. ISSN 1095-8568. Available from: https://doi.org/10.1016/j.jsv.2011.12.032

Izabela Sudrychova - Jiri Kuczaj - Ladislav Janosik - Pavel Polednak - Ivana Janosikova*

FIREFIGHTING VEHICLES BRAKING DISTANCE METERING

The paper topic is concerned with the issue of braking dynamics and adhesion coefficients of firefighting vehicles at fire rescue units. The real breaking distances at firefighting vehicles of the water tenders type are presented in the paper. The metering was made on the wet and/or dry asphalt, with different age of tires and the carload. Measured results should be used for drivers' education at fire rescue units to increase the safety during the emergency drives.

Keywords: *braking distance, braking deceleration, braking time, adhesion coefficient, firefighting vehicles*

1. Introduction

Braking on different types of road surfaces in a straight or a bend is one of the basic driving skills the driver must be able to handle in a road critical situation. To handle the critical situations is twice more important for firefighting truck drivers. Their main task is to ensure a safe and rapid transport of the fire rescue unit to an emergency site. The speed of the firefighting truck must be safe in terms of being safely stopped in a critical situation where avoiding an obstacle is impossible to be made. An analysis of Accident Statistics 2011 to 2016 showed that the speeding caused 35 traffic accidents of water tenders only (19 %) during the emergency drive. However, these accidents accounted up to 89 % of total vehicle damage (EUR 1.4 million) in the analysed period [1]. Just those facts have been the reason why the focus of this research was on that basic driving parameter of the firefighting vehicles, which is the braking distance and its change under different conditions. The metering was carried out on the firefighting vehicles deployed at the Fire Rescue Service (FRS) of the Moravian-Silesian Region. For this research, the management of the FRS of the Moravian-Silesian Region granted the firefighting vehicles with the drivers and financed the time spent on the leased training polygon of the LIBROS safe riding centre in Ostrava.

2. Firefighting vehicles

These four firefighting vehicles were used for the metering: Mercedes-Benz Econic 4×2 (Registration numbers: 5T7 9464, 6T8 9896), TATRA T815–2 TerrNo1 4×4.2 (Registration number: 9T5 2242) and TATRA T815–7 6×6.1 (Registration number: 9T5 2260).

The first tested firefighting vehicle *Mercedes-Benz Econic 1833LL 4×2* has a fire mark CAS 20/2700/200-S1T. The two-axle chassis MB Econic 1833LL 4×2 with continuous frame has been designed to operate on paved roads and has a rear axle drive that is equipped with a differential lock. The length of the vehicle is 8220 mm, the width is 2550 mm and the height reaches 3150 mm. The water tank is of a 2700 litres capacity and the foam tank is of 200 litres capacity. The operating weight is 12750 kg and the total weight is 18000 kg. The firefighting vehicle is equipped by a two-ring pressurized air system. The disc brakes are situated on both axles. The firefighting vehicle is equipped by a retarder, ABS and ASR. The front axle of the firefighting vehicle was fitted with Michelin guiding tubeless tires, X Multiway 3D 315/80 R 22.5 radial. On the dual tire rear axle, the tubeless all-season tires Michelin Grip Cold 315/80 R 22.5 radial were used. The front tires were inflated with a pressure of 750 kPa, the rear ones at 730 kPa [2]. Vehicle Registration Number 5T7 9464 tires had a DOT Code 1812 (manufactured in the 18th week of 2012) and they had a 6 mm tread depth. Tires on the second vehicle Registration Number 6T8 9896 had DOT code 1011 (manufactured in the 10th week of 2011) and they had a 5 mm tread depth.

The third tested firefighting vehicle *TATRA T815–2 Terr No1 4×4.2* has a fire marking CAS 20/4000/240-S2T. The chassis has the designation T815–231R55/411. It is a mixed two-axle chassis with an attachable front-axle gear. Both axles are equipped by a differential lock. The length of the vehicle is 7825 mm, width 2550 mm, height 3150 mm. The water tank volume is 4000 litres and the foam tank volume is 240 litres. The operating weight is 12750 kg and the total weight is 18000 kg. The car is equipped with a two-ring pressurized air system. The drum brakes are situated on both axles. The vehicle has an ABS only. The front axle of the car was fitted with Michelin, Cold 385/65 R 22.5 guiding radial tires. The rear axle with double assembly was equipped with the tubeless Barum Road Drive 315/80 R 22.5 radial tires. The front tires were inflated at 800 kPa, the rear ones at 700 kPa [3]. The tires had a DOT code 2614 (manufactured in the 26th week of 2014) and a 12 mm tread depth.

The fourth tested firefighting vehicle *TATRA T815–7 6×6.1* has a fire marking CAS 30/9000/540-S3VH. Vehicle length is 9170 mm, width 2550 mm, height 2830 mm. The water tank has a capacity of 9000 litres and the foam tank volume is 540 litres. The operating weight is 14500 kg and the total weight is 25000 kg. The car is equipped by a two-ring pressurized air system. The drum brakes are on both axles. The vehicle has an ABS only. The car is 3-axle with an all-wheel drive, a simple tire fitting and

* [1]Izabela Sudrychova, [1]Jiri Kuczaj, [1]Ladislav Janosik, [1]Pavel Polednak, [2]Ivana Janosikova
[1]Faculty of Safety Engineering, VSB - Technical University of Ostrava, Czech Republic
[2]Faculty of Economics, VSB - Technical University of Ostrava, Czech Republic
Email: ladislav.janosik@vsb.cz

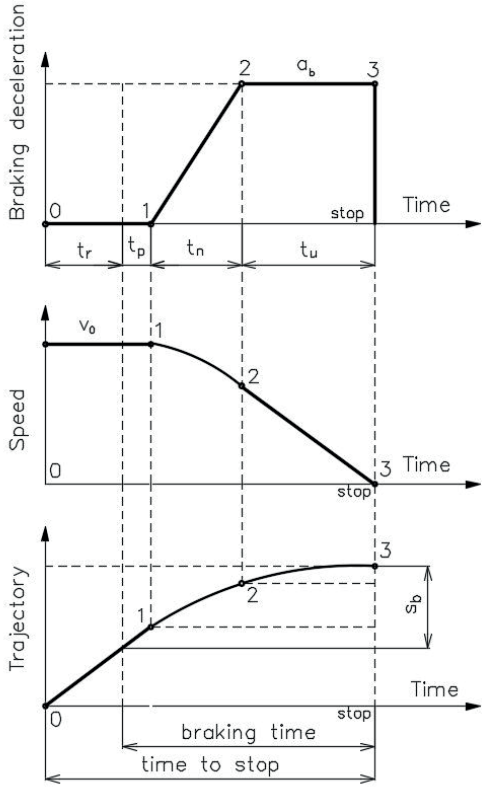

Figure 1 *The course of the braking process*

a differential lock. The front wheel drive is attachable. The car was fitted with radial year-round tires from Continental 14.00 R20 on all three axles. The tires are pressurized at 610 kPa [4]. The tires had a DOT code 0415 (manufactured in the 4th week of 2015) and a 16 mm tread depth.

3. Measuring instruments

The *Performance Box* from Racelogic Ltd, Buckingham, England, was used to measure driving characteristics. A detailed description of this device is available on the manufacturer's website [5]. The device is designed to detect the absolute positioning of the vehicle in the real time. The device then calculates the path, speed, acceleration and many other variables. The recordable frequency is 10 Hz. Its accuracy is determined by the real-time positioning of the vehicle by using signals from three satellite systems (GPS, GLONASS and a third system not identified by the manufacturer). An accuracy of 0.2 km/h at a resolution of 0.01 km/h is given for the speed measurement. An accuracy of 0.05 % (less than 50 cm per 1 km) and 1 cm resolution is given for the trajectory measurement. The accuracy and resolution of the time recording is given by the frequency of the instrument, i.e. 0.1 s. The speed, braking distance and braking deceleration of the vehicle were evaluated using this instrument. The device is equipped with an SD card to store the recorded data. The data were then transferred to the computer and further processed in the VBOX Test Suite version 1.7.55.2453.

The *MASTECH MS6520H −20 °C + 300 °C* infrared thermometer was used to measure the road surface and brakes temperatures. This contactless thermometer has an accuracy of ± 2 %, a resolution of 1 °C, an emission level of 0.95 and an optical resolution of 1:10. The thermometer has a laser pointer, it writes the minimum, maximum and average measured temperature.

4. Theoretical basis of the braking process

The theoretical course of the braking process can be depicted on three graphs (see Figure 1) that describe variations in speed, path, and acceleration over time [6]. The necessary variables are then calculated in the following Equations (1) to (3). For the calculation needs, one does not need to include driver's response time t_r. Within experiments, the driver knows the moment of braking. He only keeps a constant speed until the start of braking is indicated on the test path.

The breaking distance s_b is calculated according to:

$$s_b = v_0 \cdot t_{pr} + \frac{1}{2} \cdot \frac{v_0^2}{|a_b|}. \quad (1)$$

The initial speed v_0 is the speed at which the vehicle was moving before the braking started. The preparation time t_{pr} is characterized by the delay time t_p and the reaction time t_n. The delay time is the time between the moment the brake pedal is depressed and the moment of brake system starts to operate, i.e. when the brake lining abuts against the brake pad. The

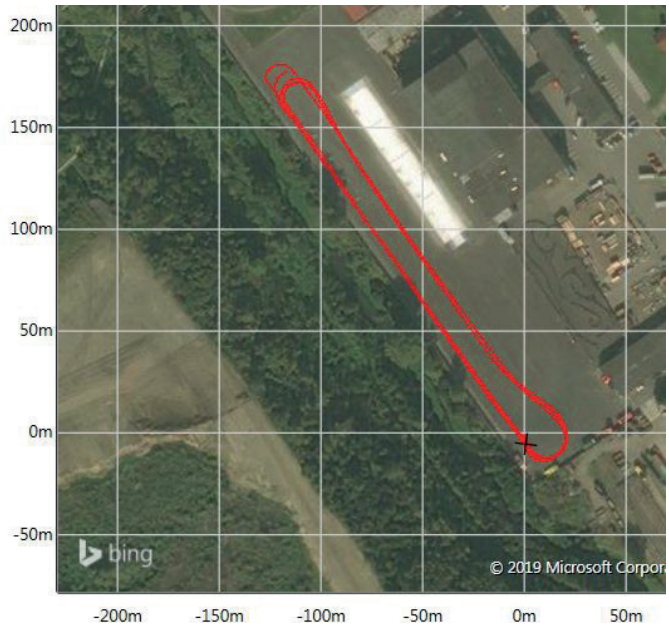

Figure 2 *Vehicle M-B Econic position record when testing*

reaction time is the time before the brakes start to work fully. The preparation time is calculated according to:

$$t_{pr} = t_p + \frac{t_n}{2}. \quad (2)$$

According to [6], the variables values are usually t_p = 0.05–0.15 s, t_n = 0.03–0.15 s. The average values used for the assessment of traffic accidents are given t_p = 0.1 s and t_n = 0.2 s [7]. Theoretically, one can calculate the braking deceleration a_b according to:

$$|a_b| = g \cdot \mu. \quad 3)$$

The coefficient of adhesion μ can be taken from the literature for a theoretical calculation, e.g. [4]. At first, it is necessary to calculate the required breaking distance for the safe execution of the experiments.

By adjusting Equation (1), one obtains the equation for calculating the real braking deceleration a_b, based on the experimentally measured values, where s_b is the braking distance, t_{pr} the preparation time and v_0 the initial velocity:

$$|a_b| = \frac{v_0^2}{2 \cdot s_b - (2 \cdot v_0 \cdot t_{pr})}. \quad (4)$$

For this calculation, the delay time t_p = 0.1 s and the reaction time t_n = 0.02 s were calculated. The same values were used for all the three vehicle types as they were determined by the same design type of the braking system. After adjusting the Equation (3), one can calculate the adhesion coefficient μ.

5. Methods

The experimental measurement of braking distances took place at the training centre of the LIBROS Safety Centre in Ostrava, Palacky 1114 Street, in 2018, March 14. The surface of the experimental track was dry asphalt (bituminous, weathered, 8 years old). The first measuring started at 7:00 a.m. and the experimental driving was completed at 3:00 p.m. The air temperature was 10 °C at the beginning of the experiment. At 9:10, started to rain and the air gradually cooled to 5.5 °C. An example of a M-B Econic (registration mark 6T8 9896) vehicle position recording in the orthophoto map when evaluating the first set of experiments in the VBOX Test Suite software is shown in Figure 2. The vehicle's starting position is marked with a cross in the figure.

To determine the real adhesion coefficients μ according to Equations (3) and (4), it was necessary to determine the breaking distance of a vehicle s_b. The breaking distance is given by the point of change (decrease) in its initial velocity v_0, at which the driver started to brake until the moment of stopping the vehicle. The braking time was also found from the graphs.

The exact speed of the vehicle was checked by the driver using the Performance Box, which was attached to the vehicle's windscreen in driver's field of view. For the M-B Econic, the initial speed before starting braking was determined at v_0 = 60 km/h. For TATRA vehicles, the initial speed v_0 = 50 km/h was determined.

The procedure for each experiment was as follows. The Performance Box was placed in the car. The driver started the vehicle after activating the device and establishing a satellite connection and then began to accelerate to the agreed initial speed v_0. The driver started to brake as much as possible after reaching and stabilizing that speed. This experimental drive was carried out 5 times on a defined circuit. One measured run on a test circuit lasted about 80 seconds. The Performance Box was moved to the next vehicle after finishing of each measured series. These experiments were conducted for each of the 4 vehicles tested.

Realized experiments on the training polygon were divided into the following three stages from the perspective of the load and the state of the road surface:

Table 1 *Input driving characteristics with full water tank on dry asphalt*

Vehicle (registration mark) Parameter	MB Econic (6T8 9896)	TATRA 815-7 (9T5 2260)	TATRA 815-2 (9T5 2242)	MB Econic (5T7 9464)
Test time [hh:mm]	07:00	07:42	08:10	08:22
Air temperature [°C]	10.0	10.0	10.0	10.0
Road surface temperature [°C]	6.6	6.6	6.0	6.7
Initial speed [km/h]	60	50	50	60
Front brake temperature [°C]	192	150	78	195

Table 2 *Input driving characteristics with full water tank on wet asphalt*

Vehicle (registration mark) Parameter	MB Econic (5T7 9464)	MB Econic (6T8 9896)	TATRA 815-2 (9T5 2242)	TATRA 815-7 (9T5 2260)
Test time [hh:mm]	09:22	09:41	10:05	10:20
Air temperature [°C]	6.0	6.0	7.0	6.0
Road surface temperature [°C]	6.5	5.7	5.5	5.8
Initial speed [km/h]	60	60	50	50
Front brake temperature [°C]	243	241	87	94

Table 3 *Input driving characteristics with empty water tank on wet asphalt*

Vehicle (registration mark) Parameter	MB Econic (6T8 9896)	MB Econic (5T7 9464)	TATRA 815-2 (9T5 2242)	TATRA 815-7 (9T5 2260)
Test time [hh:mm]	13:45	14:05	14:20	14:40
Air temperature [°C]	7.0	9.0	8.0	9.0
Road surface temperature [°C]	5.6	5.9	6.1	6.2
Initial speed [km/h]	60	60	50	50
Front brake temperature [°C]	186	183	70	47

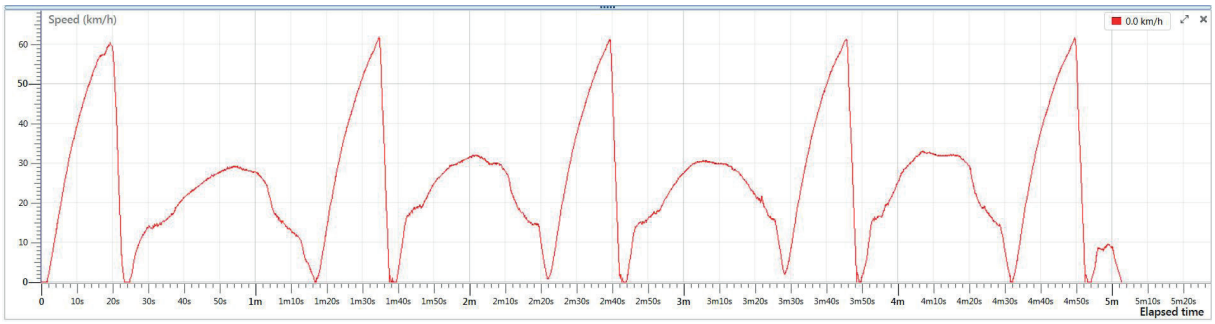

Figure 3 *Speed record based on M-B Econic vehicle time during testing*

- driving with a full water tank on dry asphalt (see Table 1),
- driving with a full water tank on wet asphalt (see Table 2),
- driving with drained water tank on wet asphalt (see Table 3).

The fourth stage of experiments with a drained water tank on dry asphalt fell out from the original plan due to the change of weather.

The outside air temperature was recorded by the thermometers installed in the vehicles before each measurement. The contactless thermometer was used to measure the surface temperature of the road on which the vehicle was moving. The measurement start time was also recorded. At the end of the 5 measurements the brake temperature was measured by a contactless thermometer. In the following Tables 1 to 3, all of these recorded environmental and vehicle data are summarized.

6. Results

The presentation of individual experiments results is summarized in the following sections in the time sequence in which they were carried out. Figure 3 shows the M-B Econic's speed record (6T8 9896) during the first stage of the experiment. The record shows the continuous course of all the five measured rides.

Figure 4 shows a detail of the first run processing of the above record. The vehicle speed is presented here in two graphs depending on time and distance. The marked limits can be visually checked on the upper graph for a braking time of about 3.3 s and a braking distance of 26.3 m. The resulting values were determined by the VBOX Test Suite to evaluate all the measurements by specifying that the initial velocity is equal to v_0

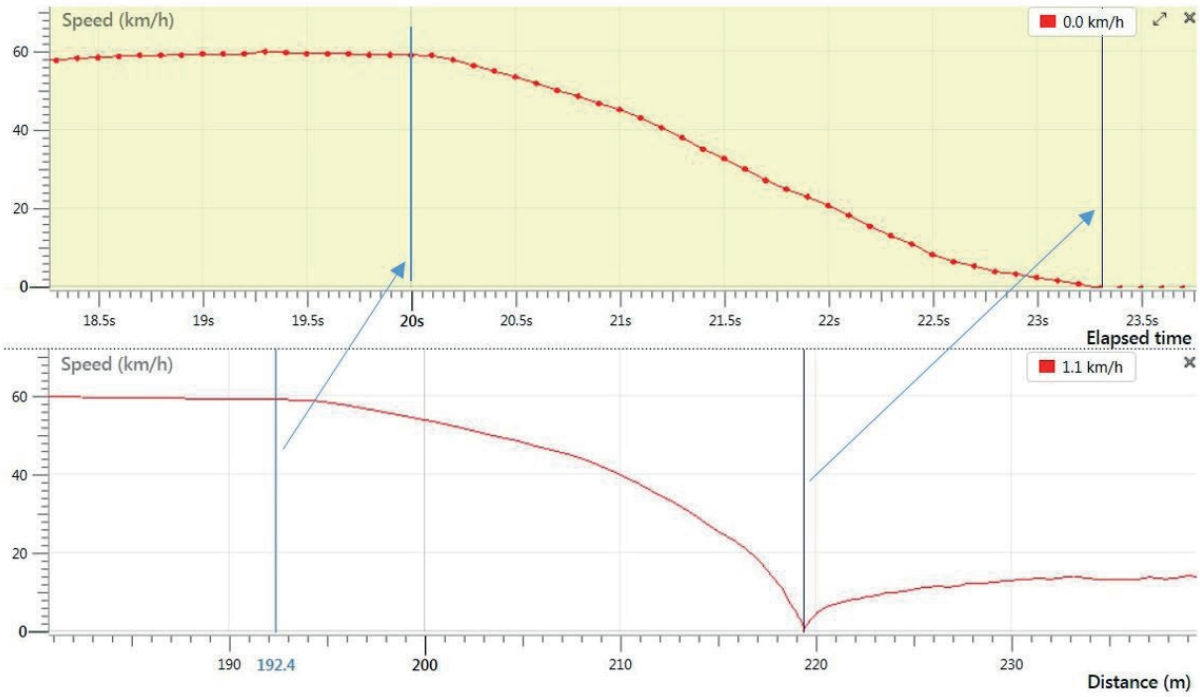

Figure 4 *Detail of the first run processing*

Table 4 *Results of braking distances measuring on dry asphalt with full water tank*

order	MB Econic (6T8 9896)		TATRA 815-7 (9T5 2260)		TATRA 815-2 (9T5 2242)		MB Econic (5T7 9464)	
	time (s)	breaking distance (m)	time (s)	breaking distance (m)	time (s)	breaking distance (m)	time (s)	breaking distance (m)
1	3.26	26.30	2.61	18.86	2.83	16.88	2.92	25.02
2	2.58	21.82	2.88	18.02	2.40	17.39	3.27	25.34
3	3.08	21.37	2.71	16.03	2.37	16.74	3.35	24.57
4	2.58	21.97	2.41	17.10	2.36	17.15	3.20	26.70
5	2.64	21.69	2.46	17.32	2.82	17.50	2.77	23.58

Table 5 *Results of braking distances measuring on wet asphalt with full water tank*

order	MB Econic (5T7 9464)		MB Econic (6T8 9896)		TATRA 815-2 (9T5 2242)		TATRA 815-7 (9T5 2260)	
	time (s)	breaking distance (m)	time (s)	breaking distance (m)	time (s)	breaking distance (m)	time (s)	breaking distance (m)
1	2.86	23.70	2.89	23.89	3.39	29.38	2.78	20.12
2	2.71	23.23	2.62	22.74	2.66	19.09	2.57	18.19
3	2.87	23.86	3.17	24.15	3.05	18.74	2.95	17.79
4	3.33	23.64	3.54	25.29	2.61	18.35	2.87	22.74
5	7.68	28.27	3.28	25.59	2.52	17.84	2.43	17.32

and the final velocity is zero. The program-determined parameters are shown in Tables 4 to 6, divided into individual measurement stages and according to vehicles in the time sequence of the experiments.

The CAS 20 TATRA 815-2 4×4 (9T5 2242) exceeded the agreed initial speed v_0 = 50 km/h before braking during the first measurement on the wet asphalt with a full tank and repeatedly with an empty tank on the wet asphalt. This distorted the evaluation results. Therefore, these values were not included in the resulting average of the measured braking distances.

At CAS 20 MB Econic 4×2 (5T7 9464) vehicle, when measured on the wet asphalt with a full tank, the driver relieved the brakes. Subsequently, the vehicle was not completely stopped and the stopping distance was therefore distorted. For this reason, this experiment is not included in the resulting average of the measured values. On the same vehicle, when measured on the wet asphalt with an empty tank, a brief momentary release of the power supply occurred at 14:09 during the fourth run on the circuit. There is only a part of the record available with the vehicle starting, the record ended at reaching the speed of 56 km/h. After a quick

Table 6 *Results of braking distances measuring on wet asphalt with empty water tank*

order	MB Econic (6T8 9896)		MB Econic (5T7 9464)		TATRA 815-2 (9T5 2242)		TATRA 815-7 (9T5 2260)	
	time (s)	breaking distance (m)	time (s)	breaking distance (m)	time (s)	breaking distance (m)	time (s)	breaking distance (m)
1	2.56	21.28	2.54	21.62	3.09	26.86	2.36	17.32
2	2.74	23.56	2.67	22.79	2.29	15.72	2.51	16.11
3	2.61	21.82	2.70	23.12	2.36	16.23	2.42	15.94
4	2.65	22.38	-	*power failure*	2.42	17.02	2.47	16.05
5	2.70	22.60	2.71	23.99	2.46	17.13	2.56	16.30

Table 7 *Resulting breaking deceleration* a_b *[m/s²]*

Vehicle (registration mark)	TATRA 815-2 (9T5 2242)	TATRA 815-7 (9T5 2260)	MB Econic (5T7 9464)	MB Econic (6T8 9896)
Dry asphalt surface, full water tank	6.18	6.05	5.98	6.68
Wet asphalt surface, full water tank	5.68	5.45	6.38	6.17
Wet asphalt surface, empty water tank	6.43	6.51	6.60	6.78

Table 8 *Resulting adhesion coefficient* μ *[-]*

Vehicle (registration mark)	TATRA 815-2 (9T5 2242)	TATRA 815-7 (9T5 2260)	MB Econic (5T7 9464)	MB Econic (6T8 9896)
Dry asphalt surface, full water tank	0.63	0.62	0.61	0.68
Wet asphalt surface, full water tank	0.58	0.56	0.65	0.63
Wet asphalt surface, empty water tank	0.66	0.66	0.67	0.69

Table 9 *Comparison of the coefficients of adhesion*

Road surface	Theoretical coefficients of adhesion	Calculated coefficient of adhesion
dry asphalt	0.6–0.9	0.61–0.68
wet asphalt	0.3–0.8	0.58–0.65

check by the driver, the power was restored during the ride to the starting position for the fifth run.

The measured braking distances were averaged and the average braking deceleration a_b and the adhesion coefficient μ were calculated according to Equations (3) and (4). The results are shown in Tables 7 and 8.

The resulting values may be distorted by the ABS function. The ABS was activated with the different effect while testing and the wheels were not always blocked, which would probably lead to greater braking deceleration and hence greater coefficient of adhesion.

7. Discussion

The age of the tire counts among many factors that affect the adhesion and thus the resulting braking distance of the vehicle. It is generally believed that the age of the tire affects the adhesion factor. In these experiments with M-B Econic vehicles, the tires produced in March 2011 were used on one vehicle and those produced in May 2012 were used on the second vehicle. The results for specifically tested vehicles did not directly confirm the influence of the tire age on the braking distance.

The expectation that a vehicle with a drained water tank would have a shorter breaking distance has been confirmed.

In Table 9, the theoretical coefficients of adhesion [6] are compared to the measured values. On the wet asphalt, the measured coefficients of adhesion are within the theoretical interval [6]. On dry asphalt, the measured values are closer to the lower limit of the reported interval. The results are likely to be affected by the repeated multiple braking of the vehicles and thus the warming of the brakes.

8. Conclusion

Measurements and calculations found that the coefficient of adhesion between the dry and wet asphalt did not differ significantly. The biggest difference was at the vehicle T815-7, where the full water tank adhesion coefficient was 0.62 on the dry asphalt and 0.56 on wet asphalt (the difference is 0.06).

Another point of interest resulted from the comparison of two M-B Econic cars, when the coefficient of adhesion in two of the three measurements was better for a vehicle with older tires with a more worn out pattern. For a vehicle with the newer tires, the adhesion coefficient was better only with a full water tank and on the wet asphalt. To confirm whether this is caused by tires,

more measurements on other vehicles would be required. So far, it can only be said that tires on vehicles parked in garages, where they are not exposed to direct sunlight, do not have significantly different properties compared to younger tires.

A surprising finding was a significant improvement in adhesion on wet asphalt tests, where the water tank was discharged for all the vehicles. If the adhesion theoretically does not depend on the weight of the vehicle, then the ABS must be the cause. This system limits the efficiency of the brake system as the brake temperature does. Each brake system has a certain temperature at which it is the most efficient. The breaking efficiency is not optimal if the brake is at a low temperature or vice versa, then the braking effect is noticeably weakened.

The front brakes temperature was ascertained after each measurement series. A much greater increase in disc brakes on the M-B Econic cars was noticed. They cannot be compared directly to the other two TATRA cars in obtained results. These vehicles had a lower starting speed v_0 due to the limitation of the runway length (approximately 200 m) available to the vehicles for testing. The second aspect is another design of drum brakes on these vehicles.

Acknowledgments

This research was realized within the project of specific research *„Safe ride of fire fighting vehicles to an emergency"*, project registration number SP2017/51 and under the support of the FRS of the Moravian-Silesian Region based on the *„Agreement of the Cooperation"*with the Faculty of Safety Engineering, VSB – Technical University of Ostrava.

References

[1] JANOSIK, L., JANOSIKOVA, I., COCHLAR, M., JEMELIK, S. economic aspects of firefighting vehicles safe driving within EU civil protection. 4th International Conference on European Integration 2018: ICEI 2018: proceedings 1st part. Ostrava: VSB – Technical University of Ostrava, 2018. ISBN 978-80-248-4169-4, p. 556–565.

[2] THT. Water tender: CAS 20/2700/200-S1T Mercedes-Benz Econic 4×2 [online]. Policka: THT Policka, s.r.o., 2016. [Viewed 2019–02–18]. Available from: https://www.tht.cz/en/water-tenders/cas–20-s–1-t-mercedes-benz-econic–4×2

[3] THT. Water tender: CAS 20/4000/240-S2T T815–2 4×4.2 [online]. Policka: THT Policka, s.r.o., 2016. [Viewed 2019–02–18]. Available from: https://www.tht.cz/en/water-tenders/cas–20-t815-2–4×4

[4] THT. Water tender: CAS 30/9000/540 – S 3 VH T815–7 6×6.1. THT [online]. Policka: THT Policka, s.r.o., 2016. [Viewed 2019–02–18]. Available from: https://www.tht.cz/en/water-tenders/cas30-s3r-t815–7

[5] VBOX Motorsport. Products [online]. Racelogic Ltd. [Viewed 2019–02–18]. Available from: https://www.vboxmotorsport.co.uk/index.php/en/products/performance-meters/performancebox

[6] VLK, F. *Dynamics of motor vehicles* (in Czech). Brno: Frantisek Vlk publishing, 2003. ISBN 80–239–0024–2.

[7] VLK, F. *Working on dynamics of motor vehicles* (in Czech). Brno: Frantisek Vlk publishing, 2001. ISBN 80–238–6574–9.

COMMUNICATIONS – Scientific Letters of the University of Zilina
Author guidelines

- All papers have to deal with the topic of transport and be submitted strictly within one of the listed subtopics. Please, refer to list of topics and subtopics here and indicate it clearly when submitting your paper.
- Submitted papers must be unpublished and must not be currently under review for any other publication.
- Manuscripts written in good English must include abstract and keywords also written in English. The abstract should not exceed 10 lines.
- Submitted manuscripts should not exceed 20 pages including figures and graphs
- Submission should be sent by e-mail – as an attachment – to the following address: komunikacie@uniza.sk.
- The author's exact mailing address, full names, E-mail address, telephone or fax number, the name and address of the organization and workplace (also written in English) must be enclosed.
- For all manuscripts a double-blind peer review by at least two independent reviewers and language correction is mandatory.
- After reviewing and incorporating the editor's comments, the final draft (before printing) will be sent to authors for final review and minor adjustments.

The full author quidelines are available at:
http://komunikacie.uniza.sk/index.php/communications/guidelines

komunikácie
COMMUNICATIONS

VEDECKÉ LISTY ŽILINSKEJ UNIVERZITY
SCIENTIFIC LETTERS OF THE UNIVERSITY OF ZILINA
VOLUME 21 Issue 3

https://doi.org/10.26552/com.J.2019.3

Address of the editorial office:
University of Zilina
EDIS – Publishing House
Univerzitna 8215/1
010 26 Zilina
Slovakia

E-mail: komunikacie@uniza.sk

Individual issues of the journal can be found on:
http://komunikacie.uniza.sk

Each paper was reviewed by two reviewers.

Journal is excerpted in **SCOPUS** and **EBSCO.**

Published quarterly by University of Zilina in
EDIS – Publishing House of University of Zilina

Registered No: EV 3672/09

ISSN (print version) 1335-4205
ISSN (online version) 2585-7878

ICO 00397 563

August 2019